POLITECNICO DI MILANO

Department of Aerospace Engineering
PhD in Aerospace Engineering - XXIV Course

BALLISTICS OF INNOVATIVE SOLID FUEL FORMULATIONS FOR HYBRID ROCKET ENGINES

Advisor:
Prof. Luigi T. DE LUCA

Head of the Doctoral Program:
Prof. Sergio RICCI

PhD Dissertation of:
CHRISTIAN PARAVAN
Matr. 738533

26 March 2012

ABSTRACT

Ballistics of solid fuel formulations for hybrid propulsion was investigated with experimental and numerical approaches. Experimental activity was conducted by a lab-scale 2D radial burner enabling visualization of the combustion process. A non intrusive, optical time-resolved technique for regression rate measurement was designed and validated. Combustion tests were performed for relative ballistic grading of different fuel formulations and for investigation of hybrid fuel ballistics under forced transient regime. For the relative ballistic grading, combustion tests were performed on fuel formulations based on HTPB (Hydroxyl Terminated PolyButadiene) and SW (Solid paraffin Wax) with chamber pressure ranging from 7 to 16 bar, under oxygen with initial mass flux of nearly 400 $kg/(m^2s)$. Under the investigated conditions HTPB exhibited a regression rate dependent from oxidizer mass flux but not influenced from chamber pressure. HTPB was considered as baseline for relative ballistic grading of the investigated fuels. SW based fuels exhibited a marked dependence of regression rate from chamber pressure. With respect to baseline at an oxidizer mass flux of 300 $kg/(m^2s)$, regression rate enhancement for SW burning decrease from 500% to 260% when chamber pressure is increased from 7 to 16 bar. Commercial and lab–scale energetic additives of different kind and particle-size were used for solid fuel loading. Considering commercially available additives, different variants of nano-sized aluminum powder (ALEX) and micron-sized magnesium-boron (MgB) powders were tested. Under the investigated conditions, tested ALEX exhibited a marked regression rate increase with respect to baseline for high oxidizer mass fluxes [up to 80% at 350 $kg/(m^2s)$ for fluoroelastomer alcohol-coated powder]. Nevertheless due to high sensitivity to oxidizer mass flux, this performance enhancement is lost during combustion. A remarkable exception is the fluoropolymer-coated nano-sized aluminum (VF–ALEX). This additive can provide a significant regression rate increase over the whole oxidizer mass flux range, providing an average regression rate enhancement with respect to baseline of 30%. Considering MgB powders, MgB90 (20% Mg) can provide significant regression rate enhancement of 64% for oxidizer mass fluxes of 350 $kg/(m^2s)$. HTPB doped with this additive is less sensitive than the ALEX-doped counterpart to oxidizer mass flux changes. With SW-based fuels promising high performance without granting mechanical properties, regression rate enhancement achievable by HTPB-based solid fuel loaded with MgB and VF-ALEX offers interesting possibilities for hybrid propulsion development. Ballistic characterization of a HTPB-based fuel loaded with aluminum hydride (AlH_3) was conducted under pure oxygen and under an oxidizing mixture 70% oxygen + 30% nitrogen. Test conducted in presence of nitrogen exhibited a regression rate enhancement with respect to baseline that was not achieved when conducting similar tests in oxygen. Investigation of hybrid solid fuel ballistics was conducted also by a numerical approach aiming to the determination of the regression rate of the solid fuel grain under convective heat transfer regime. Analysis focused on HTPB burning in gaseous oxygen. The proposed approach is based on the definition of effective values of thermophysical parameters considered for the determination of parameters of interest as Reynolds number (Re) and convective heat transfer coefficient. Effective values are determined considering the actual, instantaneous oxidizer to fuel ratio determined during the experimental sessions. With the proposed approach the convective model can properly estimate the experimental regression rate for mass flux values above 280 kg/(m^{2}s), with a difference with respect to experimental data of 10%. For lower oxidizer mass fluxes higher differences between experimental and numerical values are achieved. Under the investigated conditions this result underlines the relative importance of radiative heat transfer in the heat feedback from flame to the regressing surface for low values of oxidizer mass flux (in turn inducing a reduced convective heat transfer). Investigation of hybrid fuel ballistics under forced transient condition was performed considering HTPB burning with oxidizer mass flow throttling during combustion. In particular, during the combustion tests oxidizer mass flow was throttled down in a first transient leg followed by a second transient leg in which oxidizer mass flow rate was increased. Under the investigated conditions during the throttling down transient, regression rate exhibits a monotone decrease of regression rate with no marked overshoot/undershoot phenomena. The throttling up transient is characterized by a regression rate increase possibly yielding to overshoot phenomena. The latter could be caused by thermal lag effects in the solid phase. Nevertheless, under the investigated conditions, HTPB behavior revealed an intrinsic stability in transient phases related to throttling events.

CONTENTS

LIST OF FIGURES

LIST OF TABLES

NOMENCLATURE

ACRONYMS AND ABBREVIATIONS

ALEX	=	Aluminum Exploded (nAl produced by EEW)
AMROC	=	American Rocket society
APS	=	Air–Passivated
APT	=	Advanced Powder Technology
AN	=	Ammonium Nitrate
AP	=	Ammonium Perchlorate
B90	=	Boron with 90% purity
B95	=	Boron with 95% purity
BET	=	Brunauer Emmet Teller
CCP	=	Condensed Combustion Product
CEA	=	Chemical Equilibrium with Applications
CSD	=	Chemical System Division
CL	=	Characteristic Length (for Re evaluation)
CTBN	=	Carboxyl–Terminated Polybutadiene–Acrylonitrile
DARPA	=	Defense Advanced Research Projects Agency
DMA	=	Dynamic Mechanical Analysis
EEW	=	Electric Explosion of Wire
F–ALEX	=	Fluorotelomer Alcohol Coated ALEX
FLOX	=	Fluorine Oxygen mixture
FP7	=	7th Framework Program (of European Union)
fps	=	frame per second
FS	=	Full Scale
FTOH	=	Fluorotelomer Alcohol
GAP	=	Glycidyl Azide Polymer
GIRD	=	Gruppa Isutcheniya Reaktinovo Dvisheniya (Group of Investigation on Reactive Motion)
HFI	=	Hexane Tetrahydrofuran Isopropanol
HPDP	=	Hybrid Propulsion Demonstration Program
HRE	=	Hybrid Rocket Engine
HT	=	Hat Transient
HTPB	=	Hydroxyl–Terminated PolyButadiene
I_{sp}	=	Specific Impulse, s
JP	=	Jet Fuel
L–ALEX	=	Octadecanoic Acid Coated ALEX
LEX	=	Lithergol EXperimental
LOX	=	Liquid OXygen
LRE	=	Liquid Rocket Engine
MgB	=	Magnesium–Boron
μAl	=	Micron–sized Aluminum

ACRONYMS AND ABBREVIATIONS (Continued)

NA	=	Not Available
nAl	=	Nano–sized Aluminum
NASA	=	National Aeronautics and Space Administration
NAMMO	=	Nordic Ammunition Group
NL	=	Next Leg
NPS	=	Not Air–Passivated
O/F	=	Orbital Technologies Corporation
ORBITEC	=	Oxidizer–to–Fuel Ratio
ORPHEE	=	Operating Research Preject for Hybrid Engine in Europe
PB	=	PolyButadiene
PMM	=	PolyMethylMethacrylate
PMMA	=	PolyMethylMethacrylate (Acrylic)
PL	=	Previous Leg
PSU	=	Pennsylvania State University
Re	=	Reynolds number, $\rho u(CL)/\mu$
SEP	=	Société Européenne de Propulsion (European Society of Propulsion)
SL	=	Quasi–steady Leg
SNECMA	=	Société Nationale d'Etude et de Construction de Moteurs d'Aviation (National Society for the StUdy and the Construction of Aviation Engines)
SPARTAN	=	SPAce Exploration Research for Throtteable Advaced ENgine
SRM	=	Solid Rocket Motor
SA	=	Octadecanoic Acid (or Stearic Acid)
SPLab	=	Space Propulsion Laboratory
SW	=	Solid Paraffin Wax
TOT	=	Thickness Over Time
TL	=	Transient Leg
TMD	=	Theoretical Maximum Density
UTC	=	United Technology Center
VF–ALEX	=	Fluorel and Ester Coated ALEX
VFP	=	Vortex Flow Pancake
w	=	With
wrt	=	With Respect To
XRD	=	X–Ray Diffraction

GREEK SYMBOLS

α	=	Absorptivity
δ	=	Thickness (of Reactive/Boundary Layer)
γ	=	Specific Heats Ratio
Δ	=	Difference
$\Delta_{\%}$	=	Percent Error (of Predicted r_f)
ϵ	=	Emissivity
ϵ_{rough}	=	Surface Roughness, μm
η	=	Convective Heat-transfer Coefficient, $W/(m^2K)$
κ	=	Thermal Diffusivity, m^2/s
ϑ	=	Flame to Solid Fuel Surface Temperature Ratio, T_{fl}/T_w
μ	=	Dynamic Viscosity, $Pa \cdot s$
ξ	=	Standard Deviation
π	=	Empirical Exponent in Eq. 2.43
ρ	=	Density, kg/m^3
σ	=	Stefan–Boltzmann Constant, $W/(m^2K^4)$
χ	=	Parameter in Eq. 2.22
X_e	=	Entrainment Parameter, $N^{1/2}$

LATIN SYMBOLS

a	=	Multiplier Term in Approximating/Interpolating Equations
A_b	=	Burning Area, m^2
a_s	=	Particle Spherical Diameter (evaluated by S_{sp}), $6/(\rho_{Al} \cdot S_{sp})$
B	=	Mass Transfer Number
C	=	Specific Heat , J/kgK
c'	=	Constant in Eq. 8.18
C_{Al^0}	=	Active Aluminum Content, % with respect to total mass
C_B	=	Boron Content, % with respect to total mass
C_F	=	Friction Coefficient
C_{Mg}	=	Magnesium Content, % with respect to total mass
C_p	=	Constant Pressure Specific Heat , J/kgK
D	=	Diameter, mm
D_{10}	=	Mean Particle Diameter, μm
D_{43}	=	Mass–Averaged Particle Diameter, μm
f	=	Darcy–Weiesbach Friction Factor
Fr	=	Friction Factor in Eq.2.45
G	=	Mass Flux (Referred to Solid Grain Port Section)
h	=	Enthalpy, J/kg
k	=	Conductivity, $W/(mK)$
L_p	=	Fuel Grain Length, m
M_m	=	Molar Mass, g/mol
$\dot{m}$	=	Mass Flow Rate, kg/s
$\dot{m}_{ent}$	=	Entrainment Component of Mass FLux from Fuel Surface, $kg/(m^2 s)$
$\dot{m}_l$	=	Mass Flow Rate of Liquid Flowing Through Melt Layer per Unit Length, $kg/(ms)$
n	=	Exponent in Approximating/Interpolating Equations
Nu	=	Nusselt number, $\eta D/k$
p	=	Pressure, MPa (except where otherwise stated)
Pr	=	Prandtl Number, $\mu c_p/k$
$\dot{q}$	=	Heat Flux, $J/(m^2 \cdot s)$
R_d	=	Read Value
r_f	=	Regression Rate, mm/s
R_u	=	Universal Gas Constant, $J/(kmol\, K)$
Re	=	Reynolds Number, $\rho u(CL)/\mu$
s_{st}	=	Surface Tension, mN/m
S_{sp}	=	Specific Surface, m^2/g
St	=	Stanton Number, $Nu/(Re \cdot Pr)$
T	=	Temperature, K
t	=	Time, s
u	=	Horizontal Velocity, m/s
v	=	Vertical Velocity, m/s
x	=	Horizontal (Longitudinal) Coordinate
y	=	Vertical Coordinate (Perpendicular to Regressing Surface)

SUBSCRIPTS

$\%$	$=$	Percentage Value
bl	$=$	Boundary Layer
c	$=$	Combustion Chamber
$conv$	$=$	Convective
D	$=$	Diameter
d	$=$	Decomposition
dyn	$=$	Dynamic
e	$=$	Core Flow
ent	$=$	Entrainment
f	$=$	Fuel
fin	$=$	Final
fl	$=$	Flame
g	$=$	Gas Phase
i	$=$	$i-th$ Sampled Value
ign	$=$	Ignition
in	$=$	Initial
m	$=$	Melting Point
ox	$=$	Oxidizer
$oxid$	$=$	Oxidation
rad	$=$	Radiative
s	$=$	Solid Phase
SL	$=$	Quasi–steady Leg
TL	$=$	Transient Leg
v	$=$	Vaporization
w	$=$	Wall (Solid Fuel Surface)
x	$=$	Horizontal (Longitudinal) Direction

SUPERSCRIPTS

$*$	$=$	Without Blowing
0	$=$	Pure Substance

CHAPTER 1

INTRODUCTION

Thermo-chemical propulsive systems are the leading technology for access to space and in–space propulsion. In this field SRMs and LREs are mature technologies servicing in several applications [1][2]. Nevertheless, the former lacks of operating flexibility, and produces highly pollutant exhausts, whereas the latter, though high performing, is characterized by complicated design and higher costs than SRMs [3][4]. HREs are thermo-chemical propulsion systems in which fuel and oxidizer are stored in different states of matter. In the most common configuration (*direct hybrid*), the former is solid and the latter is liquid (or gaseous), see Figure 1.1. A *reverse hybrid* configuration, with solid oxidizer and liquid fuel, is also possible. Nevertheless the latter requires a more critical manufacturing process of the solid grain and yields no significant practical advantages over direct hybrid [3][4]. This work will focus on ballistics of direct HREs.

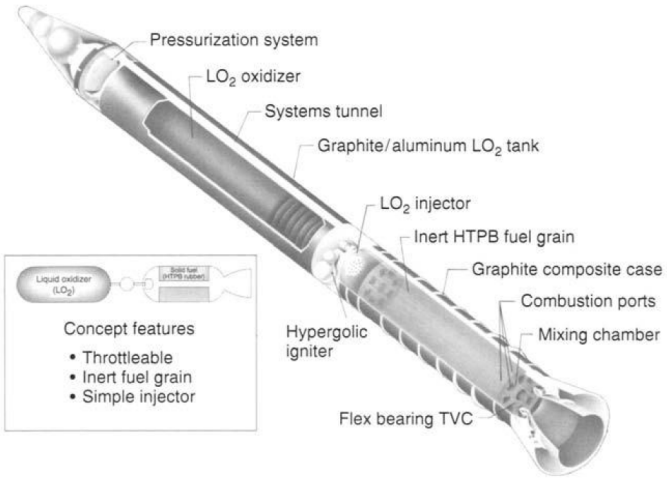

Figure 1.1: General configuration of an HRE [5]

In an HRE combustion can take place only when oxidizer is enabled to flow toward the solid fuel grain. A boundary layer develops due to the flow of fluid reactant over the solid grain. Once ignition of the system has occurred, vaporization of the solid fuel grain is achieved. Vaporized fuel diffuses into the boundary layer. A flame is established in the boundary layer where oxidizer and fuel meet under proper conditions. Energy is then transferred from the flame to the grain by convective and radiative heat transfer thus enabling vaporization of new mass from the solid phase. This new vaporized mass sustains the combustion process [6]. During combustion solid fuel is consumed by vaporization and therefore it regresses. The rate solid fuel surface regresses at is called *regression rate* and is one of the main parameters for performance evaluation of HREs.

Combustion process in HREs is driven by a diffusive flame. Fundamentals of this phenomenon were investigated by Marxman et al. [6][7][8]. In the proposed model regression rate of solid fuel grain depends mainly on total mass flux toward the solid fuel grain (and resulting from G_{ox} and fuel mass flow from the regressing surface).

1.1 Motivations

HREs offer several advantages over LREs and SRMs [3][4]. When compared to SRMs, HRE advantages include:

- Higher specific impulse[1]. Specific impulse of HRE is in the range from 275s and 350s while SRM are characterized by I_{sp} lower than 270s.
- Thrust modulation. In HRE thrust can be throttled controlling oxidizer mass flow rate toward the solid fuel grain.
- Multiple ignitions and extinctions (on/off capability). Controlling oxidizer fluid reactant flow toward the solid grain combustion can be stopped and system can be then re–ignited. SRMs do not enable such a operating flexibility.
- Safety. Due to separation between fuel and oxidizer, solid fuel grain is relatively inert, with reduced risks of ignition during manufacturing, transportation and storage due to shocks, vibrations and/or static electricity.
- Insensitivity to cracks into solid grain. Due to diffusive nature of HRE flame, combustion process requires diffusion of the reactants one into the other. Therefore fuel mass flow rate depends mainly on oxidizer mass flux and not on burning area.
- Reduced environmental impact. Due to the absence of oxidizer in the solid phase (e.g. AP, AN), combustion products are characterized by a lower environmental impact with respect to SRMs.

HREs advantages with respect to LREs are mainly due to a simpler architecture (only one reactant is in the liquid phase thus requiring feed–line and injector design and realization) enabling possible operating cost reduction and increased reliability. On the other hand, with respect to other thermochemical propulsion systems, HREs are affected by drawbacks hindering the possible advantages coming from their application to industrial/operating systems:

- Low regression rate of the solid fuel grain. This results in low thrust levels achievable with simple grain geometries (e.g. single port perforations). HREs requires high regressing surfaces for large thrust applications [3][4].
- Low combustion efficiency. While LREs and SRMs are characterized by relatively high combustion efficiencies (99% and 98% respectively), HREs presents a relatively rough, low quality combustion with efficiencies of 95%.
- O/F shift. During operation O/F ratio of HREs continuously changes because of solid fuel consumption and consequent variations in solid grain central port diameter. This yield to performance shift during burning and engine operating phases.

Low regression rate and low combustion efficiency of HREs are related to the diffusive flame characterizing these systems. The overcoming of these limitations is crucial in order to achieve all the possible advantages coming from HREs exploitation.

[1] Specific impulse (I_{sp}) is one of the main performance parameters of a propulsive system. It is defined as the ratio between thrust produced by the system and the mass flow rate of propellant flowing through the nozzle to provide that thrust.

1.2 Objective of this Thesis

This thesis focuses on the ballistics of HREs with a double objective:

1. Experimentally identify solid fuel formulations featuring regression rate enhancement as well as a suitable set of general properties (as mechanical properties of the grain, handling and costs).
2. Evaluate effects of forced transient burning on the ballistics of HREs considering, in particular, oxidizer mass flow throttling.

In the first part of the thesis dedicated to HRE performance enhancement, both HTPB-based and solid paraffin wax-based fuel formulations are considered. Metal fillers of different kind and particle–size have been considered for solid fuel doping. A numerical investigation conducted by a ballistic model for regression rate evaluation under convective heat transfer regime was developed during this part of the activity. The second listed objective of the work is of particular relevance due to the lack of detailed works on the topic in the open literature. The thrust–throttling of HREs is an attractive feature for possible space systems for soft–landing [9].

1.3 Plan of Presentation

This thesis will be presented according to the following scheme:

- Chapter 2: an introduction to HRE fundamentals, development and state of the art will be given.
- Chapter 3: solid fuel formulations considered in this study will be introduced.
- Chapter 4: experimental setup for combustion tests (relative ballistic grading of different fuel formulations and forced transient burning regime) will be presented.
- Chapter 5: the developed time-resolved technique for regression rate will be introduced and discussed.
- Chapter 6: the results of experimental investigation of solid fuel relative ballistic grading will be discussed in details.
- Chapter 7: numerical investigation of solid fuel ballistics, conducted with a semi–empirical approach aimed to regression rate evaluation will be presented and discussed.
- Chapter 8: ballistics of solid fuel formulation under forced transient operating conditions will be introduced.
- Chapter 9: in the final chapter conclusions of the work, together with some suggestions for further developments, will be given.

CHAPTER 2

STATE OF THE ART OF HYBRID ROCKET PROPULSION

In this chapter an overview of the development of HREs is given. Fundamentals of solid fuel burning phenomena and techniques for regression rate enhancement are presented and critically discussed.

2.1 HRE from the Beginning to the State of the Art

2.1.1 HRE Development

An HRE is a thermo–chemical propulsive system in which fuel and oxidizer are stored in different states of matter. The first test flight of a hybrid rocket was performed by Korolev and Tickhonravov on August 17, 1933. The system, named GIRD–09, used a gasoline gel as fuel and LOX as oxidizer [4]. In the same decade, based on a concept initially proposed by Andrussow, motor tests of 10 kN thrust and burning time up to 120 s were conducted by Noggerath and Lutz at I.G. Farben Laboratories in Germany. Solid carbon was used as fuel and nitrous oxide (N_2O) was taken as oxidizer [3][4]. Tests highlighted the low regression rate of the solid fuel grain due to carbon high enthalpy of sublimation. Starting from the 1940s further tests were performed in the USA by California Pacific Rocket Society. During this experience, a rocket using LOX as oxidizer and rubber as solid fuel was flown to an altitude of about 9 km in June 1951. Though the effort of this research group did not yield to the publication of detailed ballistic analysis, it is due to the work of this research team that it was possible to observe that in HREs the diffusive flame acts as a shield for possible critical instabilities due to cracks in the solid grain since "The chamber pressure of a solid-liquid rocket engine is proportional to the oxidizer flow and not to the internal surface area exposed to the flame. ..." [4]. In the mid 1950's, efforts in the research activity on HREs continued with the work of Moore and Berman at General Electric (using 90% hydrogen peroxide and polyethylene in a rod and tube grain design) and with the contribution of Avery studying reverse hybrid rocket engines at Applied Physics Laboratory where he tested systems using JP as liquid fuel and a ammonium nitrate as solid oxidizer. Other versions of the reverse hybrid were further studied by both Thiokol and UTC[1] in the mid-1960 utilizing hydrazine-based liquid fuels and solid oxidizers as AP, hydrazinium diperchlorate, and nitronium perchlorate. These solid charges were pressed, usually with a non-reactive fluorocarbon as a binder. This approach was eventually abandoned because of poor combustion behavior and insufficient performance improvement to justify the difficulties experienced in reverse hybrid approach (oxidizer fillers compression). During the same decade both theoretical and experimental investigations made

[1] UTC became CSD of UTC in 1970 continuing the work on HREs. In some publication UTC and CSD are referenced as UTC/CSD.

important progresses. On the theoretical point of view, the work of Marxman and co–workers yield to the development of the convective, diffusion limited model that is still in use nowadays for hybrid combustion investigation (detailed description of the model is given in Section 2.2.1) [6][7][8]. On the other hand, different sounding rocket programs were conducted in Europe and USA. European programs were carried out by ONERA (with SEP and SNECMA) in France and by Volvo Flygmotor in Sweden. The ONERA program, LEX, was based on a hypergolic propellant formulation based on red fuming nitric acid as oxidizer and an amine fuel consisting of nylon–metatoluene–diamine. The motor had a thrust of 10 kN and enabled thrust throttling over a 5:1 range to optimize flight performance. With a gross launch weight of 75 kg, a propellant and a payload weight of 52 kg and a 5 kg respectively, the propellant mass fraction was 74%. The first flight took place in 1964 and during the whole program eight flights were performed reaching altitudes above 100 km. A larger, more complicated version, the LEX–04, conducted twelve successful ground tests but did not performed flight tests. The Swedish program by Volvo Flygmotor was initiated in 1962 and was based on a hypergolic combination using nitric acid and polybutadiene with an aromatic amine. After initial flight tests where mechanical properties of the solid fuel grain resulted a limiting factor for system operating capability. Therefore an improved version of the initial fuel was later developed with superior mechanical properties (in particular, softening point of the solid phase was raised). Two sounding rockets were planned using Sagaform A, the SR–1 and SR–2. The SR-1 design listed a payload of 25 kg with a launch weight of 361 kg and a propellant weight of 264 kg. The SR-2 was designed for a capability about four times greater than SR–1. Despite some reports to the contrary, there has been no confirmation that these rockets were actually flown [4]. American sounding rocket programs were conducted by UTC and Beech Aircraft in the frame of a program aiming to the realization of target drones, an overview of the characteristics of these systems is reported in Figure 2.1.

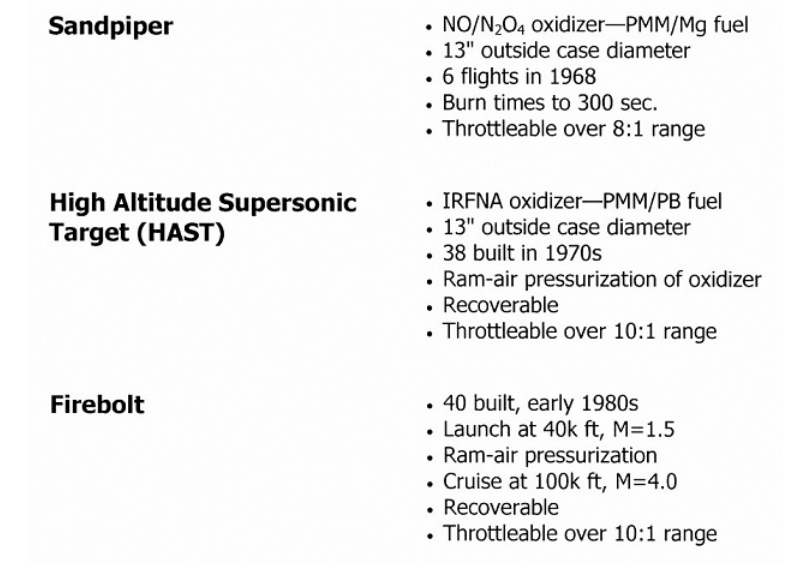

Figure 2.1: HRE–based target drones developed by UTC during the 1960s [4].

In 1967 UTC realized and tested an HRE delivering 180 kN thrust using PB rubber loaded with 45% aluminum as fuel, and nitrogen tetraoxide, N_2O_4, as oxidizer. Solid fuel grain was designed with a wagon wheel configuration in order to lessen the influence of low regression rate on achieved thrust. This technical solution, shown in Figure 2.2, would have become the base of projects developed in following years by other research groups and industries.

Between the late 1980s and the early 1990s, AMROC designed and tested several sub–scale hybrid motors and, in particular, the H–500 and the H–250 rocket engines. The H–500 was capable of delivering a thrust of 312 kN for 70 s using LOX/HTPB as propellant, see Figure 2.4. The H-250 was a scale-up of this latter project reaching a thrust of 1.1 MN due to a solid grain design with diameter of 1.8 m (6 ft) and 15 ports in a wagon wheel configuration with an inert center port

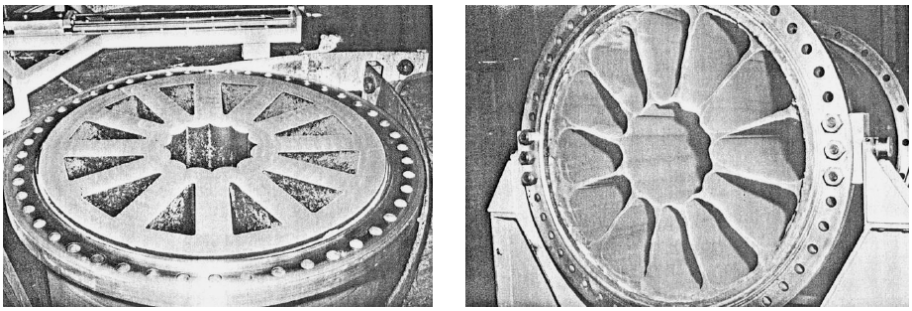

Figure 2.2: UTC wagon wheel solid fuel grain (based on PB loaded with aluminum) delivering 180 kN thrust before (left) and after firing (right) [4].

closed at the head-end. In a more recent program developed in the USA, and named HPDP, an industrial consortium composed by NASA, DARPA, Rocketdyne, Lockheed Martin, Thiokol, and CSD fired a 1.1 MN thrust hybrid motor using a modified HTPB fuel with LOX as the oxidizer. In contrast to the AMROC motor, the grain had 7 ports plus a center burning port and a web thickness more than 50% larger. This was a more efficient design and the reduced burning surface area with respect to AMROC motor was compensated by an increased oxidizer mass flux.

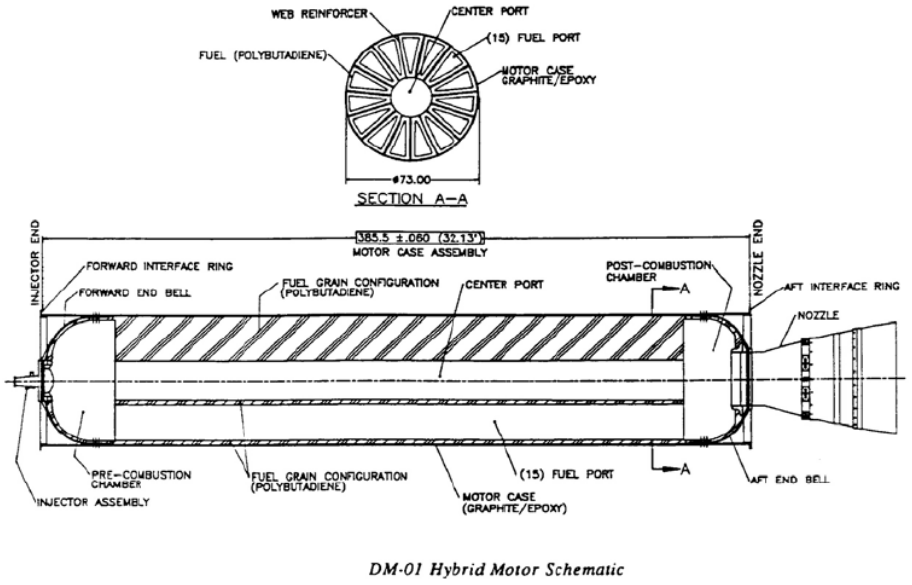

Figure 2.3: Scheme of DM–01 (PB rubber/LOX) designed by AMROC [3]. Note wagon wheel grain design to achieve large regressing area for enhanced thrust level.

A milestone in hybrid propulsion development came from the success of *SpaceShipOne* at Ansari X–Prize in 2004. The latter was a competition aiming to produce technical development in the field of non–governmental access to space [3][4]. *SpaceShipOne* is a sub–orbital vector designed and developed by Scaled Composites, see Figure 2.5. *SpaceShipOne* mission profile was based on a first phase where the sub–orbital vehicle was carried to an altitude of 15 km by *White Knight*, a mother aircraft; this first leg of mission profile was then followed by the detachment of the sub–orbital vector that reached the altitude of 100 km by an integrated propulsion system based on an HRE. Finally *SpaceShipOne* performed re–entry into atmosphere by a glide flight [10]. *SpaceShipOne* propulsive system was studied by SpaceDev an industry whose background was coming from heritage of AMROC work. *SpaceShipOne* thrust was produced by an HRE using N_2O as oxidizer and HTPB as fuel in a solid grain configuration with four ports to improve burning surface. This motor enabled *SpaceShipOne* to reach a thrust of 74 kN for

Figure 2.4: Test of AMROC H–500 motor, using LOX/HTPB as propellant [4].

a burning time of 87 s. Due to the success of that experience, that was related to the low–cost and high–safety characteristics of hybrid propulsion, an improvement of $SpaceShipOne$ project named $SpaceShipTwo$ is being developed by Scaled Composites and Virgin Group [3][10].

Figure 2.5: $SpaceShipOne$ carried by the mother–aircraft $White\ Knight$ (left) and during the boost phase after separation (right) [10].

In USA and Europe significant efforts in research on HRE technology have been conduced in last years by different research groups. In the USA the Pennsylvania State University the group lead by Kuo has conducted a detailed investigation on hybrid combustion phenomena [11][12]. The work focused on HTPB-based fuels loaded with metal additives and is extensively discussed in Section 2.3.2. In the frame of the recent European FP7 program ORPHEE an intensive experimental investigation involving universities, industries and research centers was performed with the aim of identify solid fuel formulations enabling significant regression rate enhancement [15]. In ORPHEE project both HTPB-based and solid paraffin-based fuels (both eventually doped with energetic additives) were considered. Paraffin–based fuels appear attractive because of possible significant regression rate enhancement due to the entrainment of melted fuel droplets, a phenomenon originally investigated at Stanford University by Karabeyoglu et al. [13][14] and extensively discussed in Section 2.2.2. In the year 2010 the SPARTAN FP7 project started with the aim of studying the possible application of using a HRE with HTPB as fuel to perform a soft–landing on Mars surface [9].

In Italy four main research groups are active in the investigation of hybrid propulsion. The first one, with an important (and pioneering) activity dating back to the 1970s, is supervised by A. Russo Sorge at the University of Naples, [17]–[25]. Other research teams are active at Politecnico di Torino, [26]–[28], University of Padua, [29][30], and Politecnico di Milano. SPLab of Politecnico di Milano has developed a variety of experimental setups and diagnostics for the study of hybrid

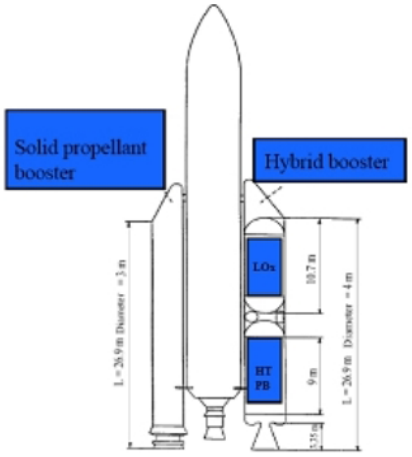

Solid-propellant booster		hybrid booster	
Solid propellant	: 237.0 t	HTPB	: 65.1 t
		Oxidizer	: 144.9 t
		Other	: 9.0 t
Structure	: 19.5 t	Structure	: 18.0 t
Insulation	: 4.7 t	Insulation	: 1.0 t
Nozzle	: 6.1 t	Nozzle	: 6.1 t
Igniter	: 0.3 t	Turbopump	: 0.5 t
Structural mass	: 30.6 t	Structural mass	: 25.6 t
Total mass	: 267.6 t	Total mass	: 244.6 t

Figure 2.6: Comparison between Ariane 5 solid propellant boosters and the possible hybrid propellant counterpart [16]

combustion phenomena and solid fuel characterization, [31]–[40].

2.1.2 Overview of Revised Concepts and Conclusion

Investigation on HREs through the years yielded to the identification of the low regression rate of the solid fuel grain as the limiting factor for the application of this technology to launch systems. Mainly polymeric fuels have been investigated, and particular attention was given to HTPB due to its wide use in SRM. While granting excellent mechanical properties when used as a binder for solid propellants/fuels, HTPB is not tailored for HREs from the ballistic point of view. Nevertheless the best results in terms of thrust level have been achieved by HTPB/LOX systems using multi–port grain configurations where the low regression rate of the solid fuel grain is balanced by large pyrolysis surfaces. Application of similar solutions to the substitution of the solid propellant booster of a launcher as the European Ariane 5, could enable a significant a mass saving for the whole system [16], though an increase in aerodynamic drag due to increased cross-section of the booster due to the reduced volumetric efficiency (multi–port grain design), see Figure 2.6). In order to achieve high thrust level with simple grain geometries (e.g. single port configuration), increases in solid fuel regression rate are required. In order to do this, loading of fuel grains with energetic additives as well as changes in the solid fuel formulations with materials different from HTPB (for example with entrainment–producing fuel formulations with suitable mechanical properties) must be considered and are object of the ongoing research projects. The potential of hybrid propulsion could be currently exploited for in–space propulsion applications where high thrust–to–weight ratio is not a stringent requirement (though volume–related parameters should be considered during trade–off). Urgent application as de–orbiting systems for decommissioned spacecrafts could benefit from HREs peculiarities as high safety and operating flexibility.

2.2 Fundamentals of Hybrid Rocket Combustion

In this section an overview of the fundamentals of hybrid rocket combustion in a turbulent boundary layer will be given. Starting point of the review will be the diffusion–limited model developed by Marxman and co–workers [6][7][8]. After a discussion of the basis of this model, the extension of the classic theory for solid fuel formulations will be introduced. The latter part of the section will be based on the work of Karabeyoglu and co–workers at Stanford University [13][14].

2.2.1 Marxman's Diffusion–limited Model

Convective Model

The model developed during the 1960s by Marxman and co–workers is still used nowadays as a reference for the studies on hybrid combustion process. The model is developed considering the flow of oxidizing reactant over the solid fuel grain surface. After ignition, solid fuel melts and vaporizes. Fuel vapors diffuse into the boundary layer generated by oxidizer flow. A diffusive flame is then established in the boundary layer where oxidizer and fuel vapors meet at stoichiometric conditions, see Figure 2.7. Heat feedback from the flame zone to the regressing surface provides energy for the gasification of new fuel, thus yielding to solid grain regression due to consumption and sustaining the process. According to the model, heat transfer is mainly due to convection (for non–metallized fuel formulations) [6].

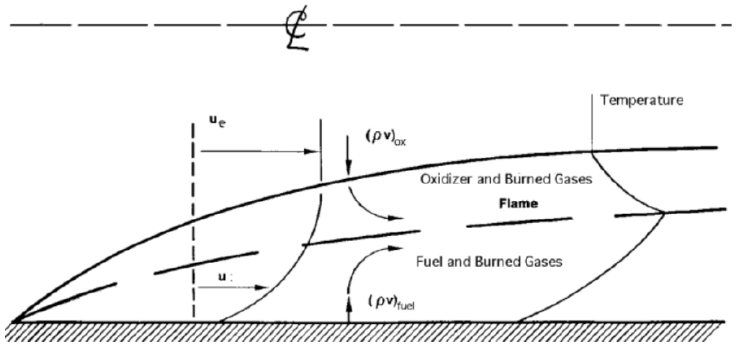

Figure 2.7: Hybrid rocket combustion process, reacting boundary layer [6]

In the proposed model the flame zone is assumed to be a thin layer, while it should be a finite region with boundaries given by the flammability limits of the considered oxidizer and fuel, see Figure 2.8. The flame divides the boundary layer into two regions. In the first region the velocity and the temperature gradient are concordant, increasing from the surface to the flame. In the second region, extending from the flame to the core flow, the velocity and the temperature gradients are opposite in sign. The temperature profile exhibits a maximum at the flame zone, see Figure 2.7. The first region is fuel rich, due to the presence of gasified fuel diffusing within the boundary layer to react with oxidizer. The second region is oxidizer rich. In both regions combustion products are present.

Starting point of the analysis is the energy balance at the regressing surface of the solid fuel grain under quasi–steady condition. Considering a convective heat transfer regime, neglecting radiation and in-depth conduction into the fuel slab, the following Eq. 2.1 can be written:

$$\dot{q}_{w,conv} = \rho_f \, r_f \, h_{v,f}. \tag{2.1}$$

In Eq. 2.1, the vaporization enthalpy of solid fuel, $h_{v,f}$, can be expressed as sum of heat of degradation of polymer and sensible enthalpy, as reported in Eq. 2.2. The term $\Delta h_{d,f}$ in Eq. 2.2 can be expressed as sum of the depolimerization and vaporization enthalpies of the solid fuel. Marxman and co–workers considered Plexiglas as solid fuel during their experiments. As a simplifying hypothesis they assumed that the starting material decomposes in the constituent monomer.

$$h_{v,f} = c_{p,f}(T_w - T_i) + \Delta h_{d,f} \tag{2.2}$$

Considering the continuity in heat flux, the convective left hand term of Eq. 2.1 can be expressed in terms of conductive heat flux at the regressing surface according to Eq. 2.3.

$$\dot{q}_{w,conv} = \eta \cdot (T_{fl} - T_w) = k_g \frac{\partial T}{\partial y}\bigg|_{y=0} \tag{2.3}$$

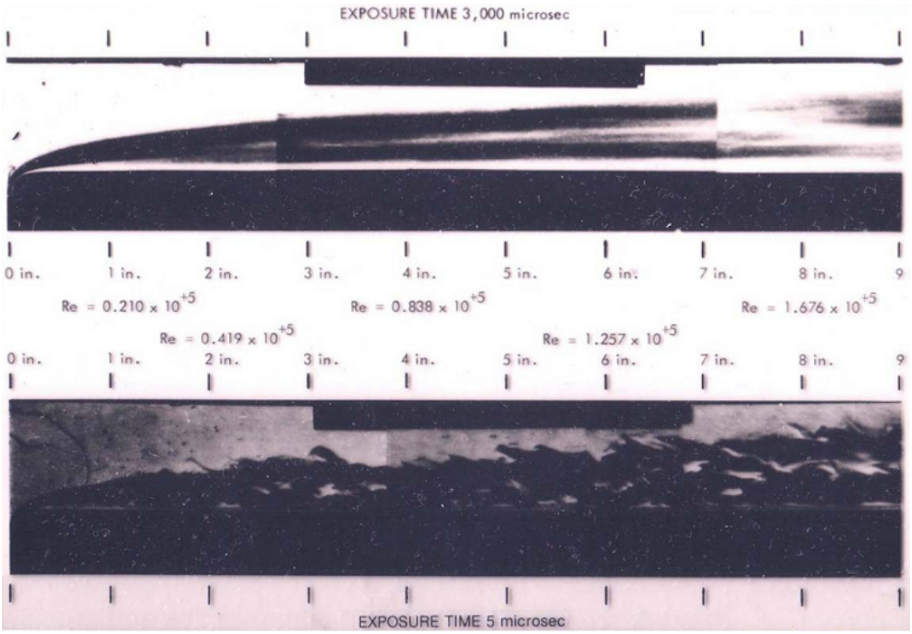

Figure 2.8: Schlieren image of combustion process in a turbulent boundary layer over a flat surface (Plexiglas/LOX) [3].

The reacting boundary layer of HREs is characterized by mass addition from the solid fuel regressing surface (*blowing*). This induces a reduction in the convective heat transfer coefficient (*convective blockage*). Blockage effect is the responsible for limitations in convective heat transfer from the flame to the gasifying surface and is therefore one of the causes for low regression rate of HREs.

$$\rho_f \, r_f = (\rho v)_w = \frac{\dot{q}_w}{h_v} \tag{2.4}$$

Equation 2.4 introduces blowing into the model by considering vaporized fuel flux at the regressing surface, $(\rho v)_w$. Now, introducing hypotesis of unit Lewis and Prandtl numbers, Reynolds analogy can be exploited to get a relationship between the Stanton number, and the friction factor as reported in Eq. 2.6 and in Eq. 2.5.

$$St = \frac{Nu}{Pr \; Re} = \frac{\dot{q}_w}{\rho_e u_e \Delta h_{fl,w}} \tag{2.5}$$

$$St = \frac{C_F}{2} Pr^{-\frac{2}{3}} \tag{2.6}$$

Equating Eq. 2.5 and Eq. 2.6, it is possible to evaluate the term $q_{w,conv}$ and Eq. 2.4 can be re–written as reported in Eq. 2.7.

$$r_f = \frac{C_F}{2} \frac{\Delta h}{h_{v,f}} \frac{\rho_e u_e}{\rho_f} \tag{2.7}$$

As previously stated, blowing induces a reduction of convective heat transfer. In order to account for this phenomenon, Marxman assumed the correction factor of Eq. 2.8 to properly evaluate the friction factor with blowing, C_F (see Eq. 2.9) starting from the value for a boundary layer without mass addition, C_{F^*} (see Eq. 2.10).

$$B = \frac{1}{2} \cdot \frac{(\rho v)_w}{C_f \rho_e u_e} \tag{2.8}$$

$$\frac{C_F}{C_{F^*}} = 1.27 B^{-0.77} \tag{2.9}$$

$$\frac{C_{F^*}}{2} = 0.029 Re_x^{-0.2} \tag{2.10}$$

Finally, due to the fact that in a turbulent boundary layer, the mass transfer number B can be expressed as the ratio of the enthalpy difference between flame and solid fuel surface, $\Delta h_{fl,s}$, and vaporization enthalpy of the fuel, $h_{v,f}$, [5] [6], the regression rate expression of Marxman's model can be written as

$$r_f = 0.036 \frac{(G_{ox} + G_f)^{0.8}}{\rho_f} \left(\frac{\mu}{x}\right)^{0.2} B^{0.23} \tag{2.11}$$

Equation 2.11 is here written for the usage with Imperial Units. Over the more restricted range $5 \leq B \leq 20$ typical of classical hybrid engines, the empirical approximation reported in Eq. 2.12 results more suitable than the original Eq. 2.9. Therefore the original Eq. 2.11 can be re-written as in Eq. 2.13 [3].

$$\frac{C_F}{C_{F^*}} = B^{-0.68} \tag{2.12}$$

$$r_f = 0.036 \frac{(G_{ox} + G_f)^{0.8}}{\rho_f} \left(\frac{\mu}{x}\right)^{0.2} B^{0.32} \tag{2.13}$$

The diffusion–limited model developed by Marxman and co–workers considers convective heat transfer as the main energy source for solid fuel regression. In this model the total mass flux, (G_{ox}+G_f), is the leading parameter for regression rate determination. According to Eq. 2.13, chamber pressure exerts no influence on r_f, though Marxman et al. data exhibited a pressure influence for p_c < 10 bar [47]. Possible explanation for pressure dependence of regression rate is discussed in Section 2.2.2 and Section 2.2.3.

2.2.2 Thermal Radiation Effects

Equation 2.13 is valid for a convective regime where radiation is neglected. Marxman and co–workers justified this approximation by considering that for polymeric fuel formulation without metal additives, radiation should have a poor influence on regression rate. Nevertheless also for non-metallized fuels there can be a significant contribution to regression rate due to radiation from soot and solid fuel fragments. For metal-loaded fuel formulations, radiation is an important source of energy transfer especially because radiation is not directly affected by convective blockage[2], [3][6][11]. Marxman and co–workers corrected the initial purely convective model inserting radiative heat transfer [6][7][8]. In the proposed modification of the original convective model, total heat–flux to the solid grain surface was identified as sum of convective and radiative heat-fluxes. Radiative heat–transfer was written in the form reported in Eq. 2.14, where solid grain surface and hot gases emissivity/absorptivity are considered.

[2]Note that even though radiative heat transfer is not directly affected by convective blockage effect, an increase in the latter parameter can be achieved if radiative heat transfer is increased because of increased blowing.

$$\dot{q}_{w,rad} = \sigma \cdot \epsilon_s \cdot \left(\epsilon_g T_{fl}^4 - \alpha_g T_w^4\right) \tag{2.14}$$

Radiative heat transfer required a proper modification in the mass transfer number definition, as reported in Eq. 2.15.

$$\frac{B_{rad}}{B} = 1 + \frac{q_{w,rad}}{q_{w,conv}} \left(\frac{B_{rad}}{B}\right)^{0.77} \tag{2.15}$$

Approximating Eq. 2.15 over the interval of values of B typical of HRE in operating condition ($5 \leq B \leq 100$), the following Eq. 2.16 is achieved.

$$\frac{B_{rad}}{B} = e^{1.3 \frac{\dot{q}_{w,rad}}{\dot{q}_{w,conv}}} \tag{2.16}$$

Considering radiative heat transfer, Eq. 2.1 can be re–written in the form of Eq. 2.17 where the coupling between convective and radiative heat transfer is considered.

$$\rho_f \, r_f = \frac{q_{w,conv}}{h_{v,f}} e^{-\frac{q_{w,rad}}{q_{w,conv}}} + \frac{q_{w,rad}}{h_{v,f}} \tag{2.17}$$

From their analysis Marxman et al. noted that radiative heat transfer in the order of half of the convective heat transfer results in a net increase in regression rate around 10% of the non–radiative case (due to the coupling between radiative and convective heat–transfer).

Influence of radiative heat transfer on the combustion process of HREs has been investigated by several investigators through the years, major contributions on this topic are due to the work of Strand et al., Estey et al., and of Pennsylvania State University [41][42][43].

The work by Estey et al. was conducted with the aim of identifying scaling–laws for performance of HREs differing for geometric parameters and operating conditions [41]. In this study radiative heat–flux was expressed in the form of Eq. 2.18 that is derived from Eq. 2.14 neglecting the surface term due to its relatively low temperature with respect to flame temperature and evaluating the emissivity of the gas phase by the term reported in parentheses.

$$q_{w,rad} = \sigma \cdot T_g^4 \cdot (1 - e^{-\alpha_g p_c D}) \tag{2.18}$$

Correlating large– and small–scale motor data, Estey et al. found that with the use of Eq. 2.18 enabled a better correlation between available data for metal–loaded fuel formulations, while for non–loaded formulation classical convective heat–transfer theory worked best.

Strand et al. studied influence of radiative heat–transfer in hybrid combustion process by a lab–scale hybrid slab motor [42]. Experimental setup enabled pressure measurement as well as determination of average regression rate and average oxidizer–to–fuel ratio. Optical observation of reacting boundary layer and optical exhaust plume were conducted. Due to their experimental results Strand et al. suggested that radiative heat flux due to combustion gaseous products as CO, CO_2, H_2O and soot particles could significantly influence hybrid combustion process under the investigated conditions. This result was obtained considering Eq. 2.18 (with a definition of k_g based on data taken from emissivity of a non–metallized solid propellant, [42]) for the radiative heat flux contribution of combustion gases and Eq. 2.19 for the contribution of soot.

$$\dot{q}_{w,rad} = \sigma \cdot T_g^4 \cdot (1 - e^{a_p N_p}) \tag{2.19}$$

In Eq. 2.19 the exponent in the right hand side, $a_p N_p$, the product of a constant, a_p, with the particle number density, N_p. This exponent can be evaluated according to Eq. 2.20 considering the

soot particle weight fraction, b_{soot}. This latter parameter was evaluated by Strand et al. solving Eq. 2.19 and Eq. 2.20 for the radiative heat flux measured in the experimental condition characterized by p_c of 11 bar and assuming a O/F of 2.

$$\dot{a}_p N_p = 0.134 \cdot \frac{b_{soot} p_c}{1 + O/F - b_{soot}} \tag{2.20}$$

In this analysis, the assumption that soot particles have the same temperature of the flame zone was made. This hypothesis is in reasonable agreement with the fact that soot particle size should be lower than 0.1 μm and therefore should reach equilibrium with the surrounding environment very quickly emitting thermal radiation over the whole infrared spectrum. Under the investigated conditions Strand et al. study yield to the consideration of the important relative weight of radiative heat transfer accounting for nearly 50% of the total heat flux. Such a weight should result reduced increasing p_c and O/F.

The work developed by Pennsylvania State University research team on the effect of radiative heat transfer on HRE is based on a semi-empirical approach based on combustion tests performed in a slab motor where regression rate is determined by X-ray radiography and ultrasound techniques [11][43] [44] [45]. Starting point of this analysis was the observation of regression rate dependence from p_c under the investigated conditions, see Figure 2.9. Due to this result and considering data from Strand (in particular, the relative importance of radiative heat–flux emission from soot with respect to the contribution from combustion gases as CO and CO_2 and H_2O), Chiaverini et al. used Eq. 2.21 to represents experimental data. In Eq.2.21 soot temperature was assumed to be 95% of equilibrium flame temperature, while the emissivity of soot is represented via the term X_s defined by Eq. 2.22. Chiaverini et al. assumed Eq. 2.22 to be valid over their O/F of 1.5–3.5 in spite of the fact that it was determined on the basis of Strand et al. data with O/F of 2–3 [11].

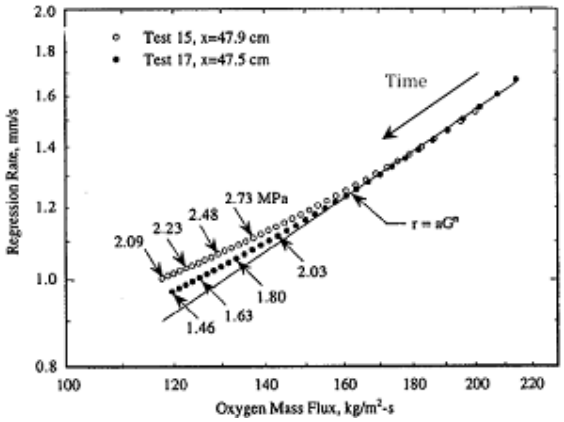

Figure 2.9: Radiative heat–flux effect on regression rate for HTPB/GOX. Due to increases in p_c regression rate enhancement is achieved because of radiative heat transfer. In a pure convective regime, with log–log axis regression rate should follow a straight line, due to the exclusive influence of G alone [44].

$$\dot{q}_{rad,soot} = \sigma T_g^4 \left(1 - e^{X_s}\right) \tag{2.21}$$

$$X_s = 0.51 - 0.113 \cdot O/F, \qquad (1.5 \leq O/F \leq 3.5) \tag{2.22}$$

Considering achieved results, Chiaverini et al. proposed a possible semi-empirical correlation for combustion data interpolation, see Eq. 2.23. Equation 2.23, was derived from studies of Marxman and co–workers. In the original form of Eq. 2.23 both c and d were considered equal to 1,

while Chiaverini et al. a least square procedure for data fitting was used, yielding to $a = 0.524$, $b = 0.6$, $c = 1.3$ and $d = 0.75$.

$$\rho_f \, r_f = a \, St \, B \, G \, \vartheta^b \left[c \left(\frac{\dot{q}_{w,rad}}{\dot{q}_{w,conv}} \right)^d + e^{-c(\dot{q}_{w,rad}/\dot{q}_{w,conv})^d} \right] \tag{2.23}$$

Figure 2.10 shows experimental results from Chiaverini et al. about the weight of radiative heat flux during a combustion test of HTPB under GOX. At the beginning of the combustion process, convective heat flux has a high relative weight with respect to radiative heat flux. The latter is mainly due to soot, the contribution of combustion gaseous products being quite low.

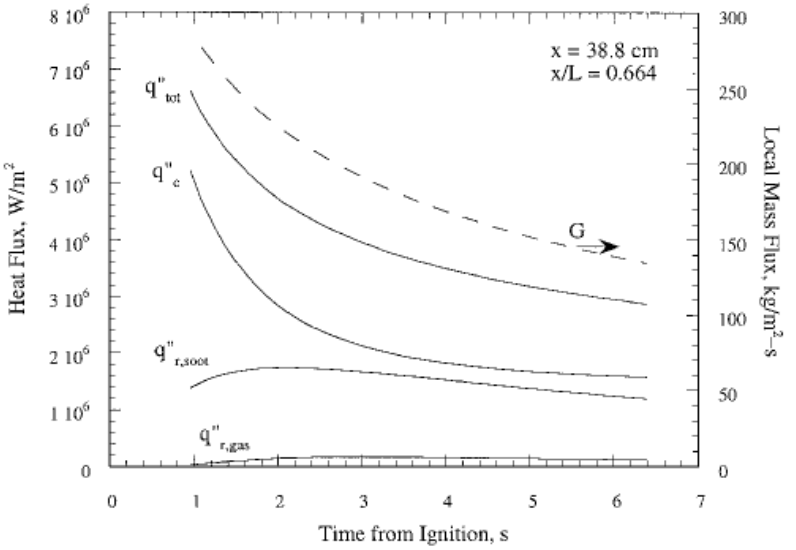

Figure 2.10: HTPB burning under GOX in slab configuration, influence of convective and radiative heat fluxes to the total heat flux [43]

2.2.3 Pressure Effect

The diffusion–limited model developed by Marxman and co–workers considers the convective heat transfer as the main parameter for regression rate determination (see Eq. 2.13). Therefore other operating parameters should exert no (or limited) influence on regression rate. Nevertheless in some studies a regression rate dependence from pressure was observed. According to available data usually pressure increases induce regression rate enhancement till a threshold value is reached. From this threshold, pressure influence on r_f became negligible. Nevertheless in some study combustion pressure increases yield to a reduction in regression rate [46]. An overview of results concerning combustion chamber pressure effect on regression rate for polymeric fuels with various oxidizers is reported by George et al. [47].

One of the first analysis on pressure effect on regression rate was conducted by Smoot and Price [48][49][50]. Smoot and Price conducted experimental investigation on butyl rubber and poly–urethane fuels using fluorine and mixtures of fluorine/oxygen as oxidizer [48]. Metallized fuel loaded with LiH were also investigated confirming results achieved for non–metallized formulations [49]. Tests were conducted at p_c below 12 bar for G_{ox} ranging from 10 to 120 $kg/(m^2 s)$. Under the investigated conditions, in the range $G_{ox} < 25$ $kg/(m^2 s)$ r_f resulted dependent from G_{ox}, but independent from p_c, while in the range $G_{ox} > 70$ $kg/(m^2 s)$ r_f resulted independent from G_{ox}, but dependent from p_c. In the intermediate region, where 25 $kg/(m^2 s) < G_{ox} < 70$ $kg/(m^2 s)$, both G_{ox} and p_c, exerted influence on r_f. Smoot and Price attributed the pressure dependence at high G_{ox} to the rate limiting chemical kinetic processes and to possible heterogeneous reactions at solid fuel surface. Therefore the classical turbulent boundary layer regression rate model based

on convective heat transfer mechanism was extended to include the effects of condensed phase surface reactions. In particular, in the low G_{ox} region diffusion–limited model similar to the Marxman's model was derived. For the intermediate region, Eq. 2.24 was proposed, though no details where given on the exponent n. Finally, for the high G_{ox} region Eq. 2.25 was proposed. The latter equation is quite similar to the Vielle–de St. Robert's law typical of SRM.

$$r_f = \frac{a\, G^{0.8}\, b\, p_c^n}{a\, G^{0.8} + b\, p_c^n} \tag{2.24}$$

$$r_f = a \cdot p_c^m \tag{2.25}$$

From further and recent investigations influence of pressure on regression rate can be summarized according to data reported in Figure 2.11. For high G_{ox}, Smoot and Price observation of a kinetics limited regime for hybrid combustion yields to r_f enhancement for increasing p_c, while for low G_{ox} the experimental trend appears more related to radiation effects previously discussed (see Figure 2.10). Similar considerations on pressure influence on regression rate could explain the pressure dependence of the data collected by Marxman et al. for $p_c < 10$ bar.

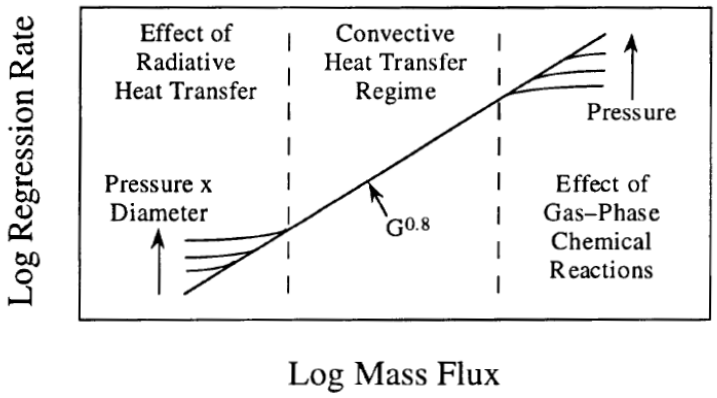

Figure 2.11: Summary of pressure influence on regression rate for non–metallized fuels [11].

2.2.4 Entrainment

The original diffusion–limited model developed by Marxman and co–workers (Eq. 2.13) was developed considering polymeric fuels burning in oxygen [6][7][8]. Recent investigations, conducted at Stanford University by Karabeyoglu et al. highlighted the marked regression rate increase offered by particular solid fuels as solid paraffin wax and other alkanes [13][14]. Regression rate increase of these latter fuels is up to 400% with respect to (conventional) polymeric fuels and is due to the entrainment of melted solid fuel droplets by the oxidizer mass flow, see Figure 2.12.

When energy is transferred to the solid fuel grain, the latter rises its temperature. This temperature rise is confined to a thin region close to the grain surface. Heating of this region yields to melting of solid fuel surface. Therefore, a thin layer of melted fuel is formed at grain surface. When this liquid fuel layer has low viscosity and low surface tension, oxidizer flow can destabilize it thus yielding to the entrainment of the melted droplets. The latter phenomenon provides a significant additional contribution to overall regression rate since the classic vaporization component is still present, see Eq. 2.26. For conventional, polymeric fuels, the contribution to the overall regression rate of the term $r_{f,ent}$ is negligible or totally absent.

$$r_f = r_{f,v} + r_{f,ent} \tag{2.26}$$

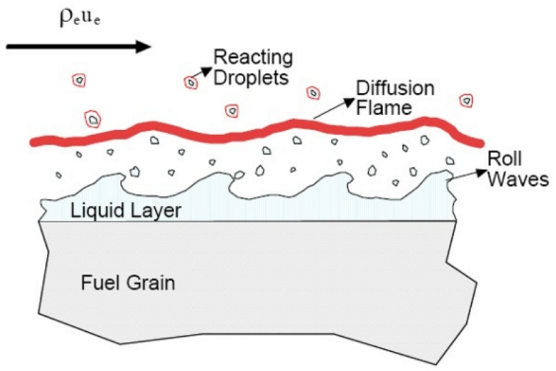

Figure 2.12: Entrainment of melted fuel droplets from surface melted layer of fuel grain by oxidizer flow [13].

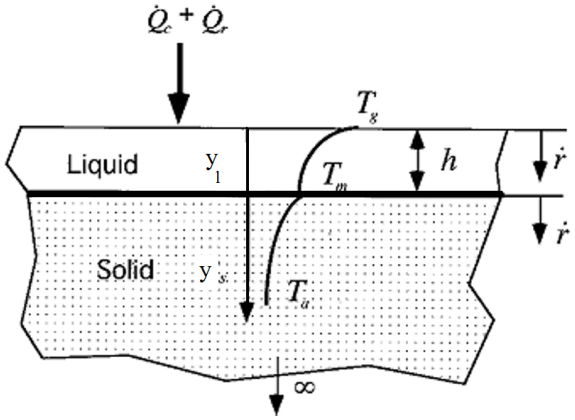

Figure 2.13: Entrainment model, solid fuel grain/oxidizer flow boundary. Note melted fuel layer at fuel boundary [13].

The main advantage of entrainment–producing fuels with respect to classical formulations is the enhanced regression rate due to $r_{f,ent}$. Nevertheless, in order to achieve real performance enhancement combustion of melted fuel droplets is required.

Entrainment Model

A mathematical formulation of the entrainment phenomenon was developed by Karabeyoglu et al. [13][14] and is hereby reported in order to extend the classical theory presented in Section 2.2.1.

First step in the one–dimensional entrainment model developed by Karabeyoglu et al. is the determination of the thickness of the melted fuel layer, see Figure 2.13.

Entrainment model considers the total heat feedback from the flame to the fuel grain. Buoyancy effects in the fuel liquid layer are considered negligible and are not taken into account. Solid fuel and liquid layer are assumed to be rigid bodies both moving at the regression rate r_f. Therefore, no changes can occur in the liquid layer thickness during the combustion process. Physical properties in the melted layer and in the solid phase are considered constant.

Considering the total radiative heat flux impinging on the regressing surface (see Figure 2.13), the radiative heat fluxes in the solid and liquid layers can be defined according to Eq. 2.27. From the latter equation, in this one–dimensional model, radiative heating at any position in the fuel grain can be defined according to Eq. 2.28.

$$\dot{q}_{rad,l}\left(y_l\right) = \dot{q}_{rad} e^{-\alpha_l y_l} \qquad \dot{q}_{rad,s}\left(y_s\right) = \dot{q}_{rad}\left(y_l\right)_{y_l=h} e^{-\alpha_s y_s} = \dot{q}_{rad} e^{-\alpha_l h} e^{-\alpha_s y_s} \tag{2.27}$$

$$\int_0^h \alpha_l \dot{q}_{rad} e^{-\alpha_l y_l} \mathrm{d}y_l + \int_0^\infty \alpha_s \dot{q}_{rad} e^{-\alpha_l h} e^{-\alpha_s y_s} \mathrm{d}y_s = \dot{q}_{rad} \tag{2.28}$$

In order to write the energy balance equation for the solid and the liquid phases, some consideration on the reference frames involved into the problem is required (see Figure 2.13). Due to the density difference between solid and liquid phases, the particles in the melt layer possess a non–zero velocity in an inertial reference frame. this latter velocity, indicated as v_l can be evaluated by a mass balance written at the solid–liquid boundary yielding to Eq. 2.29.

$$v_l = \left(\frac{\rho_s}{\rho_l} - 1 \right) \cdot r_f \tag{2.29}$$

Now, energy balance equation can be written for the liquid and solid phases (see Eq. 2.30 and Eq. 2.31 respectively).

$$\frac{\mathrm{d}^2 T}{\mathrm{d}y_l^2} + \frac{1}{\delta_l} \frac{\mathrm{d}T}{\mathrm{d}y_l} = -\frac{\alpha_l \dot{q}_{rad,tot}}{\kappa_l \rho_l C_l} e^{-\alpha_l y_l} \tag{2.30}$$

$$\frac{\mathrm{d}^2 T}{\mathrm{d}y_s^2} + \frac{1}{\delta_s} \frac{\mathrm{d}T}{\mathrm{d}y_s} = -\frac{\alpha_s \dot{q}_{rad,tot}}{\kappa_s \rho_s C_s} e^{-\alpha_s y_s} \tag{2.31}$$

In Eq.2.30 the characteristic thermal thickness in the liquid phase is defined, see Eq. 2.32. While the characteristic thermal thickness for the solid phase, is defined according to Eq. 2.33.

$$\delta_l = \frac{\kappa_l \rho_l}{r_f \rho_s} \tag{2.32}$$

$$\delta_s = \frac{\kappa_s}{r_f} \tag{2.33}$$

Analytical solution of Eqs. 2.30–2.31 can be found by the boundary conditions defined according to Figure 2.13. Therefore for Eq. 2.30, T(0) = T_v and T(h) = T_m, while, for Eq.2.31 one gets T(0) = T_m and $T(h) = T_\infty$. Temperature field in the condensed phase (liquid and solid phases) can therefore being determined.

Energy balance between liquid and solid phases, and between liquid fuel and oxidizer flow can therefore be written as reported in Eq. 2.34 and in Eq. 2.35. Note that in Eq. 2.35 no enthalpy is required for $r_{f,ent}$ to leave the regressing surface. Summing Eqs. 2.34–2.35, the total heat flux from the flame zone to the solid fuel grain is achieved, see Eq. 2.36.

$$-k_l \left(\frac{dT}{dy_l} \right)_{y_l = h} + k_s \left(\frac{dT}{dy_s} \right)_{y_s = 0} - h_{m,f} \rho_s r_f = 0 \tag{2.34}$$

$$\dot{q}_c + \kappa_l \left(\frac{dT}{dy_l} \right)_{y_l = 0} - h_{v,f} \rho_s r_{f,v} = 0 \tag{2.35}$$

$$\dot{q}_w = \dot{q}_r + \dot{q}_c = \Delta h_{m,v} \rho_s r_f + \Delta h_v \rho_s \tag{2.36}$$

Therefore, the vaporization enthalpy of the solid fuel, $h_{v,f}$ (introduced in Eq. 2.1 for the diffusion–limited theory) can be written as in Eq. 2.37.

$$h_{v,f} = \frac{\dot{q}_w}{\rho_s r_f} = C_l \Delta T_{m,v} + C_s \Delta T_{m,in} + h_{m,f} + h_{v,f} \frac{r_{f,v}}{r_f} \tag{2.37}$$

Now, writing explicity in Eq. 2.34 the expression of the temperature derivatives evaluated starting from Eq. 2.30 and Eq. 2.31 the result reported in Eq. 2.38 is achieved defining the following parameters:

- $\psi = e^{\frac{-h}{\delta_l}}$
- $R_l = a_l \, \delta_l$

$$\psi = \frac{h_m \left(R_l - 1\right) + h_v \frac{\dot{q}_r}{\dot{q}_w} \psi^{R_l}}{h_e \left(R_l - 1\right) + h_v \frac{\dot{q}_r}{\dot{q}_w}}. \tag{2.38}$$

Since Eq. 2.38 does not enable the definition of a solution for the general case, two limiting cases identified according to the value assumed by R_l are considered:

1. $R_l \gg 1$:
   under these conditions, radiative heat flux is significantly absorbed by the melted layer of the condensed phase (as for carbon black–loaded fuel formulations). Melted layer thickness is in this case defined by Eq.2.39

$$\delta_{melted\,layer} = \delta_l \ln\left(1 + \frac{C_l \Delta T_{v,m}}{h_m}\right) \tag{2.39}$$

2. $R_l \ll 1$:
   in this case all the radiative heat flux is absorbed by the solid phase, thus

$$\delta_{melted\,layer} = \delta_l \ln\left(1 + \frac{C_l \Delta T_{v,m}}{h_m - h_v \frac{\dot{q}_{rad}}{\dot{q}_w}}\right) \tag{2.40}$$

Note that, in both cases, for the melt layer thickness $\delta_{melted\,layer} \propto 1/\dot{r}$.

Stability of the Liquid Layer

Liquid film stability is detailed investigated in [14]. Qualitative information on stability of the liquid film can be achieved considering the work developed by Gater and L'Ecuyer [51]. In this treatment $\dot{m}_{ent}$ can be defined according to Eq. 2.42 after definition of the term X_e.

$$X_e = \frac{p_{dyn}^{0.5}}{s_{st}\left(\frac{T_g}{T_w}\right)^{0.25}} \tag{2.41}$$

$$\dot{m}_{ent} = \rho_l \dot{r}_{ent} = 1.41 \cdot 10^{-3} \left(X_e - 2109\right) \dot{m}_l \tag{2.42}$$

Considering peculiarities of HRE operating conditions and results of the stability theory presented in [14], Karabeyoglu et al. suggest the following relation for evaluation of $\dot{m}_{ent}$

$$\dot{m_{ent}} \propto \frac{p_{dyn}^{\pi_1} h^{\pi_2}}{\mu_l^{\pi_3} s_{st}^{\pi_4}}. \tag{2.43}$$

According to linear stability theory, Eq. 2.43 should be characterized by values π_1 and π_2 in the range 1–1.5, thus resulting quite similar to the values identified by Gater and L'Ecuyer experimental studies [14].

The Complete Model

Diffusion–limited model require modifications in order to properly extend it to entrainment–producing fuels. This modifications are mainly due to the following reasons:

1. Entrainment alters the ratio $\Delta h_{w,fl}$ / $h_{v,f}$ comparing in the definition of the mass transfer number. This is due to a change in $h_{v,f}$ because of the lower energy required for vaporization of the fuel and a change in $\Delta h_{w,fl}$ part of the regressing fuel being in liquid form.

2. The term St/St^* is modified because of the presence of liquid droplets. Neglecting the effect of melted fuel droplets on momentum and energy transfer, and assuming that droplets combustion does not take place in the region between the regressing surface and the flame, the considered ratio is affected only by the part of the fuel that undergoes vaporization, see Eq. 2.44, [13].

$$\frac{St}{St^*} = f\left(B_v\right). \tag{2.44}$$

3. Interaction with the oxidizer mass flow induces small waves on melted fuel surface. These small waves increase surface rugosity and therefore the convective heat exchange between the flame zone and the surface [13] [14].

The complete theory including entrainment effect on the overall regression rate for given fuel formulation can therefore be expressed as follows, see Eq.2.45.

$$r_{f,v} + \left[R_{he} + R_{hv}\left(\frac{r_{f,v}}{r_f}\right)\right] \cdot r_{f,ent} \quad = Fr \cdot \frac{0.03\mu_g^{0.2}}{\rho_f} \cdot \left(1 + \frac{\dot{q}_{rad}}{\dot{q}_{conv}}\right) B \frac{St}{St^*} G^{0.8} x^{-0.2} \tag{2.45}$$

In Eq. 2.45, the non–dimensional energy parameters for entrainment and vaporization of the fuel are introduced in order to account for the different heating histories of the droplet and the gasified fuel. The latter two parameters are defined according to Eq. 2.46 and Eq. 2.47. The term Fr present in Eq. 2.45 is defined according to Eq. 2.48, and accounts for the increased heat transfer due to the waves formed at melted fuel layer surface due to interaction with oxidizer mass flow.

$$R_{hv} = \frac{C_l \Delta T_{v,m}}{\Delta h_{ent} + \Delta h_{v,f}} \tag{2.46}$$

$$R_{he} = \frac{\Delta h_m}{\Delta h_{ent} + \Delta h_{v,f}} \tag{2.47}$$

$$Fr = 1 + \frac{14.1 \cdot \rho_g^{0.4}}{G^{0.7} \cdot (T_g/T_v)^{0.2}} \tag{2.48}$$

Figure 2.14 and Figure 2.15 provide an overview of the possible regression rate enhancement by entrainment of melted fuel droplets. In the first one pentane is considered as fuel, and entrainment and vaporization contribution to the total r_f as evaluated by the presented liquid film theory is plotted as a function of G, [13]. As can be seen by the reported trends, under the investigated conditions entrainment effect is more and more marked as G is increased, while for the lower mass flux values, the entrainment contribution is lessened. Figure 2.15 shows relative ballistic grading with respect to HTPB of different fuel formulations producing high r_f due to entrainment. Poor regression rate enhancement characterizing isopropanol and HFI–based fuel formulations could be due to the relatively high viscosity of the melt phase possibly hindering entrainment (see Eq. 2.43).

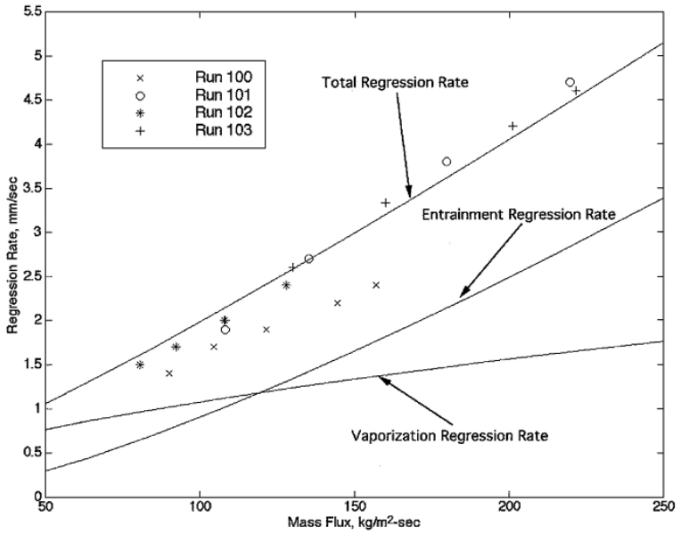

Figure 2.14: Regression rate due to vaporization and entrainment, total effect [13].

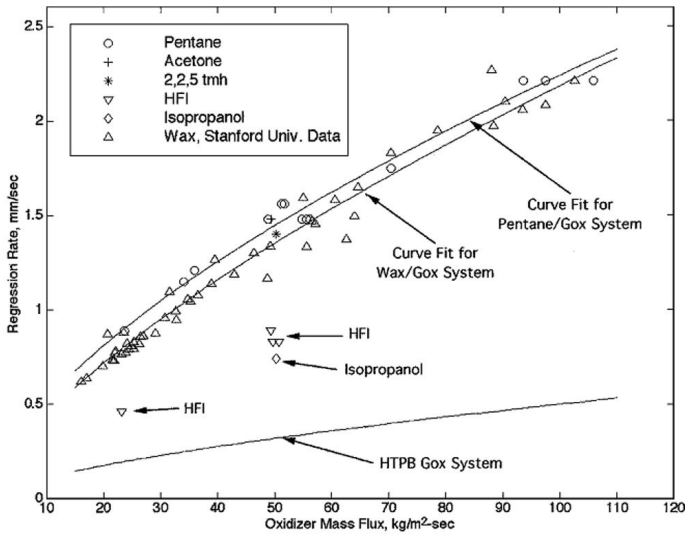

Figure 2.15: Relative ballistic grading with respect to HTPB for entrainment–producing fuels (in particular, note SW performance) [13]. Under the investigated conditions, $r_f \propto G_{ox}^{0}.69$

2.3 Regression Rate Enhancement

Different techniques have been proposed in order to enhance regression rate of hybrid rocket systems. These methods can be classified within two main categories: the fluid dynamic methods and the chemical methods. The former consider the interaction between flowing oxidizer and solid fuel, while the latter concentrates on solid fuel composition and doping by energetic additives.

2.3.1 Fluid Dynamic Methods

Fluid dynamic methods for regression rate enhancement includes non standard–flow oxidizer injection techniques and the induction of turbulent, recirculation flows into the combustion chamber. Due to the relationship between turbulence level of the oxidizer flow and convective heat–transfer phenomena.

The use of solid fuel formulations whose melted layer can be entrained by oxidizer mass flow during combustion can be considered as a possible fluid dynamic technique to enhance the regression rate. The latter solution is detailed discussed in Section 2.2.4.

Swirl–Oxidizer Injection

Swirl flow enables increasing of turbulence levels and reactant mixing into the oxidizer flowing through the solid fuel grain. The main constraint of this technique is related to the swirl dumping along the solid fuel grain length hindering the possible application of this technique for large scale systems. In order to lessen this effects, grains with helical–shaped port perforation have been proposed for head–end swirl–oxidizer injection [54]. Swirl oxidizer flow injection with helical grain configuration can provide significant regression rate increases, up to 80% with respect to standard flow tests [54]. Nevertheless, during combustion helical geometry is consumed by combustion. Therefore helical geometry effects are lessened yielding to possible combustion irregularities during the combustion phase.

During the 1990s, in the frame of ORBITEC research activities on HREs, Knuth et al. developed a vortex hybrid motor schematically shown in Figure 2.16. The peculiarity of this engine is the swirled injection of the oxidizer from the aft part of the combustion chamber (see *GOX inlet* in Figure 2.16). With the injection scheme designed by Knuth et al. a pair of coaxial, bidirectional vortexes are generated in the combustion port [52]. Motors with thrust levels up to 300 lb_f (nearly 3560 N) were designed and tested with different fuel formulations. Due to the intense turbulence levels and mixing in the port perforation, high regression rates as well as high uniformity were achieved under the investigated conditions. In particular, testing HTPB under GOX with a G_{ox} of 100 $kg/(m^2 s)$ a regression rate increase of 400% with respect standard flow engines was achieved by the vortex hybrid configuration [11][52].

Swirl injection was considered also in the VFP developed by Haag et al. [53]. In VFP combustion chamber has a cylindrical shape. Fuel grains with circular shape are placed at the top and at the bottom surfaces of the combustion chamber. Nozzle is placed at the bottom surface of the system of combustion chamber, while oxidizer injectors are sandwiched between the solid fuel grains. Oxidizer injection creates a vortex into the combustion chamber and, after ignition, both fuel grains regress. Oxidizer mass flux, as well as oxidizer inlet velocity and distance between solid fuel grains exhibited strong influence on regression rate [53]. For the tested fuel/oxidizer, achieved regression rate resulted one order of magnitude over the one achieved with conventional hybrid configuration.

Turbulence Generators

According to Reynolds analogy discussed in Section 2.2.1, convective heat–transfer coefficient is related to friction coefficient. Therefore, increasing friction coefficient by screens of metallic wires embedded in the solid fuel grain could eventually promote regression rate increase [3].

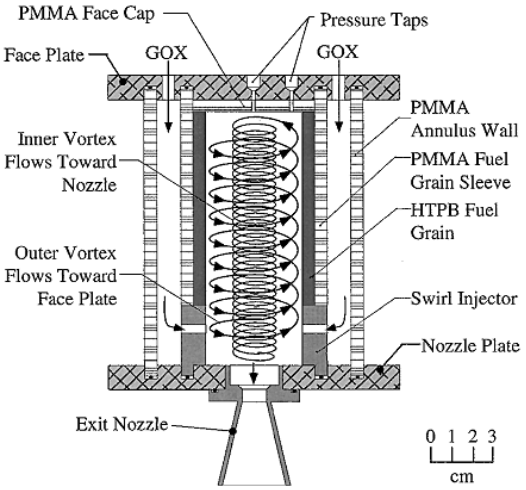

Figure 2.16: VH–20 vortex hybrid rocket engine using HTPB/GOX as propellant. Note swirled injection is performed in the aft part of the engine. The shown configuration can deliver a thrust of 20 lb_f (89 N)[52].

Similarly, rod of conductive material can be radially embedded in the solid fuel grain. As solid fuel regresses, the metal rod emerges from the gasification surface. This yield to a double effect: first, local regression rate is increased by turbulent wake induced by the rod and, second, the rod can enhance heat conduction in depth of the fuel grain, possibly yielding to regression rate increase. Shin et al. tested this latter solution, regression rate increase with respect to conventional configuration resulted almost negligible [55].

2.3.2 Energetic Additives

A way to increase the regression rate of solid fuel formulations consists of incorporating in the fuel grain high-energy ingredients, such as powders of metals, hydride or oxidizer powders [3][4][12]. According to literature data, the latter choice is effective in producing regression rate enhancement by AP addition to the solid fuel, [47][56]. Considering HTPB loaded with 25% AP burning in GOX with oxidizer mass flux of 160 $kg/(m^2s)$, regression rate enhancement with respect to non–filled HTPB of 200% can be achieved. This latter datum reaches 300% when considering a HTPB-based grain formulation filled with 25% AP and 5% burning catalyst (Fe_2O_3) [56]. Nevertheless, solid grains filled with oxidizing powders are not usually considered for applications. This is due to the fact that doping the solid fuel grain with solid oxidizers possibly hinders the advantage of high safety of hybrid systems. This is due to considerations on grain manufacturing and storage, but also because of possible pressure–dependence in regression rate related to AP. Solid grain doping by oxidizer particles could also inhibit the on/off ability characterizing HREs[3] [56].

Usage of metal powders and hydrides as energetic additives enables the solid fuel grain to keep its nature of relatively inert material, while the augmented heat release at/near the regressing surface increases the heat feedback to the solid fuel grain and thus its regression rate. Metal–doped fuel formulations have been investigated till the 1960s, when available metal additives were in the micron–size range [12]. Lips performed experiments to assess the effects of micron–sized Aluminum addition to different polymer-based fuels. Under the investigated test conditions, for burning conducted under FLOX-40 (40% Fluorine, 60% Oxygen) and considering variable mass fractions of additive in a polyurethane binder, solid fuel loaded by 60% μAl and 10% carbon provided the highest achieved regression rate [57]. In the same study magnesium–coated aluminum,

[3]For solid fuel filled with oxidizer particles, PDL value should be evaluated in order to assess influence of this latter parameter on possible on/off capability of the system.

AlMg, with different magnesium mass fractions was tested. AlMg coated by magnesium with coating mass fraction of 50% achieved results close to the one of the 60% μAl/10% C fuel formulations. Lips evaluated also the binder formulation effects on regression rate under a reference condition. For fuel formulations loaded with 60% μAl and with 40% binder, the highest measured regression rate was achieved by CTBN [57]. Strand et al. conducted tests on aluminized fuel formulations based on HTPB loaded with 40% μAl and 30% coal [58]. Being metal additive size in the range of micron-sized materials, achieved regression rate enhancement were mainly related to an increase in radiative heat flux from flame zone to solid fuel surface which opacity was increased by doping with coal. A limited contribution was probably given by enhanced flame temperature due to aluminum combustion. This consideration can be generalized for micron–sized aluminum powders. Common aluminum particles are covered by a thin alumina shell. Due to this micron–sized aluminum particles can ignite only at temperatures close to alumina melting, [59] [60]. Materials characterized by a lower ignition temperature (and mechanism), as magnesium, could deliver different performance [3]. Boron is an attractive additive for hybrid propulsion both for rocket motors and airbreathing propulsion (solid-fuel ramjets) [12][61][62][63]. Boron is characterized by the highest volumetric heat of oxidation of metal/metalloid additives, see Figure 2.17. Nevertheless the exploitation of boron high energy potential is hindered by its hard ignition and poor combustion efficiency [63]. Boron particles are covered by boron oxide, B_2O_3, shell. The latter is characterized by a relatively low melting point and a high viscosity of the liquid phase [63][64]. During heating, boron oxide shell melts and due to its viscosity it hinders diffusion of oxygen toward boron–core [63]. This yield to possible non–ignition of the boron particle. In order to achieve ignite boron particles removal of the liquid B_2O_3 from the particles should occur due to the operating conditions [63]. Since high temperatures promote boron ignition, studies evaluating the possibility of lessening the hard ignition of boron by doping with other metals as Mg, Ti or fluorine–containing polymers [63].

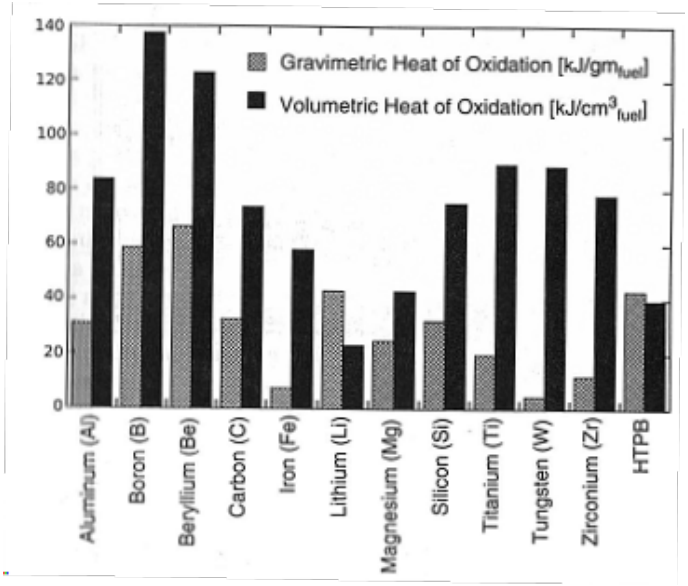

Figure 2.17: Heats of combustion with oxygen (heat of oxidation) of different metal fuels [12]

In the late–1990s progress in the nano-materials field brought focus on chances offered by this novel class of additives. Nano-particles are characterized by dimension $\leq$ 100 nm at least in one direction. At the nano–scale level, metal particles exhibit enhanced chemical reactivity with respect to their micron–sized counterparts due to their large S_{sp}, [60]. This higher reactivity enable nano–size additives to release their energy closer to the regressing surface during combustion, thus yielding higher regression rate increases than micron–sized metal additives [12][60]. Due to availability, cost and combustion characteristics the most interesting nano-sized additive for energetic materials is nAl.

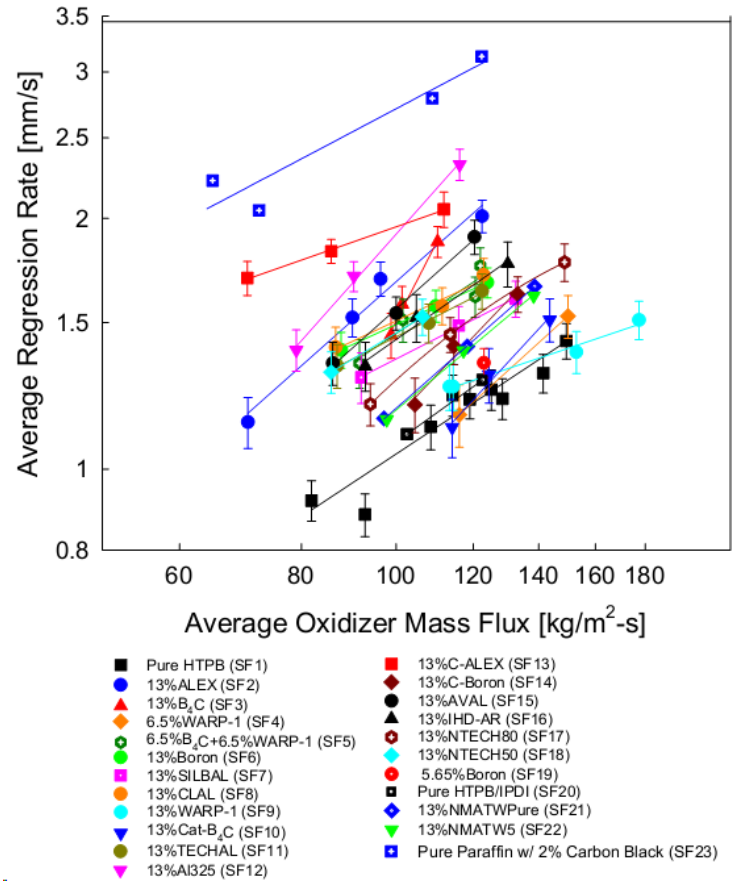

Figure 2.18: Regression rate vs. oxidizer mass flux for several loaded HTPB–based fuel formulations, [12].

Nano–sized aluminum can be produced by a variety of methods, [65]. Nevertheless the most available nAl powder is ALEX, nAl produced by the EEW technique, [66]. Standard ALEX powder presents a shell structure with an external layer of alumina surrounding (and shielding from further oxidation) the Al core, [60][67][68]. Considering nAl, ignition temperature of particles with nominal dimension of in the range of 100 nm occurs at temperatures close to the melting point of aluminum (943 K) or below [64]. This enhanced ignition characteristic with respect to standard micron–sized aluminum particles is related to the *melt dispersion mechanism* [69][70]. Base of this phenomenon is the breakage of the alumina shell due to the high stress induced by the thermal expansion of particle core. An overview of the possible performance enhancement achievable by nAl–doped HTPB–based fuels is shown in Figure 2.18 where data achieved by Penn State University research team are reported. Of all the tested formulations, HTPB loaded with 13% Viton–A coated ALEX can deliver a regression rate increase with respect to HTPB baseline formulation of 130% with an oxidizer mass flux of 112 $kg/(m^2 s)$ [12].

The main drawback of nano–sized additives is due to the difficult effective dispersion of the particles into solid fuel matrix [71][72].
Loading solid paraffin–based grains with metal additives can significantly increase the regression rate of the solid fuel formulation (see Figure 2.19).

Hydrides are attractive energetic additives for solid fuel performance enhancement. Nevertheless these material exhibit high chemical reactivity with commonly employed binders as HTPB. Osmon tested $LiAlH_4$ as possible candidate fuel for regression rate enhancement [74]. Osmon used PE as binder (with a mass fraction of 5% and 95% $LiAlH_4$), and 90% H_2O_2 as oxidizer. Recently, similar studies have been conducted by Larson et al. and DeSain et al. at Penn State University [75][76]. Interest in solid paraffin wax as possible binder for $LiAlH_4$ due to the low reactivity of alkanes limiting possible degradation of the additive (e.g. dehydrogenation). Chemical

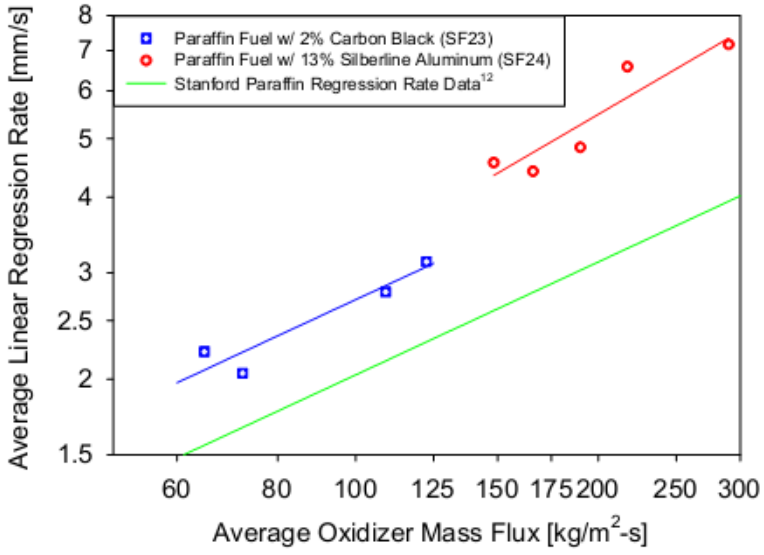

Figure 2.19: Regression rate vs. oxidizer mass flux for paraffin–based fuels. Note high regression rate enhancement for formulation loaded with 13% Silberline nano–aluminum flakes (red solid line) [12].

compatibility with binder is the main drawback of hydrides for application in HTPB–based solid fuel formulations. Possible alternative binders for hybrid and solid rocket motors application is given by Humble [77]. At any rate, none of the experiments conducted in by Osmon, Larson et al. and DeSain et al. enables a relative ballistic grading of hydride–loaded formulations with respect to non–loaded fuels. On the other hand, hydrides have been extensively investigated from the theoretical (thermochemical) point of view [78][79]. Due to the presence of hydrogen, hydrides can provide specific impulse enhancement with respect to standard solid fuel/propellant formulations [60][73][78]. In this respect aluminum hydride, AlH_3 is particular attractive due to its extremely high density for hydrogen storage [73]. Aluminum hydride consists of about 10% hydrogen by mass, thereby providing a higher density of hydrogen than liquid hydrogen [80][81]. Nevertheless, problems in AlH_3 stabilization limit its availability (AlH_3 is not available at commercial level) and therefore the application of this otherwise promising additive [82].

2.3.3 Overview of Revised Concepts

The intrinsic limitation of HREs is mainly the low regression rate hindering possible high thrust levels with simple grain geometry (e.g. single port perforation). For relatively small motors, servicing for micro–satellites or specific maneuvers (e.g. attitude control, de–orbiting systems) technical solutions based on oxidizer swirl injection and non–conventional configurations as the vortex hybrid developed at ORBITEC appear particularly promising. Nevertheless, when aiming to large scale applications (e.g. light or heavy launchers, boosters) high thrust level requirement with simple grain geometry yields to the research of novel energetic formulations and a better comprehension of hybrid combustion process.

CHAPTER 3

TESTED SOLID FUEL FORMULATIONS

In this section the ingredients used for manufacturing of the tested solid fuel formulations and their characteristics are presented. In the experimental investigation HTPB–based and solid paraffin wax–based fuels were considered. Both base–fuel formulations were loaded with metal additives differing for kind and particle–size with the aim of evaluating the effect of doping on regression rate under the investigated conditions.

HTPB–based fuels are considered due to the high overall mechanical properties of this binder leading to its widespread use in rocket industry [83]. HTPB versatility enables solid fuel loading with different additives. On the other hand HTPB formulation is not specifically optimized for rocket–applications.

Solid paraffin wax–based fuels are considered in the experimental analysis due to the high regression rate increase with respect to polymer–based fuel formulations [13][14]. Low chemical reactivity of wax–based fuels enabled testing of highly reactive additives exhibiting low chemical compatibility with HTPB.

Table 3.1 and Table 3.2 provide an overview of the HTPB– and solid paraffin wax–based fuel formulation. Details of each ingredient and of manufacturing procedure are given in Section 3.4.1 and in Section3.4.2. An investigation of the mechanical properties of some of the tested fuels is reported in Section with the aim of providing an insight of the manufacturing procedure influence on dispersion of the metal additives into a polymeric HTPB–based matrix.

Table 3.1: HTPB–binder standard formulation.

Ingredient (Short Hand Notation)	**Mass Fraction** %	**Density, ρ, kg/m^3**
Hydroxyl–Terminated Polybutadiene R45 (HTPB R45)	79.03	901
Dioctyl Adipate (DOA)	13.07	925
Isophorone Diisocyanate (IPDI)	7.69	1060
Dibutyltin Diacetate (TIN)	0.22	1310
HTPB Binder	100	≈920

Table 3.2: Solid paraffin wax–binder formulation.

Ingredient (Short Hand Notation)	**Mass Fraction** %	**Density, ρ, kg/m^3**
Solid Paraffin Wax (SW)	88	890
Octadecanoic Acid (SA)	10	845
Carbon	2	2100
SW Binder	100	≈900

3.1 HTPB–binder: Ingredients

3.1.1 HTPB–R45

HTPB–R45 supplied by Fiat Avio was used in this study. Characteristics of the material are presented in Table 3.3. HTPB belongs to the class of polyols and is characterized by the presence of hydroxyl groups by means of which macromolecules can be linked together by a proper curing agent with a urethane reaction. HTPB reacts with diisocyanate providing a polyurethane, a stable and easily storable material [83][84][85][86].

Table 3.3: Characteristics of HTPB-R45 by Fiat Avio.

Property	**Value**
Molecular Weight, Mn, g/mol	2800
Hydroxyl Functionality	2.352
Hydroxyl Value, OH_V, meq/g	0.84
Specific Gravity at 23°C, g/cm^3	0.901

3.1.2 Dioctyl Adipate

In the present work DOA was used as plasticizer. Plasticizer does not produce any reaction with other ingredients of polymeric binder formulation. Due to its relatively low viscosity, plasticizer enables better mixing of the compound during manufacturing. Plasticizer is also responsible for final product elasticity after curing. DOA is an ester of n–octanol and adipic acid with chemical formula $C_{22}H_{42}O_4$ and is supplied by ACROS–Carlo Erba.

In previous studies conducted at SPLab, the effect of plasticizer on ballistic properties were investigated. Considering ballistics of HTPB–based fuel formulations burning under oxygen–nitrogen mixtures, minor effects on regression rate were identified as related to this ingredient [36].

3.1.3 Isophorone Diisocyanate

IPDI was used in this study as curing agent. The latter is the component enabling the link of different HTPB macromolecules. By a urethane reaction, the N–C–O groups of IPDI reacts with the –OH groups of HTPB yielding to a solid–phase material. The –NCO over –OH ratio of this urethane reaction define the curing level of the compound. HTPB–binder manufactured at SPLab is characterized by a curing level of 1.04. The latter value is chosen in order to provide the highest possible number of urethane bonds in the binder matrix.

Manufacturing tests were performed with a reduced curing level with the aim of evaluate the effects of the latter parameter on ballistics of HTPB–based fuel formulations. With curing levels below 0.8 cured material exhibited very poor mechanical properties. Burning tests performed on samples with reduced –NCO/–OH yielded to combustion with poor visualization quality related

to the low mechanical properties of the solid fuel grain. Due to these reduced material properties, regression rate of the solid fuel cannot be properly evaluated.

IPDI chemical formula is $C_{12}H_{18}N_2O_2$, and is supplied to SPLab by Alfa Aesar GmbH & Co.KG. Due to its high reactivity with –OH groups IPDI requires proper storing conditions and manufacturing under controlled environmental conditions.

3.1.4 Dibutyltin diacetate

Reaction rate for the curing of HTPB polymer with IPDI can be enhanced by dibutyltin diacetate. This grants a faster curing and more complete reaction between HTPB functional groups and –NCO terminations of IPDI.

Dibutyltin diacetate chemical formula is $(CH_3CO_2)_2Sn[(CH_2)_3CH_3]_2$, the material is supplied to SPLab by Sigma Aldrich. As for IPDI, dibutyltin diacetate requires proper storage conditions preventing oxidation of the material yielding to a loss of its catalytic effect on curing.

3.2 SW–binder: Ingredients

3.2.1 Solid Paraffin Wax

Paraffin waxes are alkanes, chemical compounds of carbon and hydrogen with general chemical formula C_nH_{2n+2}. In the alkanes family, paraffin are characterized by relatively low chemical reactivity with other elements under ambient conditions. In fact the name paraffin is derived from the latin *parum affinis*, meaning *with low affinity*. For $n \geq 16$, paraffin can be found at solid state under ambient conditions [87].

SW used in this study is characterized by a melting temperature in the range 57–59°C and is supplied to SPLab by Carlo Erba Reagenti, Italy.

3.2.2 Octadecanoic Acid

Octadecanoic acid is a weak carboxylic acid with chemical formula $CH_3(CH_2)_{16}COOH$, in the common practice it is also indicated as stearic acid. Octadecanoic acid is solid under ambient conditions. During manufacturing SA is melted and mixed with melted SW in order to reduce SW frailty thus enhancing mechanical properties of the final wax–based grains, [36]. Octadecanoic acid is supplied to SPLab by Sigma–Aldrich.

3.2.3 Carbon

Carbon powder is used in SW–binder formulation in order to enhance the possible radiative heat transfer between the flame zone and the regressing surface [11] [13] [36]. Figure 3.1 shows a microscope image of tested carbon in order to provide an evaluation of its particle–size. A wide size–distribution is observed in the powder (not treated by any dispersion technique prior visualization).

3.3 Tested Additives

Base characterization of solid fuel formulations was conducted on non–loaded HTPB and SW fuels. Non–loaded HTPB was taken as baseline for relative ballistic grading of different fuel formulations. In order to evaluate regression rate increase, HTPB– and SW–based fuels were doped with energetic additives. An overview of the tested fuel formulations is given in Table 3.4 and Table 3.5, while detailed characterization of each additive is reported in Sections 3.3.1–3.3.5. The carbon powder used as filler in HTPB–based fuel formulations doped with nAl is the same presented in Section 3.2.3.

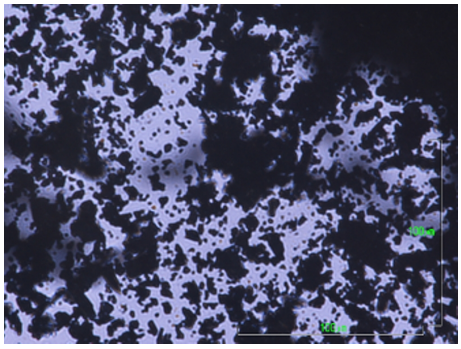

Figure 3.1: Microscope image of carbon powder used in the study

For all tested formulations but nFe– and MgB–doped fuels, mass fraction of additives is selected in order to grant equi–molar content of considered metal and AlH_3 moles contained in HTPB + 11.2% AlH_3. In MgB–based additives B molar content is half of the AlH_3 molar content in HTPB + 11.2% AlH_3 (Mg is considered as an additive for B ignition). Due to its high molar mass, yielding to high mass fraction in order to achieve equi–molar conditions with tested metals, no condition was imposed on nFe mass fraction.

Table 3.4: Tested HTPB–based fuel formulations. Refer to Sections 3.3.1–3.3.5 for further details.

HTPB Loaded with Metals	**HTPB Loaded with Hydrides**
HTPB + 2% C + 10% ALEX	
HTPB + 2% C + 10% L–$ALEX_{APS}$	
HTPB + 2% C + 10% L–$ALEX_{NPS}$(100 nm)	
HTPB + 2% C + 10% L–$ALEX_{NPS}$(50 nm)	
HTPB + 2% C + 10% F–$ALEX_{APS}$	
HTPB + 2% C + 10% VF–$ALEX_{APS}$	HTPB + 11.2% AlH_3
HTPB + 1% C + 5% nFe	
HTPB + 2.5% MgB90 (10% Mg)	
HTPB + 2.4% MgB95 (10% Mg)	
HTPB + 2.8% MgB90 (20% Mg)	

Table 3.5: Tested SW–based fuel formulations. Refer to Sections 3.3.1–3.3.5 for further details.

SW Loaded with Metals	**SW Loaded with Hydrides**
	SW + 11.2% AlH_3
SW + 2.8% MgB90 (20% Mg)	SW* + 7.1% $LiAlH_4$
	SW* + 5% Li_3AlH_6

* No SA included in the fuel formulation

3.3.1 Nano–sized Aluminum Powders

Different nAl powders are considered in this work, see Table 3.4 and Table 3.6. Nano–sized aluminum powders were produced by EEW by Advanced Powder Technology LLC, Tomsk, Russian Federation [88]. Details on production operating parameters are reported in [89]. All tested powders, except L–$ALEX_{NPS}$, were passivated in a controlled atmosphere by dry air stream immediately after production and are therefore coated by an alumina layer [64] [67] [90]. Air–passivated powders are manufactured at lab–scale for coating process [89]. Industrial powder L–$ALEX_{NPS}$ characterized by the absence of an alumina layer around Al particles, is considered as a convenient comparison for lab–scale powders ballistic performance evaluation [68].

Nano–sized aluminum powders are tested due to their attractive features (high reactivity and combustion enthalpy). The use of both APS and NPS powders is intended for investigation of

alumina shell effect on combustion properties. The variety of coatings applied to nAl powders is performed in order to investigate of possible effects under HRE burning conditions.

Table 3.6: Tested nAl powder coating composition and nominal dimension [89]

Powder	Applied Coating	Particle Nominal Size, nm
ALEX	–	100
L–ALEX$_{APS}$	Octadecanoic acid	100
L–ALEX$_{NPS}$	Octadecanoic acid	100, 50
F–ALEX$_{APS,E}$	Fluoroelastomer alcohol 10:1	100
VF–ALEX$_{APS,F}$	Fluorel^{TM}and ester from esterification of FTOH with maleic anhydride	100

Coating and Physical Characterization

Coating of L-ALEX$_{APS}$ is obtained adding ALEX powder in a hydrocarbon solution in which SA is solved. The mixture is then put in a ultrasonic dive mixer for about 20 minutes. After that, the mixture is filtered through a thin polypropylene membrane. Coating of F-ALEX$_{APS,E}$ followed a similar procedure with telomer alcohol solved in isopropyl alcohol and final evaporation of residual solvent. VF–ALEX$_{APS,F}$ is manufactured starting from ester from esterification of trihydroperfluoro–undecyl alcohol with maleic anhydride. The ester was then added to a solution of Fluorel^{TM}[91] in dimethyl sulfoxide. After this, ALEX soluted in isopropyl alcohol/dimethyl sulfoxide was placed in the solution. The whole compound was sonicated by an ultrasonic dive mixer for about 25 minutes before being filtered by a thin polypropylene membrane. In preparation of coated formulations, ingredients were scaled in order to achieve a mass fraction of coating of 5–10% with respect to initial nAl mass. Figure 3.2 and Figure 3.3 shows TEM images of some of the tested nAl powders. Sintering of particles due to production phase and coating process is clearly recognizable from TEM images and is common to all tested additives [89].

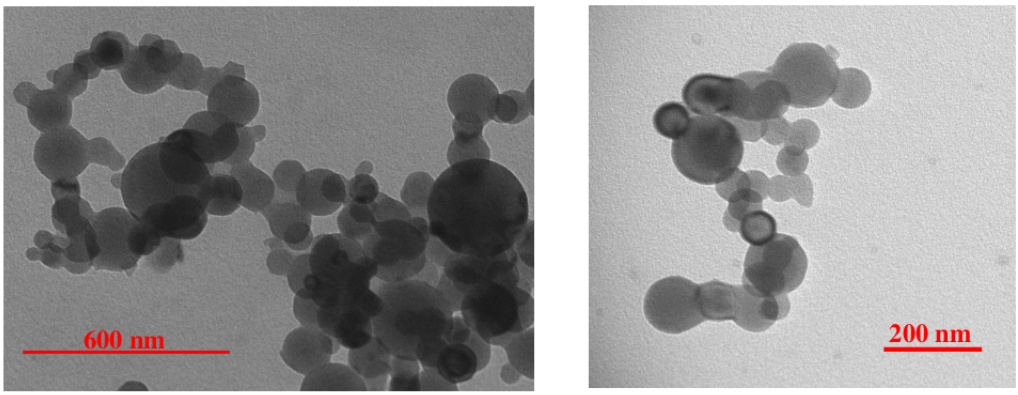

Figure 3.2: TEM image of L–ALEX$_{APS}$ (a) and L–ALEX$_{NPS}$ (b) [89].

Figure 3.4 reports DSC/TGA analysis of ALEX. Under investigated conditions a first mass loss is observed for T $<$ 500°C (773 K) identified in Table 3.8 as Δm_1. The latter is related to several possible reasons

- evaporation of humidity adsorbed on particles (the only possible cause of mass loss for standard ALEX powder) [89];
- evaporation of residual solvent (for powders treated with chemical reactants);
- decomposition of the coating subtle layer around the particles for all coated powders;

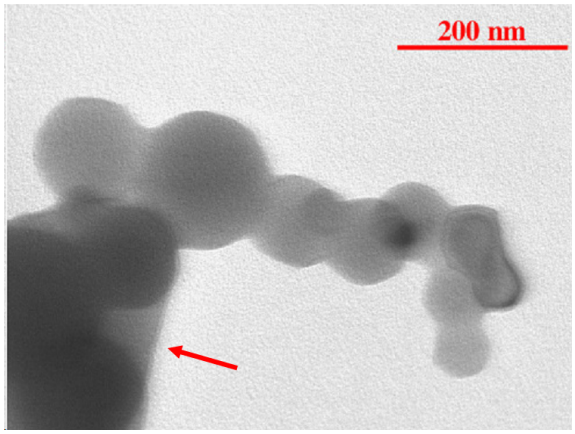

Figure 3.3: TEM image of F–ALEX$_{APS,E}$, note cluster of particles sorrounded by coating [89].

- adsorbed gases desorption.

After the initial mass loss Δm_1, a mass gain is observed (up to the value Δm_{tot}). Under the inveatigated conditions (relatively low heating rate) two oxidation peaks are visible for ALEX powder [64][67][68][93]. Tested nAl powders physical parameters and reactivity data are reported in Table 3.7 and Table 3.8. More complete information, including XRD data of the tested powders showing that peaks of Al are the only recognizable phases, are reported in [89]. For the investigated nAl powders, Al^0 content was evaluated by volumetric method based on the evolution of hydrogen obtained when placing a small sample of nAl in an aqueous solution of 5% mass fraction content of sodium hydroxide. Data reported in Table 3.7 show that the highest active aluminum content for the 100 nm tested powders is achieved by ALEX, while coated additives are characterized by lower values. This is due to the presence of an additional coating that increase particle mass and dimension with respect to standard ALEX. Additional coating causes reduction of S_{sp} of coated powders with respect to the one of ALEX, this is possibly related due to the lab–scale level of coating manufacturing process (with coating material eventually covering cluster of particles and/or promoting the formation of new clusters). Alumina shell surrounding air-passivated particles explains differences in Al^0 content between L-ALEX$_{NPS}$ and L-ALEX$_{APS}$.

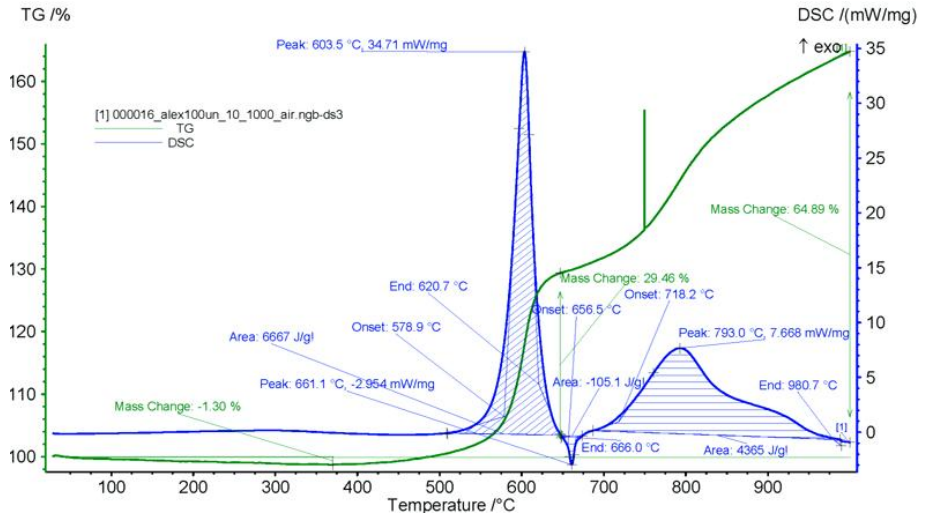

Figure 3.4: DSC/TGA of ALEX tested under air with heating rate of 10 K/min (reference sample α–Al_2O_3) [89].

According to data reported in Table 3.8, under the investigated DSC/TGA conditions F–ALEX$_{APS,E}$ has the lowest temperature of intensive oxidation onset (T$_{onset,\,1st\,peak}$) in the tested

Table 3.7: Physical parameters of tested nAl powder. S_{sp} evaluated by BET, Al^0 evaluated by volumetric method after 1 hr. hydrogen evolution [89].

		100 nm			**50 nm**
Analysis	**ALEX**	**L–ALEX**$_{APS}$	**F–ALEX**$_{APS}$	**VF–ALEX**$_{APS}$	**L–ALEX**$_{NPS}$
$S_{sp}, m^2/g$	11.8	9.1	11.3	6.9	11.3
a_s, nm	202	267	205	345	228
C_{Al^0}, % [a]	89	70	88	78	89
[a] Evaluated wrt total mass					

Table 3.8: Evaluated by DSC/TGA analysis on nAl powders considered in the present study (air, heating rate 10 K/min) [89]. Data for 100 nm L-ALEX$_{NPS}$ not available.

			100 nm		**50 nm**
Parameter	**ALEX**	**L–ALEX**$_{APS}$	**F-ALEX**$_{APS,E}$	**VF–ALEX**$_{APS,E}$	**L-ALEX**$_{NPS}$
Δ m$_1$ % [a]	1	3	1	6	5
T$_{onset,\,1st\,peak}$, K	852	860	851	888	855
T$_{oxid,\,1st\,peak}$, K	876	868	884	895	877
ΔH$_{oxid,1}$, J/g	6667	5489	6938	4171	8540
ΔH$_{oxid,2}$, J/g	4365	4223	4679	3119	3620
ΔH$_{oxid,1}$/ΔH$_{oxid,2}$	1.5	1.3	1.5	1.1	2.4
ΔH$_{oxid,1+2}$, J/g	11032	9712	11617	8090	12160
Δm$_{tot}$ [b,c], %	65	62	69	48	66
α(773–1273 K), % [d]	82	99	87	69	83

[a] Weight loss prior of oxidation onset, percent value wrt nAl sample total mass
[b] Percent value wrt nAl sample total mass
[c] For T up to 1273 K (1000°C)
[d] $\alpha(Al \rightarrow Al_2O_3) = \Delta m_{tot}/(C_{Al^0} \cdot 0.89)$

powder set. Nevertheless difference with ALEX is negligible (see Table 3.8). Considering the temperature of the first oxidation peak, L–ALEX$_{APS}$ exhibits the best performance. VF–ALEX$_{APS}$ is characterized by the highest temperature of intensive oxidation onset, and the lowest heat releases in both recognized oxidation peaks. This low reactivity of VF–ALEX$_{APS}$ evidenced by DSC/TGA data could be related to data concerning S$_{sp}$ reported in Table 3.7. Speculating on the basis of DSC/TGA, considering the total heat release during the two oxidation peaks, 50 nm L–ALEX$_{NPS}$ should be the best candidate as energetic additive.

3.3.2 Nano–sized Iron Powders

Nano–sized iron powder was produced with EEW by APT LLC, Tomsk, Russian Federation [88]. A TEM image of nFe reveals a wide particle size distribution into the tested sample, see Figure 3.5, while characteristic dimension is in the range 50–110 nm [88]. Particle clustering and cold cohesion are a common feature for nano–sized particles (nFe and nAl, see Section 3.3.1). Nano–sized iron is effective in lowering the onset temperature of decomposition of cyclotetramethylene–tetranitramine (HMX) and AP. Oxidation onset temperature of nFe results relatively low though the oxidation process results quite slow [94][95][96]. Nano–sized iron powder was considered as a possible candidate for solid fuel loading due to Fe high density possibly yielding to significant mass burning rate enhancement. As received, nFe powder was dispersed in hexane due to its flammability.

3.3.3 MgB Powders

MgB is an energetic additive developed by MACH I, King of Prussia, Pennsylvania, USA [97]. MgB is an innovative composite metal powder where boron is bonded to magnesium. No detail is given by the manufacturer on the nature of the bonding between magnesium and boron.

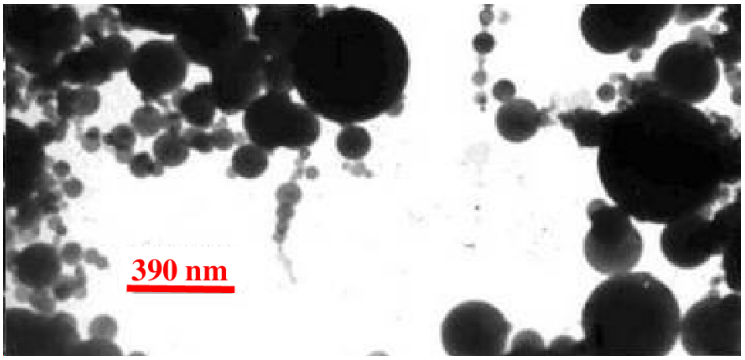

Figure 3.5: TEM of nFe, note relatively wide particle–sizes distribution [88]

Boron offers the highest volumetric heat of oxidation in oxygen between metals/metalloids, but is characterized by difficult ignition and poor combustion efficiency [12] [63]. MgB–based additives are micron–sized powders designed with the aim of lessening boron burning difficulties thus yielding to exploitation of its energetic potential. Tested powder mass–composition and physical characterization are reported in Table 3.9 and Figures 3.6–3.7. Being micron–sized, MgB particles do not require dedicated techniques in order to be properly dispersed into the binder matrix. Due to this feature, MgB–powders were tested for both HTPB– and SW–based fuel formulations.

Table 3.9: Tested MgB–powders characterization. Composition [97], and physical characterization by Malvern Mastersizer 2000 (Reina, 2011).

Powder	**C_B–C_{Mg}, % wrt total mass**	**B purity, %**	**D_{43} μm**	S_{sp} m^2/g
MgB90 (10% Mg)	90–10	90	7.1	3.3
MgB95 (10% Mg)	90–10	95	4.4	4.1
MgB90 (20% Mg)	80–20	90	5.2	3.5

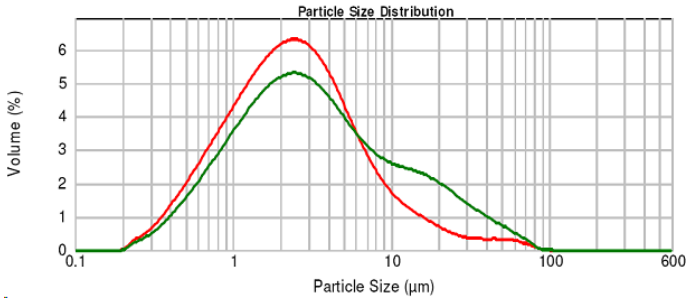

Figure 3.6: Particle–size distribution for MgB90 (10% Mg) [green curve] and MgB95 (10%) [red curve] as evaluated by Malvern Mastersizer 2000 (Reina, 2011). Note MgB95(10%Mg) high volume fraction of particles with particle size above 10 μm. Each curve is defined as average of three performed tests.

3.3.4 Metal Hydrides

An overview of the tested metal hydrides is reported in Table 3.10. Detailed information on hydrides chemical characteristics and chemical compatibility with binders used in rocket industry is available in [73][74].

Since its arrival at SPLab, AlH_3 had been stored in a isolated environment till manufacturing of tested samples on October 2011. Storage condition prevented the powder to be exposed to wet air. A SEM of the used powder is reported in Figure 3.8. SEM image shows regular-shaped crystals

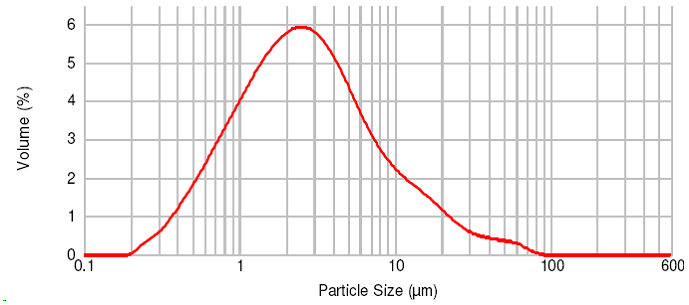

Figure 3.7: Particle–size distribution for MgB90 (20% Mg) as evaluated by Malvern Mastersizer 2000 (Reina, 2011). Curve is defined as average of three performed tests.

Table 3.10: Investigated hydrides basic data.

Additive	$Mm,\ g/mol$	**Density,** $\rho,\ kg/m^3$	**Dehydrogenation Temperature**, K	Supplier
AlH_3 [a]	30.0	1476	433-483	–
$LiAlH_4$ [b]	37.9	917	410	Chemetall GmBH
Li_3AlH_6 [c]	53.8	994	463–483	Chemetall GmBH

[a] [80][98][99]
[b] [73]
[c] [73][100]

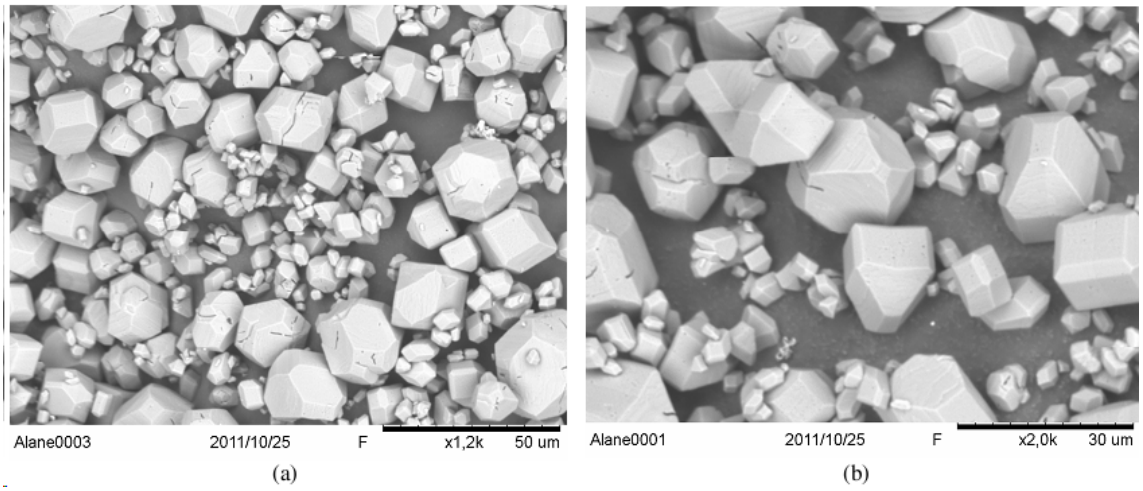

Figure 3.8: SEM of tested AlH_3. Note high regularity of shape of visibile crystals, a characteristic of stable α-alane. Crystals dimensions range from ≈50 μm down to ≈5μm. Bigger crystals present cracks possibly related to ageing of the samples but no porosity due to dehydrogenation can be identified.

without marked dehydrogenation, while cracks are clearly visible. The latter are probably due to aging process of the powder and is not considered as a possible cause/consequence of hydrogen desorption from the crystals. Aging phenomena could be related to thermal stresses acting on the crystals of α–AlH_3. Hydrogen content into alane powder was determined by DSC (TA Instrument 2010). Under the investigated conditions (nitrogen atmosphere, heating rate 10 K/min) the purity of the powder was indirectly evaluated by measurement of the endothermic peak associated to dehydrogenation. Achieved result show a purity above 90% for the tested AlH_3 (Maggi, 2011).

The considered AlH_3 powder did not exhibit apparent dehydrogenation reaction with both HTPB– ans SW–based fuels during manufacturing.

$LiAlH_4$ and Li_3AlH_6, due to the poor compatibility with HTPB [73][74] were tested only on SW–based fuel formulations. Moreover due to poor compatibility with acids, $LiAlH_4$ and Li_3AlH_6 were added to SW–grains with modified formulation due to SA elimination (SW mass fraction was correspondingly increased).

3.3.5 Tested Additive Comparison

In order to achieve a relative grading of investigated additives reactivity under reference conditions, ignition temperature was evaluated by means of a conductive–heating technique. Experimental setup for additives characterization and experimental procedure are detailed described in [101]. Ignition tests have been performed in a quiescent air atmosphere, with p_c of 1 bar. Achieved results are reported in Table 3.11.

Table 3.11: Ignition temperature as evaluated under conductive heating in quiescent air at 1 bar. Note decreasing T_{ign} of MgB with respect to reference Boron (B90), for a convenient comparison data for Mg are reported. Confidence interval 95%, five tests performed for each additive [101] [40].

Metal Additive	T_{ign}**, K**
ALEX	865 ± 15
L–$ALEX_{APS}$	823 ± 48
L–$ALEX_{NPS}$, (100 nm)	777 ± 49
L–$ALEX_{NPS}$, (50 nm)	791 ± 51
F–$ALEX_{APS}$	892 ± 9
VF–$ALEX_{APS}$	NA
nFe	NA[c]
B90[a]	1004 ± 31
Mg[b]	869 ± 56
MgB90 (10% Mg)	870 ± 42
MgB95 (10% Mg)	835 ± 20
MgB90 (20% Mg)	927 ± 57
AlH_3	614 ± 35
$LiAlH_4$	398 ± 31
Li_3AlH_6	451 ± 9

[a] Micron–size B, (0.7 μm)
[b] Micron–size Mg (4 μm)
[c] No ignition achieved under the tested condition

Data reported in Table 3.11 show the high reactivity of tested hydride yielding to low T_{ign}. In particular, $LiAlH_4$ is characterized by a very low ignition temperature, close to the dehydrogenation temperature (see Table 3.10). In comparison with $LiAlH_4$, Li_3AlH_6 exhibits a lower reactivity under the investigated conditions (higher T_{ign}), while data scattering appear quite reduced. This is possibly due to the fact that Li_3AlH_6 is an intermediate product of $LiAlH_4$ decomposition [102]. Considering metal powders, MgB–based additives exhibit reduced T_{ign} with respect to pure boron. In spite of this result, under the investigated conditions Mg influence on MgB ignition temperature presents some difference between MgB90 (10% Mg) and MgB90 (20% Mg).

ALEX–serie additives are characterized by T_{ign} lower than the melting point of Al. Comparing results reported in Table 3.11 with those of Table 3.8 a general agreement between DSC/TGA and performed ignition tests is noticed. In particular, ALEX and F–ALEX$_{APS}$ exhibits T_{ign} close to the $T_{oxid,\,1st\,peak}$. In spite of the achieved data scattering the average T_{ign} characterizing the performed tests of L–ALEX$_{APS}$ and L–ALEX$_{NPS}$ results quite lower with respect to the DSC/TGA data.

3.4 Manufacturing Procedure

Relative ballistic grading requires proper manufacturing procedure granting high quality of the tested fuel formulations. SPLab has developed a variety of experimental hardware and procedures for this purpose. In Section 3.4.1 and Section 3.4.2, SPLab manufacturing procedures for HTPB– and SW–based fuels are presented.

Relative ballistic grading is performed by the experimental facility presented in Chapter 4. In this test rig cylindrical–shaped single port strands are tested. Samples are cast in a stainless steel case. Strand central port has a nominal initial diameter of 4mm, while radial web thickness and solid fuel grain length are 7mm and 30mm respectively.

3.4.1 HTPB–based Fuels

Tested fuels were manufactured according to a dedicated SPLab internal procedure. Manufacturing was performed in a chemical laboratory with dedicated facilities and controlled environment. Procedure operating steps are hereby presented, considering the manufacturing of nano–particle loaded fuel.

1. Required quantity of HTPB is poured into a Teflon beaker (after check of static electric charge absence). Teflon beaker is then placed in an oven with thermostat temperature of 60°C for 30 minutes.
2. Teflon beaker is extracted from the oven and placed in a vacuum chamber. When HTPB temperature is lessened to ambient temperature, beaker is extracted from the vacuum chamber.
3. DOA and dibutyltin diacetate catalyst are poured into the Teflon beaker (after check of static electric charge absence).
4. The beaker containing HTPB, DOA and catalyst is placed in a bath of oil at 60°C. The beaker is then closed and connected to mixing impeller and vacuum pump. Aim of the heat treatment on the compound is to lessen HTPB viscosity in order to enable efficient extraction of gas inclusions into the fuel.
5. The three components are then mixed under vacuum for 30 minutes.
6. If metal additives or other fillers are required for the considered fuel formulation, they are prepared in the proper amount into a Pyrex beaker (to lessen static electric charge problems).

   - If different fillers are used (as for nAl–loaded fuel formulation), a preliminary mixing of the powders is performed.
   - If nano–sized additives are used, Pyrex beaker is placed in an ultrasonic bath for 15 minutes for sonication. Aim of the ultrasonic irradiation is to disaggregate clusters eventually formed by powder nano-particles cold–cohesion.

7. HTPB, DOA and catalyst are extracted from 60°C oil bath and are placed in vacuum bell for 15 minutes (or till the end of apparent bubbling from the beaker).
8. Additive is added to HTPB, DOA, and catalyst. The compound is then mixed in the 60°C oil bath. No vacuum–cycle is performed on the compound for the first 5 minutes of mixing in order to properly disperse the additive. Then vacuum pump is activated and the formulation is mixed for 10 minutes under vacuum.

9. The Teflon beaker is then extracted from oil bath and placed in the ultrasonic bath for 15 minutes.
10. The compound is extracted from ultrasonic bath and then cooled under vacuum in a proper bell (if necessary, additional cooling with air is performed after bubbling from the compound is over).
11. IPDI is added to the compound during impeller mixing.
12. Compound is mixed for at least 10 minutes to grant proper IPDI dispersion.
13. Compound is poured into moulds.
14. Moulds are closed and placed in a 60°C oven for 25 hours.

For MgB– and hydride–doped HTPB–based fuels the manufacturing procedure is performed at ambient temperature due to possible chemical interactions between energetic additive and binder matrix. Dedicated dispersion procedures as ultrasonic irradiation are not required for micron–sized additives and are therefore generally not performed. Manufacturing procedure for nFe–loaded samples require different manufacturing procedure.

Manufacturing Procedure of HTPB doped with Nano–sized Iron

Nano–sized iron was received in suspension in hexane due to powder flammability. Manufacturing of HTPB loaded with nFe required removal of excess hexane. In order to avoid possible cold clustering due to hexane removal with addition of dry powder to the HTPB resin a different approach was followed. Manufacturing started with HTPB pre–treatment, according to the point 1. and 2. of Section 3.4.1. Then the solution with hexane and nFe was added to the HTPB. The compound was stirred under vacuum at 80°C till complete (or almost complete) hexane removal. The beaker with the compound was then weighted in order to evaluate the mass of nFe added to HTPB. Sonication was performed during this part of the procedure to lessen cold cohesion of nFe particles. The procedure was repeated till the required amount of nFe was added to HTPB. After this, procedure continued similarly to what reported in section 3.4.1.

3.4.2 SW–based Fuels

Manufacturing procedure for SW–based fuels is articulated according to the following operating steps.

1. Required amounts of SW, SA and carbon are placed in a Pyrex beaker (after check of static electric charge absence).
2. Pyrex beaker is placed in a heated oil bath with temperature of 70°C till complete melting of SW and SA.
3. Compound is mixed for 10 minutes by an impeller inserted in the beaker.
4. Energetic additive (if required) is added to the compound. The fuel formulation is then mixed for 10 minutes.
5. Compound is gradually poured into moulds. Operation in performed in multiple steps in order to avoid possible imperfections in the solid fuel grain.
6. After complete filling, the mould are left at ambient temperature for complete cooling.

In SW–based fuel manufacturing procedure no vacuum cycle is performed. For hydride–doped solid fuel formulations, oil bath temperature can be tailored in order to avoid possible dehydrogenation phenomena or other chemical reactions.

Table 3.12: TMD and measured densities of tested fuel formulations. Though no–vacuum cycle, SW–based fuel exhibits low porosity values. Negative values of porosity due to possible excesses of ingredients with respect to nominal values.

Fuel Formulation	**TMD,** kg/m^3	$\rho_{f,\,Measured}$ kg/m^3	$\Delta\rho_{f,\,\%}$, **%, Eq.3.1**
HTPB	920	918±1	+1
HTPB + 2% C + 10% ALEX	992	991±2	+1
HTPB + 2% C + 10% L–ALEX$_{APS}$	992	1006±7	−1
HTPB + 2% C + 10% L–ALEX$_{NPS}$ (100 nm)	992	990±2	+2
HTPB + 2% C + 10% L–ALEX$_{NPS}$ (50 nm)	992	991±2	+1
HTPB + 2% C + 10% F–ALEX$_{APS}$	992	1006±7	−1
HTPB + 2% C + 10% VF–ALEX$_{APS}$	992	997±3	−1
HTPB + 1% C + 5% nFe	963	927±2	+4
HTPB + 2.5% MgB90 (10% Mg)	928	939±4	−1
HTPB + 2.4% MgB95 (10% Mg)	929	938±2	−1
HTPB + 2.8% MgB90 (20% Mg)	930	902±1	+3
HTPB + 11.2% AlH_3	956	962±1	−1
SW	900	899±1	+1
SW[a]	900	909±1	−1
SW + 2.8% MgB90 (20% Mg)	913	910±3	+3
SW + 11.2% AlH_3	939	NA[b]	NA[b]
SW[a] + 7.1% $LiAlH_4$	903	875±10	+3
SW[a] + 5% Li_3AlH_6	906	877±10	+2

[a] No SA in SW binder
[b] Test not performed due to material availability

3.5 Characteristics of Manufactured Fuel Formulations

In this section some physical characteristics of the manufactured fuel formulations are discussed. Focus is on the achieved densities of manufactured fuels (a simple but effective quality control) and on evaluation of the dispersion level of the tested nano–sized additives into binder matrix.

3.5.1 Density and Porosity

Density of manufactured fuels was evaluated by a gravimetric method with Gibertini Europe 500 precision balance. The achieved fuel densities were compared to TMD, in order to evaluate tested formulation porosity according to Eq. 3.1. Table 3.12 shows an overview of the achieved results.

$$\Delta\rho_{f,\%} = 100 \cdot \frac{TMD - \rho_{f,\,Measured}}{TMD} \tag{3.1}$$

According to the achieved data overall quality of the manufactured fuels is high due to the low values of the calculated porosities. HTPB–based fuel doped by MgB90 (20% Mg) exhibits rather high porosity confirming a possible reaction between energetic filler and HTPB–binder components. Porosity of HTPB + 1% C + 5% nFe is possibly affected by residual hexane in HTPB matrix.

3.5.2 Nano–sized Aluminum Dispersion

Exploitation of the possible performance enhancements achievable by nano–sized additives requires a proper dispersion of the energetic filler into binder matrix down to the nano-scale. Particle cold cohesion phenomena during storage/manufacturing yield the formation of large

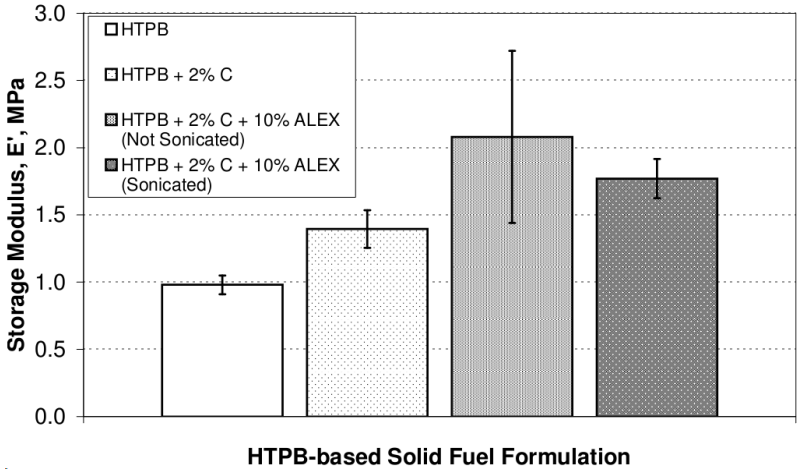

Figure 3.9: ALEX–doped sonicated and non–sonicated fuels tested by DMA, storage modulus [furnace temperature 313 K (40°C), oscillation frequency 10 Hz, oscillation amplitude 15 μm].

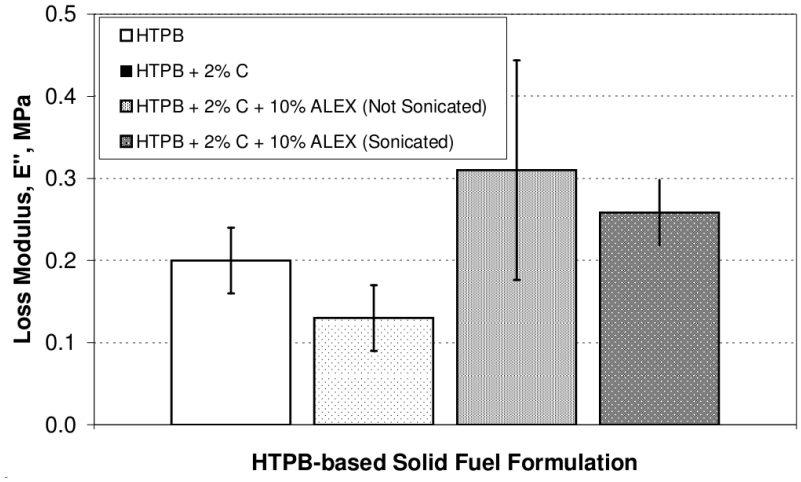

Figure 3.10: ALEX–doped sonicated and non–sonicated fuels tested by DMA, loss modulus [furnace temperature 313 K (40°C), oscillation frequency 10 Hz, oscillation amplitude 15 μm].

particle clusters instead of the wanted nano-sized powders. Moreover, nAl powders produced by EEW are subjected to sintering due to wire explosion during the production phase [64][66]. Dedicated studies are under progress at SPLab in order to lessen/avoid these phenomena by proper dispersion techniques [40]. In the present work, two sessions of sonication were performed during manufacturing to avoid particle clustering and enhance dispersion of nAl in the binder matrix (see Section 3.4.1). The effects of sonication were evaluated by mechanical tests conducted on the manufactured fuel by DMA. Cured HTPB (see Table 3.1) is taken as the reference formulation. HTPB loaded with 2% C was considered to evaluate the C effects on solid fuel mechanical properties enhancement. Then two different nAl–loaded fuels have been investigated. Both of them contains 10% mass fraction of ALEX and 2% of C, but they differ from the sonication phase. The first nAl–loaded fuel was treated in an ultrasonic bath according to what is reported in Section 3.4.1. In the second fuel formulation fillers were added without any sonication treatment. Results achieved by DMA tests are reported in Figure 3.9 and in Figure 3.10. Under the investigated conditions, sonication of fuel formulation enables a reduction in data scattering of DMA measurements. This is considered as an enhancement of additive dispersion, since clusters are possible causes of non uniform mechanical properties [103].

CHAPTER 4

EXPERIMENTAL SETUP

Ballistic investigation of solid fuel formulations is performed by a 2D radial micro–burner, see Figure 4.1. The test rig was originally designed by Bosisio and Raina [31][32], and then modified by Paravan [34][36], and finally by Duranti, Sossi and Paravan [39][40].

Combustion test is performed on cylindrical strands with single central port perforation accommodated in stainless steel cases. Nominal initial diameter of the port is 4 mm, while solid fuel web thickness is 7 mm and strand length is 30 mm. With the current design of the test facility oxidizer mass flow rates up to 250 nlpm [corresponding to initial nominal G_{ox} of 470 kg/(m^{2}s)] can be achieved for the so far explored chamber pressure range from 4 to 16 bar.

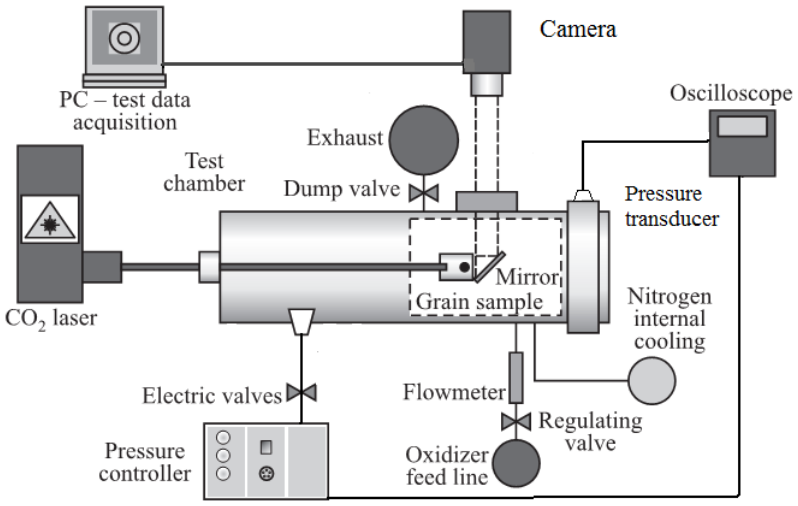

Figure 4.1: 2D radial micro–burner overview [36].

4.1 Experimental Setup Description

The 2D radial micro-burner is intended for ballistic investigation of different fuel formulations, therefore the main parameter to be evaluated is the regression rate. The latter is measured by a non–intrusive optical technique by tracking of the regressing surface at sample head–end section all along the combustion (see Chapter 5 for details). This is a peculiar feature of the test rig and is related to the facility original design. In order to enable oxidizer flow injection without

optical obstacles for the visualization of sample head–end, the injector configuration shown in Figure 4.2 was adopted.

Injector is connected to oxidizer inlet by a stainless steel pipe. The latter delivers the oxidizer flow to a pre–injection chamber. This is a cylindrical hollow volume intended to provide homogeneous characteristics to the flow before it passes through the injector–head to reach the injector terminal accommodating the strand. Injector–head consists of eight radial channels enabling the flow of the oxidizer from the pre–injection chamber to the injector terminal without visual obstacles. The cross–section of each of the eight injection channels can be varied by regulating stems, thus enabling control of the characteristics of the flow reaching the sample. Both standard and swirl flows can be achieved with regulation of the stems by ad–hoc designed screws, see Figure 4.2.

As can be seen by Figure 4.2 and Figure 4.3, the volume of the pre–injection chamber is close by two flanges. The fore flange is connected to the terminal part of the injector, while the aft flange has no connections. Both flanges lodge a quartz window, so that sample head–end image can be reflected by a 45° mirror. As shown in Figure 4.1, the latter enables the image of the sample to be captured by a video camera (without any deformation of the reflected image).

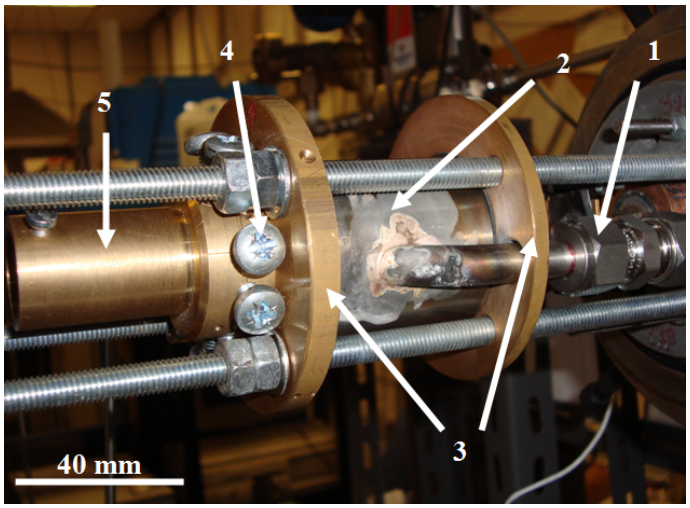

Figure 4.2: 2D radial micro-burner injector. The following elements are highlighted: *1* oxygen feed line, *2* pre–injection chamber, *3* flanges for optical quartz windows accommodation, *4* injector–head with screws for oxidizer injection control (standard/swirl flow), *5* injector terminal (sample lodging).

Injector is lodged in the combustion chamber, a cylindrical–shaped volume realized in AISI 316 stainless steel. Combustion chamber is composed by two parts: the first one is fixed while the second one can be moved. Injector is mounted to the mobile part, while the fixed part is connected to the dump pipeline and enables lodging of optical accesses to the interior of the chamber. When combustion chamber is closed, a thread crown and a high–pressure O–ring grant insulation of the interior of the combustion chamber from external atmosphere (see Figure 4.1). Maximum allowable pressure for the combustion chamber is 30 bar, nevertheless the presence of optical accesses limits the maximum operating pressure to 20 bar.

Two different inlets are connected to the mobile part of the combustion chamber: the oxidizer feed line, delivering the mass flow taking part into the combustion process, and a nitrogen secondary flow intended for cooling of the interior of the chamber during test and preventing soot from the combustion to obstacle the visualization of the burning process. Oxidizer mass flow rate is measured and controlled by a digital flowmeter, Bronkhorst EL–FLOW SELECT, see Table 4.1. Flowmeter can be conveniently triggered and constant/variable $\dot{m}_{ox}$ operating profile can be designed via proprietary software.

The dump line connected to the fixed part of the combustion chamber carries exhaust gases

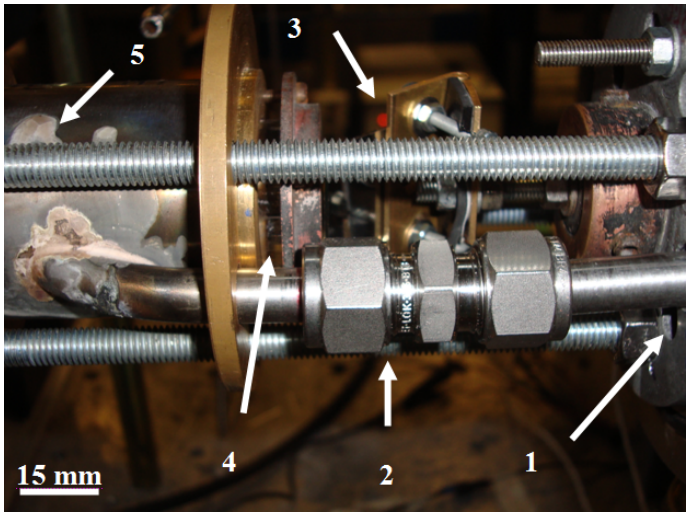

Figure 4.3: 2D radial micro–burner injector, aft part. The following elements are highlighted: *1* nitrogen cooling inlet, *2* oxygen inlet, *3* 45° mirror (back), *4* optical quartz window accommodated in rear flange, *5* pre–injection chamber.

Table 4.1: Digital flowmeter Bronkhorst EL–FLOW SELECT data [104].

Datum	**Value**
Working Pressure, bar	4–20
Maximum Allowable Pressure, bar	25
Data Sampling Frequency, Hz	10
Maximum Allowable $\dot{m}_{ox}$, nlpm	250
Sensitivity, nlpm	0.1
Error,	$\pm(0.5\% \cdot \mathrm{R}_d + 0.1\%$ FS)

from the combustion chamber to electro–valves (data reported in Table 4.2). A pressure controller drives electro–valves in closed–loop by comparing the set threshold value with the instant chamber pressure measured by a pressure transducer (Kulite CT–190). As a result, chamber pressure is characterized by a quasi–steady value, see Figure 4.4. Due to this closed–loop control, oxidizer mass flow rate and chamber pressure can be regulated independently.

An oscilloscope collects pressure data while providing triggering with both flowmeter and the digital camera used for video–recording, see Figure 4.1. In order to properly trigger hardware controlled by different proprietary software, a home–made external trigger was realized.

Depending on performed test operating conditions, video recording can conveniently performed by Xybion SVC-09 or Photron Ultima APX, see Tables 4.3–4.4.

Strand ignition is achieved by a pyrotechnic primer charge inserted in the central port of the strand at the head–end side. The primer charge is in turn ignited by a laser beam impinging on it and produced by a CO_2 Valfivre laser (see Figure 4.1). Due to the energy released by primer charge combustion products, the solid fuel burning is started. This ignition technique grants high reliability while resulting low intrusive (no oxidizer flow perturbation is produced after charge

Table 4.2: Data for Peter & Paul electrovalves.

Datum	**Value**
Model	79K9DGM
Response Time, ms	4–16
Maximum Allowable Pressure Drop, bar	35
Outlet Orifice Diameter, mm	4 (5/32 in)

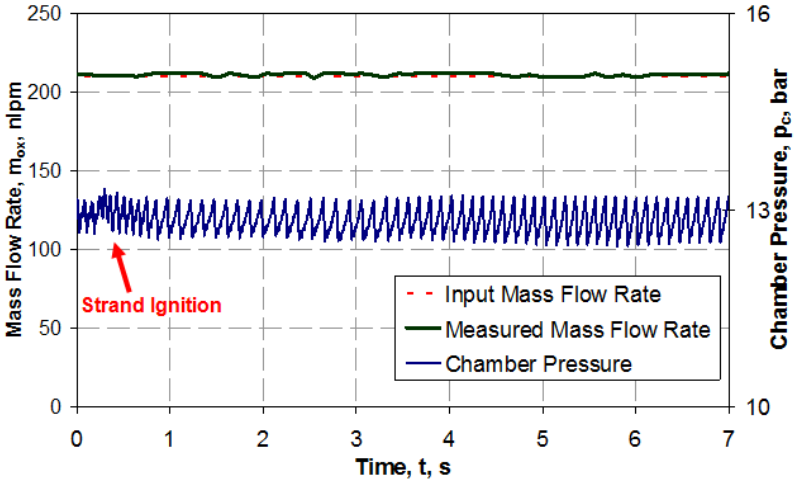

Figure 4.4: Typical operating profile for a ballistic characterization test. Note quasi–steady value of p_c. Primer charge and Strand ignition is identified by a marked peak in chamber pressure in time (see red arrow).

Table 4.3: Data for Xybion SVC–09 digital camera.

Datum	**Value**
Sensor	MOS 98HE225
Picture Elements, pixel	485x376
Maximum Frame Rate, fps	25

Table 4.4: Data for Photron Ultima APX digital camera.

Datum	**Value**
Sensor	CMOS
Maximum Resolution, pixel	1024x1024
Maximum Frame Rate, fps	120000 (with video resolution of 128x16)
Maximum Memory Size, GB	8
	Corresponding to 12 s at 500 fps
	and video resolution of 1024x1024 pixels

ignition).

A pneumatic line delivering air with a pressure of 7 bar provides external cooling of the combustion chamber and during burning. A water heat exchanger grants cooling of the exhaust gases dump line. The latter is of particular importance due to possible long burning time of tested fuel under certain operating conditions.

All pneumatic connections of test rig are realized in AISI 316 stainless steel. This enables the possibility of testing different oxidizer. Oxidizer is supplied in cylinders, therefore different oxidizer can be easily tested, granting high flexibility. A proper pressure reducer connects cylinders to the flowmeter.

4.2 Burning Test: Typical Run

Testing activity conducted on the 2D radial burner requires preliminary checks and scheduled operations before and after test execution. These procedures grant full operating capability of the facility which, in turn, means quality of the produced tests. Due to this, a short description of a typical run with the 2D radial micro-burner is given in this section.

Preliminary Operations

Preliminary operations required to grant the correct functioning of the 2D radial micro-burner start with hardware warm-up (digital flowmeter, computer, oscilloscope, pressure control chain elements, and laser). In particular, a warm-up time of 30 minutes is required by the digital flowmeter. During this time checks on the fixed connections of the combustion chamber are performed in order to avoid possible leakages of dump pipeline and external cooling system is checked, after this, alignment of laser and optical paths must be verified. Laser path verification is mandatory in order to grant homogeneous ignition of the primer charge: anisotropic ignitions could result in irregular ignitions of the tested strand thus altering the quality of the combustion. In order to avoid this, optical elements of the laser path are regulated to grant laser beam impingement at the center of a calibration sample. An element sensitive to infrared radiation is inserted in the latter at head-end side. This element acts as a testing charge, enabling verification/regulation of laser beam impinging point. After this combustion chamber is closed and proper optical alignment of 45° mirror and camera is controlled by visualizing a calibration sample that is lit up by a led-light pointing from the laser optical access (see Figure 4.1). Calibration sample is an empty cylindrical steel case with graph paper at the head-end section. Due to the regular image of the graph paper optics (in particular the 45° mirror and the camera position/focus) are regulated so that possible image distortions are avoided. At this point a brief calibration video is recorded. This video will be used in the post-analysis phase in order to get a proper conversion factor between millimeters (of the graph paper) and pixels (of the recorded image). Camera operating parameters are regulated to grant correct video–recording of the combustion (in particular shutter and diaphragm are regulated to provide proper exposure of the sensor during combustion). Next step of the preliminary operations is the check of the absence of leakages from the inlet/outlet pipelines connecting the cylinders to the combustion chamber, and the latter to the dump pipeline. This is done by a cold test during which the combustion chamber is pressurized by a 7 bar internal line of air. During this phase the functioning of the pressure control chain and digital flowmeter response to input by operator are verified. At this point test rig is ready for experimental session.

Strand Preparation

After production strands are commonly stored in polyethylene boxes and eventually in a insulated environment with inert atmosphere (glove box). In order to prepare the samples for the combustion a primer charge with length of 1 mm and nominal diameter of 4 mm is placed in the central port of the strand at the head-end side (see Figure 4.5). Particular attention is given to the preparation of the primer charge in order to avoid possible irregular boundaries and shapes that could yield to irregular ignition of the sample. Once primer charge is inserted, strand is placed into injector terminal (see Figure 4.2), combustion chamber is closed and inlet/outlet pipes are connected to it.

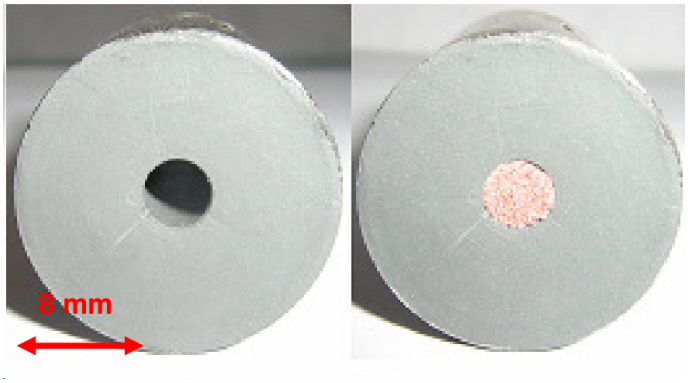

Figure 4.5: HTPB–based fuel loaded with nAl with and without primer charge into central port perforation.

Testing Phase: Operating Sequence

Once sample is inserted into injector terminal and chamber is closed, operator starts the testing sequence. For tests conducted with steady operating conditions, First, external air–cooling is activated, then combustion chamber is slowly pressurized with nitrogen. Secondary flows enable p_c to rise till the selected threshold value is reached. When this happens pressure regulator commands electro-valves thus granting quasi-steady chamber pressure.

At this point the operator starts video acquisition which in turn triggers the flowmeter. Then the operator commands laser ignition. Flowmeter enables the selected oxidizer mass flow rate to reach the sample while laser beam impinges on primer charge surface igniting it. energy released by primer charge combustion yields to ignition of the tested strand. From this point burning test proceeds under quasi–steady chamber pressure and constant $\dot{m}_{ox}$, see Figure 4.4.

When combustion is finished operator stops oxidizer flow and then nitrogen flow. A by-pass on the dump lime excludes electro–valves thus enabling combustion chamber discharge. Air is used as secondary flow for combustion chamber cooling. In the meanwhile operator saves data of the performed combustion (recorded video, pressure and flowmeter traces) for use in the analysis phase.

After The Combustion: Maintenance

Once combustion is performed chamber is cooled by internal air flow. When chamber temperature is lessened, operator closes air inlet and start maintenance operations. A light maintenance is performed after each test, while a heavier maintenance is scheduled according to the number of performed tests to grant facility full operating capability. After combustion chamber is opened and sample is removed. Interior of the chamber is cleaned (especially the lateral windows enabling visualization of the performed tests). Interior of the injector is cleaned and chamber-end seals are checked (and eventually substituted) to grant the insulation during next combustion. After maintenance a cold test is always performed in order to verify facility functionality. Scheduled maintenance requires complete overhaul of each component of the facility, from injector to electro–valves. This maintenance comprehends the execution of burning tests on standard formulations in order to verify the full operating capability of the test rig.

CHAPTER 5

TIME–RESOLVED TECHNIQUE FOR REGRESSION RATE

Accurate determination of solid fuel regression rate under different testing conditions is required for both base phenomena investigation and proper relative ballistic grading of different fuel formulations. An overview of the experimental procedures for ballistic investigation of hybrid systems is given by Cauty et al. [45].

A non–intrusive optical time–resolved technique for regression rate has been developed at SPLab in the frame of the activities of this study. Due to the peculiar characteristics of the test rig used for ballistic characterization (see Section 4.1), the technique is based on diameter sampling in time. Time–resolved technique for regression rate is detailed discussed in Section 5.2. Before introducing the measurement technique developed at SPLab, an introduction to the features of available measurement techniques is given.

5.1 Regression Rate Measurement Techniques

Several techniques can be employed for regression rate determination [45]. Some of this techniques are similar to those used for the investigation of the ballistics of SRMs [1]. A base classification can be made between intrusive and non–intrusive techniques. Usually at lab–scale level non–intrusive techniques are preferred, but for sub–scale or real–scale motors intrusive techniques can be required in order to collect proper (local) data.

5.1.1 Intrusive Techniques

Intrusive techniques for regression rate measurement are based on the embedding of sensors within solid fuel grains. Embedded sensors provide the associated transducers variation of some physical parameter related to the solid fuel regression. Typically electric resistance sensors and thermocouples are employed, though capacitance sensors are available too [45] [18] [107]. A resistance–based sensor for direct measurement of regression rate was proposed by Monti and Mazzola. Monti and Mazzola developed an original measurement technique for regression rate [18]. Their idea was to realize a thin layer of resistive material reproducing the cross section of the considered solid grain. Electric resistance of this sensor could be tracked in time by proper hardware. During combustion with the sensor and the solid fuel regressing at the same r_f, a direct and continuous measurement of the latter parameter could be achieved. Electric resistance methods offer possible advantages as good accuracy and low cost. Similarly (but with a lower accuracy) regression rate can be evaluated by thermocouples embedded in the solid fuel grain. In this case

the approach is quite similar to the classic fuse–wire method used for SRM [1], but the possible advantage of a measurement of the solid fuel grain temperature profile characterization [22].

5.1.2 Non–Intrusive Techniques

The most widespread technique for regression rate determination is non–intrusive, and is based on solid fuel mass (or thickness) measurement before and after combustion [6][108]. This relatively simple technique provides information in term of time–averaged regression rate, and is subject to low accuracy and possible ambiguous determination of the exact burning duration. Other experimental methods can provide more detailed information [45]. In particular, ultrasound technique can provide accurate, instantaneous values of the local regression rate with a relatively cheap setup though possible limitations can be due to the coupling with the tested fuel (e.g. ultrasound absorption). Space–averaged, instantaneous regression rate can be achieved by evaluation of the Helmholtz mode frequency [109]. The measurement of regression rate performed at Penn State University by X–ray radiography is probably the most accurate experimental technique available enabling instantaneous regression rate measurement over all the solid fuel grain length [110][111]. The latter is an optical–based technique with the main drawback of a high cost hardware.

5.2 SPLab Time–resolved Technique

The 2D radial micro–burner of SPLab enables combustion of cylindrical strands of solid fuel with single port perforation (with initial nominal diameter of 4 mm and web thickness of 7 mm). Due to the original design of test rig injector, a visualization of the head–end of the sample during the combustion process can be achieved, see Figure 5.1. Combustion test is recorded in digital format and then analyzed by a dedicated software. The latter recognizes individual pixels of the processed video, so that distances between different selected points can be measured. A reference video acquisition of a graduated sample enables determination of a proper conversion factor between pixels and convenient length units (typically, millimeters).

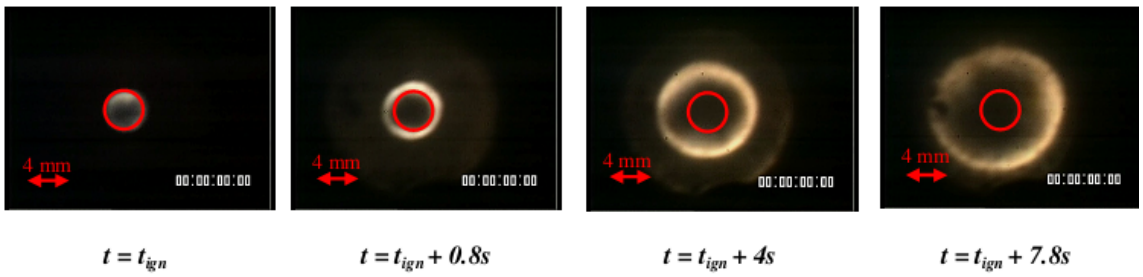

Figure 5.1: Regressing surface evolution in time for HTPB burning under GOX. Operating conditions: oxidizer mass flow rate of 70 nlpm [corresponding to initial G_{ox} of 130 $kg/(m^2 s)$], p_c 10 bar. Red circle marks the initial port diameter (D_0, 4 mm).

Time-resolved technique is based on diameter sampling in time. Starting from strand ignition (the moment central port is visible at due to primer charge complete combustion), space–averaged diameter is defined. In order to define the $\bar{D}_i$ by averaging different instantaneous diameters, for example the vertical and the horizontal diameters, see Figure 5.2.

The sequence of the sampled $\bar{D}_i$ is a discrete information in time. In order to achieve a continuous information in time, the series of the discrete $\bar{D}_i$ is interpolated in time by Eq. 5.1. The latter equation is valid starting from t_{ign}. In the data treatment procedure, the latter is a parameter ad–hoc defined in order to avoid the maximize the fitting of Eq. 5.1, [39][40]. A detailed discussion of this parameter is reported in Section 5.2.1.

$$D(t) - D_0 = a_D \cdot (t - t_0)^{n_D},\ t \geq t_{ign} > t_0 \tag{5.1}$$

Figure 5.2: Space–averaged sampled diameter is defined according to the measurement of diameter along two different radial directions (typically vertical and horizontal).

Equation 5.1 is chosen for diameter interpolation in time due to its monotone trend in time [108]. During combustion under steady operating conditions, central port diameter increases in time due to fuel consumption. This behavior can be properly approximated by Eq. 5.1. Starting from Eq. 5.1 the instantaneous ballistics of the investigated solid fuel can be determined considering operating conditions (i.e. $\dot{m}_{ox}$ and p_c), see Eqs. 5.2–5.5. In particular, regression rate can be defined by time–derivative of Eq. 5.1.

$$r_f(t) = \frac{1}{2} \cdot \frac{\partial \bar{D}(t)}{\partial t} = \frac{1}{2} \cdot a_D \cdot n_D (t - t_0)^{n_D - 1},\ t \geq t_{ign} > t_0 \tag{5.2}$$

$$G_{ox}(t) = \frac{\dot{m}_{ox}(t)}{\pi \cdot \frac{\bar{D}(t)^2}{4}} = \frac{\dot{m}_{ox}(t)}{\pi \cdot \frac{[D_0 + a_D \cdot (t - t_0)^{n_D}]^2}{4}},\ t \geq t_{ign} > t_0 \tag{5.3}$$

$$\dot{m}_f(t) = \rho_f \cdot r_f(t) \cdot A_b(t) = \rho_f \cdot r_f(t) \cdot L_p \cdot \pi \cdot \bar{D}(t) = \rho_f \cdot r_f(t) \cdot [D_0 + a_D \cdot (t - t_0)^{n_D}],\ t \geq t_{ign} > t_0 \tag{5.4}$$

$$O/F(t) = \frac{\dot{m}_{ox}(t)}{\dot{m}_f(t)} = \frac{\dot{m}_{ox}(t)}{\rho_f \cdot r_f(t) \cdot [D_0 + a_D \cdot (t - t_0)^{n_D}]},\ t \geq t_{ign} > t_0 \tag{5.5}$$

Data directly derived from Eq. 5.1 enable definition of instantaneous ballistics of tested strand. Time–averaged data can be easily defined by integration of Eqs. 5.1–5.5. Note that a congruency check for the achieved analytical $\bar{D}(t)$ and $r_f(t)$ in time. In particular, according to Eq. 5.2, regression rate at t_{ign} can be expressed as Eq. 5.6.

$$r_f(t_{ign}) = \frac{1}{2} \cdot a_D \cdot n_D (t_{ign} - t_0)^{n_D - 1} \tag{5.6}$$

Considering Eq. 5.1, the latter equation can be re–written as

$$r_f(t_{ign}) = \frac{1}{2} \cdot n_D \frac{(\bar{D}(t_{ign}) - \bar{D}_0)}{t_{ign} - t_0} \tag{5.7}$$

Substituting the first sampled diameter, $\bar{D}_1$, to $\bar{D}(t_{ign}$ congruency between analytical diameter interpolation in time and sampled values requires the satisfaction of Eq. 5.8 (within an allowable tolerance).

$$\Delta r_f(t_{ign}) = r_f(t_{ign})_{Eq.5.6} - r_f(t_{ign})_{Eq.5.7} \tag{5.8}$$

Sampled diameters discrete values can be used in order to evaluate ballistics of the tested strand by TOT. In detail, regression rate and oxidizer mass flux can be defined according to Eqs. 5.9–5.10. The TOT is a data treatment technique often used in literature. The main advantage of TOT data is the fact that no treatment is required for the ignition transient [40][108][112]. In spite of this advantage, TOT is intrinsically affected by large errors due to error propagations, especially when performing measurements over reduced (t_{i+1}-t_i) intervals.

$$r_{f,\,TOT(i,\,i+1)} = \frac{1}{2} \cdot \frac{\bar{D}_{i+1} - \bar{D}_i}{t_{i+1} - t_i} \tag{5.9}$$

$$G_{ox,\,TOT(i,\,i+1)} = \frac{\dot{m}_{ox}(t = t_{i+\frac{1}{2}})}{\frac{\pi}{4} \cdot \frac{\bar{D}_{i+1} + \bar{D}_i}{2}} \tag{5.10}$$

Due to its wide use in open literature, TOT data achieved by Eqs. 5.9–5.10 are used in order to check the consistency of time–resolved analytical data. This is done considering overall TOT and analytical time–averaged data, see Eqs. 5.13–5.14.

$$\langle r_f(t) \rangle = \frac{1}{t - t_{ign}} \cdot \int_{t_{ign}}^{t_{fin}} r_f(t) \cdot dt \tag{5.11}$$

$$\langle G_{ox}(t) \rangle = \frac{1}{t - t_{ign}} \cdot \int_{t_{ign}}^{t_{fin}} G_{ox}(t) \cdot dt \tag{5.12}$$

$$\Delta \langle r_f(t_{fin}) \rangle = \langle r_f(t_{fin}) \rangle_{Eq.5.11} - \left\langle r_{f,TOT(in,\,fin)} \right\rangle_{Eq.5.9} \tag{5.13}$$

$$\Delta \langle G_{ox}(t_{fin}) \rangle = \langle G_{ox}(t_{fin}) \rangle_{Eq.5.12} - \left\langle G_{ox,TOT(in,\,fin)} \right\rangle_{Eq.5.10} \tag{5.14}$$

Due to consistency checks, possible suspicious analytical trend as asymptotes due to the interpolating law for $\bar{D}(t)$ (Eq.5.1) can be checked by TOT.

The developed time–resolved technique enables definition a_D and n_D for each single performed tests. In order to summarize results achieved under the same operating conditions for a given fuel, the performed tests are collapsed into an ensemble curve. The latter is evaluated interpolating the $\bar{D}(t)$ of the performed test by a average–curve still defined according to Eq. 5.1. For single tests and ensemble the analytical $r_f(G_{ox})$ defined starting from Eq. 5.1 can be approximated by the commonly used Eq. 5.15, [6].

$$r_f = a_r \cdot G_{ox}^{n_r} \tag{5.15}$$

Application to ensemble curves of Eq. 5.1 (or Eq. 5.15) enable definition of proper error bars. These are defined in t (or G_{ox}) domain. Evaluation of the error bars for a given ensemble require definition of a proper interval of t (or G_{ox}). In this interval the Eq. 5.1 (or Eq. 5.15) of all the performed single tests are defined. Over this interval, error bars are evaluated by confidence intervals centered on the average $\bar{D}(t)$ (or r_f) resulting from the values of diameters (or r_f) for the single tests at that given t (or G_{ox}). Confidence intervals are evaluated by 95% accuracy.

5.2.1 Ignition Transient

The developed time–resolved technique provides an analytical definition of $\bar{D}(t)$ that is valid starting from t_{ign}, see Eq.5.1. The latter parameter is related to the ignition transient of the solid

fuel under the investigated conditions. Ignition transient duration can be defined as a time interval, $\Delta t_{ign} = t_{ign} - t_0$. The latter can be defined as the time interval ranging from the time at which the first stimulus for ignition reaches the solid fuel grain, to the one quasi–steady burning regime is achieved at. In SPLab time–resolved technique ignition transient is defined by an ad–hoc definition [40]. In particular t_{ign} is defined as the time maximizing the data fitting of Eq.5.1 (if assigned to the first sampled diameter).

Ad–hoc defined Δt_{ign} are in agreement with the ignition delays evaluated by a model developed by Ohlemiller and Summerfield [114]. As discussed in Section 4.1, tested strand is ignited by a primer charge. Primer charge is placed in sample central port at the head–end section. A laser beam impinging on it provides energy for primer charge ignition. Combustion of the primer charge delivers energy to the solid fuel grain mainly by convection due to the oxidizer flowing in the strand central port. In a convective heat–transfer regime, Ohlemiller and Summerfield approach enables simplification in the complete set of balance equations describing ignition transient. Under these simplifying assumptions Δt_{ign} ca be evaluated according to Eq. 5.16.

$$\Delta t_{ign} = \frac{\pi}{4} \cdot \kappa_s \cdot \frac{\rho_f C_f \Delta T_{s-\ in,v}}{\dot{q}_c} \tag{5.16}$$

In Eq. 5.16 the following parameters are introduced:

- $\Delta T_{s-\ in,v}$, temperature difference between the initial and pyrolysis temperatures of the solid fuel grain.
- $\dot{q}_c$, the convective heat flux into the solid fuel grain providing the energy required for solid fuel ignition.

The convective heat flux term of Eq. 5.16 requires a proper definition [115]. Considering solid fuel strand dimensions and investigated operating conditions, a comparison between ad–hoc evaluated Δt_{ign} and values achieved by Eq. 5.16 is presented in Table 5.1 for HTPB burning under GOX with different p_c.

Table 5.1: HTPB burning in GOX, convective ignition delay ($\Delta t_{ign,conv}$) and ad–hoc evaluated Δt_{ign}. Note general trend agreement for increasing p_c. High difference for 7 bar tests due to irregular primer charge ignition.

Fuel	p_c**, bar**	$\mathbf{G}_{ox}(\bar{D}(t_{ign}))$**,** $kg/(m^2 s)$	$\Delta t_{ign,conv}$**, s, [114]**	$\Delta t_{ign,ad-hoc}$**, s**
HTPB	7	296.2	0.031	0.070
HTPB	10	370.4	0.021	0.034
HTPB	13	353.2	0.022	0.059
HTPB	16	365.3	0.021	0.046

CHAPTER 6

BALLISTIC INVESTIGATION: EXPERIMENTAL RESULTS AND DISCUSSION

In this chapter the results of the experimental investigation of the ballistics of the HTPB– and SW–based solid fuel formulations will be presented and discussed. The solid fuel formulations introduced in Chapter 3 had been investigated by 2D radial micro–burner in order to evaluate the regression rate by the developed time–resolved technique (see Chapter 5). Diameter change in time will be represented by Eq. 6.1. As common in the open literature, a compact power–law approximation will be used for r_f vs. G_{ox} data for single tests and ensemble average data in order to easily compare achieved results, see Eq. 6.2.

$$\bar{D}(t) - D_0 = a_D \cdot (t - t_0)^{n_D},\ t \geq t_{ign} > t_0 \tag{6.1}$$

$$r_f = a_r \cdot G_{ox}^{n_r},\ t \geq t_{ign} > t_0 \tag{6.2}$$

Ballistics of HTPB fuel will be introduced first, to provide a detailed view of time–resolved technique operating steps. HTPB will be considered as baseline for relative ballistic grading of the investigated fuel formulations. In order to evaluate regression rate enhancements with respect to baseline under similar operating conditions, the parameter $\Delta r_{f,\%}$ is defined for ensemble average curves at a given G_{ox} (with respect to baseline), see Eq. 6.3. Averaging the $\Delta r_{f,\%}$ achieved over the whole investigated range an average (percent) regression rate increase is defined. Standard deviation of test–averaged $\Delta r_{f,\%}$ evaluates performance sensitivity to G_{ox} changes [higher values of $\xi(\Delta r_{f,\%})$ being related to higher G_{ox} sensitivities].

$$\Delta r_{f,\%} = 100 \cdot \frac{r_{f,\,Tested\,Fuel} - r_{f,Baseline}}{r_{f,Baseline}} \tag{6.3}$$

Tested formulations were burnt under GOX, with oxidizer mass flow rate of 210 nlpm [corresponding to initial nominal G_{ox} of nearly 400 $kg/(m^2 s)$], while p_c ranged from 7 to 16 bar.

6.1 HTPB Fuel

HTPB fuel was tested under p_c from 7 to 16 bar with the aim of evaluating the influence of this operating parameter on the measured regression rate.

Introduction to the Time–resolved Technique

Results for ballistic characterization of HTPB fuel tested at 10 bar are reported in Figures 6.1–6.3 and in Table 6.1 in order to show the operating steps of the developed time–resolved technique. Figure 6.1 shows diameter change in time for the performed tests and for the ensemble average. Measured space–averaged diameters are sampled with a frequency in the range 1–5 Hz (depending on visualization quality). The highest sampling frequencies are used for the initial phases of the combustion process. Toward the end of the combustion test, overall visualization quality could require a reduction in diameter sampling frequency in order to lessen possible errors. Due to the ad–hoc definition of t_{ign}, interpolation of sampled diameters in time yields to high data fitting of Eq. 6.1 (see Table 6.1). Ensemble average can properly represent the overall trend of the performed tests, as testified by the high data fitting for the corresponding Eq. 6.1. Ensemble average of HTPB exhibits low errors for a_D and n_D as well as a R^2 higher than 0.98 under the investigated condition.

As shown in Chapter 5, starting from diameter change in time, r_f and G_{ox} are evaluated by Eqs. 5.2–5.3. Achieved results are shown in Figure 6.2 for r_f vs. G_{ox}. In the latter figure time runs from right to left since the maximum value of G_{ox} (in time) corresponds to the smallest evaluated diameter (in turn corresponding to t_{ign}). According to what is reported in Figure 6.2, r_f exhibits a monotone decreasing trend for decreasing G_{ox} (and increasing time). This finding is in general agreement with the behavior of a convective heat transfer regime governing the combustion process.

Approximating the time–resolved trends of r_f(t) and G_{ox}(t) by Eq. 6.2, the result reported in Figure 6.3 is achieved. A marked difference between experimental data and power law approximation characterizes the region where $G_{ox} > 300$ kg/(m^{2}s). This behavior is common to single tests and ensemble average and is the cause for the relatively poor data fitting of Eq. 6.2 reported in Table 6.1. The trend of Eq. 6.2 in Figure 6.3 is related to the definition of the relationship r_f(t) vs. G_{ox}(t). The time–resolved technique evidences a high data fitting for Eq. 6.1 with sampled space–averaged diameters. The behavior of $\bar{D}$(t) exhibits a monotone, increasing trend in time with a steeper behavior at the beginning of the combustion (see Figure 6.1). The achieved trend of $\bar{D}$(t) produces decreasing behavior in time for both r_f(t) and G_{ox}(t). When considering r_f(t) vs. G_{ox}(t), the implicit time–dependency yields to a power–law approximation strongly dependent from the lowest oxidizer mass fluxes (where lower r_f causes higher burning times). This yields to the definite difference of experimental data with respect to the trend of Eq. 6.2. Due to this, a different power–law approximation of the available data is reported in Figure 6.4. In this latter figure equi–spaced G_{ox} values are considered for the approximation of $r_f(G_{ox})$ by Eq.6.2. In spite of a low data fitting for the power–law approximation, a remarkable value of n_r close to the 0.8 indicated by diffusion–limited, convection driven models is achieved, see Table 6.4. The low data fitting of this latter power–law approximation is mainly due to the behavior of experimental data for high G_{ox}. This effect does not exert high influence on the overall time–averaged regression rate characterizing the tests as witnessed by data reported in Table 6.2. The marked difference between experimental data and power–law approximation for high G_{ox} could be due to possible transient phenomena related to the stabilization of the reacting boundary layer. The latter could be evaluated, at least in a qualitative way, by considering characteristic times of the considered phenomena [116][117]. Gas phase and surface characteristic times enables a quasi–steady treatment of the phenomenon. Similar expressions for possible unsteady regime in the boundary layer yield to a concordant result. Nevertheless it must be pointed out that the latter relationships are developed for a flat–plate geometry with no reactions in the boundary layer, thus differences with the HRE conditions could be possible.

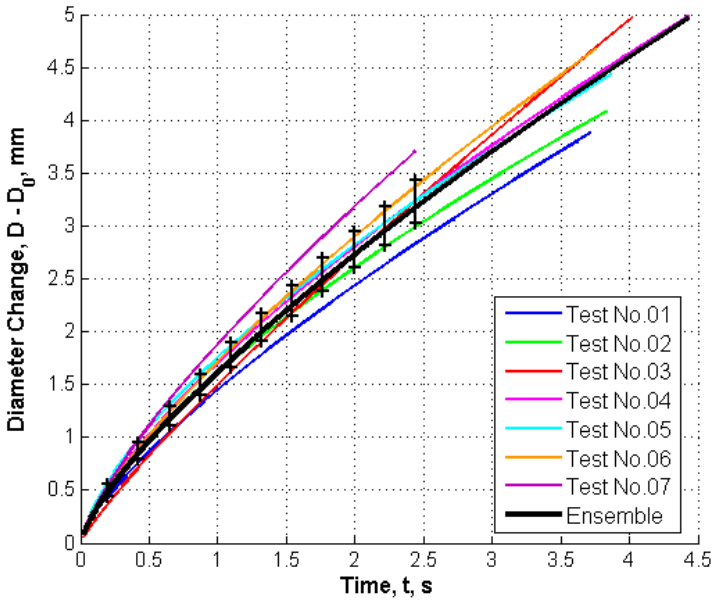

Figure 6.1: HTPB burning in GOX under p_c of 10 bar, instantaneous diameter evolution in time for single tests and ensemble average.

Before passing to a more complete discussion of the results achieved for the ballistic characterization of HTPB under different p_c, some result is presented in Figure 6.5 where ensemble average of HTPB burning under p_c of 10 bar is considered. In particular Figure 6.5 highlights possible differences in data achievable with time–dependent measurements. SPLab time resolved–technique provides instantaneous space–averaged data exhibiting good agreement with TOT overall values once integrated in time–averaging process (consistency checks, see Table 6.2). Time–resolved technique enables a better insight of the phenomenon with respect to the simple TOT data, especially when considering short time intervals (were TOT–errors could result dramatic [108]). Often in the open literature few detailed information are available about the exact data treatment of the proposed average data. In particular, when comparing data from different works, the influence of the possible space– and time–averaging processes should be considered as well as the possible differences in operating conditions. Due to this in Figure 6.5 time–resolved instantaneous data and overall TOT are compared with a possible TOT–like regression rate evaluated according to Eq.6.4 and Eq.6.5.

$$< r_f(t_{fin}) >= \frac{r_f(t_{ign}) + r_f(t_{fin})}{2} \tag{6.4}$$

$$< G_{ox}(t_{fin}) >= \frac{G_{ox}(t_{ign}) + G_{ox}(t_{fin})}{2} \tag{6.5}$$

Pressure Effect

A detailed view of the time–resolved ensemble average curves for HTPB burning in GOX under an initial nominal G_{ox} of 400 $kg/(m^2 s)$ for p_c in the range from 7 to 16 bar is reported in Figure 6.6.

Table 6.3 shows a summary of the results achieved by power–law approximation of r_f vs. G_{ox} by Eq. 6.2 and the approach presented in Figure 6.4 (interpolation on equi–spaced G_{ox}). As can be seen, n_r values in the range from 0.5 to 0.7 are achieved. Under the investigated conditions

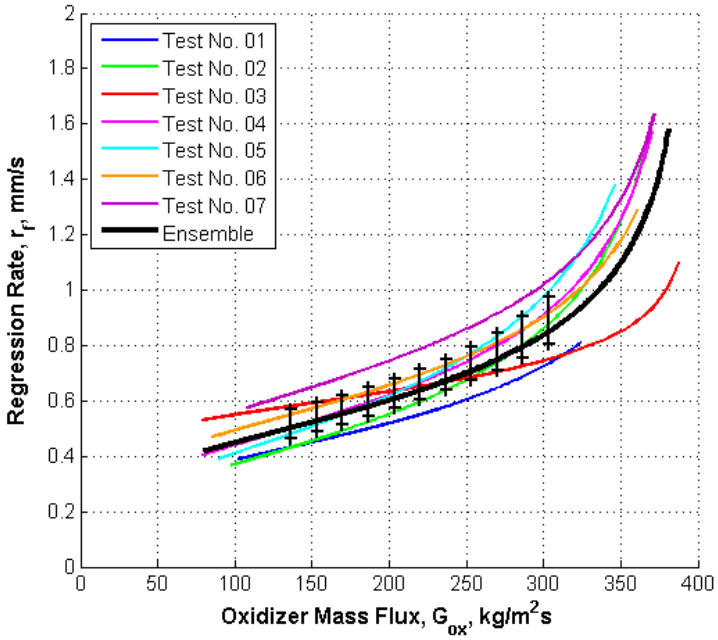

Figure 6.2: HTPB burning in GOX under p_c of 10 bar, $r_f(G_{ox})$ for single tests and ensemble average (instantaneous data). Note here time runs from right to left.

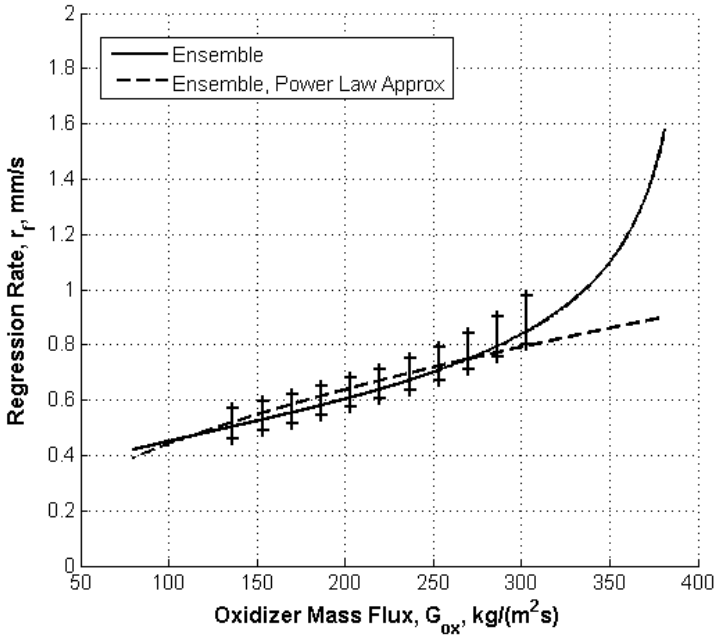

Figure 6.3: HTPB burning in GOX under p_c of 10 bar, $r_f(t)$ vs. $G_{ox}(t)$ for ensemble average with the power-law approximation of Eq. 6.2 (note time runs from right to left).

Table 6.1: HTPB burning in GOX under p_c of 10 bar, ballistic parameters for Eq. 5.1 and Eq. 6.2. Low quality data fitting for r_f vs. G_{ox} approximation due to poor agreement between power–law approximation and actual data, see Figure 6.3.

Test No.	a_D	n_D	R^2, Eq.6.1	a_r	n_r	R^2, Eq.6.2
01	2.104 ± 0.027	0.848 ± 0.010	0.998	0.031 ± 0.001	0.542 ± 0.006	0.964
02	1.715 ± 0.008	0.757 ± 0.004	0.999	0.010 ± 0.001	0.773 ± 0.011	0.930
03	1.881 ± 0.022	0.759 ± 0.009	0.998	0.151 ± 0.004	0.279 ± 0.005	0.888
04	1.448 ± 0.010	0.751 ± 0.007	0.999	0.027 ± 0.001	0.603 ± 0.008	0.927
05	1.613 ± 0.015	0.691 ± 0.006	0.999	0.014 ± 0.001	0.723 ± 0.009	0.950
06	1.498 ± 0.009	0.862 ± 0.004	0.999	0.045 ± 0.002	0.517 ± 0.007	0.936
07	1.702 ± 0.016	0.722 ± 0.006	0.999	0.032 ± 0.002	0.604 ± 0.011	0.923
Ensemble	1.646 ± 0.003	0.740 ± 0.002	0.982	0.038 ± 0.001	0.533 ± 0.002	0.914

Table 6.2: Consistency checks for HTPB burning in GOX under p_c of 10 bar. Check results expressed as percentages with respect to TOT data.

Test No.	**Eq.** 5.8	**Eq.** 5.13	**Eq.** 5.14
01	0.1	0.2	-2.2
02	-0.1	1.8	-0.4
03	-0.2	-1.9	-8.1
04	0.1	0.3	-2.4
05	0.1	0.6	-0.4
06	0.5	-1.0	-3.0
07	1.0	-0.7	-1.1

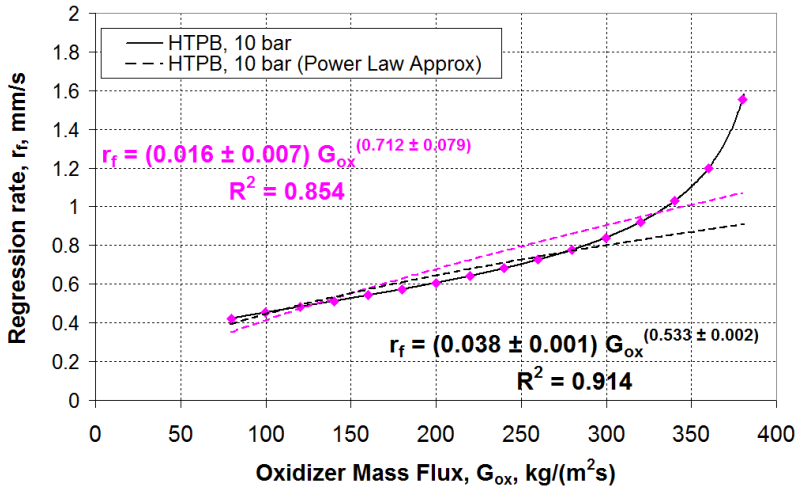

Figure 6.4: HTPB burning in GOX with p_c of 10 bar, time–resolved data. Comparison between power–law approximations (Eq. 6.2, dashed lines). Considering r_f(t) vs. G_{ox}(t) derived from Eq. 6.1 time–discretization yields to the a high dependency of Eq.6.2 by low values of G_{ox} (black curves). Power law approximation over equi–spaced G_{ox} achieved by time–resolved technique (purple diamonds) exhibits a n_r value close to 0.8. The latter approach is used for data treatment of the present work. Error bars are not reported for better readability.

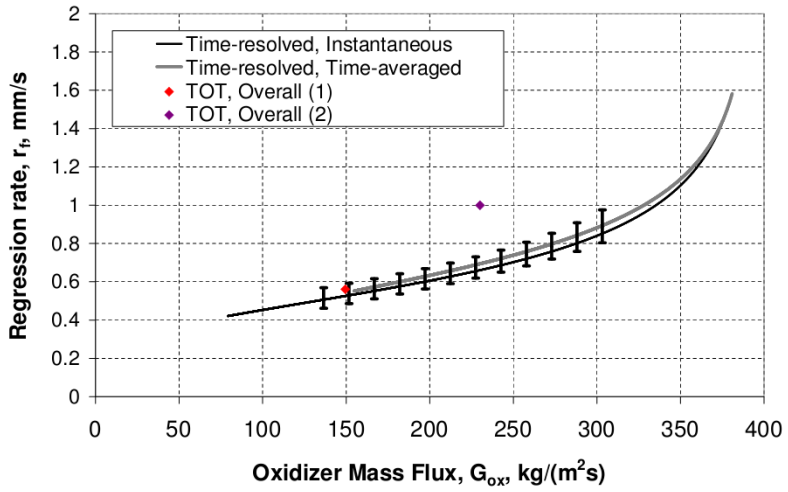

Figure 6.5: HTPB burning under GOX with p_c of 10 bar comparison between different data treatment starting from measured $\bar{D}_i$. Time–resolved instantaneous and time–averaged data (from Eq. 6.1 and 5.11 respectively) are compared to overall TOT–based r_f, [(1), see Eqs. 5.9–5.10, and (2) defined by Eqs. 6.4– 6.5). Note relative low influence of high G_{ox}–instantaneous data on $< r_f(t_{fin}) >$ achieved by time–resolved technique.

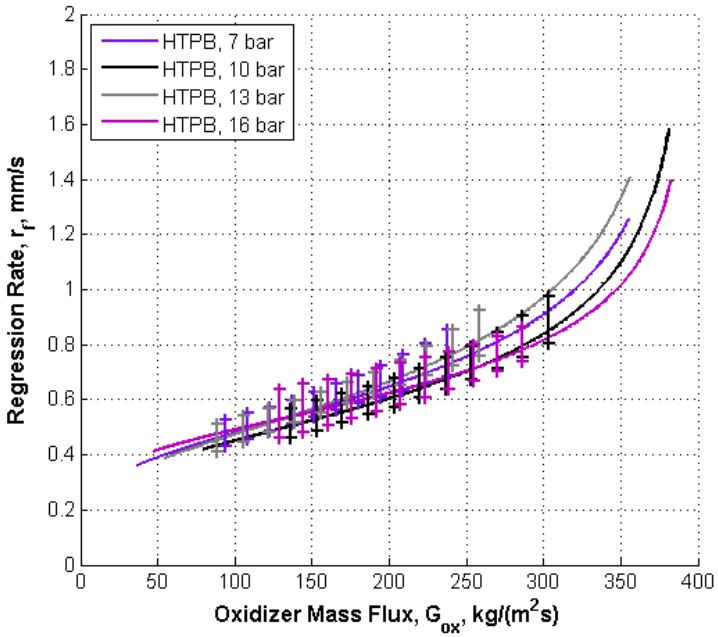

Figure 6.6: HTPB burning in GOX for p_c in the range from 7 to 16 bar, r_f vs. G_{ox} (instantaneous data). Under the investigated conditions p_c exhibits no definite influence on r_f.

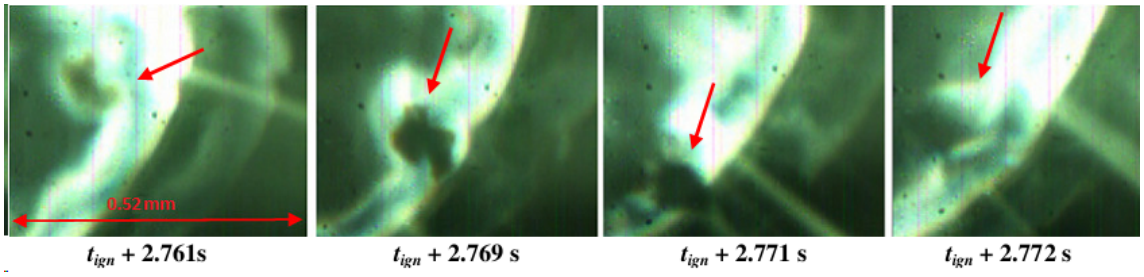

Figure 6.7: HTPB burning in GOX with p_c of 13 bar, close visualization. CCPs detaching from regressing surface.

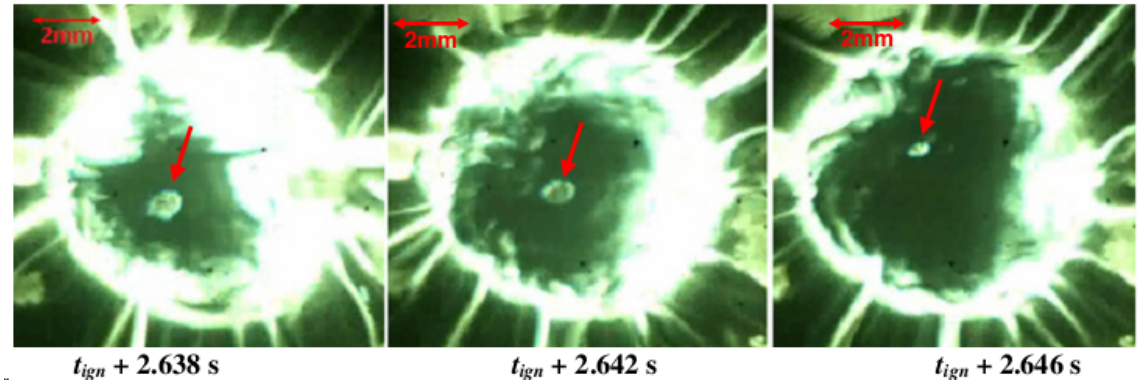

Figure 6.8: HTPB burning in GOX with p_c of 16 bar. CCPs detaching from regressing surface. Red arrow marks CCP detached from the regressing surface.

p_c exhibits no definite influence on r_f of HTPB. This is testified by Eq. 6.6 where a power–law interpolation is performed considering G_{ox} and p_c as free parameters. For the considered range of values of G_{ox}, a faint dependence of r_f from p_c is observed.

$$r_f(G_{ox},\, p_c) = (0.033 \pm 0.006) \cdot G_{ox}^{(0.601 \pm 0.031)} \cdot p_c^{(-0.048 \pm 0.052)},\ R^2 = 0.857 \tag{6.6}$$

This (faint) p_c dependence can be related to radiative heat–transfer and solid fuel grain fragmentation effects [37]. In fact, toward the end of the combustion process (low G_{ox}), fuel fragments are seen to detach from the fuel grain (see Figure 6.7 and Figure 6.8). Fragmentation produces r_f enhancement with respect to solid fuel vaporization due to heat feedback from the flame zone to the regressing surface. Under the investigated conditions, solid fuel grain fragments appear to detach from the regressing surface more and more as p_c is increased. Removing data of diameter evolution in time for $G_{ox} < 120\ kg/(m^2 s)$, values of n_r close to 0.8 are achieved, as shown in Table 6.4. This exclusion of the available data yields to the double interpolation for r_f vs. G_{ox} and p_c reported in Eq. 6.7. Under the investigated conditions, Eq. 6.7 testifies non–influence of p_c on ballistics of HTPB, in spite of poor data fitting of experimental data. Dependence of r_f from G_{ox} is characterized by a 0.8 value for the corresponding exponent in Eq. 6.7.

$$r_f(G_{ox},\, p_c) = (0.010 \pm 0.003) \cdot G_{ox}^{(0.795 \pm 0.042)} \cdot p_c^{(-0.002 \pm 0.047)},\ R^2 = 0.869 \tag{6.7}$$

Considering possible peculiar phenomena involved in solid fuel burning for G_{ox} lower than 120 $kg/(m^2 s)$, is reported in Figure 6.9 where time–resolved data are presented in a nondimensional form for convenience (being evaluated with a previous arrangement of the experimental setup [34] [36]). Nondimensional r_f presented in Figure 6.9 is evaluated by considering the instantaneous $r_f(t_{ign})$ for tests performed with p_c of 10 bar. Under the investigated conditions achieved

Table 6.3: HTPB burning in GOX, power–law approximation for r_f vs. G_{ox} of ensemble average curves, see Eq.6.2. Note the difference in n_r value for 7 bar tests.

Fuel, p_c	a_r	n_r	R^2, Eq. 6.2
HTPB, 7 bar	0.046±0.010	0.520±0.044	0.899
HTPB, 10 bar	0.015±0.010	0.712±0.079	0.854
HTPB, 13 bar	0.024±0.007	0.650±0.054	0.907
HTPB, 16 bar	0.022±0.009	0.644±0.072	0.849

Table 6.4: HTPB burning in GOX, power–law approximation for r_f vs. G_{ox} of ensemble average curves, see Eq.6.2. Considering $G_{ox} > 120\ kg/(m^2 s)$, HTPB ballistics is driven by diffusion–limited, convective–heat transfer regime.

Fuel, p_c	a_r	n_r	R^2, Eq. 6.2
HTPB, 7 bar	0.046±0.012	0.765±0.062	0.926
HTPB, 10 bar	0.006±0.003	0.872±0.099	0.854
HTPB, 13 bar	0.008±0.003	0.857±0.069	0.926
HTPB, 16 bar	0.015±0.007	0.711±0.081	0.854

data exhibits a r_f increase for p_c increase from 7 to 10 bar, while no significant influence is exerted when passing from 10 to 13 bar. The latter results show relative pressure independence of regression rate for p_c > 10 bar also for these test conditions. The pressure effect for 7 bar $< p_c <$ 10 is due to radiative heat transfer effect due to the reduced contribution of convective–heat transfer, as well as fragmentation phenomena. This is testified by the low value of n_r for the 7 bar tests reported in Figure 6.9.

6.2 SW Fuel

The SW fuel formulation was tested under p_c of 7 bar, 13 bar and 16 bar. An image sequence for SW burning in GOX under p_c of 16 bar is reported in Figure 6.10. Achieved results are shown in Figure 6.11, Table 6.6 and summarized by Eq. 6.8 where r_f is approximated by a power–law considering G_{ox} and p_c as free parameters. When compared to baseline formulation, paraffin–based fuel exhibits a strong pressure dependence under the investigated conditions, as testified by the exponent of p_c in Eq. 6.8 (-0.415 vs. 0.879 for G_{ox}). As shown by Figure 6.13 a strong regression rate enhancement with respect to HTPB characterizes SW–fuel over the whole investigated range. Considering p_c of 7 bar, for G_{ox} of 200 $kg/(m^2 s)$ SW fuel exhibits an instantaneous r_f increase with respect to HTPB of 293%. Nevertheless, due to a strong dependence from p_c, at 16 bar this increase reduces to 187%. Data scattering for SW fuel formulations results higher than for HTPB (see error bars in Figure 6.11). Nevertheless, the strong pressure dependence is definite and could be related to the changes in the interaction between oxidizer flow and melted fuel for different chamber pressures, with higher values of p_c promoting stability of liquid layer.

$$r_f(G_{ox},\, p_c) = (0.062 \pm 0.018) \cdot G_{ox}^{(0.879 \pm 0.045)} \cdot p_c^{(-0.415 \pm 0.069)},\ R^2 = 0.908 \tag{6.8}$$

High data scattering for SW–fuels is related to the poor mechanical properties of the solid fuel grain. Due to low melting temperature and overall poor mechanical characteristics, SW can exhibit scattered ignition diameters affecting the first steps of the combustion process. Though not affected by apparent marked anisotropies, [34][36], SW ensemble average curves are affected by this ignition effect. Moreover, poor mechanical properties of the solid grain yield to SW strand collapses during the combustion. Due to this effects only three tests for SW are performed at 7 bar. This in turn causes larger error bars due to higher Student's t values.

Figure 6.12 shows a comparison between SW and HTPB fuels for p_c of 16 bar. A modified fuel formulation with no SA (and increased solid wax content) is reported in the same figure. This lat-

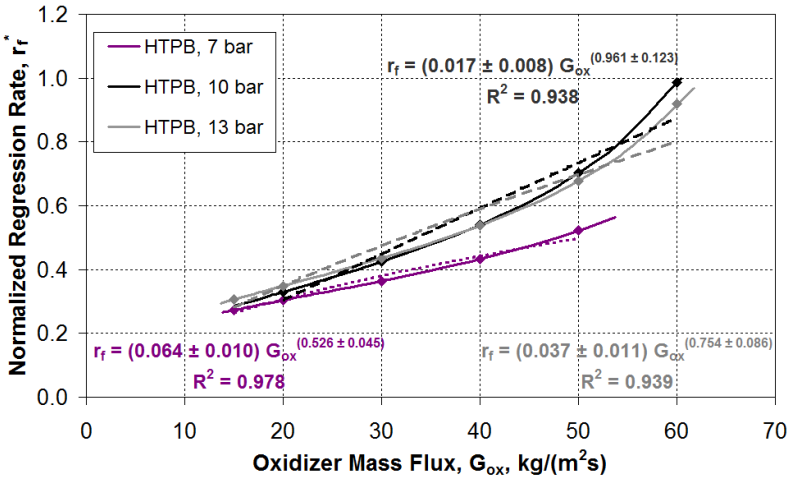

Figure 6.9: HTPB burning in GOX with p_c in the range 7–13 bar for initial nominal GOX of 70 $kg/(m^2 s)$. Due to relatively low G_{ox}, convective heat transfer is reduced thus yielding to increased effects of radiative heat–transfer and solid fuel fragmentation. Regression rate normalized with respect to $r_f(t_{ign})$ at 10 bar.

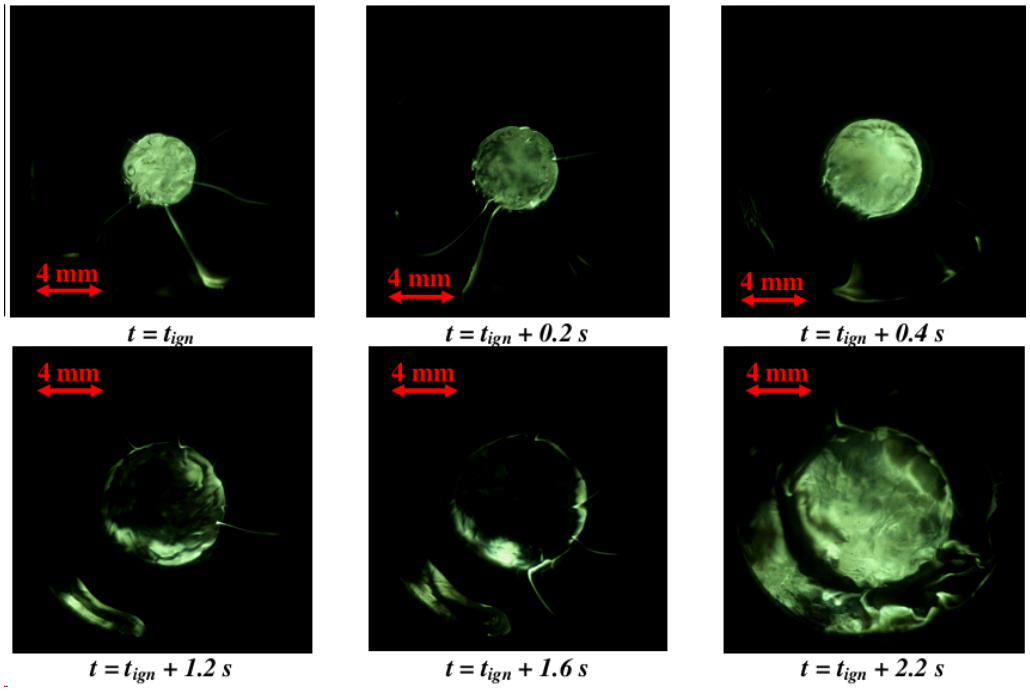

Figure 6.10: SW fuel burning in GOX under p_c of 16 bar, regressing surface evolution in time, note possible anisotropies at ignition due to SW poor mechanical properties ($t = t_{ign}$), followed by apparent regular combustion (minor anisotropies). Incipient collapse of solid fuel grain is visible for $t = t_{ign} + 2.2$ s.

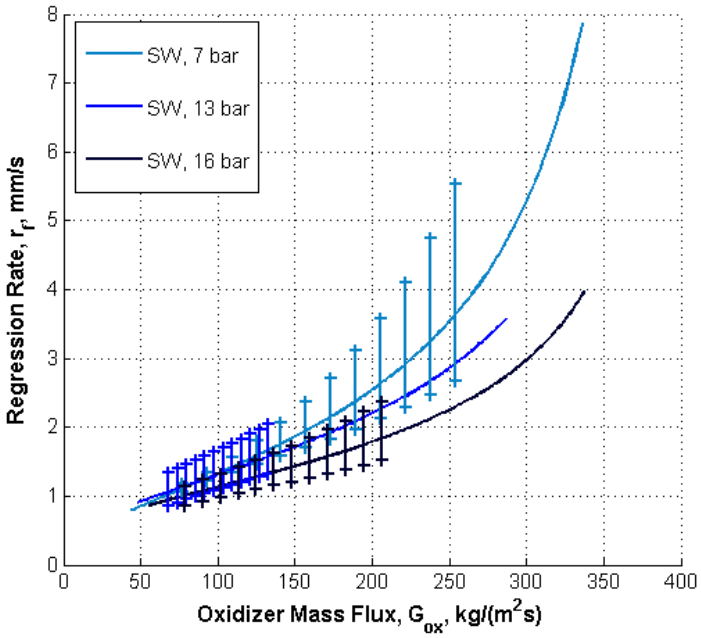

Figure 6.11: SW-based fuel burning in GOX for p_c in the range from 7 bar to 16 bar (ensemble average). In spite of data scattering due to poor mechanical properties of the solid fuel grain, a decreasing trend of r_f for increasing p_c is achieved under the investigated conditions (Massini, 2011).

ter formulation at G_{ox} of 200 $kg/(m^2 s)$ exhibits a r_f increase of 278% with respect to HTPB under similar operating conditions (see Figure 6.12 and Figure 6.13). This r_f increase is higher than the one achieved by SA–containing fuel under the same conditions. Solid paraffin wax without SA exhibits performance increases with respect to baseline (HTPB) similar to those of SW at 7 bar, though the latter fuel is characterized by a stronger sensitivity to G_{ox} (see Table 6.7). Nevertheless also data scattering is increased (only three tests performed for this formulation due to grain collapses). SA is added into SW formulation is order to achieve mechanical properties enhancement. Removal of this ingredient probably leads to a faster combustion due to higher fuel melting with respect to standard SW formulation. As shown by Table 6.5 single curve data scattering does not affect congruency checks, thus granting quality of the achieved results.

An overview of the $\Delta r_{f,\%}$ of SW fuel with respect to baseline (HTPB) under similar conditions is reported in Figure 6.13. Percent average r_f increases of SW fuel over the whole investigated range is reported in Table 6.7. As highlighted by the high n_r value characterizing SW burning under 7 bar, this fuel at such a lower pressure exhibits a marked sensitivity to G_{ox} [note high $\xi(\Delta r_{f,\%})$] in Table 6.7). Detriment of SW r_f for increasing pressure is caught by $\Delta r_{f,\%}$ trend (decreasing for increasing p_c), see Table 6.7.

6.3 HTPB Fuel Loaded with Nano–Sized Metals

Metallized HTPB fuels were tested under different p_c. In order to achieve relative ballistic grading of the different formulations, HTPB burning under similar operating conditions was considered as baseline.

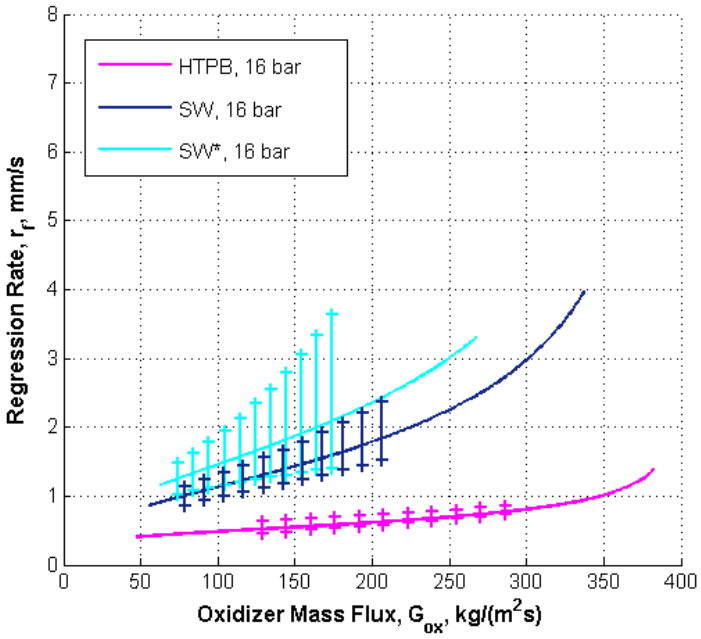

Figure 6.12: SW-based fuel burning in GOX for p_c of 16 bar. Due to entrainment of melted fuel droplets significant regression rate enhancement is achieved with respect to HTPB (Massini, 2011).

Table 6.5: Consistency checks for SW–based formulations burning in GOX under p_c of 16 bar. Check results expressed as percentages with respect to TOT data.

Fuel, p_c	**Test No.**	**Eq.** 5.8	**Eq.** 5.13	**Eq.** 5.14
SW, 16 bar	01	-0.2	-1.1	-1.1
	02	0.3	-3.2	2.0
	03	0.2	-0.9	-0.1
SW[a], 16 bar	01	0.7	-3.4	-1.0
	02	0.6	-1.3	-0.1
	03	0.1	-0.2	-1.7

[a]SW without SA

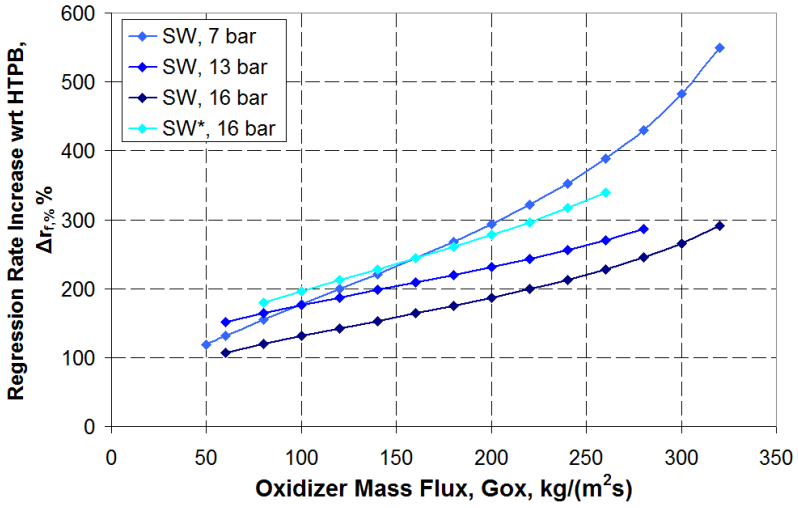

Figure 6.13: SW-based fuel burning in GOX, regression rate increase with respect to HTPB under similar conditions (* SW formulation without SA).

Table 6.6: SW burning in GOX, power–law approximation for r_f vs. G_{ox} of ensemble average curves, see Eq.6.2. High sensitivity to G_{ox} characterizes SW at 7 bar (see high n_r).

Fuel, p_c	a_r	n_r	R^2, Eq. 6.2
SW, 7 bar	0.010±0.004	1.082±0.077	0.929
SW, 13 bar	0.046±0.010	0.737±0.042	0.963
SW, 16 bar	0.034±0.009	0.763±0.052	0.942
SW[a], 16 bar	0.056±0.010	0.710±0.036	0.975
[a] SW without SA			

Table 6.7: SW burning in GOX with p_c in the range from 7 to 16 bar. Average $\Delta r_{f,\%}$ and its standard deviation for 80 $kg/(m^2s) < G_{ox} < 260kg/(m^2s)$. SW burning at p_c of 7 bar exhibit marked sensitivity to G_{ox} [see high $\xi(\Delta r_{f,\%})$].

Fuel, p_c	$\Delta r_{f,\%}$	$\xi(\Delta r_{f,\%})$
SW, 7 bar	254	75
SW, 13 bar	215	35
SW, 16 bar	171	36
SW[a], 16 bar	255	53
[a] SW without SA		

6.3.1 HTPB Fuel Loaded with Nano–sized Aluminum

HTPB loaded with nAl was tested with p_c of 10 bar. Fuel formulations were characterized by 10% nAl mass fraction, a 2% mass fraction of C was added to the fuel formulation for mechanical properties enhancement. This latter filler exhibits limited or no influence on r_f, as testified by burning tests data reported in [106].

HTPB Loaded with ALEX Powder

The ballistic characterization of HTPB loaded with ALEX with respect to baseline is illustrated in Figure 6.14 in terms of r_f vs. G_{ox}. Four tests were performed, but only the resulting ensemble curve is shown. The latter is characterized by a t_{ign} of 0.006 s, showing a significantly reduced ignition delay compared to the corresponding baseline under the same operating conditions (0.034 s, see Table 5.1). This finding is in agreement with ALEX high reactivity as shown in DSC/TGA and ignition tests discussed in Chapter 3 (see Table 3.8 and Table 3.11). HTPB loaded with ALEX features an impressive initial r_f increase. Nevertheless due to strong sensitivity to G_{ox}, the initial $\Delta r_{f,\%}$ of 58% with respect to baseline at 380 $kg/(m^2s)$ reduces to 48% at 370 $kg/(m^2s)$ and vanishes for $G_{ox} < 150$ $kg/(m^2s)$. Due to Al density, HTPB loaded with ALEX exhibits mass burning rate enhancement with respect to baseline over the whole investigated range with an increase of 71% at 380 $kg/(m^2s)$ decreasing (as G_{ox} decreases) up to 4% at 100 $kg/(m^2s)$.

The behavior of ALEX at high G_{ox} does not significantly alter the trend of $< r_f >$ vs. $<G_{ox}>$ with respect to the instantaneous values. Considering oxidizer mass flux of 350 $kg/(m^2s)$, time–averaged regression rate increase of ALEX–doped fuel with respect to baseline is 43%, while the corresponding instantaneous increase is 37%. At 250 $kg/(m^2s)$ the values are 19% and 15% respectively, while for the G_{ox} of nearly 155 $kg/(m^2s)$ (corresponding to baseline overall time–averaged value), instantaneous increase of instantaneous ALEX r_f with respect to baseline is 3%, while the corresponding time–averaged overall increase is 6%. Marked sensitivity from G_{ox} of ALEX–doped fuel is evidenced by data shown in Table 6.8, where power law approximation given by Eq. 6.2 is reported. Considering equi–spaced values of G_{ox} covering the whole investigated range, an n_r value of higher than 1 is achieved. On the other hand, considering a restricted G_{ox} interval, a power–law approximation similar to those of baseline is achieved (see Table 6.3). Under the investigated conditions, this behavior is probably due to a change in ALEX effect on solid fuel grain ballistics. At the beginning of the combustion process, ALEX is effective in producing r_f

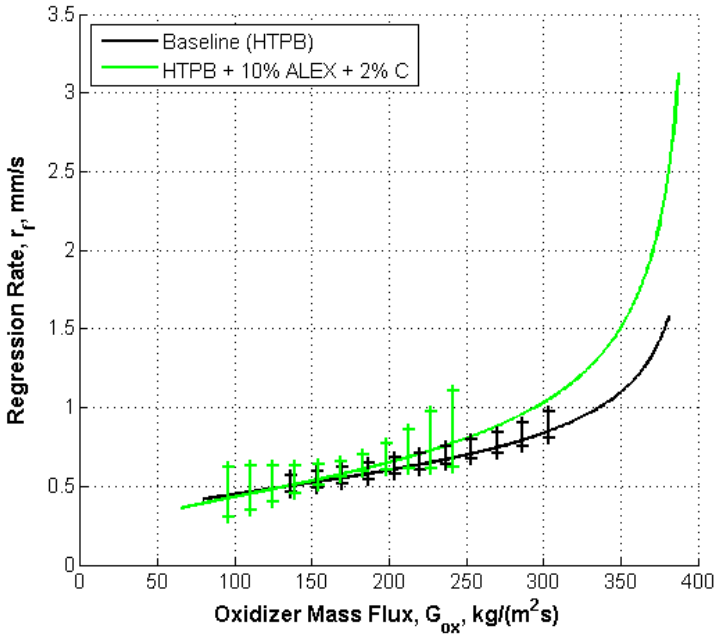

Figure 6.14: HTPB + 2% C + 10% ALEX burning in GOX with p_c of 10 bar, r_f vs. G_{ox} (ensemble average). Note definite r_f increase for high G_{ox}.

Table 6.8: HTPB loaded with 10% ALEX and 2% C burning in GOX with p_c of 10 bar, r_f vs. G_{ox} (ensemble average). Note high sensitivity to G_{ox} of ALEX–doped fuel (high value for n_r) .

Fuel, p_c	a_r	n_r	R^2, Eq. 6.2
HTPB + 2% C + 10% ALEX, 10 bar	0.002±0.001	1.111±0.136	0.804
HTPB + 2% C + 10% ALEX, 10 bar[a]	0.023±0.004	0.633±0.033	0.976
[a] Approximation for 80 $kg/(m^2s) < G_{ox} <$ 260 $kg/(m^2s)$			

enhancement due to the high heat feedback to the regressing surface. When G_{ox} convective heat transfer from the flame to the solid fuel is reduced, ALEX starts behaving as a thermal sink. This behavior could be testified by sintering/aggregation phenomena observed (under slightly different operating conditions) in a 2D slab micro–burner and on a previous version of the 2D radial burner, see Figures 6.15–6.16.

HTPB Loaded with L–ALEX Powder

Three different kinds of L–ALEX powders were tested under p_c of 10 bar. Tested powders have the same coating composition (octadecanoic acid, SA) but differ for the presence/absence of an alumina shell surrounding the Al core of the particles. In the first case, immediately after production by EEW the powder was passivated in air and then coated (L–ALEX$_{APS}$), while in the second case the coating is applied immediately after production, without air passivation (L–ALEX$_{NPS}$). Two different variants of L–ALEX$_{NPS}$ powders, with nominal dimensions of 100 nm and 50 nm respectively, were considered, while the tested L–ALEX$_{APS}$ had a nominal dimension of 100 nm. Tested powder particle–sizes as determined from S_{sp} measured data are reported in Table 3.7. Achieved results yield to an a_s value of nearly 200 nm for the considered powders. Other data related to powder characterization are reported in Table 3.8 and Table 3.11. Experimental session results are reported in Figures 6.17 – 6.18 and Table 6.9.

Under the investigated conditions performance of coated powders results higher than those of ALEX with the only exception of L–ALEX$_{NPS}$ (100 nm), see Figure 6.17. The latter additive provides regression rate increase similar to the one of ALEX for G_{ox} of 330 $kg/(m^2s)$. Never-

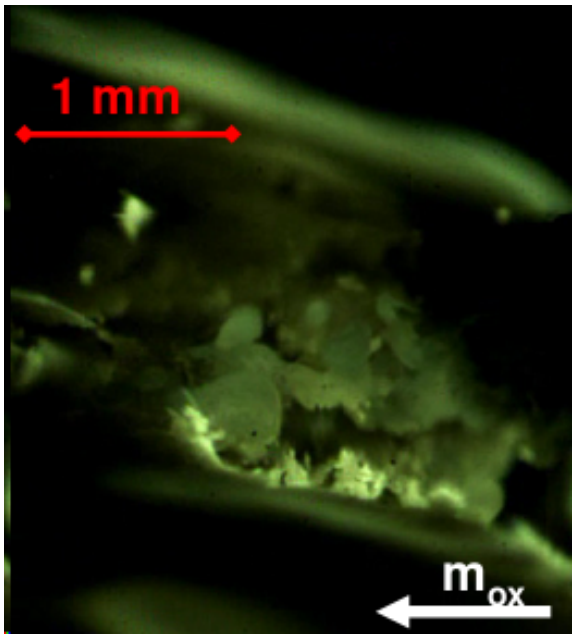

Figure 6.15: HTPB + 5% ALEX burning in 60% O_2–40% N_2 with p_c of 10 bar in a micro–slab burner [37]. In spite of low G_{ox} [nearly 10 $kg/(m^2s)$] with respect to 2D radial micro–burner, note sintered/aggregated structures at solid fuel surface.

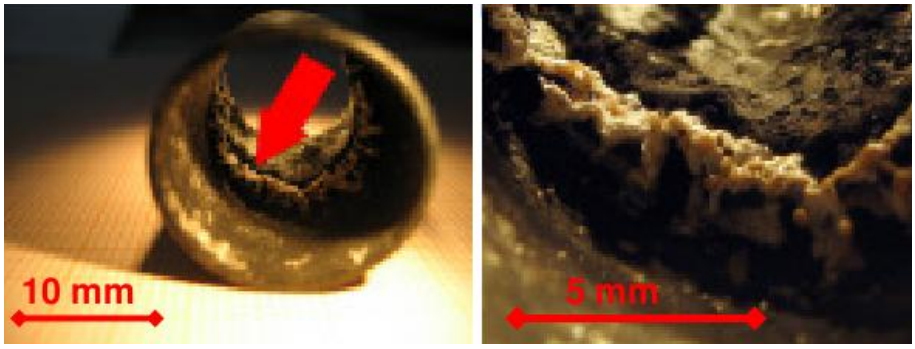

Figure 6.16: HTPB + 2% C + 10% ALEX burning in GOX with p_c of 10 bar with initial G_{ox} of 130 $kg/(m^2s)$. Sintered structures/aggregates at strand head–end (Green and Fanton, 2010).

Table 6.9: HTPB loaded with different L–ALEX powders and 2% C burning in GOX with p_c of 10 bar, power law approximation of r_f vs. G_{ox} (ensemble average curve). Note high sensitivity to G_{ox} of ALEX–doped fuel (high value for n_r) .

Fuel, p_c	a_r	n_r	R^2, Eq. 6.2
HTPB + 2% C + 10% L–ALEX$_{NPS}$ (100 nm), 10 bar	.0005±.0003	1.348±0.033	0.934
HTPB + 2% C + 10% L–ALEX$_{NPS}$ (50 nm), 10 bar	0.002±0.001	1.214±0.124	0.872
HTPB + 2% C + 10% L–ALEX$_{APS}$ (100 nm), 10 bar	0.007±0.002	0.891±0.054	0.954

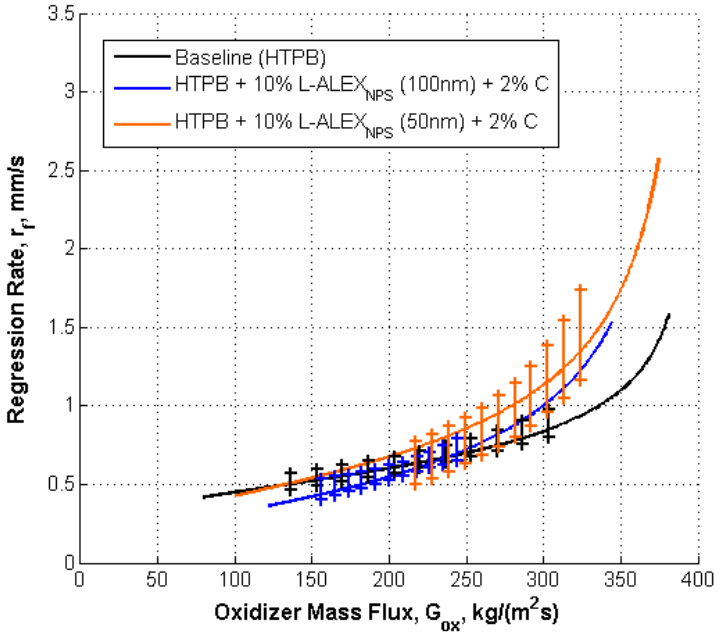

Figure 6.17: HTPB doped with 2% C and different L–ALEX$_{NPS}$ powders (100 nm and 50 nm) burning in GOX with p_c of 10 bar, r_f vs. G_{ox}. Note significant r_f enhancement for $G_{ox} > 300$ $kg/(m^2s)$.

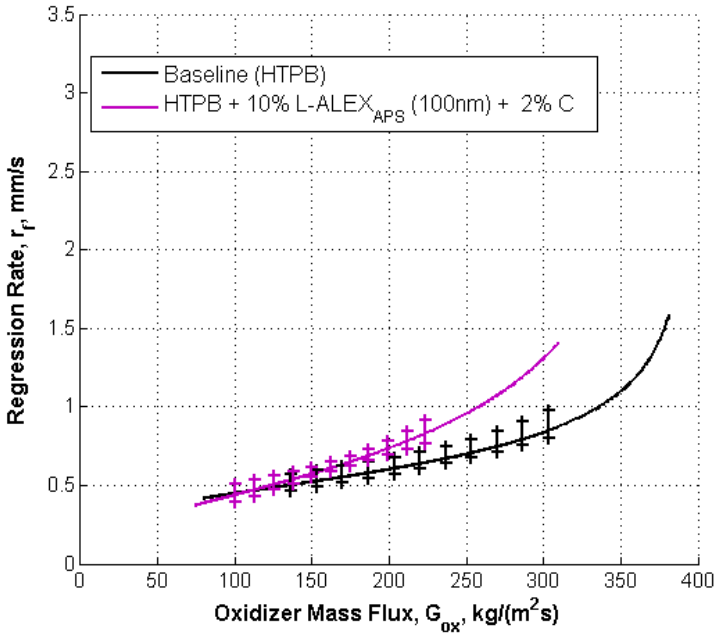

Figure 6.18: HTPB + 2% C + 10% L–ALEX$_{APS}$ burning in GOX with p_c of 10 bar, r_f vs. G_{ox}.

Table 6.10: HTPB loaded with different L–ALEX powders and 2% C burning in GOX with p_c of 10 bar, power law approximation of r_f vs. G_{ox} (ensemble average curve) for $G_{ox} < 260\ kg/(m^2s)$.

Fuel, p_c	a_r	n_r	R^2, Eq. 6.2
HTPB + 2% C + 10% L–ALEX$_{NPS}$ (100 nm), 10 bar	0.003±0.001	0.964±0.048	0.983
HTPB + 2% C + 10% L–ALEX$_{NPS}$ (50 nm), 10 bar	0.012±0.002	0.769±0.039	0.980
HTPB + 2% C + 10% L–ALEX$_{APS}$ (100 nm), 10 bar	0.013±0.002	0.767±0.037	0.977

theless due to high sensitivity to oxidizer mass flux, ballistic performance of L–ALEX$_{NPS}$ (100 nm) lies below those of other energetic additives and for G_{ox} 230 $kg/(m^2s)$ a performance detriment with respect to baseline is achieved. Better performance are achieved by L-ALEX$_{NPS}$ (50 nm) exhibiting a $\Delta r_{f,\%}$ of 47% at 330 $kg/(m^2s)$ and 3% at 100 $kg/(m^2s)$, see Figure 6.17. Performance of L-ALEX$_{NPS}$ (50 nm) with respect to L–ALEX$_{NPS}$ (100 nm) can be related to the smaller particle-size enabling higher reactivity in the powder. Fuel formulation loaded with L–ALEX$_{NPS}$ exhibits regression rate increases of 56% at 300 $kg/(m^2s)$, and 10% at 100 $kg/(m^2s)$. Performance enhancement of this latter formulation is therefore higher with respect to L–ALEX$_{NPS}$ under the investigated conditions. This result can be related to the crucial role played by alumina shell surrounding the Al particle core in air passivated powders. Under rapid heating conditions (as those of solid fuel burning), alumina shell enables melt dispersion mechanism [69] [70]. The latter originates fast reaction of APS nAl under rapid heating conditions thus yielding achieved regression rate increase. Due to the difference in heating rates, alumina shell effect and other possible causes (as dispersion effectiveness into the binder matrix), a direct correlation between data from powders physical analysis and ballistic characterization cannot be achieved with the available results. On the basis of DSC/TG analysis and due to measured S_{sp}, L–ALEX$_{APS}$ (100 nm) should be less effective than L–ALEX$_{NPS}$ (50 nm) in regression rate enhancement, while ballistic characterization shows an opposite trend under the investigated conditions. Differences in operating conditions between DSC/TGA and combustion tests can explain such a difference, nevertheless a better understanding of the complex phenomena involved in nAl combustion is required to properly relate physical analyses and ballistic data, especially for organic coated powder.

Table 6.10 shows power law approximation by Eq. 6.2 for ensemble curve of tested formulations in the range $G_{ox} < 260\ kg/(m^2s)$. Comparing this results with those reported in Table 6.9, a decrease in r_f sensitivity to oxidizer mass flux is achieved under the investigated conditions. This effect is possibly related to the aggregation phenomena discussed for ALEX. Note that the values of n_r reported in Table 6.10 are quite close to those characterizing a burning regime mainly driven by convective heat–transfer.

HTPB Loaded with F–ALEX and VF–ALEX Powders

Powders with fluorine–containing coating, F-ALEX$_{APS}$ and VF-ALEX$_{APS}$, have nominal dimension of 100 nm and were both manufactured at lab–scale level. As reported in Table 3.7, a_s of 205 nm is characterizes F–ALEX$_{APS}$, while VF–ALEX$_{APS}$ presents bigger particles with a_s of 345 nm. Results achieved during ballistic characterization are reported in Figure 6.19 and Table 6.11.

Under the investigated conditions the best performance in terms of r_f increases at high G_{ox} is achieved by fuel formulation loaded with F-ALEX$_{APS}$, see Figure 6.19. With a G_{ox} of 330 $kg/(m^2s)$, increase with respect to baseline is 68%, corresponding to a notable fuel mass burning rate enhancement of 82%. At G_{ox} of 100 $kg/(m^2s)$ fuel formulation loaded with F-ALEX$_{APS}$ yields a slight regression rate increase with respect to baseline of 2%. Under the investigated operating conditions, VF–ALEX$_{APS}$ exhibits a relatively small r_f enhancement in the earlier phases of the combustion, but an interesting behavior for decreasing G_{ox}. With G_{ox} of 350 $kg/(m^2s)$ VF–ALEX$_{APS}$ provides a $\Delta r_{f,\%}$ of 25 % while for $G_{ox} = 100\ kg/(m^2s)$, a remarkable r_f increase of 39% is achieved. This result contrasts with those achieved by other tested nAl powders and is peculiar of VF–ALEX$_{APS}$. This behavior can be explained considering nature of the coating (based on Fluorel™) and some physical characteristics of the powder (see Table 3.7). According to available data, S_{sp} of VF–ALEX$_{APS}$ is the lowest in the set of tested powders. The low specific surface possibly hinders powder reactivity in the earlier phases of the combustion. On the other

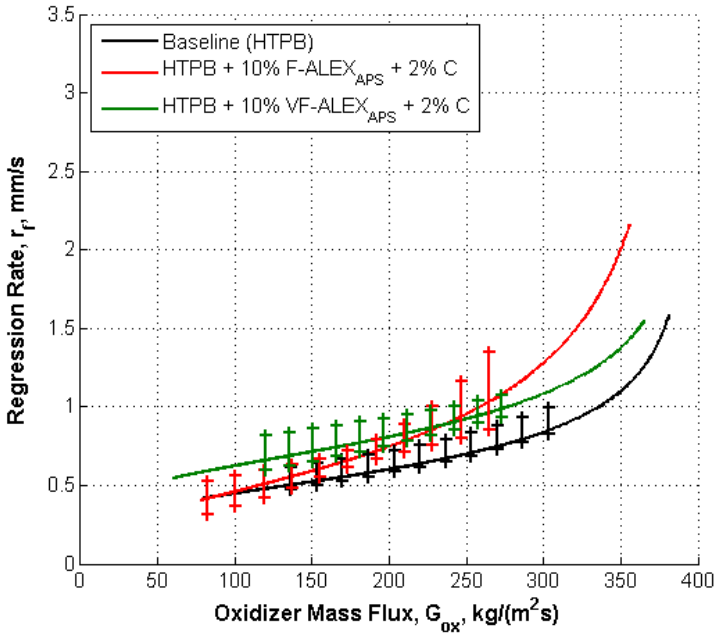

Figure 6.19: HTPB loaded with F– and VF–ALEX$_{APS}$ in GOX with p_c of 10 bar, r_f vs. G_{ox}. Note high r_f enhanceent with respect to baseline for VF–ALEX$_{APS}$ at low oxidizer mass fluxes.

Table 6.11: HTPB loaded with F– and VF–ALEX$_{APS}$ burning in GOX with p_c of 10 bar, power law approximation of r_f vs. G_{ox} (ensemble average). Note n_r values, F–ALEX$_{APS}$ exhibits a marked sensitivity to G_{ox}, unlike VF–ALEX.

Fuel, p_c	a_r	n_r	R^2, Eq. 6.2
HTPB + 2% C + 10% F–ALEX$_{APS}$, 10 bar	0.005±0.002	0.980±0.079	0.910
HTPB + 2% C + 10% VF–ALEX$_{NPS}$, 10 bar	0.051±0.013	0.542±0.050	0.879

hand, coating during its decomposition produces oxidizing species providing oxidizer for metal combustion. This effect possibly lessens sintering/aggregation of particles, thus yielding to significant regression rate for low G_{ox} where nAl performance are normally hampered (under the investigated conditions). Data reported in Table 6.11 and Table 6.12 highlights a common trend for the previously discussed nAl and F–ALEX$_{APS}$ (note n_r values), while VF–ALEX$_{APS}$ exhibits a different behavior (relatively small influence of G_{ox}).

Performance Enhancement Overview

A detailed overview of $\Delta r_{f,\%}$ achieved by the tested fuel formulations under the considered operating conditions is reported in Figure 6.20 and Table 6.13. VF–ALEX$_{APS}$ is the fuel formulation exhibiting the lowest sensitivity to G_{ox} variations [$\xi(\Delta r_{f,\%})$ = 3.6]. In addition to this, it delivers an average regression rate increase with respect to baseline of 33 %. The highest average $\Delta r_{f,\%}$ is the one of F–ALEX$_{APS}$, L–ALEX$_{APS}$ exhibits similar performance. On the other hand

Table 6.12: HTPB loaded with F–ALEX$_{APS}$ and VF–ALEX$_{APS}$ burning in GOX with p_c of 10 bar, power law approximation of r_f vs. G_{ox} for $G_{ox} < 260\ kg/(m^2 s)$(ensemble average). Note different n_r values (with F–ALEX$_{APS}$ exhibiting a behavior similar to that of baseline).

Fuel, p_c	a_r	n_r	R^2, Eq. 6.2
HTPB + 2% C + 10% F–ALEX$_{APS}$, 10 bar	0.017±0.003	0.722±0.035	0.977
HTPB + 2% C + 10% VF–ALEX$_{NPS}$, 10 bar	0.115±0.012	0.371±0.020	0.972

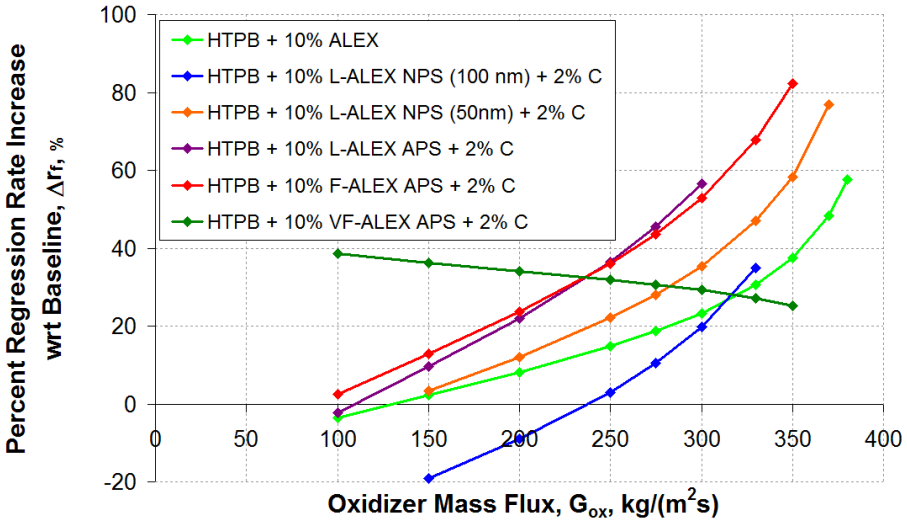

Figure 6.20: HTPB loaded with nAl burning in GOX with p_c of 10 bar, overview of $\Delta r_{f,\%}$ for different G_{ox}. Note general performance sensitivity to G_{ox} and low r_f enhancement at low G_{ox} for all tested fuels but HTPB doped with VF–ALEX$_{APS}$.

Table 6.13: HTPB loaded with nAl burning in GOX with p_c of 10 bar, overview of average $\Delta r_{f,\%}$ and its standard deviation for 100 $kg/(m^2s)$ < G_{ox} < 300 $kg/(m^2s)$. Note very low sensitivity to G_{ox} of VF–ALEX$_{APS}$ [$\xi(\Delta r_{f,\%})$=3.6%].

Fuel, p_c	$\Delta r_{f,\%}$	$\xi(\Delta r_{f,\%})$
HTPB + 2% C + 10% ALEX +, 10 bar	11	10
HTPB + 2% C + 10% L–ALEX$_{NPS}$ (100 nm), 10 bar	1.0	15
HTPB + 2% C + 10% L–ALEX$_{NPS}$ (50 nm), 10 bar	20	13
HTPB + 2% C + 10% L–ALEX$_{APS}$, 10 bar	28	22
HTPB + 2% C + 10% F–ALEX$_{APS}$, 10 bar	29	19
HTPB + 2% C + 10% VF–ALEX$_{APS}$, 10 bar	33	3.6

the highest absolute performance is achieved by F–ALEX$_{APS}$ with a $\Delta r_{f,\%}$ of 82% at G_{ox} of 370 $kg/(m^2s)$.

6.3.2 HTPB Fuel Loaded with Nano–sized Iron Powders

HTPB fuel loaded with 5% nFe and 1% C was tested in GOX with p_c of 10 bar. Achieved results are shown in Figure 6.23 and Table 6.14. Fuel loaded with nFe exhibited a poor–quality, highly anisotropic combustion as illustrated by Figure 6.21 and Figure 6.22. With respect to baseline a $\Delta r_{f,\%}$ of -31% is achieved at 370 $kg/(m^2s)$. Solid fuel slivers and fragments are seen to detach from the strand port during combustion. This strong fragmentation is the cause of the apparent performance increase achieved by nFe–doped fuel for low G_{ox}, see Figure 6.23. For G_{ox} < 200 $kg/(m^2s)$, fragmentation is so intense that measured surface consumption yields to a r_f higher than the one of baseline (see Table 6.15).

Table 6.14: HTPB loaded with 5% nFe and 1% C burning in GOX with p_c of 10 bar, power law approximation for r_f vs. G_{ox}. Note low value of n_r due to high r_f at low G_{ox} (fragmentation effects).

Fuel, p_c	a_r	n_r	R^2, Eq. 6.2
HTPB + 1% C + 5% nFe, 10 bar	0.198±0.032	0.243±0.030	0.787

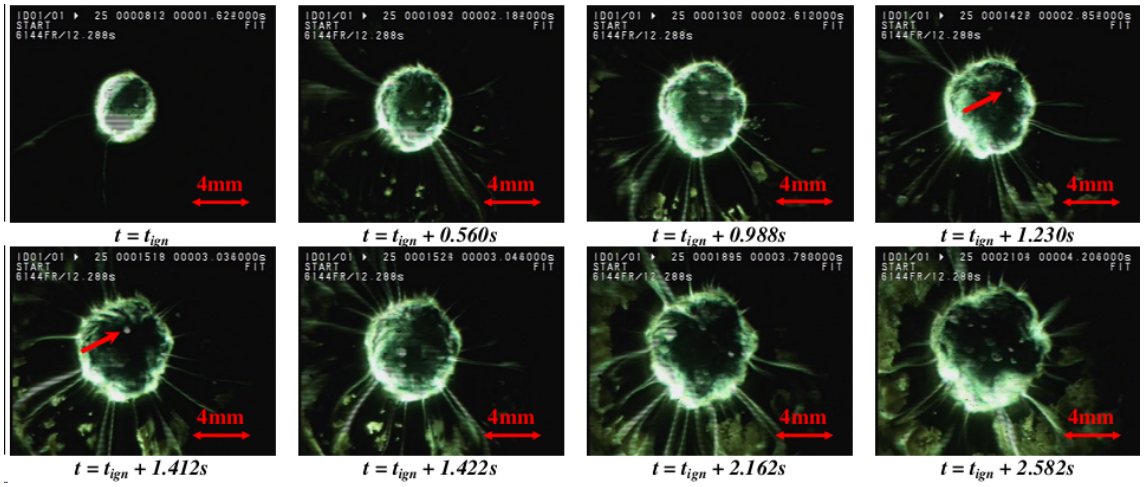

Figure 6.21: HTPB loaded with 5% nFe and 1% C in GOX with p_c of 10 bar, image sequence showing anisotropic combustion and CCP detachment (see red arrow).

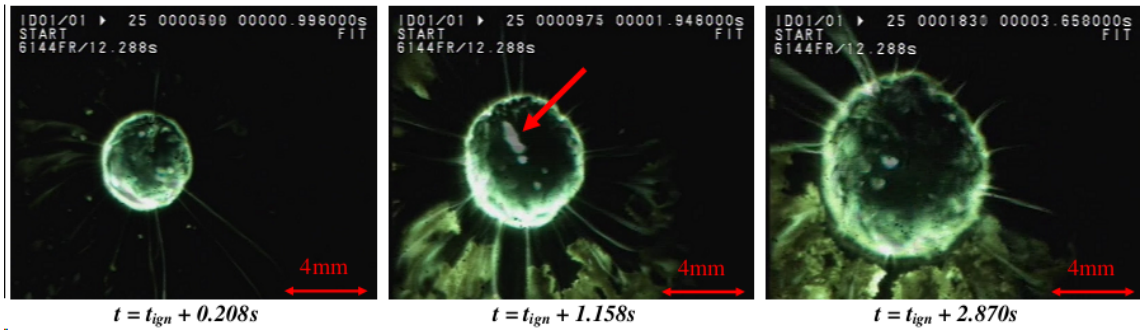

Figure 6.22: HTPB loaded with 5% nFe and 1% C in GOX with p_c of 10 bar, image sequence showing micron–sized CCP detaching from burning strand surface.

Table 6.15: Consistency checks for HTPB loaded with 5% nFe and 1% C burning in GOX under p_c of 10 bar. Check results expressed as percentages with respect to TOT data. Note high values for checks expressed by Eq. 5.13 and Eq. Eq. 5.14 due to high fragmentation.

Test No.	**Eq.** 5.8	**Eq.** 5.13	**Eq.** 5.14
01	1.3%	-5.8%	-0.4%
02	1.9%	-5.3%	-3.9%
03	1.4%	-6.6%	-9.6%
04	4.9%	-5.0%	-7.4%

Table 6.16: HTPB loaded with 5% nFe and 1% C burning in GOX with p_c of 10 bar, averaged $\Delta r_{f,\%}$ and corresponding standard deviation for the whole investigated G_{ox} range.

Fuel, p_c	$\Delta r_{f,\%}$	$\xi(\Delta r_{f,\%})$
HTPB + 1% C + 5% nFe, 10 bar	-5.7	25

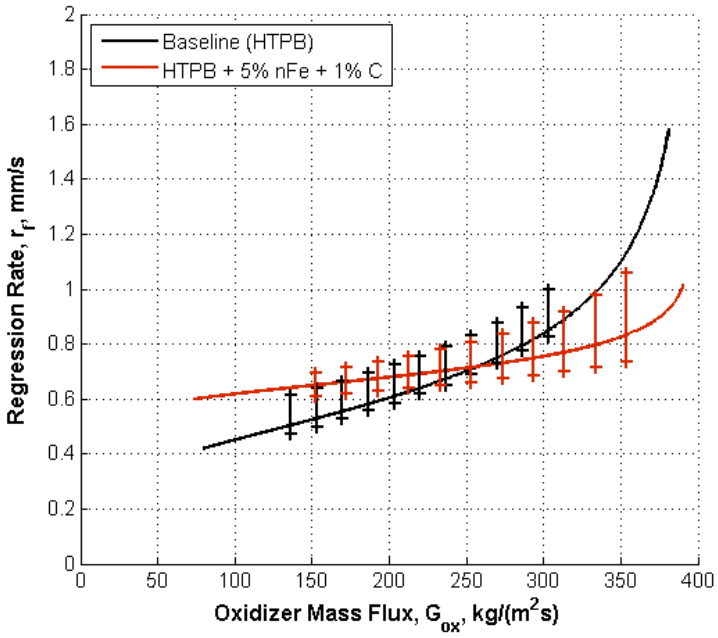

Figure 6.23: HTPB loaded with 5% nFe and 1% C in GOX with p_c of 10 bar, ensemble average curve for r_f vs. G_{ox}. Note high regression rate toward the end of the combustion (low G_{ox}) due to strong solid fuel fragmentation/CCP detachment from burning surface.

6.4 HTPB and SW Fuels Loaded with MgB

Different MgB–based metal additives were tested under different operating conditions. MgB90 (10% Mg) and MgB95 (10% Mg) were tested in a HTPB fuel at p_c of 16 bar, while MgB90 (20% Mg) was tested in both HTPB and SW fuels at p_c of 13 bar. Magnesium–boron offers a significant advantage with respect to nAl: it is micron–sized, thus it does not require dedicated procedures for proper dispersion within binder matrix. Experimental investigation results are reported in Figures 6.24–6.27.

Five tests were performed on HTPB loaded with 2.5% MgB90 (10% Mg), while three runs were conducted for HTPB loaded with 2.4% MgB95 (10% Mg). A summary of the achieved results is reported in Figure 6.24. Under the investigated conditions, fuel doped with MgB90(10%Mg) presented no significant r_f increase with respect to baseline. Moreover regressing surface exhibits anisotropies during combustion (see Figure 6.25). HTPB loaded with 2.4% MgB95 (10% Mg) exhibits a different behavior with respect to its B90 counterpart. Average ensemble shows a $\Delta r_{f,\%}$ of 33% at 300 $kg/(m^2s)$. The regression rate enhancement of HTPB loaded with 2.4% MgB95 (10% Mg) with respect to baseline is almost constant over the investigated G_{ox} range. The ballistic behavior of this solid fuel formulation is similar to the one of HTPB loaded with 2.8% MgB90 (20% Mg) shown in Figure 6.26. Performance of this latter formulation is characterized by a $\Delta r_{f,\%}$ of 59% at 300 $kg/(m^2s)$, while at 100 $kg/(m^2s)$ regression rate enhancement with respect to baseline is 33%.

Comparison of combustion quality of other tested MgB–based additives with the one of MgB90 (10% Mg) suggests a relation between the anisotropic combustion and the wide particle size distribution of the additive, characterized by a D_{43} of 7.1 μm, while MgB95 (10% Mg) and MgB90 (20% Mg) have a mass–averaged diameter of 4.4 and 5.2 μm respectively (see Figure 3.6). On the other hand, differences in ballistic performance of MgB95 (10% Mg) and MgB90 (20% Mg) under the investigated conditions could be related to the different Mg–content. Magnesium is a metal fuel characterized by easy ignition. Heat released by Mg ignition enables lessening of B ignition problems, thus yielding to combustion of the latter additive. Easy ignition of Mg could explain

different behavior between MgB–loaded and nAl–doped fuels. Performance detriment of nAl-doped formulations for low G_{ox} is lessened in MgB–based fuels by the presence of Mg. Radiative heat transfer from flame zone to the surface could play a significant role for performance enhancement (especially at low G_{ox}) and for low dependence of regression rate enhancement from G_{ox} of MgB95 (10% Mg) and MgB90 (20% Mg).

Loading SW with MgB90 (20% Mg) significant regression rate enhancement is achieved with respect to both baseline and non–loaded SW. Regression rate enhancement of MgB–doped formulation with respect to baseline at 300 $kg/(m^2s)$ is 428%. For G_{ox} of 200 $kg/(m^2s)$ $\Delta r_{f,\%}$ of MgB–doped fuel is 250% while standard SW fuel provides a $\Delta r_{f,\%}$ of 230%. Ballistics of SW + 2.8% MgB90 (20% Mg) is characterized by a strong dependence from oxidizer mass flux (see n_r in Table 6.17). A slight performance detriment with respect to SW fuel characterizes the MgB–doped formulation for $G_{ox} < 150$ $kg/(m^2s)$ (see Figure 6.27). The different trend characterizing MgB–doping of HTPB and SW (low $\Delta r_{f,\%}$ dependence from G_{ox} for HTPB vs. the strong effect for SW) is possibly due to interaction between the fuel melted layer and the metal particle.

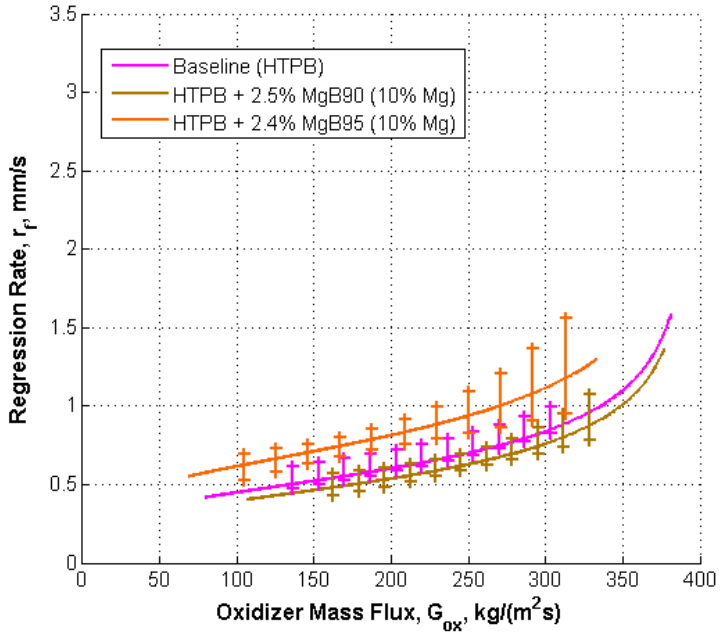

Figure 6.24: HTPB loaded with MgB90 (10% Mg) and MgB95 (10% Mg) under GOX, with p_c of 16 bar (average ensemble). The marked difference in the ballistic behavior of the two additives could be related to the different powder particle–size distribution (see Table 3.9 and Figure 3.6).

Table 6.17: HTPB and SW fuels loaded with different MgB powders burning in GOX with p_c of 13–16bar, power law approximation of r_f vs. G_{ox} (ensemble average curve, Eq. 6.2).

Fuel, p_c	a_r	n_r	R^2, Eq. 6.2
HTPB + 2.5% MgB90 (10% Mg), 16 bar	0.007±0.003	0.826±0.085	0.870
HTPB + 2.4% MgB95 (10% Mg), 16 bar	0.058±.0011	0.511±0.036	0.934
HTPB + 2.8% MgB90 (20% Mg), 13 bar	0.024±0.007	0.717±0.059	0.901
SW + 2.8% MgB90 (20% Mg), 13 bar	0.003±.0001	1.291±0.096	0.928

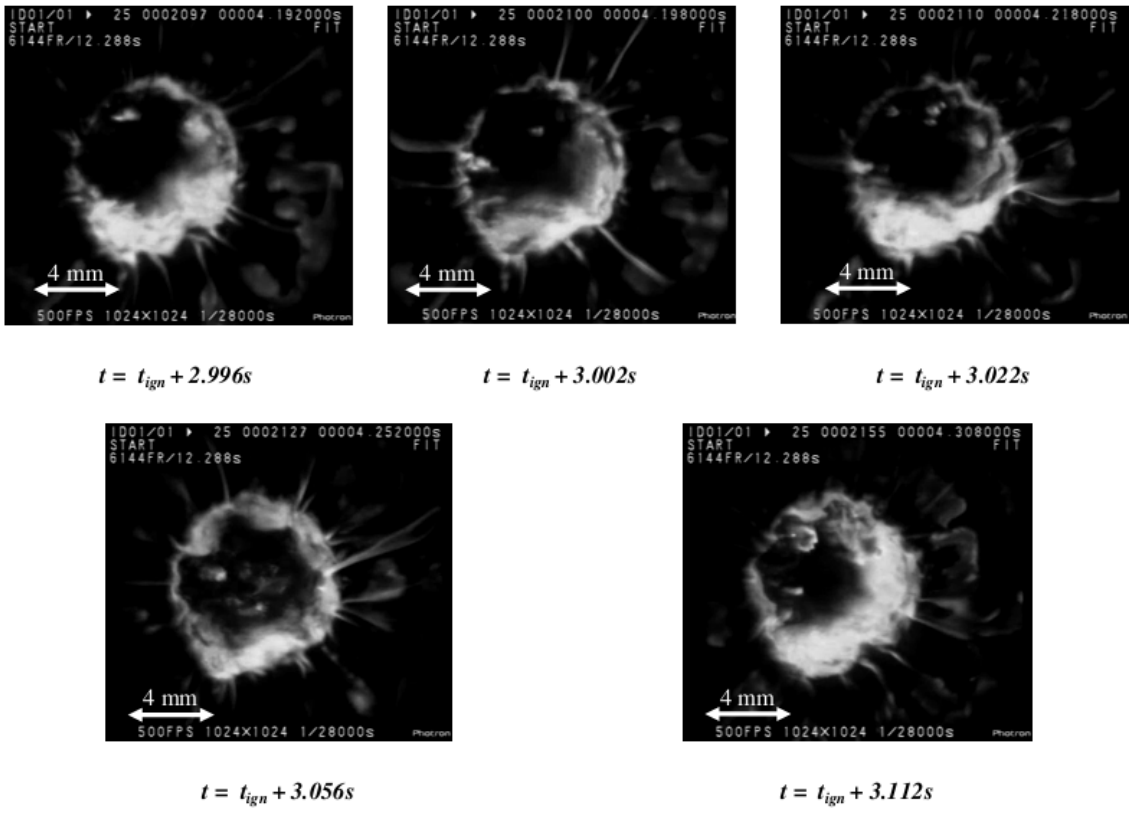

Figure 6.25: HTPB loaded with 2.5% MgB90 (10% Mg) burning under GOX, with p_c of 16 bar, combustion sequence for Test No. 01. Note anisotropic central port and CCP detaching from the regressing surface. Wide particle size distribution of the additive is considered as the main source for these irregularities.

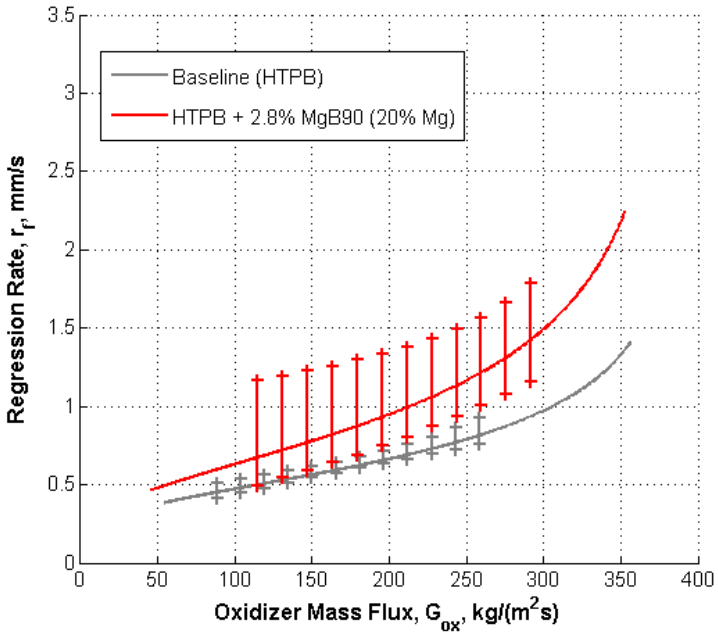

Figure 6.26: HTPB loaded with 2.8% MgB90 (20% Mg) under GOX, with p_c of 13 bar (average ensemble). Significant r_f increase is achieved over the whole investigated range.

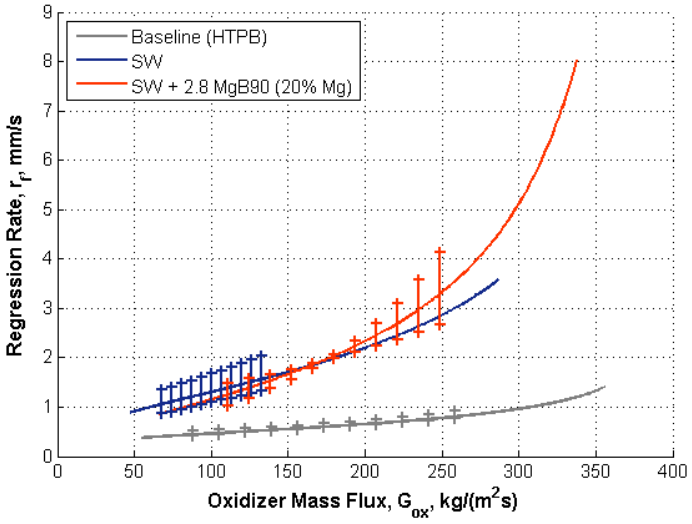

Figure 6.27: SW loaded with 2.8% MgB90 (20% Mg) under GOX, with p_c of 13 bar (average ensemble). Significant r_f increase is achieved over the whole investigated range, note $\Delta r_{f,\%}$ of 530% at G_{ox} of 330 $kg/(m^2 s)$.

Table 6.18: HTPB ans SW fuels loaded with MgB–based additives burning in GOX with p_c of 13–16 bar, overview of G_{ox}–averaged $\Delta r_{f,\%}$ and its standard deviation.

Fuel, p_c	$\Delta r_{f,\%}$	$\xi(\Delta r_{f,\%})$
HTPB + 2.5% MgB90 (10% Mg), 16 bar	-10	0.7
HTPB + 2.4% MgB95 (10% Mg), 16 bar	35	1.5
HTPB + 2.8% MgB90 (20% Mg), 13 bar	44	7.8
SW + 2.8% MgB90 (20% Mg), 13 bar	285	108

6.5 HTPB and SW Fuels Loaded with Hydrides

HTPB– and SW–based solid fuel formulations loaded with hydrides were tested with p_c of 16 bar. Aluminum hydride, lithium aluminum hydride and tri–lithium aluminum hydride were tested. Due to high reactivity and reduced chemical compatibility, $LiAlH_4$ and Li_3AlH_6 were tested exclusively in combination with SW–matrix. Moreover, standard formulation of SW fuel was modified eliminating SA in order to avoid possible reactions with lithium–containing hydrides (see Chapter 3, Section 3.3.4). The tested aluminum hydride exhibited no apparent incompatibility with standard HTPB and SW fuel formulations.

6.5.1 HTPB and SW Fuels Loaded with AlH_3

HTPB and SW fuels loaded with 11.2% AlH_3 were tested under GOX with p_c of 16 bar.

Three burning tests were performed on HTPB loaded with Alane. Combustion of alane–doped fuel revealed the presence of several CCP detaching from the regressing surface of the strand, see Figure 6.28. Results for the ballistic characterization of this fuel show no additive influence on measured r_f. These results contrast with previous findings achieved with the 2D radial–burner under different operating conditions [35]. In particular, in previous tests oxidizing mixtures O_2–N_2 were used instead of GOX. Therefore combustion tests were performed on AlH_3–doped HTPB under 70% O_2 + 30% N_2 in order to evaluate the possible effect of some interaction between fuel/oxidizer due to the presence of nitrogen. Achieved results are reported in Figure 6.29, where also HTPB burning under GOX is reported. Under the investigated conditions at G_{ox} of 380 $kg/(m^2s)$, alane–loaded fuel exhibits a marked r_f increase with respect to HTPB of 57%. Due to relatively high sensitivity to G_{ox}, this r_f enhancement decreases as oxidizer flux increases, see Figure 6.30. Ballistic performance of HTPB loaded with alane burning under 70% O_2 reveals a regression rate increases with respect to HTPB burning in GOX for $G_{ox} > 330$ $kg/(m^2s)$. This findings suggest a possible interaction between tested AlH_3 and nitrogen under the investigated conditions. Reactions as nitridation are studied in the literature for combustion of aluminum in air, [118][119]. High sensitivity of performance of alane–doped fuel from G_{ox} is probably related to the relatively large particle dimension of hydride crystals (50 μm, see Section 3.3.4) hindering heat release close to the regressing surface as oxidizer mass flux decreases.

SW fuel loaded with Alane was tested only under GOX due to limited availability of material. Ballistic characterization is reported in Figure 6.5.2. Significant $\Delta r_{f,\%}$ is achieved by SW loaded with AlH_3 with respect to baseline (HTPB). For G_{ox} of 250 $kg/(m^2s)$ ballistic of SW doped with AlH_3 exhibits a $\Delta r_{f,\%}$ of 324%, while standard SW provides a regression rate increase of 220%. As shown by data reported in Table 6.19 sensitivity of alane–doped SW results similar to the one of standard paraffin wax formulation.

Table 6.19: HTPB and SW fuels loaded with 11.2% AlH_3 burning in GOX with p_c of 16 bar, power law approximation of r_f vs. G_{ox} (ensemble average, Eq. 6.2).

Fuel, Ox, p_c	a_r	n_r	R^2, Eq. 6.2
HTPB + 11.2% AlH_3, GOX, 16 bar	0.044±0.014	0.529±0.062	0.800
HTPB + 11.2% AlH_3, 70%O_2, 16 bar	0.006±0.003	0.879±0.105	0.802
SW + 11.2% AlH_3, GOX, 16 bar	0.038±.0009	0.785±0.046	0.963

6.5.2 SW Loaded with $LiAlH_4$ and Li_3AlH_6

Results achieved in the ballistic investigation on tested double hydrides, $LiAlH_4$ and Li_3AlH_6, are reported in Figure 6.5.2, and Tables 6.20–6.21. A SW formulation without SA is used for manufacturing of fuels loaded with double hydrides due to reactivity of these materials with this (weak) acid. Under the investigated conditions, with HTPB as baseline, $LiAlH_4$–loaded fuel exhibited $\Delta r_{f,\%}$ of 448% at G_{ox} of 200 $kg/(m^2s)$. Under similar oxidizer mass flux, SW loaded with 5% Li_3AlH_6 provides a regression rate increase of 314% , while for G_{ox} of 350 $kg/(m^2s)$, a $\Delta r_{f,\%}$

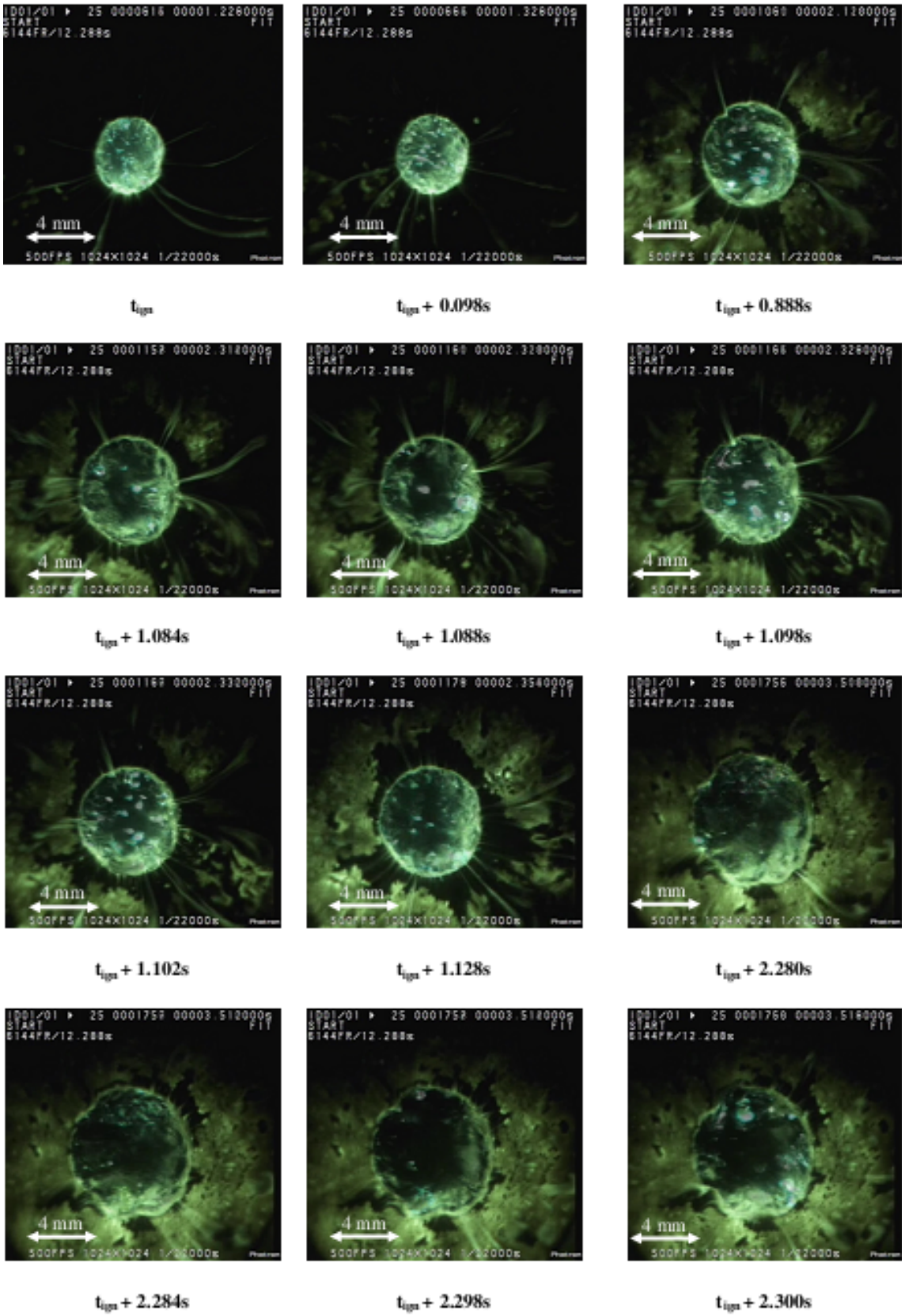

Figure 6.28: HTPB loaded with 11.2% AlH_3 burning in GOX with p_c of 16 bar, combustion sequence showing CCP detaching from strand surface.

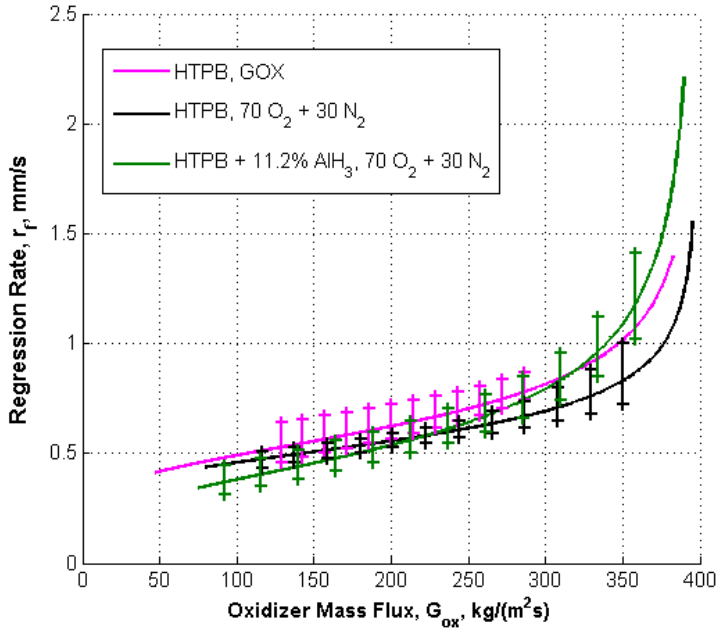

Figure 6.29: HTPB loaded with 11.2% AlH_3 burning in 70% O_2 + 30% N_2 with p_c of 16 bar, rf vs. G_{ox} (ensemble average). Note high r_f enhancement of alane–doped fuel burning in nitrogen–containing atmosphere with respect to HTPB under similar conditions and notably in GOX.

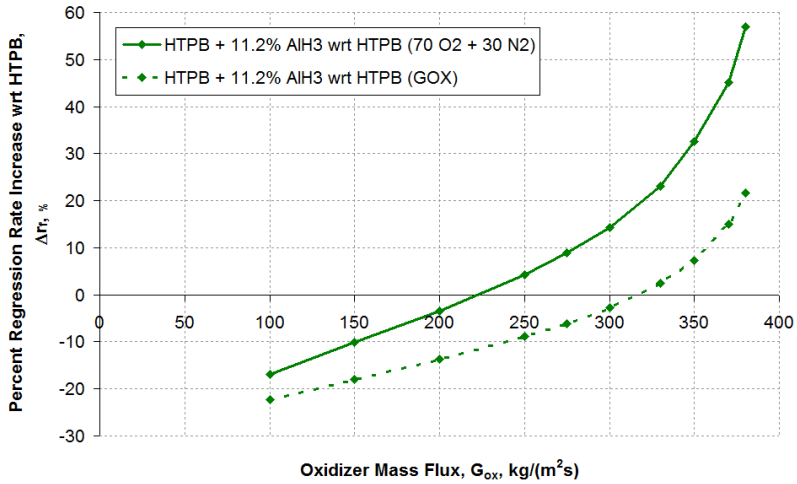

Figure 6.30: HTPB loaded with 11.2% AlH_3 burning under 70% O_2 + 30% N_2 with p_c of 16 bar, percent regression rate increases vs. G_{ox}. Two different reference condtions are used to evaluate $\Delta r_{f,\%}$: HTPB burning in 70% O_2 + 30% N_2 (solid line), and HTPB burning in GOX (dashed line).

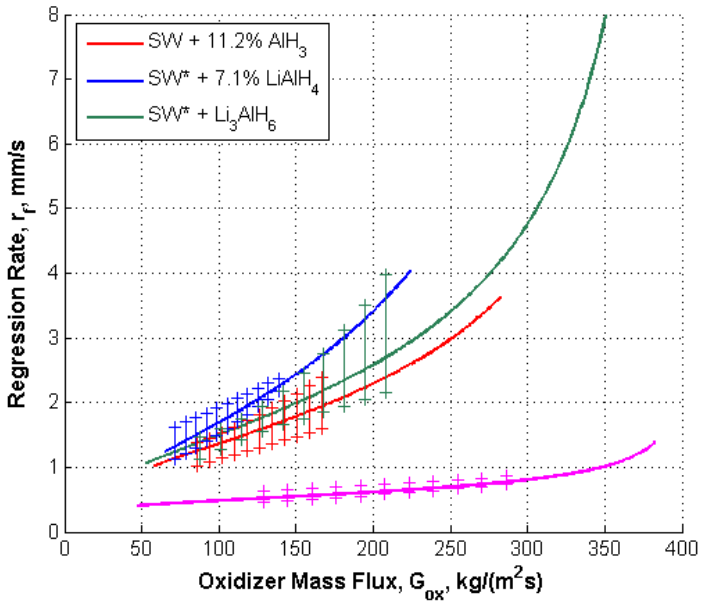

of 680% is achieved. Figure 6.31 provides an overview of $\Delta r_{f,\%}$ as a function of G_{ox} for the considered additives. Marked regression rate enhancement characterizing these fuel is related to hydrides reactivity (see Chapter 3, Section 3.3.5). Nevertheless ignition/dehydrogenation temperatures are not the only parameters influencing the process. High reactivity (low T_{ign}) can explain the performance enhancement of $LiAlH_4$, nevertheless under the investigated conditions AlH_3 provides better performances than Li_3AlH_6, though its ignition/dehydrogenation temperatures are higher than those of Li_3AlH_6, as illustrated in Figure 6.31. In the latter image, a comparison between SW–based fuels is presented. In particular, regression rate enhancement of hydride loaded fuels is evaluated with respect to the ballistics of corresponding SW–binder. As can be seen, $LiAlH_4$ delivers the highest r_f, nevertheless alane appears more effective than $LiAlH_6$ in enhancing SW–regression rate.

Table 6.20: SW fuels loaded with $LiAlH_4$ and Li_3AlH_6 burning in GOX with p_c of 16bar, power law approximation of r_f vs. G_{ox} (ensemble average), see Eq. 6.2. High data fitting for $LiAlH_4$ data due high port consumption at ignition (see Figure 6.5.2).

Fuel, p_c	a_r	n_r	R^2, Eq. 6.2
SW + 7.1% $LiAlH_4$, 16 bar	0.021±0.004	0.960±0.041	0.984
SW + 5% Li_3AlH_6, 16 bar	0.016±0.007	0.994±0.085	0.889

6.6 Conclusion

Ballistic investigation was performed on HTPB– and SW–based fuel formulations by a time–resolved technique for regression rate measurement. Combustion tests were performed mainly in GOX, for oxidizer mass flow of 210 nlpm [corresponding to initial G_{ox} of 400 $kg/(m^2s)$] and p_c in

Table 6.21: SW fuels loaded with $LiAlH_4$ and Li_3AlH_6 burning in GOX with p_c of 16bar, averaged $\Delta r_{f,\%}$ and its standard deviation for 100 $kg/(m^2s)$ < G_{ox} < 300 $kg/(m^2s)$.

Fuel, p_c	$\Delta r_{f,\%}$	$\xi(\Delta r_{f,\%})$
SW + 7.1% $LiAlH_4$, 16 bar	343	102
SW + 5% Li_3AlH_6, 16 bar	259	55

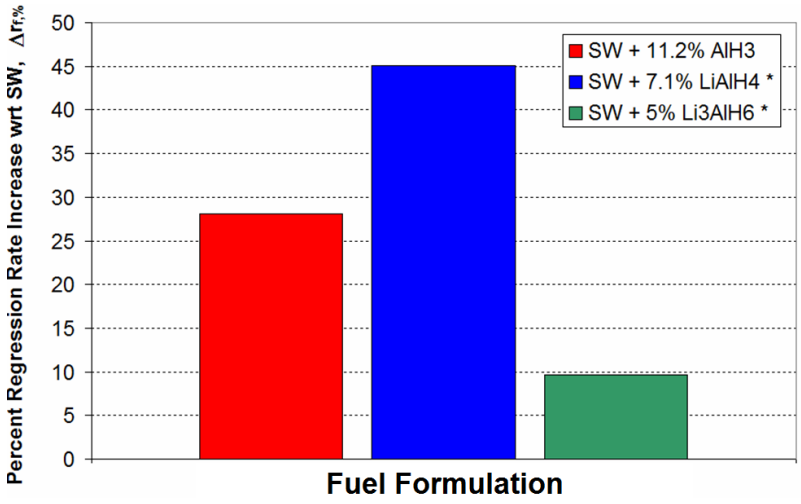

Figure 6.31: SW–based fuels loaded with hydrides burning in GOX with p_c of 16 bar and G_{ox} of 200 $kg/(m^2s)$, regression rate increase with respect to corresponding non–loaded SW formulation (*SW binder formulation without SA).

the range from 7 to 16 bar.

Ballistics of HTPB fuel was detailed investigated, revealing a dependency of r_f from G_{ox} ($r_f \alpha G_{ox}^{0.5-0.8}$), but independency from p_c. HTPB was considered as baseline for relative ballistic grading of different fuel formulations. SW–based fuel, tested for p_c in the range 7–16 bar revealed significant $\Delta r_{f,\%}$ ranging from 100% to 550% over the investigated range. Ballistics of SW formulation revealed a strong dependency from p_c, with regression rate decreasing for increasing chamber pressure.

A variety of energetic additives, selected due to of their attractive characteristics, were tested in order to evaluate their effect on regression rate of both HTPB– and SW–based fuels. An overview of the achieved results is given in Table 6.22 (HTPB–based fuels) and in Table 6.23, where time–averaged regression rate increases with respect to baseline are reported for selected values of the time–averaged oxidizer mass flux.

Considering the whole set of experimental results reported in Table 6.22, MgB90 (20% Mg) presents interesting characteristics because of the high regression rate enhancement achieved over the whole investigated range. Under the investigated conditions, for $<G_{ox}>$ of 300 $kg/(m^2s)$, time–averaged regression rate increase is the highest of the tested HTPB–based formulation (see Table 6.22). Moreover, performance enhancement of MgB90 (20% Mg) exhibits low dependence from oxidizer mass flux changes. These features make MgB90 (20% Mg) an attractive candidate for performance enhancement of solid fuels. When considering overall performance increase, also VF–ALEX$_{APS}$ shows promising characteristics, due to its behavior for low oxidizer mass flux values ($\Delta < r_{f,\%} >$ increases for decreasing $<G_{ox}>$). Tests performed on alane–doped fuel formulation revealed a possible interaction between this additive and nitrogen under the investigated conditions. With an oxidizing mixture 70% O_2 + 30% N_2 HTPB loaded with 11.2% AlH_3 revealed a significant r_f enhancement with respect to the tests conducted on the same formulation under GOX. Nevertheless, ballistics of HTPB loaded with AlH_3 is characterized by a strong dependence from oxidizer mass flux (probably due to large crystal dimension, 50 μm), thus hindering the average regression rate increase reported in Table 6.22.

Under the investigated conditions, SW–based fuels exhibited significant regression rate enhancement, see Table 6.23. In spite of high data scattering, standard SW fuel revealed a strong influence of p_c on measured r_f.

SW–loaded formulations were tested in order to evaluate the performance of additives exhibiting poor compatibility with HTPB and, in particular, $LiAlH_4$ and Li_3AlH_6. The former exhibited significant regression rate increases, strongly influenced by $<G_{ox}>$ as shown in Table 6.23. Under the investigated conditions, alane–doped SW exhibited lower regression rate increases with respect to lithium aluminum hydride (also considering the SW–binder formulation effect, as shown

Table 6.22: Overview of relative ballistic grading with respect to baseline for HTPB–based solid fuel formulations, time–averaged regression rate increases ($\Delta < r_{f,\%} >$) for selected <G_{ox}>. Note high $\Delta < r_{f,\%} >$ of MgB90 (20% Mg) over the investigated range and remarkable VF–$ALEX_{APS}$ performance for low <G_{ox}>.

	$<\mathbf{G}_{ox}>, kg/(m^2 s)$		
Fuel, $\mathbf{p}_c$	150	200	300
HTPB + 10% ALEX + 2% C, 10bar	3.5	10	28
HTPB + 10% L–$ALEX_{NPS}$ (50 nm)+ 2% C, 10bar	NA	13	38
HTPB + 10% L–$ALEX_{NPS}$ (100 nm) + 2% C, 10bar	-1.1	-7.8	18
HTPB + 10% L–$ALEX_{APS}$ (100 nm)+ 2% C, 10bar	8.6	17	49
HTPB + 10% F–$ALEX_{APS}$ + 2% C, 10bar	14	21	52
HTPB + 10% VF–$ALEX_{APS}$, 10bar	33	24	26
HTPB + 5% nFe + 1% C, 10bar	NA	6.5	4.6
HTPB + 2.5% MgB90 (10%Mg), 16bar	NA	-13	-7.1
HTPB + 2.5% MgB95 (10%Mg), 16bar	27	29	32
HTPB + 2.8% MgB90 (20%Mg), 13bar	39	44	54
HTPB + 11.2% AlH_3, 16bar[a]	-16	-1[b]	18[b]
	NA	-11[c]	0.0[c]

[a] Tested in 70% O_2 + 30% N_2
[b] $\Delta < r_{f,\%} >$ wrt HTPB in 70% O_2 + 30% N_2
[c] $\Delta < r_{f,\%} >$ wrt HTPB in GOX

in Figure 6.31). This effect is probably due to the relative large size of alane crystals and its higher dehydrogenation temperature with respect to $LiAlH_4$. In this respect $< \Delta r_{f,\%} >$ achieved by SW–doped with MgB90 (20% Mg) appear particularly attractive since this additive provides performance similar to the one of alane under the investigated conditions.

Table 6.23: Overview of relative ballistic grading with respect to baseline for SW–based solid fuel formulations, time–averaged regression rate increases ($\Delta < r_{f,\%} >$) for selected <G_{ox}>. Note high $\Delta < r_{f,\%} >$ achieved by $LiAlH_4$.

	$< \mathbf{G}_{ox}>, kg/(m^2 s)$		
Fuel, $\mathbf{p}_c$	150	200	300
SW, 7 bar	250	311	485
SW, 13 bar	203	226	NA
SW, 16 bar	163	190	255
SW[a], 16bar	235	270	NA
SW + 2.8% MgB90 (20% Mg), 13 bar	212	268	432
SW + 11.2%AlH_3, 16 bar	224	265	NA
SW[a] + 7.1% $LiAlH_4$, 16 bar	336	432	NA
SW[a] + 5% Li_3AlH_6, 16 bar	276	335	494

[a] SW without SA

CHAPTER 7

BALLISTIC INVESTIGATION: NUMERICAL SIMULATION

Ballistic characterization of HTPB fuel revealed a r_f independence from p_c under the investigated conditions (see Chapter 6, Section 6.1). Considering possible influence of radiative heat transfer and solid fuel fragmentation particularly toward the end of the combustion process [G_{ox} < 120 kg/(m^{2}s)], time–resolved data exhibit a strong dependence on G_{ox}. This experimental evidence suggests that under the investigated conditions r_f is ruled mainly by convective heat–transfer from the flame zone to the regressing surface (at least for high G_{ox} values). Starting from the achieved experimental results, providing an insight of the evolution in time of instantaneous regression rate of the solid fuel, a numerical investigation was conducted with the aim of providing an estimation of the latter parameter under the investigated conditions. The model considers the combustion of non–doped solid fuels, without entrainment and is based on convective heat transfer in the boundary layer. Considering operating conditions and initial diameter of central port perforation, convective heat transfer coefficient is evaluated considering G, surface roughness and accounting for blockage effect caused by fuel pyrolysis. The model concentrates on the r_f, without considering the possible performance of the complete system.

The original formulation of the proposed model is due to Greatrix [120] and is based on the work of Marxman et al. [6][7][8] and Smoot and Price [48].

In this phase of the investigation the original model developed by Greatrix is modified. Effective values of the thermophysical parameters (T_{fl}, $C_{p,g}$, k_g and μ_g) will be evaluated starting from experimental data.

7.1 Convective Heat Transfer: Modeling

7.1.1 Greatrix Model: Introduction

Aim of the numerical approach proposed by D.R. Greatrix is to relate heat feedback from flame to the surface under quasi–steady conditions in order to evaluate the r_f considering a convective heat transfer regime. Under the assumption of a quasi–steady regime for the solid fuel burning, standard flow oxidizer injection is considered for the definition of the fluid dynamic parameters involved in problem formulation. Geometry of the system (cylindrical grain, slab) is considered in the model by proper definition of Re [120].

Under the specified hypothesis, neglecting conduction in depth of the solid fuel grain and radiative heat flux effects, energy balance at solid fuel grain regressing surface can be written

according to Eq. 7.1. In the latter, the heat flux from the flame to the surface causes fuel pyrolysis and therefore regression of the surface. This equation is the same starting point of the model developed by Marxman et al. [6] (see Section 2.2.1).

$$\rho_f \, r_f \, [C_s \, (T_w \, - \, T_{s,in}) \, - \, \Delta h_{f,w}] \, = \, \eta \, (T_{fl} - T_w) \tag{7.1}$$

In Eq. 7.1 the convective heat transfer term is evaluated considering the mass injection from the regressing surface into the boundary layer. This mass injection in the transversal direction (with respect to oxidizer mass flow) causes a reduction in the wall friction coefficient that, in turn, is related to a reduction in the convective heat transfer coefficient. A proper correction will be introduced on the term η in order to consider this effect with respect to the value achieved in absence of blowing, η^*. The term $\Delta h_{f,w}$ is defined by Greatrix as the net surface heat of reaction, and is assumed to be absorbed by the condensed phase (thus resulting positive/negative for exothermic/endothermic reactions) [120]. In order to evaluate energy transfer from the flame zone to the regressing surface, an energy balance for the region limited by these two boundaries should be considered. This latter balance is expressed in Eq. 7.2. The latter Eq. 7.2 is accompanied by the boundary conditions reported in Eq. 7.3 and Eq. 7.4 specifying temperature values for the regressing surface and the flame zone.

$$\rho_f \, r_f \, Cp \, \frac{dT(y)}{dy} \, = \, k_g \frac{d^2T(y)}{dy^2}, \, 0 < y < \delta_{fl} \tag{7.2}$$

$$T(y \, = \, 0) \, = \, T_w \tag{7.3}$$

$$T(y \, = \, \delta_f) \, = \, T_{fl} \tag{7.4}$$

The latter equations are valid considering the absence of surface reactions involving the gas phase. Solution of Eq. 7.2 yields to the following expression for the temperature profile

$$T(y) \, = \, T_w \, + \, (T_{fl} - T_w) \cdot \frac{e^{(\rho_f r_f C_{p,g} y / k_g)} - 1}{e^{(\rho_f r_f C_{p,g} \delta_{fl} / k_g)} - 1}, \, 0 < y < \delta_f. \tag{7.5}$$

Under quasi–steady condition, continuity of heat–flux at the interface between solid and gas phases can be written according to Eq. 7.6 (recalling Eq.7.1 for surface energy balance). The derivative of T(y) featuring in Eq. 7.6 can be simply evaluated starting from Eq. 7.5: the achieved expression at the gas–side of the surface can be expressed as reported in Eq. 7.7.

$$k_g \frac{dT(y=0)}{dy} \, = \, \eta \, (T_{fl} - T_w) \, = \, \rho_f \, r_f \, [Cs \, (T_w \, - \, T_{s,in}) \, - \, \Delta h_{f,w}] \tag{7.6}$$

$$\frac{dT(y=0)}{dy} = (T_{fl} - T_w) \frac{\rho_f r_f C_{p,g} / k_g}{e^{(\rho_f r_f C_{p,g} \delta_{fl} / k_g)} - 1} \tag{7.7}$$

With the available data, the thickness of the reference energy zone, δ_{fl} can now be evaluated. In order to achieve this result, the balance given in Eq. 7.6 is considered in the form reported in Eq. 7.8. The achieved result is reported in Eq. 7.9.

$$k_g \frac{dT(y=0)}{dy} \, = \, \rho_f \, r_f \, [Cs \, (T_w \, - \, T_{s,in}) \, - \, \Delta h_{f,w}] \tag{7.8}$$

$$\delta_{fl} = \frac{k_g}{\rho_f r_f C_{p,g}} log[1 + \frac{C_{p,g}(T_{fl} - T_w)}{C_s(T_w - T_{f,in}) - \Delta h_{f,w}}] \tag{7.9}$$

Similarly, considering Eq. 7.6, and the convective heat flux term (right side term of Eq. 7.1), an expression for the effective convective heat transfer coefficient can be achieved, see Eq. 7.10.

$$\eta = k_g \frac{dT(y=0)}{dy} \frac{1}{(T_{fl} - T_w)} = \frac{\rho_f r_f C_{p,g}}{e^{(\rho_f r_f C_{p,g} \delta_{fl}/k_g)} - 1} \tag{7.10}$$

In the case of zero transpiration η can be expressed as $\eta^* = k_g/\delta_{fl}$, [120]. Substitution of this latter result in Eq. 7.10 yield to a relationship between convective heat transfer coefficients in presence/absence of blowing reported in Eq.7.11 and originally developed by Mickeley et al. [120] [121].

$$\eta = \frac{\rho_f r_f C_{p,g}}{e^{(\rho_f r_f C_{p,g} \eta^*)} - 1} \tag{7.11}$$

As can be seen by Eq. 7.11 (or by similar formulations considered in Section 2.2.1), solid fuel regression affects convective heat transfer causing a reduction for η with respect to the case with absence of blowing. The convective heat transfer coefficient in the absence of blowing can be evaluated by Reynolds' analogy for heat– and momentum–transfer at the regressing surface of the solid fuel grain. In order to do this, friction factor should be determined. The Darcy–Weiesbach friction factor for turbulent flow can be determined by the semi–empirical expression developed by Colebrook (see Eq. 7.12). Then η^* can be evaluated by Eq. 7.13.

$$C_F^* = \sqrt{-2 \cdot log_{10}(\frac{2.51}{Re_D (C_F^*)^{1/2}} + \frac{\epsilon_{rough}/D}{3.7})} \tag{7.12}$$

$$\eta^* = \frac{C_{p,g} \tau_w^*}{Pr^{2/3} u_e} = \frac{C_{p,g}^{1/3} k_g^{2/3} G C_F^*}{8 \mu^{2/3}} \tag{7.13}$$

For developing flow convective heat transfer coefficient can be evaluated according to Eq. 7.13 with a properly modified equation for the friction factor. In particular the semi–empirical correlation reported by Munson et al. [120] can be used, see Eq. 7.14. When dealing with compressibility effects due to local Mach number values, a proper correction of the friction coefficient can be performed by Eq. 7.15, [120][124].

$$C_F^* = 4[1.89 - 1.62 log_{10}(\epsilon_{rough}/x)]^{-\frac{5}{2}} - 7.04[1.89 - 1.62 log_{10}(\epsilon_{rough}/x)]^{-\frac{7}{2}} \tag{7.14}$$

$$\frac{C_{F,incompressible}^*}{C_{F,compressible}^*} = 1 + [Pr^{\frac{1}{3}} Ma^2 \frac{\gamma - 1}{2}] \tag{7.15}$$

Finally, due to substitution in Eq. 7.1 of the result achieved by Eq. 7.13, the expression of regression rate is derived (see Eq. 7.16).

$$r_f = \frac{\eta^*}{\rho_f C_{p,g}} log[1 + \frac{C_{p,g}}{C_s} \frac{(T_{fl} - T_w)}{(T_w - T_{f,in} - \Delta h_{f,w}/C_s)}] \tag{7.16}$$

The latter equation relates the convective heat transfer coefficient in the absence of blowing, η^*, to the r_f by considering thermochemical parameters of the propellant under the considered operating conditions.

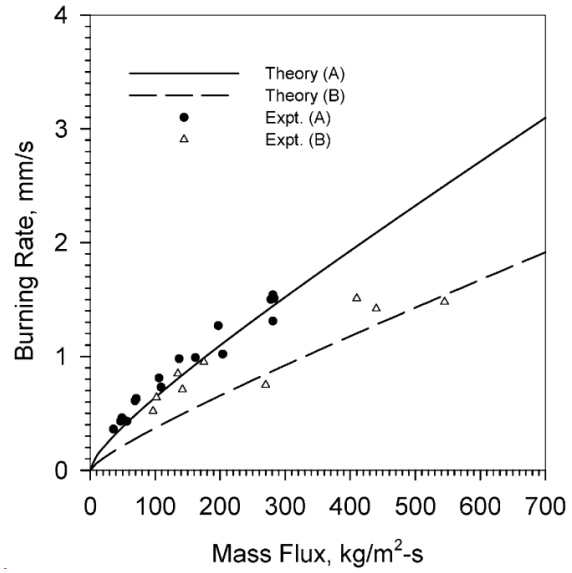

Figure 7.1: HTPB burning under GOX, experimental data (Expt.) and result by application of Eq. 7.16 (Theory), [120]. Experimental data from [5].

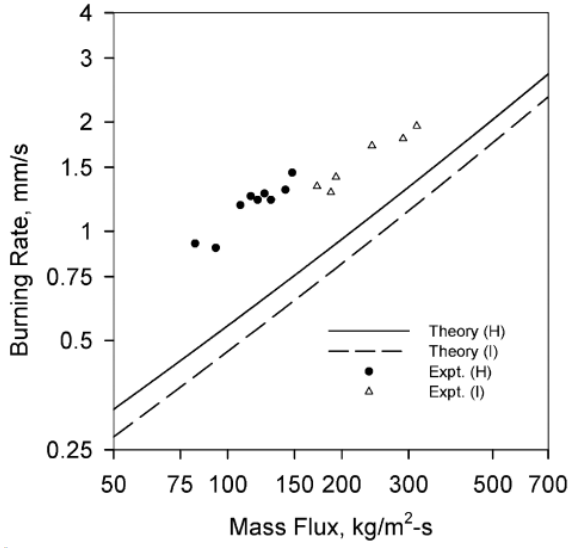

Figure 7.2: HTPB burning under GOX, experimental data (Expt.) and result by application of Eq. 7.16 (Theory), [120]. Experimental data from [123].

Table 7.1: Data and engine characteristics for Eq. 7.16, [120] (see Figure 7.1 and Figure 7.2)

Property	**Test A**	**Test B**	**Test H**	**Test I**
ρ_f, kg/m^3	920	920	920	920
$C_{p,g}$, $J/(kgK)$	1920	1920	1920	1920
C_s, $J/(kgK)$	2100	2100	2100	2100
$T_{s,in}$, K	293	293	293	293
T_{fl}, K	3000	3000	3000	3000
T_w, K	950	950	950	950
R, $J/(kgK)$	320	320	320	320
μ, Ns/m^2	$8{\cdot}10^{-5}$	$8{\cdot}10^{-5}$	$8{\cdot}10^{-5}$	$8{\cdot}10^{-5}$
k_g, $W/(mK)$	0.2	0.2	0.2	0.2
ϵ_{rough}, μm	5	5	5	5
D, mm	11	115	20	40

7.1.2 Greatrix Model: Comments

In his analysis Greatrix develops a convective heat transfer model based on an energy balance at regressing surface (under quasi–steady conditions). Application of Eq. 7.16 to experimental data for HTPB/GOX is reported in Figure 7.1 and Figure 7.2 (see Table 7.1 for input data). Greatrix model provides a good agreement with the experimental data of the A series, while a minor agreement is found for B, H and I series. In particular, considering the differences for model agreement with data from the A and the B series, different measurement procedures for r_f determination are invoked. In the A series measured diameter is the exact value at regression rate measurement, while data of the B series are evaluated considering a single averaged port diameter for the solid grain, possibly corresponding to a lower port diameter than the one characterizing the considered r_f, [120]. For data of the H and I series, differences between experimental data and model prediction (with the model underevaluating the measured r_f) is explained considering possible swirl flow effects of the test rig injector [120]. Data of the H and I series are from PSU. During a comparison between experimental data achieved by this latter laboratory and Stanford University for the same propellant (SW/GOX) and grain configuration, r_f measured with PSU resulted 50% higher than the corresponding Stanford datum [120]. This experimental finding seems to support the hypothesis of some induced swirl in PSU experimental facility. SPLab test rig is characterized by an injection system enabling both standard and swirl flow injections (see Chapter 4, Section 4.1). Considered tests are performed with a standard injector configuration.

The parameter $\Delta h_{f,w}$ comparing at the right side of Eq. 7.1 is not explicitly quantified in the analysis conducted by Greatrix (see Table 7.1) though it is asserted that, according to data achieved in experimental investigation of solid propellants, its value should be relatively small [120]. Nevertheless while the latter consideration can be valid for solid propellants, inert binders filled with additives or active binders (as GAP) it could be stressed when considering inert binders as HTPB whose pyrolysis (also under hybrid rocket conditions) results endothermic (in spite of possible exothermic steps in pyrolysis under low heating rates) [132] [133].

Fully developed boundary layers are considered for data treatment in [120], therefore convective heat transfer is evaluated considering the Darcy–Weiesbach friction coefficient defined according to Eq. 7.12. No detailed information is given about the listed thermochemical data considered for propellant characterization (see Table 7.1).

7.2 Improvements to the Original Convective Model

According to what originally proposed by Marxman et al. [6][7][8], the energy balance reported in Eq. 7.1 is considered as a starting point for the numerical investigation. Considering a convective heat transfer driven phenomenon, description of the regressing process can be achieved by Eq. 7.16. The numerical investigation will focus on HTPB/GOX. Time–resolved data

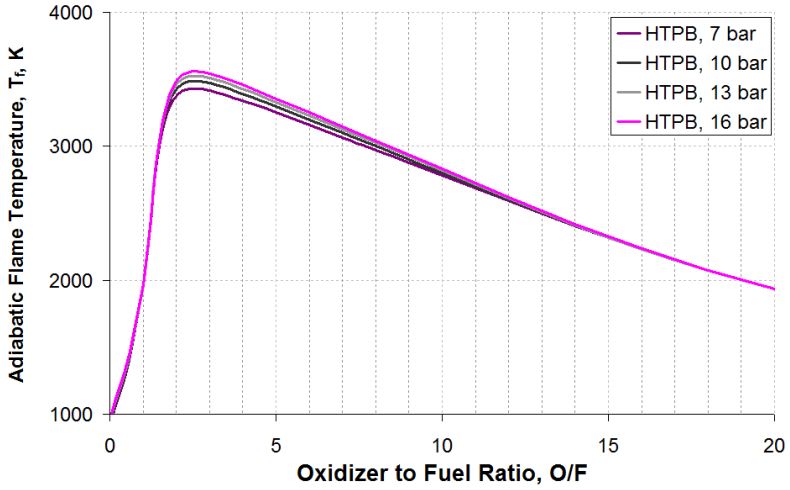

Figure 7.3: Adiabatic T_{fl} vs. O/F for HTPB burning under GOX with p_c ranging from 7 to 16 bar. Under the investigated range of p_c small changes in flame temperature are achieved.

for HTPB burning under GOX for p_c in the range from 7 to 16 bar will be considered in the analysis, and G will be considered in order to characterize the flow into the central port channel (see Table 6.3 and Table 6.4). The model aims to determine the r_f of the solid fuel under standard flow condition. Further details on the effect of non–standard injection of oxidizer are discussed in [11] [21] [23] (see Chapter 2, Section 2.3.1).

The proposed approach focuses on the energy balance between the flame zone and the regressing surface. Effective values of the thermochemical parameters will be defined considering a semi–empirical approach. In the latter the actual, instantaneous O/F of the performed tests will be considered as starting point for the evaluation of the reuired thermophysical parameters.

7.2.1 Thermochemical Investigation of HTPB/GOX

In order to properly evaluate data related to HTPB/GOX combustion, thermochemical calculations were conducted by NASA CEA2 code [127] [128]. In the thermochemical analysis data for cured HTPB were taken from [129]. Combustion problem was run for p_c from 7 to 16 bar and O/F in the range from 0.1 to 20. Aim of this investigation was to evaluate thermochemical parameters considering O/F ratio spanning from a surface condition, with fuel rich environment, to the actual global O/F for performed tests (see Figure 7.7). As testified by trend reported in Figure 7.7, O/F for the ensemble average curves is characterized by a non–monotone trend in G. The achieved behavior is related to two different trends characterizing r_f and $\dot{m}_f$ during diameter evolution in time. While the first parameter exhibits a monotone decrease for increasing time (and port diameter), $\dot{m}_f$ presents a more complex behavior due to the influence of both r_f and $\bar{D}(t)$ (see Eq. 7.17).

$$\dot{m}_f(t) = \rho_f \cdot A_b \cdot r_f = \rho_f \cdot \pi L_{port} \bar{D}(t) \cdot r_f = \rho_f \cdot \pi L_{port} [D_0 + a_D (t - t_0)^{n_D}] \cdot r_f,\ t \geq t_{ign} > t_0 \quad (7.17)$$

A summary of the achieved results is presented in Figure 7.3–7.6. For a given O/F ratio, small changes of T_{fl} are achieved under the considered operating conditions. These differences of calculated values with respect to different considered p_c are less influent for O/F≅1, and O/F≥12, see Figure 7.3. As shown by results reported in Table 7.2 for a given O/F, flame temperature exhibits a general increasing trend for increasing p_c.

According to the model developed by Marxman et al., hybrid flame is established in the boundary layer, where fuel and oxidizer meet at stoichiometric ratio. Experimental observation show that flame is established in the boundary layer, covering a finite zone whose boundaries are

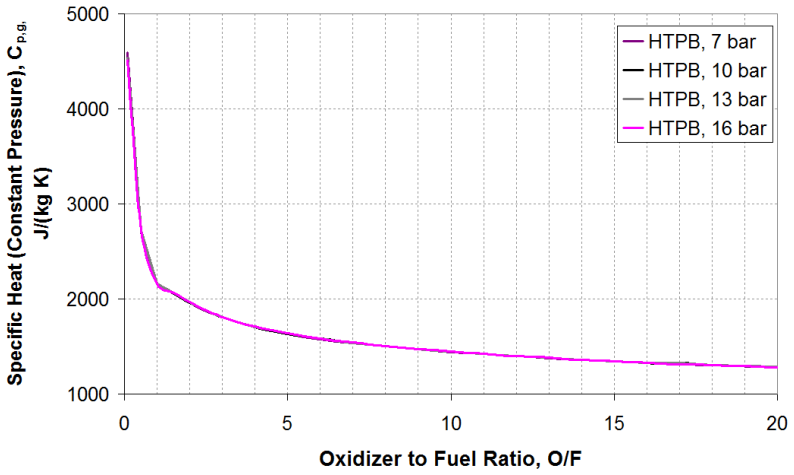

Figure 7.4: $C_{p,g}$ vs. O/F for HTPB burning under GOX with p_c ranging from 7 to 16 bar as evaluated by NASA CEA2 code.

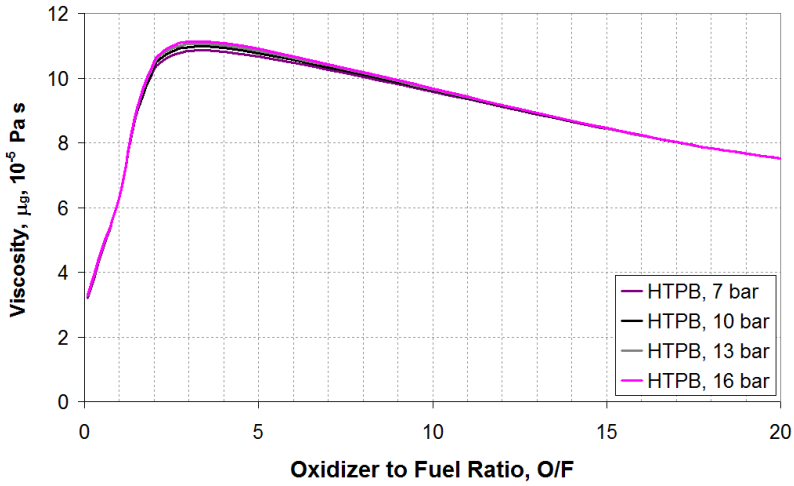

Figure 7.5: μ_g vs. O/F for HTPB burning under GOX with p_c ranging from 7 to 16 bar as evaluated by NASA CEA2 code.

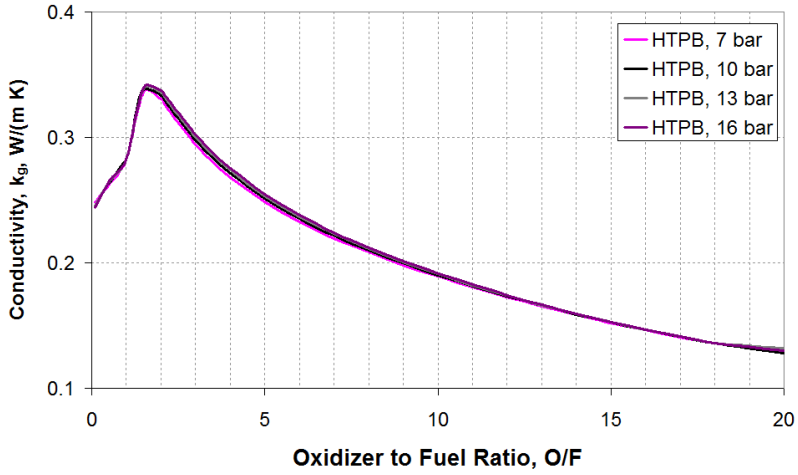

Figure 7.6: k_g vs. O/F for HTPB burning under GOX with p_c ranging from 7 to 16 bar as evaluated by NASA CEA2 code.

Table 7.2: HTPB under GOX for p_c ranging from 7 to 16 bar, thermochemical parameters as evaluated by NASA CEA2 Code for the stoichiometric condition (maximum value of T_{fl}).

Fuel, p_c	**O/F**	**T_{fl}, K**	**$C_{p,g}$, J/(kgK)**	**k_g, W/(mK)**	**μ, Ns/(m^2)**
HTPB, 7 bar	2.5	3431	1874	0.312	$10.7 \cdot 10^{-5}$
HTPB, 10 bar	2.6	3485	1861	0.312	$10.8 \cdot 10^{-5}$
HTPB, 13 bar	2.5	3526	1864	0.315	$10.9 \cdot 10^{-5}$
HTPB, 16 bar	2.6	3558	1865	0.316	$11.0 \cdot 10^{-5}$

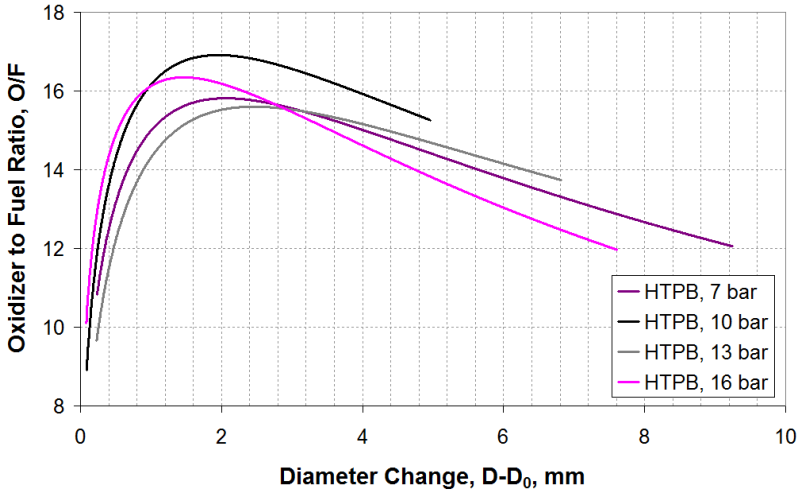

Figure 7.7: HTPB burning under GOX for p_c ranging from 7 to 16 bar, O/F as a function of central port diameter change during combustion. Note the non–monotone trend related to r_f decrease and vaporization surface increase corresponding to diameter increase in time.

given by the flammability limits of the considered propellant mixture (see Figure 2.8 in Chapter 2, Section 2.2.1). In the proposed treatment an effective flame temperature is defined considering the actual O/F ratio characterizing the performed test (see Figure 7.7). A similar procedure is adopted for all thermo–physical parameters of Eq. 7.16. Considered data are reported in Figures 7.4–7.6.

7.2.2 Pyrolysis of HTPB

The term $\Delta h_{f,w}$ in Eq. 7.1, represents the net heat release at the regressing surface [120]. HTPB undergoes pyrolysis during combustion, with net absorption of heat. Pyrolysis of HTPB is detailed discussed in [130] [131] [132] [133]. In particular, differences in pyrolysis products for low and high heating rates ($<100K/s$ vs. $>100K/s$) are completely discussed in [130] [131]. The pyrolysis of HTPB under HRE operating conditions is extensively discussed in [132] where conductive heating is used to reproduce convective (and radiative) heat flux typical of HRE operating conditions. Comparing Arrhenius parameters for conductive heating under a nitrogen atmosphere at ambient pressure with those coming from engine firing at p_c in the range 26–41 bar (375–600 psi), Chiaverini et al. reported no significant influence of p_c on pyrolysis parameters. In spite of some possible different experimental results reported in the open literature concerning possible dependence from p_c of HTPB pyrolysis, [46], data from [130] [131] [132] indicates a possible limited influence of p_c on pyrolysis under operating conditions similar to those considered in present study. Considering this, the parameter $\Delta h_{f,w}$ in Eq. 7.1 is considered independent from p_c for HTPB under the investigated conditions, and its value is defined as -430 cal/g [133]. According to literature data, solid phase specific heat is taken as 2100 $J/(kgK)$ [120][133].

Surface temperature of HTPB under burning conditions is taken in the range 820 K – 1000K [111] [133].

7.3 Numerical Simulation: Operating Steps

Starting from thermochemical data presented in Figures 7.3–7.6 and pyrolysis data discussed in Section 7.2.2, a convective heat model, based on Eq. 7.16 was implemented for the considered HTPB/GOX system. In order to get a better understanding of the phenomena involved in the complex hybrid combustion process, effective values of the thermochemical parameters are considered in the analysis. The latter are defined considering the overall, actual O/F ratio characterizing the combustion process during the performed tests. The overall O/F value is defined considering time–resolved data achieved during the experimental sessions (see Figure 7.7). This definition of the effective parameters enables a semi–empirical approach to the numerical problem.

In order to evaluate the r_f according to the modified Eq. 7.16, the convective heat transfer coefficient without blowing must be determined (see Eq. 7.13). Considering experimental evidences showing relatively uniform r_f for the whole regressing surface, [40][134][135], flow–field is assumed to be characterized by a fully developed turbulent boundary layer. Darcy–Weiesbach friction factor f^* can be therefore defined according to Eq. 7.12. As previously stated, T_w of 820 K and 1000 K will be considered [111] [133]; $\Delta h_{f,w}$ will be considered constant and its value will be given by -430 cal/g [133]. For the determination of the Re_D characterizing the phenomenon the total mass flux is considered. The latter is defined as sum of G_{ox} and G_f. Due to the use of G, it is convenient to define the ballistics of HTPB according to his parameter. Therefore, starting from data collected in Chapter 6, Eq. 7.18 will be considered for power law approximation.

$$r_f = a_r \cdot (G_{ox} + G_f)^{n_r} = a_r \cdot G^{n_r} \tag{7.18}$$

For the experimental data, parameters obtained by their approximation with Eq. 7.18 are given in Table 7.3 and Table 7.4. As can be seen by the collected data, HTPB burning under p_c of 16 bar is characterized by a relatively low value of the exponent n_r (see Table 7.3). This is due to the moderate r_f for high G_{ox} and other peculiar phenomena discussed in Chapter 6. As seen in HTPB ballistic characterization, for $G_{ox} < 120$ kg/(m^{2}s) combustion is characterized by influence of

Table 7.3: HTPB burning under GOX with p_c in the range 7–16 bar. Power law approximation for r_f vs. G.

Fuel, p_c	**a_r**	**n_r**	**R^2, Eq. 7.18**
HTPB, 7 bar	0.048 ± 0.005	0.504 ± 0.039	0.909
HTPB, 10 bar	0.015 ± 0.005	0.717 ± 0.066	0.872
HTPB, 13 bar	0.023 ± 0.006	0.650 ± 0.049	0.910
HTPB, 16 bar	0.051 ± 0.012	0.484 ± 0.043	0.883

Table 7.4: HTPB burning under GOX with p_c in the range 7–16 bar. Power law approximation for r_f vs. G [for $G \geq 140\ kg/(m^2 s)$].

Fuel, p_c	**a_r**	**n_r**	**R^2, Eq. 7.18**
HTPB, 7 bar	0.011 ± 0.003	0.774 ± 0.057	0.939
HTPB, 10 bar	0.005 ± 0.002	0.916 ± 0.087	0.887
HTPB, 13 bar	0.005 ± 0.002	0.904 ± 0.065	0.936
HTPB, 16 bar	0.016 ± 0.005	0.691 ± 0.061	0.907

possible radiative heat transfer and solid fuel fragmentation phenomena. Under the investigated conditions the latter value of oxidizer mass flux corresponds to G in the range 130–150 kg/(m^2s). Due to this, Table 7.4 reports coefficients a_r and n_r for the approximation of r_f by Eq. 7.18 over a limited range of G.

As previously stated, the convective model is developed for the combination HTPB/GOX. and considering geometry of the strands tested in the 2D radial burner (D_0, L_p). For a given operating conditions (that is, for given p_c and $\dot{m}_{ox}$), thermochemical and physical parameters are determined by NASA CEA2 Code considering experimental, time–resolved data concerning $\bar{D}$(t) and O/F(t) (see Figures 7.3–7.6).

The code developed for the numerical investigation of HTPB/GOX ballistics was developed in collaboration with M. Manzoni. In the following subsection, a detailed description of the processing steps is given.

Processing Steps for Numerical investigation on r_f

Starting point of the semi–empirical model are the ensemble average curve data concerning $\bar{D}(t)$, O/F(t) for the given operating condition identified by p_c and $\dot{m}_{ox}$. With these data available, the following operating steps are executed for each time t_i for which $t_{ign} \leq t_i \leq t_{fin}$.

1. The value of $\bar{D}(t_i)$ is considered as starting point for calculation of G_{ox} and G_f, considering the operating condition (p_c, $\dot{m}_{ox}$) and the value of O/F(t_i), see Eqs. 7.19–7.21

$$G_{ox}(t_i) = \frac{\dot{m}_{ox}}{\pi \frac{\bar{D}(t_i)^2}{4}} \tag{7.19}$$

$$G_f(t_i) = \frac{G_{ox}(t_i)}{O/F(t_i)} \tag{7.20}$$

$$G(t_i) = G_{ox}(t_i) + G_f(t_i) \tag{7.21}$$

2. Considering O/F(t_i), the proper value of the effective thermophysical parameters, $C_{p,g}$, k_g, and μ_g are evaluated by NASA CEA2 results (see Figure 7.3–7.6).

3. $Re_D[\bar{D}(t_i)]$ is defined according to Eq. 7.22 considering effetive thermophysical parameters defined in the previous step.

$$Re_D[\bar{D}(t_i)] = \frac{G(t_i) \cdot \bar{D}(t_i)}{\mu_g} \tag{7.22}$$

4. Starting from $Re_D[\bar{D}(t_i)]$, assuming values for ϵ_{rough} provided in [120], and considering the effective values for the thermochemical parameters, the convective heat transfer coefficient relative to the considered t_i, η_i^*, is determined by solution of the corresponding Eqs. 7.12, 7.13.

5. With the available parameters, $r_{f,i}$ is determined by Eq. 7.16.

6. Next step is evaluated, considering t_{i+1} and performing the previously listed operations (steps from 1 to 5).

In order to evaluate the achieved agreement between convective model and experimental results, the parameter $\Delta r_{f,\%}$ is introduced. This parameter is similar to the counterpart defined in the experimental investigation on the ballistics of different solid fuel formulations and provides the percent difference between experimental and convective model results evaluated with respect to the former value (that is considered as reference), see Eq. 7.23.

$$\Delta r_{f,\%} = 100 \cdot \frac{r_{f,Model} - r_{f,Experimental}}{r_{f,Experimental}} \tag{7.23}$$

7.4 Results and Discussion

Results achieved during the numerical investigation of the r_f of HTPB/GOX under convective regime for p_c ranging from 7 to 16 bar are presented in Figures 7.8–7.15. In the latter figures r_f vs. G and $\Delta r_{f,\%}$ vs. G evaluated for the two considered T_w (820 K and 1000 K) are presented. As early discussed, only ensemble average curve are considered for the numerical investigation.

Under the investigated conditions, Re_D evaluated considering effective values of thermophysical parameters ranges from $2.5 \cdot 10^4$ and $5 \cdot 10^3$. For the considered operating conditions, T_w of 820 K provides a better agremeent between numerical results and experimental data with respect to the other investigated surface temperature value of 1000 K.

A first remarkable result characterizes all the presented curves. As can be seen by the results achieved for the r_f vs. G trends of all the considered operating conditions, the experimental and the semi–empirical data are characterized by a similar behavior. The latter presents a marked r_f at the beginning of the test and an initial, steep decrease in r_f for decreasing G (and increasing diameter or time). This marked sensitivity of r_f to changes in G is then reduced as combustion proceeds for experimental data. Numerical data exhibits a slightly higher sensitivity to G decrease with respect to experimental trend. As a consequence, for decreasing G, $\Delta r_{f,\%}$ becomes more and more negative (numerical r_f being lower than experimental counterpart).

Considering the value $G(t_{ign})$ of each testing condition, results reported in Tables 7.5–7.6 are achieved for the parameter $\Delta r_{f,\%}$. Numerical results for T_w of 820 K exhibit a high agreement between experimental and numerical data with respcet to T_w of 1000 K. At ignition, Δr_f ranging from 6.5% and 0.5% percent are achieved for the considered ensemble average at the different chamber pressures. Considering a T_w of 820 K, the $\Delta r_{f,\%}$ indicates an underevaluation of r_f by the numerical model around 10% for mass fluxes ranging from ignition up to 280 kg/(m^{2}s) for all the considered operating conditions tested for HTPB/GOX. This result gains particular attention when considering that general power law approximation of r_f vs. G ususally considered in the literature is characterized by n_r values giving a different concavity with respect to measured time–resolved values [40][110], see Figure 6.4 in Chapter 6, Section 6.1. This achievement is mainly due to the definition of effective parameters for the evaluation of r_f in the numerical model, and,

Table 7.5: HTPB burning under GOX with p_c in the range 7–16 bar, values of $\Delta r_{f,\%}$ (see Eq. 7.23) for selected mass fluxes (T_w = 820 K). Note high agreement between experimental and numerical data at test ignition.

		$\Delta r_{f,\%}$	, **Eq. 7.23**
Fuel, p_c	**G(t_{ign})**	**250 kg/(m^{2}s)**	**100 kg/(m^{2}s)**
HTPB, 7 bar	3.4	-15	-41
HTPB, 10 bar	6.3	-15	-41
HTPB, 13 bar	5.5	-14	-41
HTPB, 16 bar	0.5	-14	-40

in particular to the use of O/F ratio as parameter to identify proper effective values of the T_{fl} and of the other thermophysical parameters, providing a good agreement in the achieved trends and, for high G, r_f values.

In spite of the excellent agreement achieved in the numerical approach for G $\geq$ 280 kg/(m^{2}s) and with effective values for T_w of 820 K, as combustion proceeds larger differences are achieved when comparing experimental and numerical data. From this point of view no difference is noticed in the numerical trends for the two considered T_w (see Tables 7.5–7.6). The parameter $\Delta r_{f,\%}$ becomes more and more negative as G decreases below 280 kg/(m^{2}s). This is related to the higher sensitivity to G for the numerical trend previously dicussed. No significant differences characterize the different operating conditions. For HTPB/GOX burning under p_c of 7 bar, $\Delta r_{f,\%}$ indicates that the numerical simulation predicts a value of r_f resulting -15% of the corresponding experimental data for a G of nearly 250 kg/(m^{2}s). For similar values of G, $\Delta r_{f,\%}$ exhibits similar values for tests performed under p_c ranging from 10 to 16 bar. Difference between experimental and numerical solution reaches values of 40–60 % for T_w of 820 K and even higher for T_w of 1000 K (see Tables 7.5–7.6).

This latter result can be understood considering the base hypothesis of the proposed convective model. Numerical investigation is conducted considering the exclusive presence of convective heat transfer. The semi–empirical nature of the model yields to the evaluation of experimental O/F for the determination of effective parameters. This, in turn, yields to an evaluation of r_f as induced by convective heat transfer to the surface in presence of blowing. The latter is evaluated starting from the experimental data (in particular, by considering the actual O/F). Therefore, in the model, model η is characterized by the blockage of the system considering the experimental r_f. This underlines the importance of radiative heat transfer for r_f determination as G (and therefore convective heat transfer) decreases. Under the investigated condition the major contribution to radiative heat transfer could be due to emission from soot, while gaseous combustion products (mainly CO, CO_2 and H_2O) exert a lower (negligible) influence [**?**][11][42][135]. In spite of this observation, empirical correlations for radiative heat transfer modeling from soot are developed considering O/F lower than those characterizing the considered testing conditions (as detailed discussed in Chapter 2, Section 2.2.2). This hinders the possibility of directly extending them to the considered case.

As discussed during experimental ballistic investigation (see Chapter 6, Section 6.1), for low G values solid fuel grain fragmentation can provide an additional (minor) contribution to thermal radiation effects, providing an increase in measured r_f with respect to the case of simple vaporization of the solid fuel. Moreover, considering the relatively low experimental r_f associated with low G, also thermal lag effects in the condensed phase (due to heat conduction into the solid fuel grain) could provide a contribution to the achieved experimental trend. Nevertheless, none of these effects in considered in the presented quasi–steady convective model.

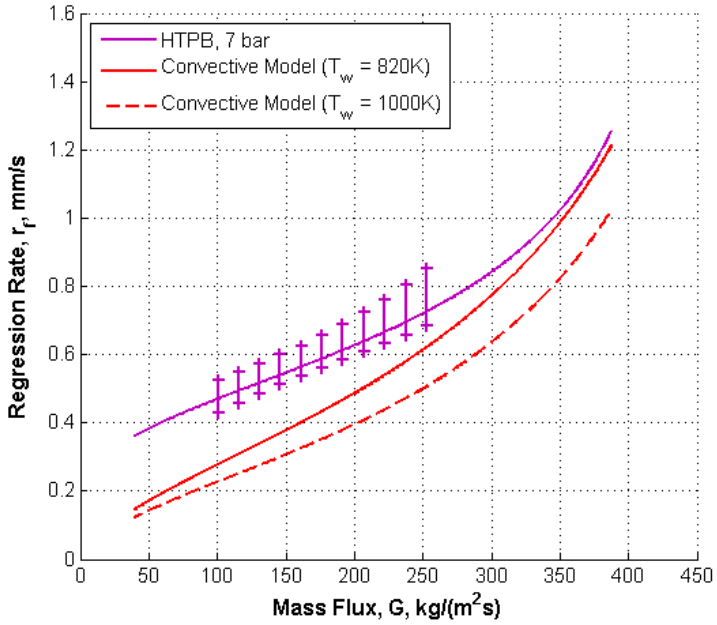

Figure 7.8: HTPB burning under GOX with p_c of 7 bar, r_f vs. G achieved by experimental and numerical investigations.

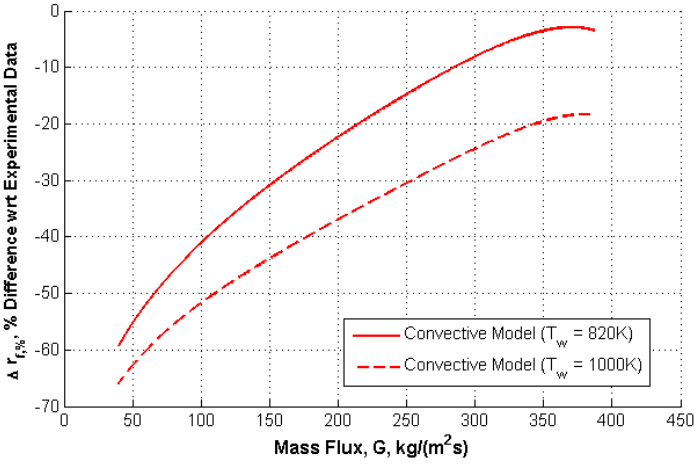

Figure 7.9: HTPB burning under GOX with p_c of 7 bar, Δr_f vs. G achieved by numerical investigations. For definition of $\Delta r_{f,\%}$ see Eq. 7.23.

Table 7.6: HTPB burning under GOX with p_c in the range 7–16 bar, values of $\Delta r_{f,\%}$ (see Eq. 7.23) for selected mass fluxes (T_w = 1000 K). Higher values of $\Delta r_{f,\%}$ characterize this operating condition due to limited convective heat transfer to the surface yielding to a underestimation of r_f over the whole investigated range.

		$\Delta r_{f,\%}$	, **Eq. 7.23**
Fuel, p_c	**G(t_{ign})**	**250 kg/(m^{2}s)**	**100 kg/(m^{2}s)**
HTPB, 7 bar	-18	-30	-52
HTPB, 10 bar	-20	-31	-52
HTPB, 13 bar	-19	-30	-51
HTPB, 16 bar	-15	-31	-51

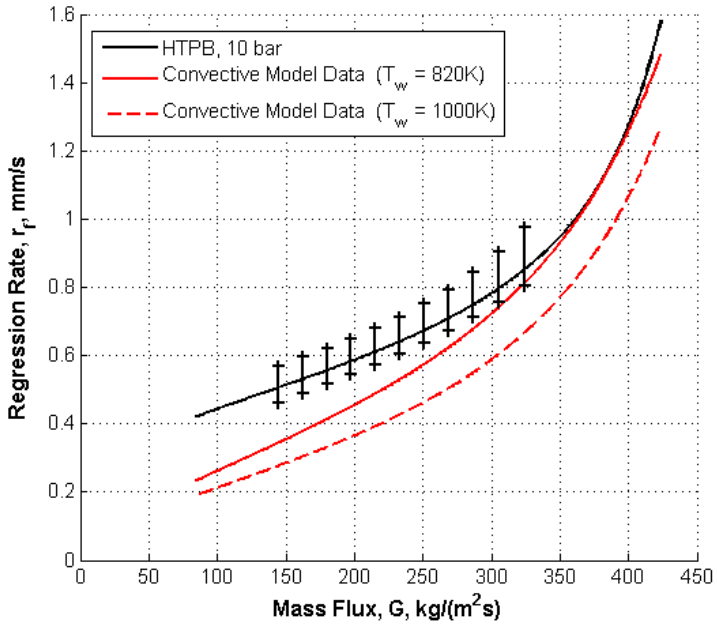

Figure 7.10: HTPB burning under GOX with p_c of 10 bar, r_f vs. G achieved by experimental and numerical investigations.

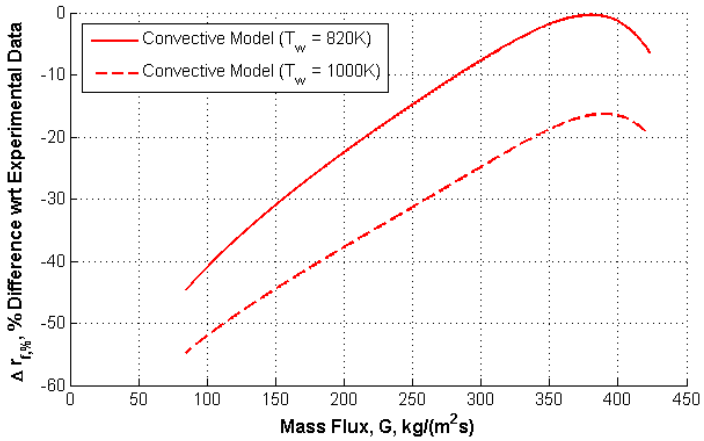

Figure 7.11: HTPB burning under GOX with p_c of 10 bar, Δr_f vs. G achieved by numerical investigation on r_f. For definition of $\Delta r_{f,\%}$ see Eq. 7.23.

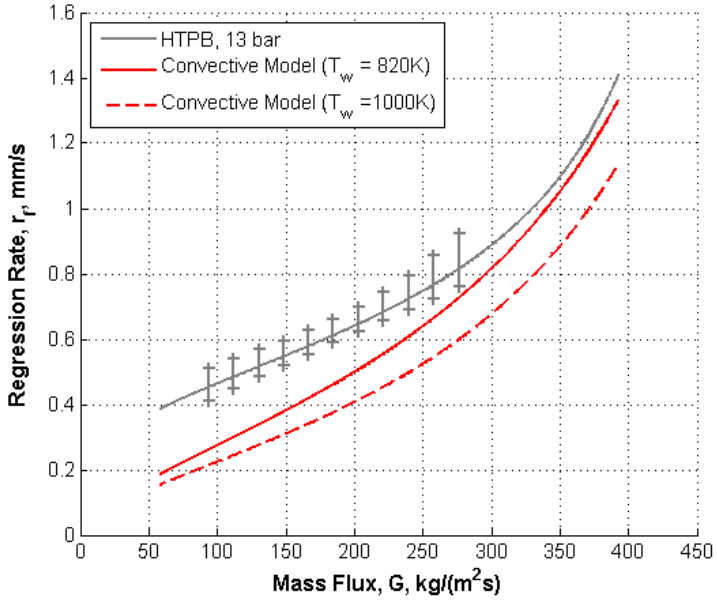

Figure 7.12: HTPB burning under GOX with p_c of 13 bar, r_f vs. G achieved by experimental and numerical investigations.

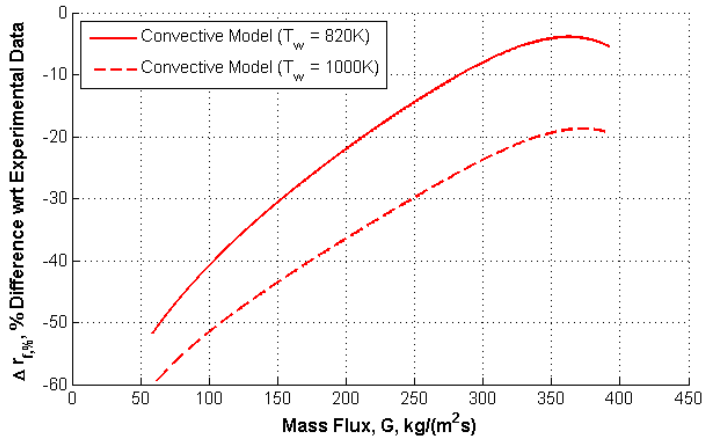

Figure 7.13: HTPB burning under GOX with p_c of 13 bar, Δr_f vs. G achieved by numerical investigations. For definition of $\Delta r_{f,\%}$ see Eq. 7.23.

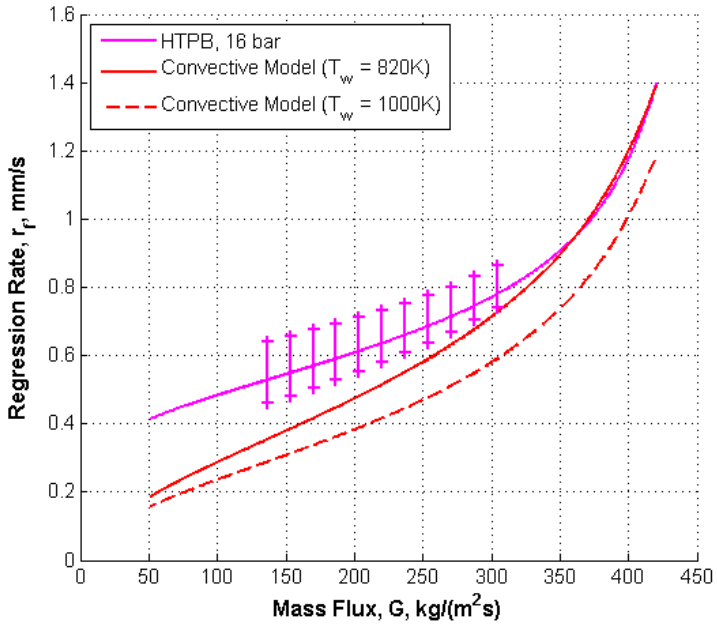

Figure 7.14: HTPB burning under GOX with p_c of 16 bar, r_f vs. G achieved by experimental and numerical investigation on r_f.

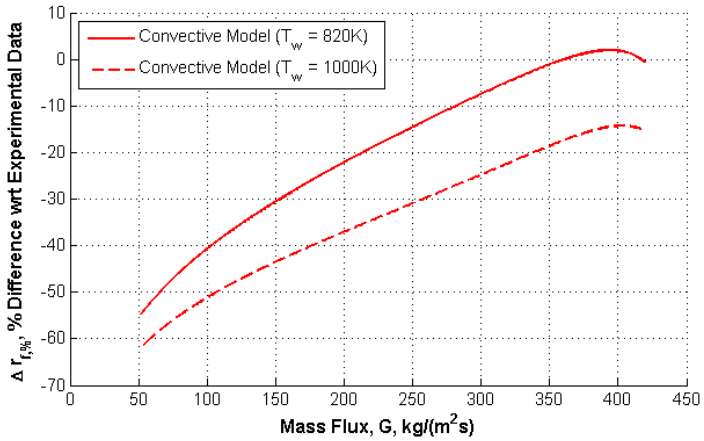

Figure 7.15: HTPB burning under GOX with p_c of 16 bar, $\Delta r_{f,\%}$ vs. G achieved by numerical investigation on r_f. For definition of $\Delta r_{f,\%}$ see Eq. 7.23.

7.5 Conclusion

Ballistics of the HTPB/GOX system was investigated by a numerical simulation developed starting from the approach presented by D.J. Greatrix [120]. The model considers the heat feedback from the flame to the surface as exclusively due to convective heat transfer. A semi–empirical approach was used. Effective values of the thermophysical parameters of interest (Re_D, T_{fl}, and other transport properties) where evaluated starting from experimental, actual O/F characterizing determined from ensemble average curves under the investigated conditions. Remarkable results where achieved in terms of agreement between model results and experimental data for $G \geq 280$ kg/(m^{2}s). Under this condition, for imposed T_w of 820 K, difference between numerical and experimental results is less than 10% of the experimental value. Moreover, the concavity of the evaluated r_f vs. G trend results similar to the experimental, time–resolved data. This latter result cannot be achieved with common approaches to the approximation of the experimental time–resolved data. For $G < 280$ kg/(m^{2}s) percent difference between experimental and numerical data increases as G decreases, with the convective model providing a r_f lower than the experimental value. This latter result possibly underline the importance of radiative heat transfer for the operating range characterized by low G values, a result confirming findings from the experimental investigation. Due to the test operating conditions, soot contribution to the heat feedback toward the solid fuel grain cannot be properly taken into account, while radiation from combustion gases is not taken into consideration due to its low impact on the r_f, [135]. In addition to this it must be clarified that the result achieved for low values of G could be due to possible thermal lag effects in the condensed phase and to solid fuel fragmentation (with the latter phenomenon exerting a limited effect).

CHAPTER 8

TRANSIENT BURNING REGIME

Rocket motors are subject to transient phases at least during ignition and shutdown [113]. Due to their characteristics, HREs and LREs enable multiple ignitions and thrust–modulation [2][3][4], the latter is a forced transient. HREs are characterized by a simpler architecture with respect to LREs. This makes HREs appealing for the design of new, challenging space missions requiring particular orbital maneuvers where thrust pulses and thrust throttling could be required, as de–orbiting of decommissioned spacecrafts and soft–landing of payloads. In particular, the latter maneuver is considered for precision landing in possible manned planetary exploration missions [9]. Soft and precision landing could be considered also in Earth civilian operations for specific tasks [9]. In spite of the importance of HREs throttleability, few studies on the ballistics of hybrid systems under forced transient burning conditions are available in the open literature, while the topic has been extensively treated for SRMs [116].

Karabeyoglu et al. conducted a theoretical study on thermal transients in solid fuel during throttling events considering PMMA– and HTPB–based fuels, [125]. In their work, Karabeyoglu et al. showed the possible overshooting/undershooting of regression rate due to throttling events. Dynamic behavior of solid fuels burning under transient regime is there related to effects of thermal lag in the condensed phase.

In the present work effects of forced transient burning on solid fuel regression rate are evaluated. Experimental analysis on transient operating conditions was conducted by the experimental setup described in Chapter 4. The non–intrusive, optical time–resolved technique for regression rate described in Chapter 5 was taken as starting point for data treatment. The experimental investigation focused on oxidizer mass flow throttling for HTPB burning under GOX. The fuel formulation is selected as a candidate for the realization a soft–landing system in the requirements of the SPARTAN FP7 project [9].

8.1 Investigation of Transient Burning Regime

In this section forced transient operating profile and data reduction technique are presented. Transient operating conditions characterized by oxidizer mass flow throttling are introduced first before passing to optical time–resolved technique for ballistic analysis.

8.1.1 Oxidizer Mass Flow Transients

As detailed discussed in Section 2.2.1, diffusion–limited models for turbulent combustion in the boundary layer identify a relationship between r_f of solid fuel grain and G_{ox} [6][7][8]. The latter is related to both oxidizer mass flow rate and instantaneous port diameter, see Eq. 8.1.

$$G_{ox}(t) = \frac{\dot{m}_{ox}(t)}{\pi \cdot \bar{D}^2(t)/4} \tag{8.1}$$

Under quasi–steady burning, $\dot{m}_{ox}(t)$ exhibits no changes in time, therefore G_{ox} changes in time are due to port diameter increase in time (in turn related to solid fuel web consumption). In the investigated transient operating conditions, $\dot{m}_{ox}$ is throttled during combustion test while p_c is quasi–steady due to servo–actuators acting on the dump line of the test rig (see Chapter 4, Section 4.1). Two different p_c of 13 and 16 bar were investigated.

Investigated conditions are characterized by a "hat–profile" with high–low–high levels of $\dot{m}_{ox}$, see Figure 8.1. Combustion starts with quasi–steady operating conditions characterized by an initial $\dot{m}_{ox}$ of 210 nlpm [corresponding to an initial nominal G_{ox} of nearly 400 $kg/(m^2s)$]. This SL is followed by a first transient leg during which $\dot{m}_{ox}$ is throttled down from 210 to 130 nlpm. In a second transient leg $\dot{m}_{ox}$ is throttled up from 130 nlpm to 210 nlpm. A transient leg is assumed to start when $\dot{m}_{ox}$ differs of $\pm$ 5% from the nominal $\dot{m}_{ox}$ mean value characterizing the considered leg. Table 8.1 provides an overview of the performed tests and of the profile of the imposed operating conditions.

Table 8.1: Overview of transient regime tests with $\dot{m}_{ox}$ throttling. Investigated fuel formulations and operating conditions.

Test No.	**Fuel/Oxidizer**	**Chamber Pressure** p_c**, bar**	**Oxidizer Mass Flow** $\dot{m}_{ox}$**, nlpm**
01HT	HTPB/GOX	13	210, 130, 210
02HT	HTPB/GOX	13	210, 130, 210
03HT	HTPB[a]/GOX	16	210, 130, 210
04HT	HTPB[a]/GOX	16	210, 130, 210
[a] HTPB/C manufactured by NAMMO [9]			

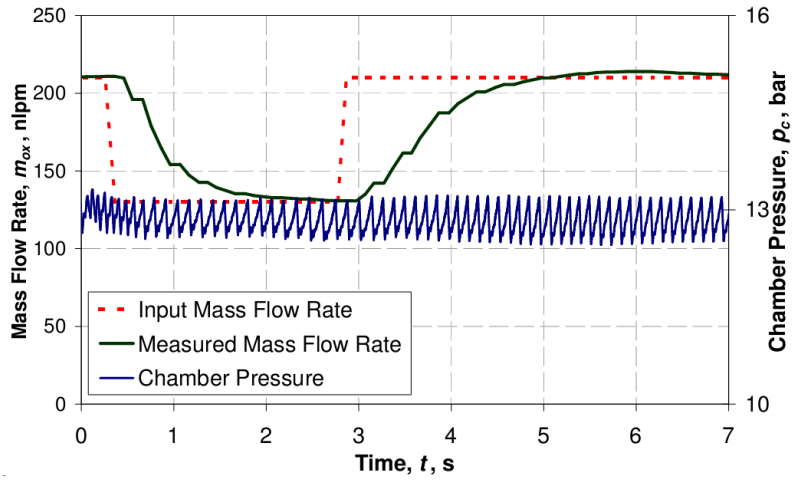

Figure 8.1: Operating profile of Test No.01HT. Oxidizer mass flow is throttled so that a "hat–profile" is achieved, while p_c is at quasi–steady level of 13 bar. Note strand ignition at t = t_{ign} = 0.205 s.

8.1.2 Optical Time–resolved Technique: Application to Transient Regime

Experimental investigation of ballistics of solid fuel burning under forced transient operating conditions is based on the non–intrusive, optical time–resolved technique detailed described in Chapter 5. Starting point for ballistic parameters determination is strand central port diameter

Table 8.2: Test No.01HT data for diameter interpolation by Eq. 8.2 for all legs. High data fitting for SL due to ad-hoc defined t_{ign}. Note high, misleading data fitting for transient legs (see Figure 8.2, and Figure 8.3).

Leg	a_D	n_D	R^2**, Eq. 8.2**
SL	1.726 ± 0.028	0.856 ± 0.016	0.999
1^{st}TL	1.645 ± 0.013	0.735 ± 0.015	0.991
2^{nd}TL	1.449 ± 0.046	0.803 ± 0.022	0.987

sampling during combustion. For the SL time–resolved ballistics is defined starting from Eq. 8.2, while a different approach is necessary for TLs. Requirement for a different data treatment for transient legs is due to the smoothing behavior of Eq. 8.2 possibly hiding non–monotone trends in space–averaged diameter change in time of forced–transient tests (thus yielding to misleading results).

$$\bar{D}(t) - D_0 = a_D \cdot (t - t_0)^{n_D},\ t \geq t_{ign} > t_0 \tag{8.2}$$

Examples of the possible misleading results in data interpolation due to the application of Eq. 8.2 to TLs are reported in Figures 8.2–8.3, and Table 8.2. In particular, considering the results for space–averaged diameter change in time reported Table 8.2 and the regression rate trends in time reported in Figure 8.3, limits of data treatment by Eq. 8.2 are evident since with simple power–law interpolation for space–averaged instantaneous diameter change in time, 1^{st} TL is not linked to SL (diameter exhibits a definite jump), neither is 1^{st} TL with 2^{nd} TL. Moreover, r_f evaluated by Eq. 8.2 exhibits abrupt discontinuities between different legs. Considering test operating profile reported in Figure 8.1 and data reported in Figure 8.3, discontinuities in r_f vs. t can be identified. When passing from SL to the first TL, a gap in regression rate is observed. Similar discontinuities appear in the transition from 1^{st} TL to 2^{nd} TL. Considering the relatively smooth trend characterizing $\dot{m}_{ox}$ during throttling (due to hardware characteristics), these gaps appear suspicious and related to mathematical treatment of sampled data instead of physics of the considered phenomenon. While granting single leg data interpolation with high fitting, Eq. 8.2 cannot properly link different legs. In this respect also use of a simple TOT technique is not appropriate. As discussed in Chapter 5, TOT is intrinsically affected by high errors. In forced transient burning, due to relatively high sampling frequency of diameter in time (up to 10 Hz), TOT technique (without previous data smoothing) results in data scattering and high errors [39]. On the other hand, as discussed in Chapter 5, Secton 5.2, considering overall TOT data for TLs (with longer burning time limiting error propagation) and comparing them with time–averaged r_f achievable starting from the data reported in Table 8.2, differences of 5.2% and 6.3% are achieved for TLs. These differences result quite high when compared to the corresponding values for quasi–steady tests (see Table 6.2), and suggest the presence of some possible combustion dynamics during the forced transient hidden by Eq. 8.2

Forced Transient Sampled Data Interpolation

Data reported in Table 8.2 and Figure 8.2 show how high data fitting is a non–sufficient condition for $\bar{D}_i$ interpolation in time under transient operating conditions. Equation 8.2 can properly interpolate data of quasi–steady burning regime as discussed in Chapter 5 and in [108][110][112], nevertheless a different interpolating law is required for forced transients. In particular, the transient regime interpolating law for $\bar{D}(t)$ requires definition of proper boundary conditions granting respect of continuity in time of measured diameters and ballistic parameters when passing from a leg to the following one. Aim of these boundary conditions is therefore to avoid possible discontinuities in $\bar{D}(t)$ and $\mathrm{r}_f(t)$.

When analyzing forced transient regime tests, SL are treated first. Then TLs are considered: 1^{st} TL data are treated before passing to 2^{nd} TL. In a SL data are treated by conventional time–resolved technique for regression rate, applying Eq. 8.2. SL data enable boundary condition defi-

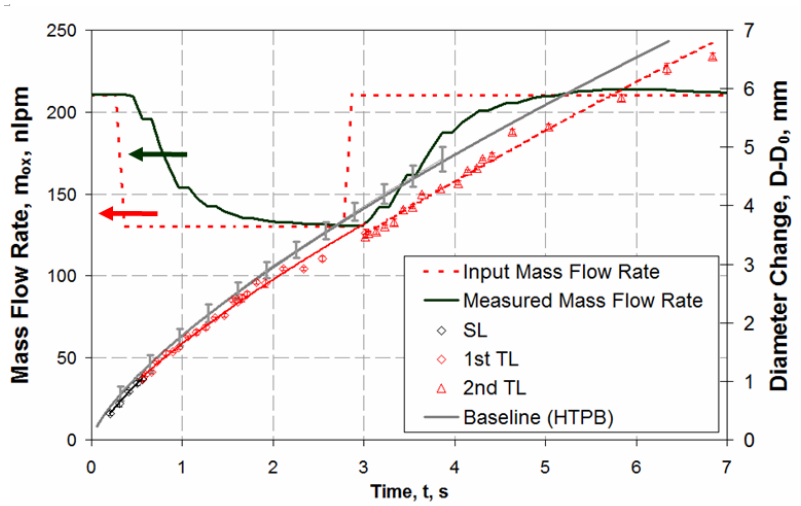

Figure 8.2: Test No. 01HT, operating profile and sampled diameters with power–law approximation for quasi–steady and transient legs (see Eq. 8.2). Baseline burning under quasi–steady operating condition is reported for convenient comparison.

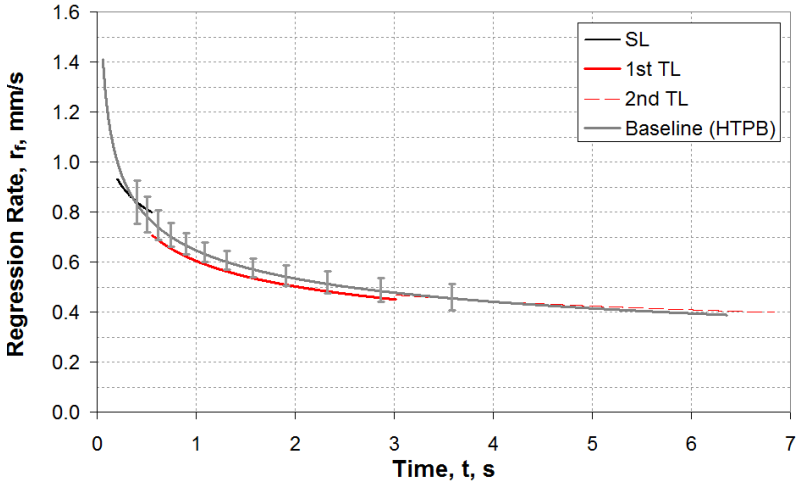

Figure 8.3: Test No. 01HT, r_f vs. t as evaluated by time–derivative of Eq. 8.2 for all legs. Note discontinuities between following legs due to application of Eq. 8.2 to TLs. Baseline burning under quasi–steady operating condition is reported for convenient comparison.

nition between SL and the following 1^{st} TL. Similarly, data achieved for 1^{st} TL are used for definition of boundary conditions for the second 2^{nd} TL. In particular, two boundary conditions are imposed for each TL. One of these conditions grants diameter continuity in time and is reported in Eq. 8.3 . The second boundary condition bonds r_f in time between following legs according to Eq. 8.5. While Eq. 8.3 and Eq. 8.5 are written for the linking of SL with 1^{st} TL, Eq. 8.4 and Eq. 8.6 consider the passage between the two transient legs.

$$\bar{D}(t_{fin,SL}) = \bar{D}(t_{in,1^{st}\,TL}), \qquad t_{fin,SL} = t_{in,1^{st}\,TL} > t_{ign} > t_0 \tag{8.3}$$

$$\bar{D}(t_{fin,1^{st}\,TL}) = \bar{D}(t_{in,2^{nd}\,TL}), \qquad t_{fin,1^{st}\,TL} = t_{in,2^{nd}\,TL} > t_{ign} > t_0 \tag{8.4}$$

$$r_f(t_{fin,SL}) = r_f(t_{in,1^{st}\,TL}), \qquad t_{fin,SL} = t_{in,1^{st}\,TL} > t_{ign} > t_0 \tag{8.5}$$

$$r_f(t_{fin,1^{st}\,TL}) = r_f(t_{in,2^{nd}\,TL}), \qquad t_{fin,1^{st}\,TL} = t_{in,2^{nd}\,TL} > t_{ign} > t_0 \tag{8.6}$$

In the boundary conditions reported in Eqs. 8.3–8.6, time–derivative of r_f is not bounded. This is intended for the capture of possible overshoot/undershoot phenomena and rapid r_f changes in time due to transient operating conditions.

Satisfaction of the imposed boundary conditions requires definition of proper constants in the space–averaged diameter interpolating equation substituting Eq. 8.2. In order to grant this as well as data interpolation, a polynomial law is adopted, see Eq. 8.7.

$$\bar{D}(t) - D_0 = a_{D,PL}(t - t_0)^{n_{D,PL}} + \\ + a_{D,1}(t - t_{fin,\,PL})^2(t - t_0)^{n_{D,1}} + a_{D,2}(t - t_{fin,\,PL})(1 - e^{k_{D,2}\,\frac{t - t_{fin,PL}}{t_{fin,NL} - t_{in,PL}}}) \tag{8.7}$$

The proposed Eq. 8.7 is defined in the dominion given by

$$t_{fin,PL} \leq t \leq t_{in,NL} \qquad t > t_{ign} > t_0.$$

Equation 8.7 has no direct relationship with possible phenomena involved in solid fuel regression during combustion in forced transient conditions. Similarly to what is proposed in [108], Eq. 8.7 is designed with the only aim of enabling a proper interpolation of available data. The first term at the right–hand side of Eq. 8.7 grants satisfaction of the imposed boundary conditions (see Eqs. 8.3–8.5). When linking SL to 1^{st} TL, $a_{D,PL}$ and $n_{D,PL}$ of Eq. 8.7 corresponds to $a_{D,SL}$ and $n_{D,SL}$ reported in Table 8.2. While considering the passage from 1^{st} TL to 2^{nd} TL, the final part of the former is approximated by a power law with the form of the first term at right hand side of Eq. 8.7 thus evaluating $a_{D,1^{st}\,TL}$ and $n_{D,1^{st}\,TL}$. The coefficients $a_{D,1}$, $a_{D,2}$ the exponent $n_{D,1}$ and the constant $k_{D,2}$, are evaluated by a iterative procedure whose objective is to minimize the difference between the interpolation results and the sampled diameters while respecting the imposed boundary conditions.
As for quasi–steady time–resolved ballistics, regression rate of TLs is evaluated by time–derivative of Eq. 8.7. Ballistics of the considered solid fuel is therefore defined according to the same procedure discussed in Chapter 5, Section 5.2 for determination of ballistic parameters of quasi–steady tests. In particular, G_{ox}(t) characterizing TLs is defined according to Eq. 8.1, considering the diameter trend identified by proper Eq. 8.7 and $\dot{m}_{ox}$(t) measured by digital flowmeter (see Chapter 4, Section 4.1). In order to evaluate the consistency of the results achieved by time–resolved technique in transient legs, two consistency conditions are identified. These conditions are based on a comparison between overall–TOT and time–averaged analytical data. The former is based on

sampled diameters and corresponding time, while the latter is defined by an integration procedure. Overall TOT data can provide a rough estimation of ballistics of the burning fuel in a TL, enabling data check starting from original sampled data. Intrinsic error affecting TOT are lessened if considered data are evaluated over long time intervals [108].

In consistency checks of TL, $< \bar{D}(t) >$ can be evaluated according to TOT by Eq. 8.8 while time–averaged analytical value is defined by Eq. 8.9 starting from data evaluated by Eq. 8.7. Similarly, TL regression rate is evaluated by overall TOT according to Eq. 8.10, while time–averaged analytical value is defined by Eq. 8.11.

$$\left\langle \bar{D}_{TOT,TL} \right\rangle = \frac{\bar{D}_{fin,TL} + \bar{D}_{in,TL}}{2} \tag{8.8}$$

$$\left\langle \bar{D}(t_{fin,TL}) \right\rangle = \frac{1}{t_{fin,TL} - t_{in,TL}} \int_{t_{in,TL}}^{t_{fin,TL}} \bar{D}(t) dt \tag{8.9}$$

$$\left\langle r_{f,TOT,TL} \right\rangle = \frac{1}{2} \cdot \frac{\bar{D}_{fin,TL} - \bar{D}_{in,TL}}{t_{fin,TL} - t_{in,TL}} \tag{8.10}$$

$$\left\langle r_f(t_{fin,TL}) \right\rangle = \frac{1}{t_{fin,TL} - t_{in,TL}} \int_{t_{in,TL}}^{t_{fin,TL}} r_f(t) dt \tag{8.11}$$

Consistency checks are therefore evaluated according to Eq. 8.12 and Eq. 8.13.

$$\Delta \bar{D}_{\%} = 100 \cdot \frac{\left\langle \bar{D}(t_{fin,TL}) \right\rangle - \left\langle \bar{D}_{TOT,TL} \right\rangle}{\left\langle \bar{D}_{TOT,TL} \right\rangle} \tag{8.12}$$

$$\Delta r_{f,\%} = 100 \cdot \frac{\left\langle r_f(t_{fin,TL}) \right\rangle - \left\langle r_{f,TOT,TL} \right\rangle}{\left\langle r_{f,TOT,TL} \right\rangle} \tag{8.13}$$

Sampled Data Smoothing

As for any measurement, diameter sampling from recorded visualization of the combustion process is affected by bias and random errors. In the case of diameter sampling of a burning strand measurement can be influenced by solid fuel grain fragmentation phenomena, combustion anisotropies and flame flickering due to operating condition transients. The first two phenomena are common between steady operating conditions burning and forced transients, the latter is peculiar of transient operating conditions regime. In transient regime tests, diameter sampling frequency is relatively high (nearly 10 Hz) and changes in operating conditions could affect visualization quality. In order to lessen the influence of these phenomena, data smoothing procedure is applied to sampled diameters.

Data smoothing is performed by a mobile average algorithm with variable step. Operating procedure is based on the *smooth* function of MATLAB [137]. This algorithm for mobile average is chosen because of the way boundary values of the original dataset are treated. In MATLAB, the *smooth* procedure defines mobile average of the input dataset without modifying the number of the original input elements and the values of the first and the last input elements. This enables data smoothing without reduction of the elements considered for the interpolation. The latter feature is particularly attractive in order to avoid reduction in time extension of a TL's dominion and to impose the identified boundary conditions.

In the smoothing procedure steps from one to seven are used in order to evaluate the mobile average of available data.

8.2 Results and Discussion

In this section, results achieved in transient regime analysis are presented and discussed. As previously stated, four tests were performed with an "hat–transient" operating profile (see Table 8.1). In order to enable a comparison between forced transient and quasi–steady regime tests, baseline data are reported in each figure. HTPB burning in GOX under quasi–steady regime is considered as baseline for convenient comparison of achieved trends. For baseline tests, operating condition is the same as for the SL of forced transient tests.

For a more effective data presentation, Tables 8.3–8.4 report data for SLs of the performed tests. As shown by data summarized in Table 8.3, SLs of three of the four performed tests are characterized by a value of exponent n_r similar to those achieved for ballistic characterization of HTPB under quasi–steady conditions (see Tables 6.3–6.4). When considering the achieved trends for r_f vs. G_{ox} Test No. 03HT is the only one exhibiting a marked difference from the other performed combustions due to a very low value of n_r. This anomalous behavior is highlighted by the results achieved for consistency checks of this test (see Table 8.4). Test No. 03HT is influenced by an irregular ignition affecting the earlier phases of the combustion. A power–law approximation considering the SLs of all the performed tests but No. 03HT and with G_{ox} and p_c as free parameters, yields to the result reported in Eq. 8.14. A value of n_r close to the 0.8 characterizing the ballistics of HTPB under quasi–steady operating conditions is achieved (see Eq. 6.4). On the other hand, p_c exerts a stronger influence on r_f in the case of SLs of forced transient tests than in the case of quasi–steady ballistics. Nevertheless this result is influenced by the limited number of performed tests and the possible differences in fuel formulation between standard HTPB and modified HTPB/C[1].

$$r_f(G_{ox}, p_c) = (0.011 \pm 0.001) \cdot G_{ox}^{(0.869 \pm 0.008)} \cdot p_c^{(-0.153 \pm 0.017)},\ R^2 = 0.856 \tag{8.14}$$

Table 8.3: Ballistic characterization of SLs of the tests performed under transient operating conditions, power law approximation for r_f vs. G_{ox}, see Eq. 6.2.

Test No.	$\mathbf{a}_r$	$\mathbf{n}_r$	$\mathbf{R^2}$**, Eq. 6.2**
01HT	0.027 ± 0.001	0.614 ± 0.002	0.992
02HT	0.010 ± 0.001	0.830 ± 0.005	0.963
03HT	0.143 ± 0.001	0.313 ± 0.001	0.964
04HT	0.005 ± 0.001	0.915 ± 0.003	0.980

Table 8.4: Consistency checks for SLs of the performed tests. Check results expressed as percentages with respect to TOT data. Note results for Test No.03HT (see Table 8.3).

Test No.	**Eq.** 5.8	**Eq.** 5.13	**Eq.** 5.14
01HT	-0.2	0.9	0.1
02HT	0.8	-0.2	0.1
03HT	-2.3	8.5	-0.2
04HT	0.9	2.6	0.3

8.2.1 Experimental Results

Sampled space–averaged diameter interpolation in time for Test 01HT is reported in Figure 8.4. In the latter figure, no smoothing is applied to sampled data. The SL extends from $t_{ign} = 0.205$ s to $t_{fin,SL} = 0.555$ s and is followed by the 1^{st} TL running from the latter time to $t_{fin,1^{st}\,TL} = 3.015$ s. Finally, 2^{nd} TL cover the time span from 3.015 s to $t_{fin,2^{nd}\,TL} = 6.841$ s. Due to the absence

[1]No detail is given by the manufacturer on the formulation of HTPB/C fuel (plasticizer, curing level, possible additives...) and on production procedure.

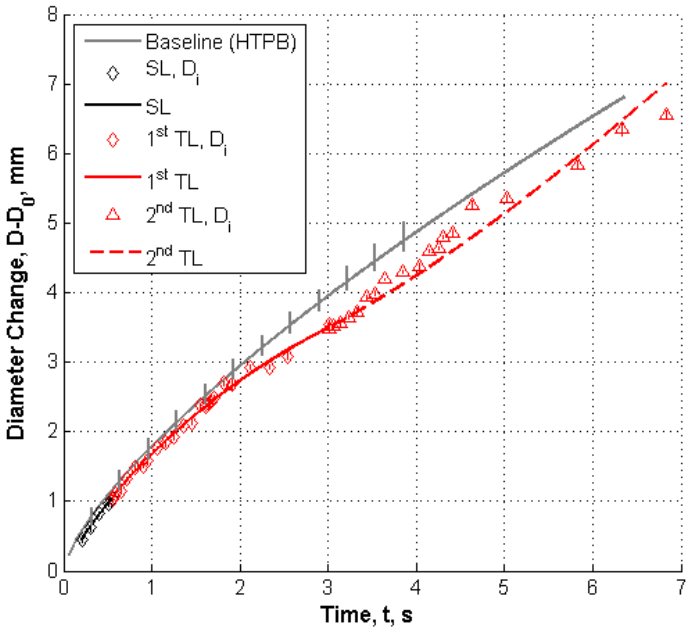

Figure 8.4: Test No.01 HT, diameter change in time (Eq. 8.2 for SL, Eq. 8.7 for TLs) with non–smoothed data for TLs.

of sampled data smoothing, the r_f vs. t trend reported in Figure 8.5 is achieved. As can be seen from data reported in Table 8.5, absence of smoothing affects in particular data of 2^{nd} TL were both interpolation data fitting and consistency check represented by Eq. 8.13 exhibit suspicious values. In particular, considering that in the imposed "hat profile" (see Figure 8.1), for t $\geq$ 4.2 s Test No. 01HT exhibits $\dot{m}_{ox}$ changes lower than 5% of the final value characterizing the 2^{nd} TL (210 nlpm). From this latter t, G_{ox} exhibits a decreasing trend in time due to the increase of $\bar{D}$(t). As a consequence r_f should be characterized by a decreasing behavior in time that is not achieved by data treatment presented in Figure 8.5 where an increase of r_f for increasing time (and increasing port diameter) is obtained also for t $\geq$ 4.2 s. This behavior of time–resolved r_f is highlighted by the interpolation data, particularly from the check based on analytical time–averaged r_f reported in Table 8.5 (with an overestimation of $r_{f,TOT,TL}$ of 14%). This highlights the importance of the double check reported in Eqs. 8.12–8.13.

Table 8.5: Consistency checks for TLs of Test No.01 HT. Results are achieved without data smoothing procedure. Note poor data fitting and high check error for r_f data of 2^{nd}TL.

Test Leg	R^2, Eq. 8.7	Eq. 8.12	Eq. 8.13
1^{st}TL	0.973	2.7	-1.7
2^{st}TL	0.833	1.3	14

A different data treatment of the original sampled space–averaged diameter in time for Test No. 01 HT can be achieved by smoothing procedure of original input. Tables 8.6–8.7 show parameters for evaluation of effectiveness of data interpolation by Eq. 8.7 for different smoothing steps of space–averaged diameters in the 1^{st} TL of Test No. 01HT. As can be seen by the presented data, increases in data smoothing step can provide increases in both interpolation fitting and consistency checks. In particular, the result of Eq. 8.13 passes from -1.7% to -0.6% when smoothing step is increased from 1 (no smoothing) to 5. On the other hand, if smoothing step is increased up to 7, data fitting for diameter interpolation reaches higher values (see Table 8.6), though consistency checks represented by Eq. 8.13 shows a increase from 0.6% to 1.5% when smoothing step passes from 5 to 7. Such an increase in difference between analytical and TOT data is related to the

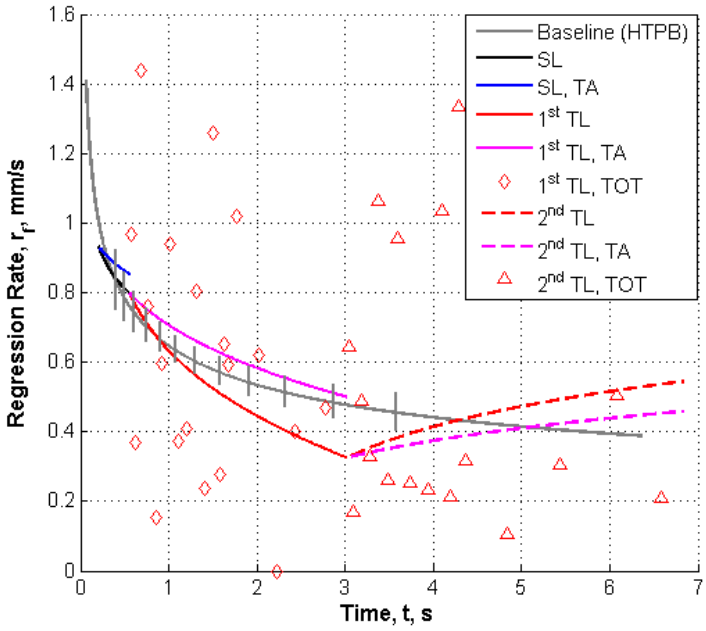

Figure 8.5: Test No.01 HT, regression rate in time (instantaneous and time–averaged analytical data and TOT results) without smoothing procedure on sampled data. Note TOT data scattering and analytical r_f trend in 2^{nd}TL (continuously increasing over the whole leg).

presence of possible oscillations in r_f trend in time, see Figure 8.7. Under the investigated conditions, considering the original input dataset, these oscillations do not significantly alter the quality of analytical results when compared to overall TOT data. Moreover they could be in agreement with (smoothed) TOT data, see Figure 8.7.

Table 8.6: Consistency checks for 1^{st} TL of Test No.01 HT, effect of smoothing procedure. Note low difference in TOT checks on r_f for data achieved with step 5, and high data fitting of Eq. 8.7 for data with step 7.

Smoothing Step	**R^2, Eq. 8.7**	**Eq. 8.12**	**Eq. 8.13**
3	0.978	2.8	-1.3
5	0.979	2.7	-0.6
7	0.991	2.6	-1.5

Presented results and consistency checks suggest that the best representation for diameter change in time for 1^{st} TL of Test No. 01HT could be achieved by a smoothing procedure with step 5 granting relatively high data fitting and good agreement with overall TOT data. With this choice for the 1^{st} TL, 2^{nd} TL data can be treated. A summary of the achieved results is reported in Table 8.9 (coefficients for Eq. 8.7) and Table 8.8 (data fitting coefficient and results of consistency checks). An overview of the effect of smoothing procedure on ballistics of 2^{nd} TL under the investigated conditions is reported in Figures 8.8 – 8.9. Considering a smoothing procedure with step 7 for data treatment for 2^{nd} TL, relatively high data fitting and low differences for analytical and overall TOT data are achieved, see Table 8.8).

Considering the discussed results the final ballistic characterization reported in Figure 8.10 (r_f vs. t) and in Figure 8.11 (r_f vs. G_{ox}) is achieved for Test No. 01 HT under the investigated conditions. As can be seen by data reported in Figure 8.10, TA data presents a relative smooth trend in time and G_{ox}.

An overview of the results achieved for the other three performed tests is given Tables 8.10–8.13. With respect to the original Eq. 8.7, an additional term is added in the data interpolation of

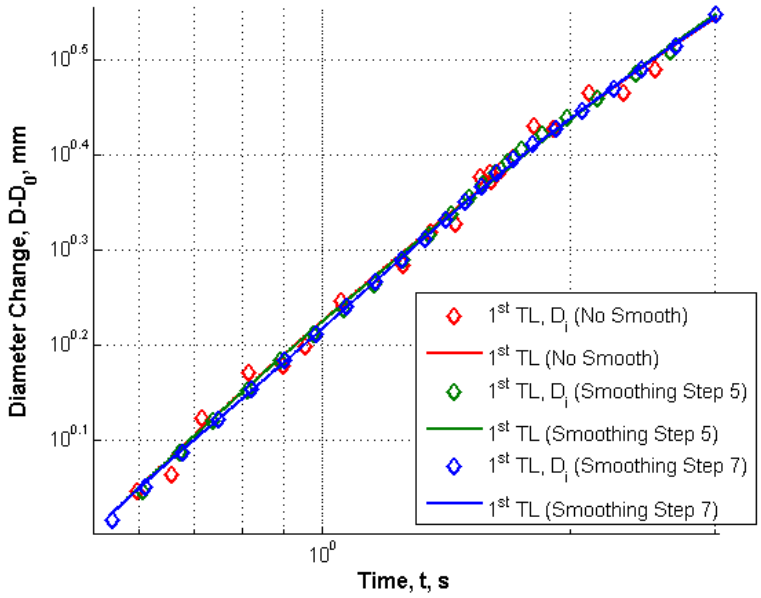

Figure 8.6: Smoothing effect on 1^{st} TL of Test No. 01HT, comparison between non–smoothed data (smoothing with step 1), and data smoothed with step 5 and 7. Note minor but effective differences in diameter change in time (see Table 8.6). Smoothing reduces data scattering enabling higher data fitting with respect to non–smoothed data. Error bars are not reported for better readability.

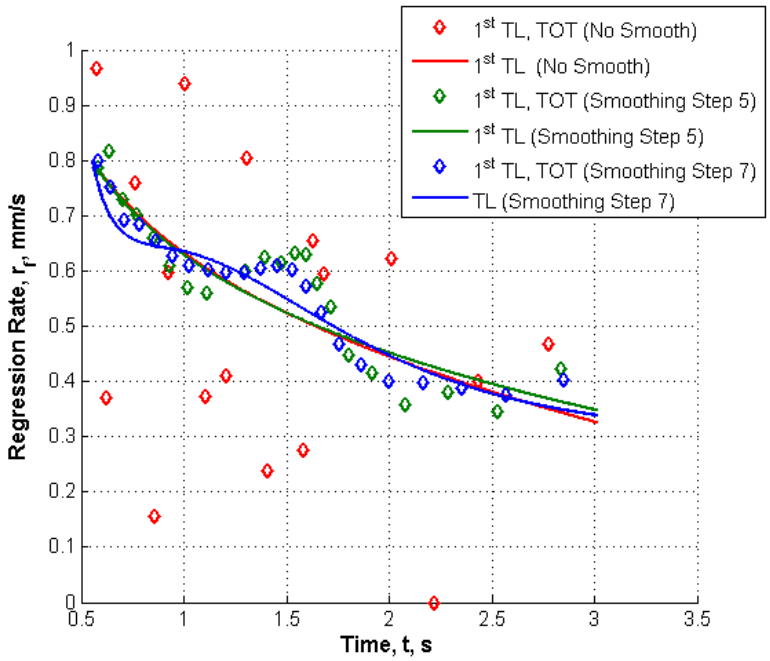

Figure 8.7: Smoothing effect on 1^{st} TL of Test No. 01HT, comparison between non–smoothed data (smoothing with step 1), and data smoothed with step 5 and 7 (detail of TOT and analytical data). Note high data scattering for non–smoothed data. For smoothing step of 5 and 7, oscillations characterize r_f trend in time (as evaluated by TOT). For smoothing step of 7, also analytical r_f presents possible (minor) oscillations in time. Error bars are not reported for better readability.

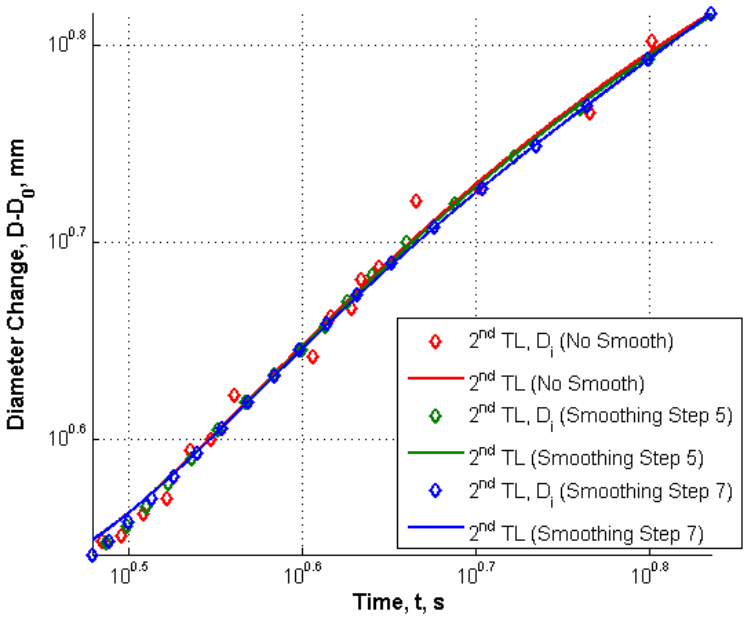

Figure 8.8: Smoothing effect on 2^{nd} TL of Test No. 01HT, comparison between non–smoothed data (smoothing with step 1), and data smoothed with step 5 and 7. Smoothing reduces data scattering. Error bars are not reported for better readability.

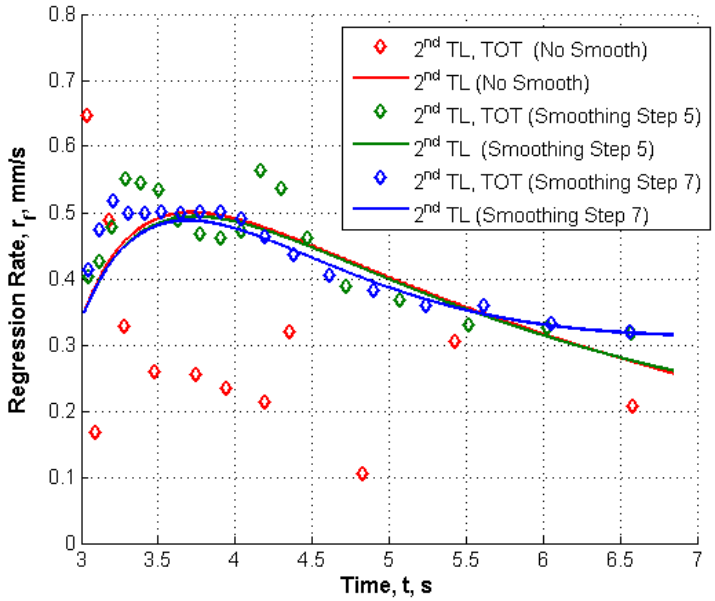

Figure 8.9: Smoothing effect on 2^{nd} TL of Test No. 01HT, comparison between non–smoothed data (smoothing with step 1), and data smoothed with step 5 and 7 (detail of TOT and analytical data). Note high data scattering for non–smoothed data. For smoothing step of 7, high agreement is achieved for analytical and TOT data. Error bars are not reported for better readability.

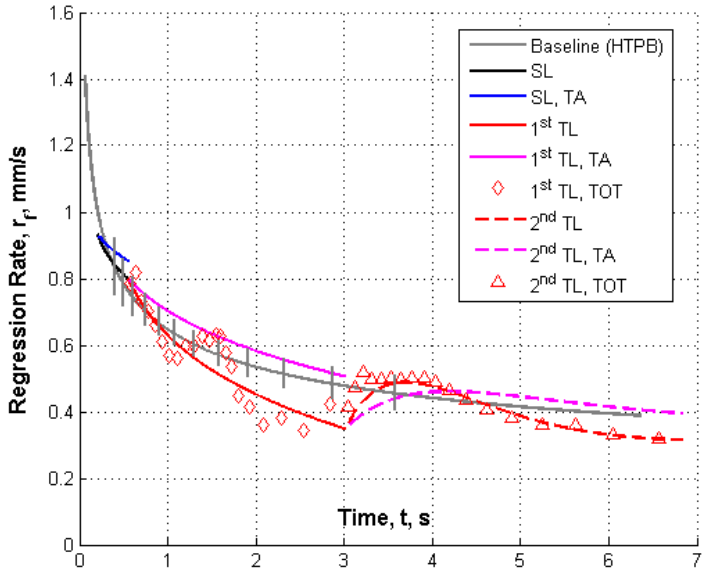

Figure 8.10: Test No. 01HT, r_f vs. t under forced transient conditions (1^{st} TL smoothed with step 5, 2^{nd} TL smoothed with step 7). Note smooth trends of TA data.

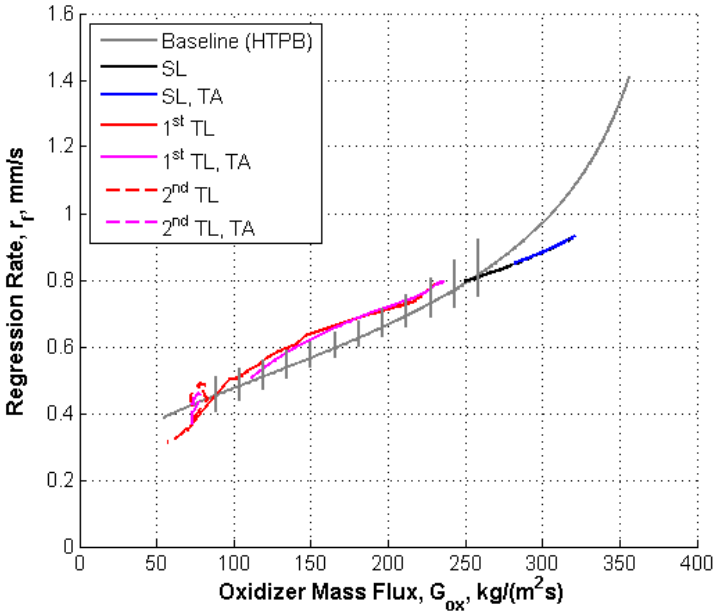

Figure 8.11: Test No. 01HT, r_f vs. G_{ox} under forced transient conditions (1^{st} TL smoothed with step 5, 2^{nd} TL smoothed with step 7).

Table 8.7: Coefficients for space–averaged data interpolation of 1^{st} TL of Test No.01 HT (see Eq. 8.7), effect of smoothing procedure.

Smoothing Step	$\mathbf{a}_{D,SL}$	$\mathbf{n}_{D,SL}$	$\mathbf{a}_{D,1}$	$\mathbf{n}_{D,1}$	$\mathbf{a}_{D,2}$	$\mathbf{k}_{D,2}$
1 (Non–smoothed data)	1.725	0.843	-0.228	-0.494	0.500	0.005
3	1.725	0.843	-0.259	-0.439	0.174	-0.304
5	1.725	0.843	-0.252	-0.555	0.001	-0.007
7	1.725	0.843	-2.661	-1.075	1.661	-5.165

Table 8.8: Consistency checks for 2^{nd} TL of Test No.01 HT, effect of smoothing procedure considering smoothed data (step 5) for 1^{st} TL.

Smoothing Step	$\mathbf{R}^2$**, Eq. 8.7**	**Eq. 8.12**	**Eq. 8.13**
1(Non–smoothed data)	0.958	2.0	2.1
3	0.981	1.9	2.2
5	0.970	1.8	2.8
7	0.974	1.6	2.1

Test No. 02HT due to poor original data fitting. The added term results similar to the second right hand side term of Eq. 8.7, resulting

$$a_{D,3}(t - t_{fin,PL})^{1.05}(t - t_0)^{n_{D,3}}.$$

Figures 8.12–8.13 present r_f vs. space–averaged diameter change for the performed tests. This representation of the results is chosen because of a better readability with respect to the r_f vs. G_{ox} data presented in Figure 8.11, especially when considering ballistics of the 2^{nd} TL where $\dot{m}_{ox}$ is increasing due to forced transient causing a non–monotone trend of G_{ox}(t) (due to diameter increase in time). Detailed r_f vs. G_{ox} data are reported in Appendix A. As can be seen by data reported in the latter figures, under the investigated conditions in three of the four presented tests 1^{st} TL exhibits a monotone decrease of r_f for increasing diameter (and time). Tests No. 03HT presents a peculiar behavior with an initial steep change of r_f in the earlier phase of the transient leg; after this, a relative flat behavior of r_f is achieved for changing diameter. Consistency checks show a good agreement between overall TOT and analytical data (see Table 8.13). With a smoothing step of 7 a significant different behavior of r_f of Test No. 03HT is achieved (see Figure 8.14 and Table 8.14). The trend for r_f of Test No. 03HT presented in Figure 8.14 presents a behavior similar to the one achieved for TOT data in the 1^{st} TL of Test No. 01HT, see Figure 8.10. Under the investigated conditions, considering the relative long time of forced transient duration (around 1 s), this non–monotone behavior of r_f could be related to convective heat transfer blockage. In forced transient, decrease of G_{ox} causes an enhancement in the blocking effect affecting heat feedback to the surface, yielding to a reduction in r_f. The latter, in turn, could bring to a reduction in blocking effect, thus increasing convective heat feedback from flame to solid fuel grain and consequently enhancing r_f. This could induce a non–monotone behavior in r_f. Nevertheless, considering data reported in Table 8.14 and the comparison between TOT and analytical data reported in Figure 8.14, the oscillations characterizing r_f in the 1^{st} TL of Test No. 03HT with smoothing step of 7 could also be related to the mathematical interpolation. Due to this, data smoothed with step 3 are considered for ballistic characterization of Test No. 03HT.

Power law approximation of r_f vs. G_ox for the 1^{st} TL of performed tests is reported in Table 8.11. As can be seen by reported data r_f exhibits a marked dependence from G_ox under the investigated conditions, though different values od n_r are achieved for the different tests (also due to the different G_ox interval characterizing the different 1^{st} TLs, see Appendix A).

An estimation of the possible transient effects on the ballistics of solid fuel burning under unsteady operating conditions can be evaluated considering characteristic time–scales associated to transients in condensed and gas phases and surface reactions of the solid fuel [116]. These time scales associated with the different zones can be evaluated according to Eqs. 8.15–8.17. Under forced transient conditions, with $\dot{m}_{ox}$ throttling, hybrid systems are possibly characterized by

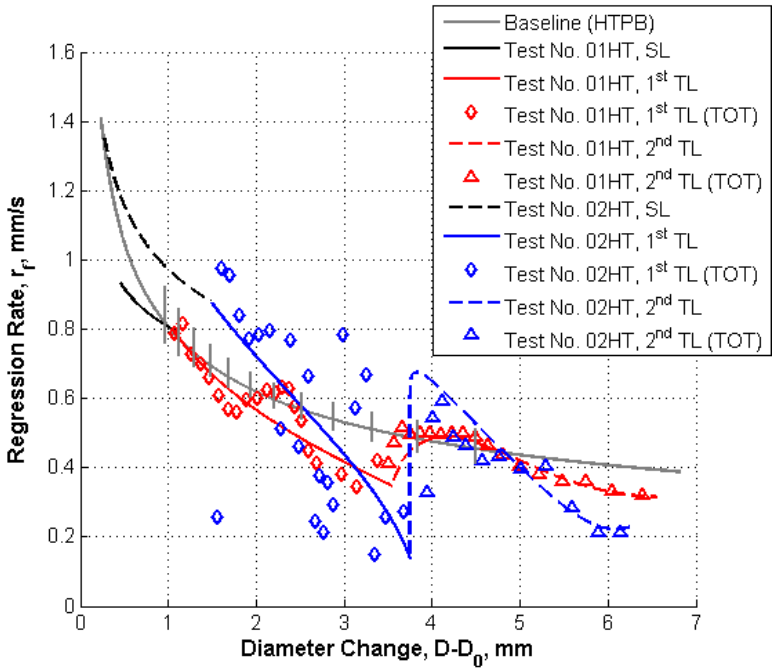

Figure 8.12: Regression rate vs. diameter change for Test No. 01HT and Test No. 02HT (analytical, instantaneous data). Note marked overshooting for 2^{nd} TL of Test No. 02HT.

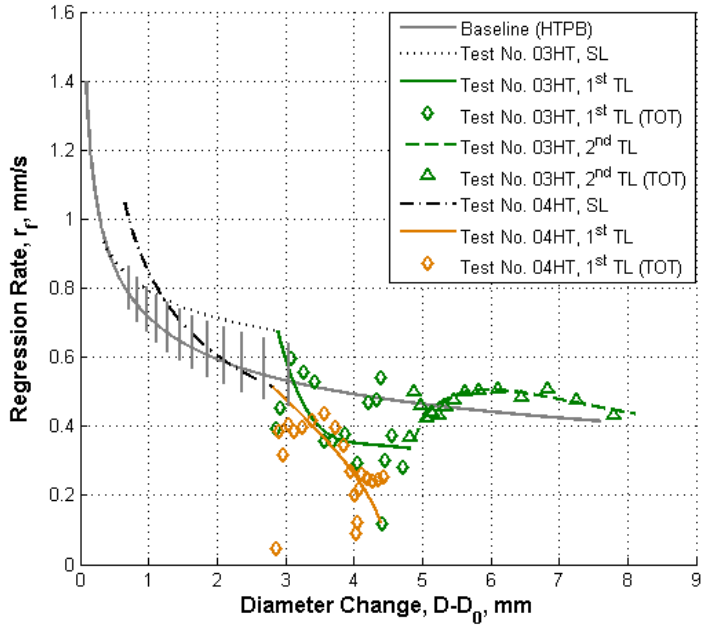

Figure 8.13: Regression rate vs. diameter change for Test No. 03HT and Test No. 04HT (analytical, instantaneous data). Due to poor quality of the combustion process, 2^{nd} TL of Test No. 04HT does not allow diameter sampling in time and is therefore not reported.

Table 8.9: Coefficients for space–averaged data interpolation of 2^{nd} TL of Test No.01 HT (see Eq. 8.7), effect of smoothing procedure (starting from ballistics achieved for 1^{st} TL with smoothing procedure of step 5).

Smoothing Step	$\mathbf{a}_{D,SL}$	$\mathbf{n}_{D,SL}$	$\mathbf{a}_{D,1}$	$\mathbf{n}_{D,1}$	$\mathbf{a}_{D,2}$	$\mathbf{k}_{D,2}$
1 (Non–smoothed data)	1.839	0.592	15.60	-2.870	0.009	1.350
3	1.839	0.592	5.432	-2.115	0.251	0.458
5	1.839	0.592	10.52	-2.502	-0.154	-1.602
7	1.839	0.592	8.804	-1.268	-3.232	-1.865

Table 8.10: Coefficients for space–averaged data interpolation of 1^{st} TL of Test Nos. 02HT–04HT (see Eq. 8.7).

Test No.	**Smoothing Step**	$\mathbf{a}_{D,SL}$	$\mathbf{n}_{D,SL}$	$\mathbf{a}_{D,1}$	$\mathbf{n}_{D,1}$	$\mathbf{a}_{D,2}$	$\mathbf{k}_{D,2}$
02HT	3	2.034	0.799	-0.284	-0.252	0.281	0.065
03HT	3	1.685	0.869	-3.324	-2.144	3.338	0.036
04HT	5	1.861	0.673	-0.101	-0.005	0.003	0.048

an additional transient effect related to dynamics of the unsteady boundary layer [136] [138]. A detailed evaluation of characteristic time for the response of a non–reacting boundary layer to velocity profile changes is reported in Eq. 8.18. The latter equation evaluates the time required by a boundary layer to rach a novel stady–state condition over its the whole extension, once perturbed by changes in u_e. As discussed in [136] [138], no detailed study concerning an extension of Eq. 8.18 to the case of a reacting boundary layer is available in the open literature. According to what is discussed in [136] [138], the constant c′ comparing in Eq. 8.18 should have a value of 0.5 under HRE operating conditions.

$$t_s = \frac{\kappa_s}{r_f^2} \tag{8.15}$$

$$t_g \approx (\frac{\rho_g \, k_g \, C_s}{\rho_s \, k_s \, C_{p,\,g}}) \cdot t_s \tag{8.16}$$

$$t_w \approx (\frac{R_u T_w}{E_a}) \cdot t_s \tag{8.17}$$

$$t_{bl} \approx (c' \cdot \frac{x}{u_e}) \tag{8.18}$$

Considering what discussed in Chapter 7, Section 7.2.1, effective values of the terms comparing in Eqs. 8.15–8.17 can be used in the calculations. While t_{bl} is estimated considering the limiting case of strand geometry and cold flow data relative to the u_e associated with a $\dot{m}_{ox}$ of 130 nlpm (the lowest value characterizing the performed tests) with a central port diameter of 12 mm.

Under the investigated operating conditions, for r_f values ranging from 0.1 to 1.0 mm/s the resulting values of $t_c$are reported in Table 8.16. Considering Eqs. 8.15–8.17, and the data reported

Table 8.11: 1^{st} TL, power law approximation for r_f vs. G_{ox} for the performed tests, see Eq. 6.2.

Test No.	a_r	n_r	R^2**, Eq. 6.2**
01HT	0.035 ± 0.001	0.575 ± 0.002	0.973
02HT	0.006 ± 0.001	0.964 ± 0.009	0.830
03HT	0.020 ± 0.001	0.684 ± 0.006	0.845
04HT	$.0023 \pm .0001$	1.126 ± 0.007	0.909

Table 8.12: Coefficients for space–averaged data interpolation of 2^{nd} TL of Test Nos. 02HT–04HT (see Eq. 8.7). Note additional term defined for 2^{nd} TL of Test No. 02HT.

Test No.	Smoothing Step	$\mathbf{a}_{D,1^{st}TL}$	$\mathbf{n}_{D,1^{st}TL}$	$\mathbf{a}_{D,1}$	$\mathbf{n}_{D,1}$	$\mathbf{a}_{D,2}$	$\mathbf{k}_{D,2}$	$\mathbf{a}_{D,3}$	$\mathbf{n}_{D,3}$
02HT	3	2.843	0.237	-2.929	-0.383	2.568	-1.211	2.508	1.376
03HT	7	1.978	0.605	29.18	-2.868	13.51	-0.005	0	0

Table 8.13: Consistency checks for 1^{st} and 2^{nd} TLs of performed tests (percentage values evaluated with respect to overall TOT data).

		1^{st} TL			2^{nd} TL		
Test No.	Smoothing Step in 1^{st}, 2^{nd} TL	R^2, Eq. 8.7	Eq. 8.12	Eq. 8.13	R^2, Eq. 8.7	Eq. 8.12	Eq. 8.13
02HT	3, 3	0.994	3.5	0.1	0.988	2.8	6.2
03HT	3, 7	0.914	1.4	-1.1	0.998	0.1	0.3
04HT	5, NA	0.957	1.3	-1.4	NA	NA	NA

in Table 8.15 it is easy to evaluate a singificant difference in the order of magnitude of the different time–scales under the investigated conditions. In particular, gas phase is characterized by faster response time than surface and solid phase. Corresponding times are therefore $t_w \approx 0.1t_c$, $t_g \approx 0.01t_c$. For the characteristic time of the boundary layer, values $\leq 10^{-2}$ s are achieved under the investigated conditions, thus the latter parameter should exert a limited influence on the considered phenomena under the investigated conditions.

Table 8.17 and Table 8.18 report data related to the time–averaged r_f characterizing each test leg and the final, instantaneous r_f of each leg. As can be seen from the reported values, SL is characterized by values of overall time–averaged r_f ranging from 1.0 to 0.66 mm/s. Due to throttling down of $\dot{m}_{ox}$, overall time–averaged r_f reduces to values close to 0.3 mm/s for the 1^{st} TL. Because of the increased diameter (due to fuel consumption during burning) and the throttling up of $\dot{m}_{ox}$, instantaneous r_f is increased with respect to 1^{st} TL values. When passing from SL to 1^{st} TL the relatively high value of r_f yields to a limited effect of possible transient effects (monotone decrease of r_f for increasing diameter and decreasing G_{ox}). Nevertheless the low r_f characterizing the final part of the 1^{st} TL yields to a possible influence of thermal lag effects of the condensed phase. The latter could exert influence on the marked r_f increases in the earlier phases of the 2^{nd} TL. Steep increase in r_f is noticed especially in the 2^{nd} TL of Test No. 02HT. Where the abrupt, initial r_f peak characterizing the leg are in agreement with the (smoothed) TOT trend.

Test No. 01 HT and No. 03 HT are characterized by a final part of the 2^{nd} TL in good agreement with the ballistics of baseline burning under quasi–steady conditions. On the other hand, r_f of Test No. 02 HT exhibits a marked difference with respect to baseline ballistics in the final part of the 2^{nd} TL. In particular, for a G_{ox} of 60 $kg/(m^2s)$, the difference in r_f between Test No. 02HT and baseline, with respect to the performance of the latter formulation is -42 %. For Test No. 01 HT under the same operating condition a difference with respect to baseline of -20% is achieved, while Test No. 03 HT is characterized by a + 25%. In spite of possible influences of poor quality of the combustion at low fluxes (due to solid fuel grain fragmentation, cooking) the peculiar behavior of test No. 02HT could be associated to the high r_f characterizing the inner phases of the 2^{nd} TL and inducing a high blockage effect on convective heat transfer that, in turn yields to a steep r_f decrease.

8.3 Conclusion

The ballistics of HTPB–based fuels under forced transient operating conditions was investigated by a non–intrusive optical technique for r_f measurement based in diameter sampling in time. During the combustion process $\dot{m}_{ox}$ was throttled according to a "hat–profile" from an initial value of 210 nlpm down to 130 nlpm and then up to 210 nlpm. Four tests were performed at two different p_c of 13 and 16 bar. An ad–hoc defined expression for diameter interpolating

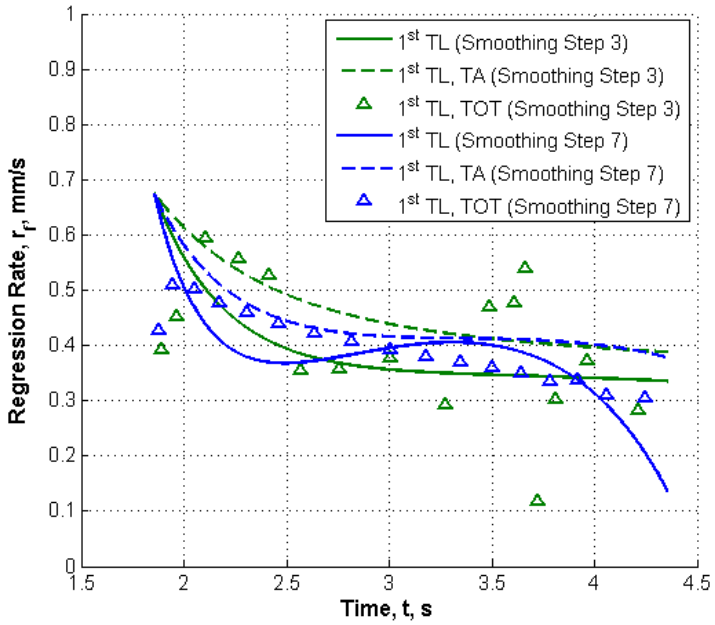

Figure 8.14: Test No. 03HT, comparison between TOT and analytical trends achieved for r_f in 1^{st} TL, for different smoothing steps. Note oscillations in r_f analytical trend for data smoothed with step 7, resulting similar to the one achieved by TOT data for the 1^{st} TL of Test No. 01HT (see Figure 8.10). Nevertheless, no oscillation characterizes r_f TOT trend for Test No. 03HT. Error bars not reported for better readability.

Table 8.14: Consistency checks for 1^{st} TL of Test No. 03HT with sampled data smoothed with step 7. Note relatively high data fitting (compared to data reported in Table 8.10) but high percent differences between analytical and TOT data.

Smoothing Step	**R^2, Eq. 8.7**	**Eq. 8.12**	**Eq. 8.13**
7	0.940	1.2	-3.6

equation was developed for the treatment of TLs. This equation enables satisfaction of boundary conditions imposed to grant $\bar{D}(t)$ and $r_f(t)$ continuity in time between following legs. Results achieved by analytical interpolation of data were compared with TOT data in order to check their consistency (as for quasi–steady ballistics, see Chapter 5 and Chapter 6).

The first remarkable result achieved by the experimental activity is the ability of the hybrid system to adapt its behavior to changes in the operating conditions without unstable response to forced transients. Under the investigated conditions during the first forced transient phase relatively smooth trends of r_f in t and G_{ox} characterize the performed tests. As shown by data reported in Table 8.11, a marked sensitivity of r_f with respect to G_{ox} characterizes the performed tests, where the latter parameter varies due to solid fuel consumption (yielding to increases in central port diameter) and due to $\dot{m}_{ox}$ throttling. On the other hand during the throttling up phase the system exhibits a r_f increase related to both $\dot{m}_{ox}$ increase and possible thermal lag effects in the condensed phase due to the relative low r_f characterizing the end of the first transient phase under the investigated conditions. Though the latter dynamic effects could result in overshooting phenomena, the observed behavior shows the natural tendency of the hybrid system to recover an operating condition similar to the one characterizing the considered quasi–steady operating conditions.

Table 8.15: HTPB data for the estimation of characteristic times of different zones for evaluation of possible transient effects, see Eqs. 8.15 – 8.17.

Parameter	**Value**
T_w, K^a	820–1000
ρ_s, kg/m^3	920
κ_s, m^2/s	1.1
C_s, $J/(kgK)$	2100
E_a, $kcal/mol^b$	36

[a] See Chapter 7, Section 7.2.1 and [133].
[b] Average value defined according to [136].

Table 8.16: Characteristic time of condensed phase (see Eqs. 8.15) evaluated according to data reported in Table 8.15. Considering thermophysical properties of solid fuel, chracteristic time for surface and gas phase results 10 and 100 faster than the solid phase.

$\mathbf{r_f}$**, mm/s**	$\mathbf{t_s}$**, s**
0.1	10.0
0.3	1.11
0.5	0.40
0.7	$2.04 \cdot 10^{-1}$
0.9	$1.23 \cdot 10^{-1}$
1.1	$8.26 \cdot 10^{-2}$

Table 8.17: Time–averaged r_f for different legs of the performed tests (see Appendix A for further details).

Test No.	$< r_f(t_{fin,SL}) >$**, mm/s**	$< r_f(t_{fin,1^{st}TL}) >$**, mm/s**	$< r_f(t_{fin,2^{nd}TL}) >$**, mm/s**
01 HT	0.852	0.505	0.394
02 HT	1.026	0.446	0.358
03 HT	0.750	0.388	0.469
04 HT	0.661	0.305	NA

Table 8.18: Final, instantaneous r_f for different legs of the performed tests (see Appendix A for further details).

Test No.	$r_f(t_{fin,SL})$**, mm/s**	$r_f(t_{fin,1^{st}TL})$**, mm/s**	$r_f(t_{fin,2^{nd}TL})$**, mm/s**
01HT	0.798	0.347	0.315
02HT	0.881	0.137	0.233
03HT	0.675	0.335	0.436
04HT	0.513	0.122	NA

CHAPTER 9

CONCLUSIONS AND FUTURE DEVELOPMENTS

Investigation on the ballistics of solid fuels for hybrid rocket propulsion was conducted with both experimental and numerical approaches. In the following sections conclusions of the work are presented and recommendation for future works are given.

9.1 Conclusions

9.1.1 Ballistics: Experimental Investigation

Experimental investigation of solid fuels was conducted in a 2D radial lab-scale burner. An optical, non–intrusive time-resolved technique for regression rate measurement was designed and validated. Time-resolved technique enables a better insight of the ballistics of regressing fuel due to the availability of instantaneous and time–averaged data.

Both HTPB–based and SW–based fuels were tested under GOX with p_c ranging from 7 to 16 bar and $\dot{m}_{ox}$ of 210 nlpm [corresponding to an initial, nominal G_{ox} of 400 $kg/(m^2s)$].

Under the investigated conditions r_f of HTPB revealed a dependency from G_{ox} but an independency from p_c. For $G_{ox} > 120\ kg/(m^2s)$, measured r_f could be approximated with a power law yielding to $r_f \propto G_{ox}^{0.8}$. HTPB fuel was considered as baseline for the relative ballistic grading of different fuel formulations. SW fuel exhibited a higher sensitivity to p_c with respect to baseline. In particular, increasing p_c a r_f detriment was achieved under the investigated conditions. Such a behavior could be related to a p_c effect on entrainment, with higher pressures exerting a stabilizing action on melted fuel layer. In spite of this, SW fuels revealed a significant regression rate increase with respect to baseline over the whole investigated range.

Both HTPB-and SW-based fuel formulations were loaded with additives in order to evaluate possible r_f enhancement. Considering the HTPB-based formulations attractive performance were demonstrated by MgB–doped fuels and, in particular by HTPB loaded with 2.8% MgB90 (20% Mg). This additive is characterized by marked r_f enhancement for high G_{ox} [+64% at 350 $kg/(m^2s)$] and low sensitivity to oxidizer mass flux changes. ALEX powders can provide higher r_f than MgB90 (20% Mg), nevertheless also their sensitivity to G_{ox} is higher thus yielding to a significant performance detriment during combustion. An exception is VF-ALEX$_{APS}$ that is characterized by an almost constant regression rate enhancement 30% over the whole range of G_{ox} characterizing the test. Nevertheless, it must be considered that the molar amount of B contained in HTPB loaded with 2.8% MgB90 (20% Mg) is half of the molar aluminum content in the formulation doped with VF-ALEX$_{APS}$. Therefore increasing the molar content of MgB90 (20% Mg) in

HTPB could yield to further performance increase. Additives exhibiting high reactivity also under ambient conditions as $LiAlH_4$ where tested in SW-binder exhibiting significant r_f increases (and high sensitivity to G_{ox}). Nevertheless the poor mechanical properties of the solid grain hinders the possible (great) advantages related to SW high r_f. During the experimental activity a ballistic characterization of HTPB loaded with AlH_3 under 70% O_2 revealed a r_f higher than the one achieved by the same formulation under GOX, due to this evidence a possible reaction between Al contained in alane and nitrogen was postulated under the tested operating conditions.

9.1.2 Ballisitcs: Numerical Simulation

Experimental results evidenced that, under the investigated conditions, the ballistic behavior of HTPB could be modeled by considering a convective heat transfer regime from the flame to the surface. A numerical approach aiming to the determination of the regression rate of the solid fuel grain under convective heat transfer regime was therefore conducted. Analysis focused on HTPB burning in gaseous oxygen. The proposed approach is based on the definition of effective values of thermophysical parameters considered for the determination of parameters of interest (as T_{fl}, thermal transport properties, and convective heat transfer coefficient). Effective values are determined considering the actual, instantaneous oxidizer to fuel ratio determined during the experimental sessions. With the proposed approach, considering a T_w of 820 K, the convective model can properly estimate the experimental regression rate for mass flux values above 250 kg/(m^2s), with a difference with respect to experimental data of 15%. Moreover, r_f vs. G trend achieved by model data result in agreement with the corresponding time–resolved data (characterized by a marked initial r_f and high sensitivity to G) that is not caught by common approaches. For lower oxidizer mass fluxes higher differences between experimental and numerical values are achieved. Under the investigated conditions this result underlines the relative importance of radiative heat transfer in the heat feedback from flame to the regressing surface for low values of oxidizer mass flux (in turn inducing a reduced convective heat transfer).

9.1.3 Transient Burning Regime

The ballistics of HTPB–based fuels under forced transient operating conditions was investigated by the developed non–intrusive optical technique for r_f measurement based in diameter sampling in time. Investigated conditions were characterized by a "hat–profile" with high–low–high levels of $\dot{m}_{ox}$. The initial phase of the tests was characterized by quasi–steady operating conditions [nominal, initial G_{ox} of nearly 400 $kg/(m^2s)$]. This condition was then modified by a $\dot{m}_{ox}$ decrease in time, followed by a $\dot{m}_{ox}$ increase back to the initial value characterizing quasi–steady leg of the test. In each of the performed tests, ballistics of HTPB was characterized during all the phases and, in particular, in the throttling down and the throttling up transients (1^{st} TL and 2^{nd} TL, respectively). During the 1^{st} TL, r_f exhibited a relatively smooth decrease in time due to the reduction in G_{ox} associated to $\dot{m}_{ox}$ decrease and diameter increase in time. In the 2^{nd} TL, r_f was characterized by an initial increase due to $\dot{m}_{ox}$ growth causing an initial increase in G_{ox}. In this phase possible overshooting of the system were noticed. Then r_f was characterized by a decreasing trend for decreasing G_{ox}. The observed overshooting could be mainly due to thermal lag effects in the solid phase due to the decrease in r_f characterizing the 1^{st} TL. Nevertheless, under the investigated conditions, hybrid system ballistics was characterized by a stable response to operating condition changes, thus providing experimental evidence of hybrid system versatility.

9.2 Recommendations for Future Works

According to the achieved experimental results, the following points should be considered for future work development.

- Though low additive mass fraction could result in lower performance losses due to reduced presence of CCP, a ballistic characterization of HTPB loaded with higher mass fractions of MgB90 (20% Mg) could evidence possible further performance enhancement. Thus an

extended study on MgB ballistics/mechanical properties is recommended. Being micron-sized, MgB does not require any dedicated dispersion technique down to the nano-scale (an attractive feature when considering possible large scale applications).

- An extended study on VF-ALEX$_{APS}$ manufacturing effects on powder reactivity and ballistic performance (with the aim of lessening the presence of relatively big cluster of particles probably hindering VF–ALEX$_{APS}$ r_f enhancement in the earlier phase of the combustion process). And a detailed research activity on other coatings producing oxidizing species during their decomposition (AP, AN, nitrocellulose ...).
- An experimental/numerical investigation of the coupling between convective and radiative heat transfer could lead to a better insight of the combustion process on the one hand and, on the other hand, an improvement of the proposed approach for r_f numerical investigation for the quasi-steady regime.
- Starting from the achieved experimental results for transient burning regime, further tests should be performed in order to evaluate system response to different $\frac{d\dot{m}_{ox}}{dt}$. Final aim of this testing activity should be the realization of a numerical model for the evaluation of possible solid phase thermal lag effects influencing hybrid system response.

APPENDIX A

TRANSIENT REGIME DATA

In this appendix, a summary of the results achieved for forced transient analysis are detailed reported. In particular, r_f vs. G_{ox} instantaneous and time-averaged trends (presented in Chapter 8 only for Test No. 01HT) are reported for all the performed tests. Equations A.1–A.3, presented and discussed in Chapter 8 are considered for data reduction.

$$\bar{D}(t) - D_0 = a_D \cdot (t - t_0)^{n_D},\ t \geq t_{ign} > t_0 \tag{A.1}$$

$$r_f = a_r \cdot Gox^{n_r},\ t \geq t_{ign} > t_0 \tag{A.2}$$

$$\bar{D}(t) - D_0 = a_{D,PL}(t - t_0)^{n_{D,PL}} + \\ +a_{D,1}(t - t_{fin,\,PL})^2(t - t_0)^{n_{D,1}} + a_{D,2}(t - t_{fin,\,PL})(1 - e^{k_{D,2}\frac{t - t_{fin,PL}}{t_{fin,NL} - t_{in,PL}}}) \tag{A.3}$$

Table A.1: HTPB burning in GOX under p_c of 13 and 16 bar, ballistic parameters for Eq. A.1 of SLs. Resulting data for power law approximation of r_f vs. G_{ox} by Eq. A.2 is reported in Table 8.3.

Test No.	**p_c, bar**	**a_D**	**n_D**	**R^2, Eq.6.1**
01HT	13	1.725±0.028	0.843±0.015	0.999
02HT	13	2.034±0.080	0.799±0.028	0.992
03HT	16	1.685±0.030	0.869±0.020	0.996
04HT	16	1.861±0.015	0.673±0.010	0.998

Table A.2: HTPB burning in GOX under p_c of 13 and 16 bar, time–averaged r_f and G_{ox} for SLs of performed tests. Consistency checks results are reported in Table 8.4.

Test No.	**p_c, bar**	$< G_{ox}(t_{fin,\,SL}) >$**,** $kg/(m^2 s)$	$< r_f(t_{fin,\,SL}) >$**, mm/s**
01HT	13	281.9	0.852
02HT	13	268.4	1.026
03HT	16	208.3	0.750
04HT	16	192.6	0.661

Table A.3: HTPB burning in GOX under p_c of 13 and 16 bar, time–averaged r_f and G_{ox} for 1^{st} TL of performed tests. Consistency checks results are reported in Chapter 8, Section 8.2.1.

Test No.	**p_c, bar**	**Smoothing Step**	$< G_{ox}(t_{fin,\,1^{st}TL}) >$, $kg/(m^2 s)$	$< r_f(t_{fin,\,1^{st}TL}) >$, **mm/s**
01HT	13	5	110.6	0.505
02HT	13	3	93.2	0.446
03HT	16	3	75.8	0.388
04HT	16	5	77.5	0.305

Table A.4: HTPB burning in GOX under p_c of 13 and 16 bar, time–averaged r_f and G_{ox} for 2^{nd} TL of performed tests. Consistency checks results are reported in Chapter 8, Section 8.2.1. Note data for Test No. 04HT are not available due to combustion quality hindering data sampling.

Test No.	**p_c, bar**	**Smoothing Step**	$< G_{ox}(t_{fin,\,2^{nd}TL}) >$, $kg/(m^2 s)$	$< r_f(t_{fin,\,2^{nd}TL}) >$, **mm/s**
01HT	13	7	71.3	0.394
02HT	13	3^a	69.7	0.358
03HT	16	7	56.3	0.469
04HT	16	NA	NA	NA

^{a}An additional term is added to Eq. A.3, see Chapter 8, Section 8.2.1.

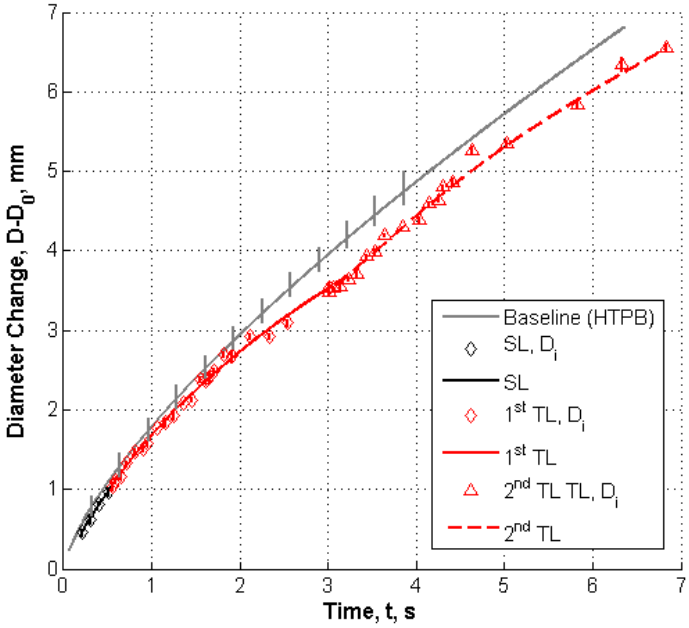

Figure A.1: Test No. 01HT, diameter change in time (see Eq. A.1 for SL and Eq. A.3 for TLs). Sampled diameters of 1^{st} TL smoothed with step 5, data of 2^{nd} TL smoothed with step 7.

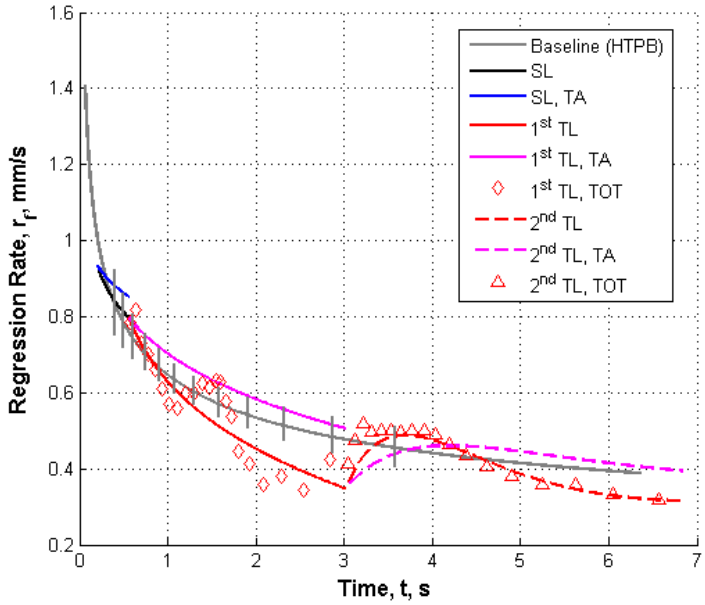

Figure A.2: Test No. 01HT, r_f vs. t (r_f defined as time–derivative of Eq. A.1 for SL and Eq. A.3 for TLs). Sampled diameters of 1^{st} TL smoothed with step 5, data of 2^{nd} TL smoothed with step 7. Note high agreement between TOT and analytical data for 2^{nd} TL.

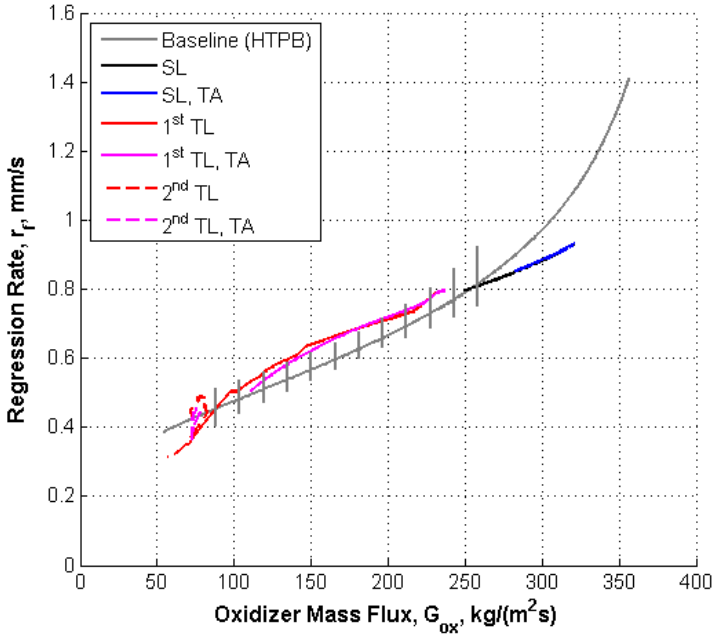

Figure A.3: Test No. 01HT, r_f vs. G_{ox} (r_f defined as time–derivative of Eq. A.1 for SL and Eq. A.3 for TLs). Sampled diameters of 1^{st} TL smoothed with step 5, data of 2^{nd} TL smoothed with step 7.

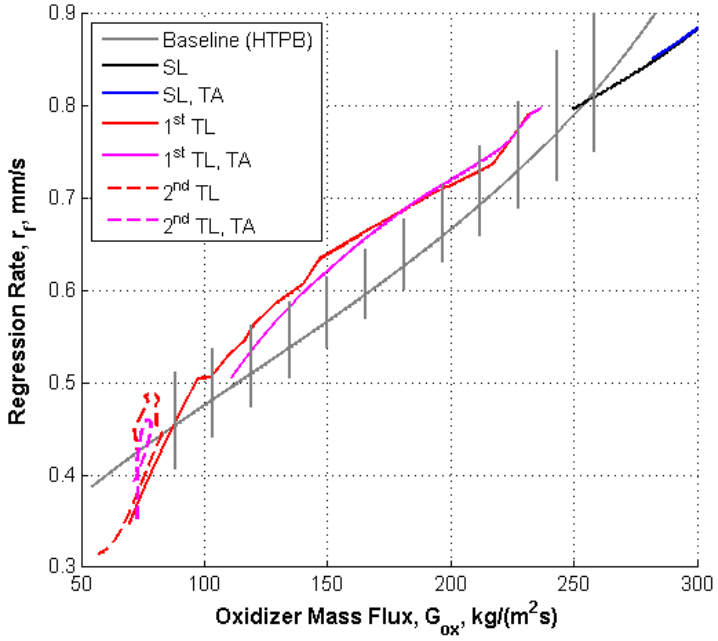

Figure A.4: Test No. 01HT, detail of r_f vs. G_{ox} (r_f defined as time–derivative of Eq. A.1 for SL and Eq. A.3 for TLs). Sampled diameters of 1^{st} TL smoothed with step 5, data of 2^{nd} TL smoothed with step 7. Note confused G_{ox} trend due to $\dot{m}_{ox}(t)$ and $\bar{D}(t)$ increases during the earlier phases of the transient followed by A monotone decrease (reduced or null $\dot{m}_{ox}(t)$ variation and $\bar{D}(t)$ increase due to fuel consumption).

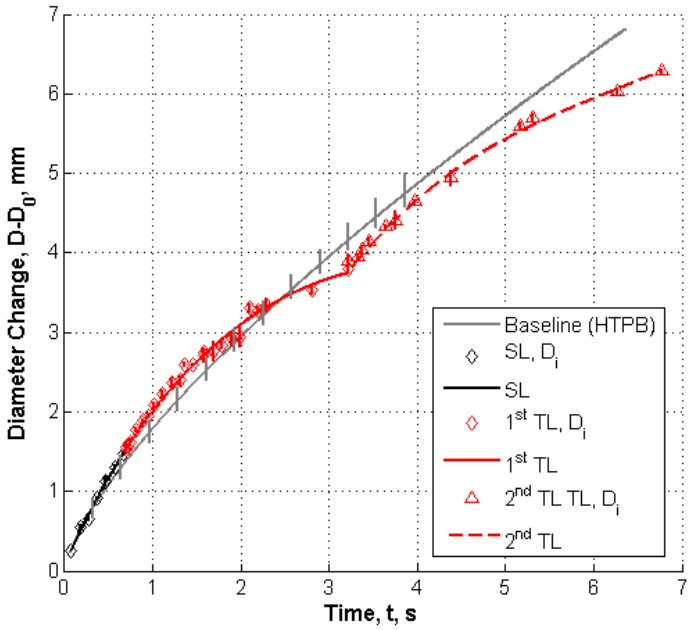

Figure A.5: Test No. 02HT, diameter change in time (see Eq. A.1 for SL and Eq. A.3 for TLs). Sampled diameters of 1^{st} TL smoothed with step 3, data of 2^{nd} TL smoothed with step 3. An additional term is added to the original Eq. A.3 for 2^{nd} TL.

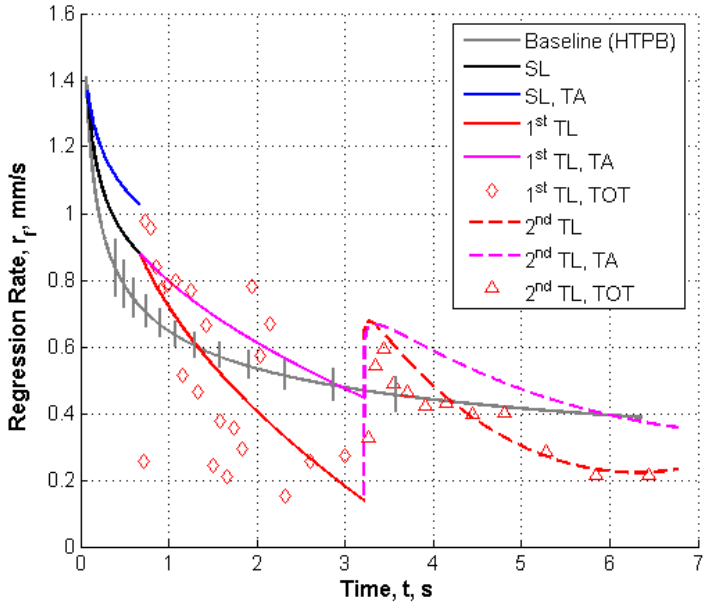

Figure A.6: Test No. 02HT, r_f vs. t (r_f defined as time–derivative of Eq. A.1 for SL and Eq. A.3 for TLs). Sampled diameters of 1^{st} TL smoothed with step 3, data of 2^{nd} TL smoothed with step 3. Note marked overshoot of r_f in 2^{nd} TL (with good agreement between TOT and analytical data).

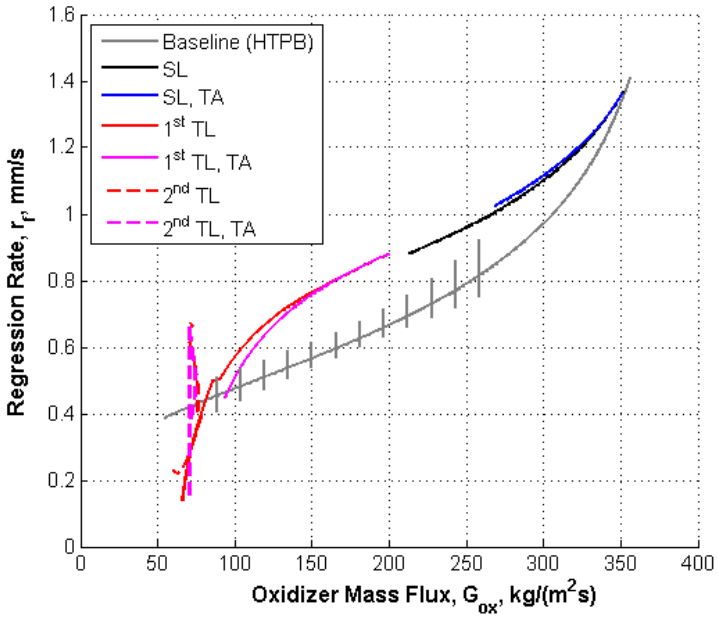

Figure A.7: Test No. 02HT, r_f vs. G_{ox} (r_f defined as time–derivative of Eq. A.1 for SL and Eq. A.3 for TLs). Sampled diameters of 1^{st} TL smoothed with step 3, data of 2^{nd} TL smoothed with step 3.

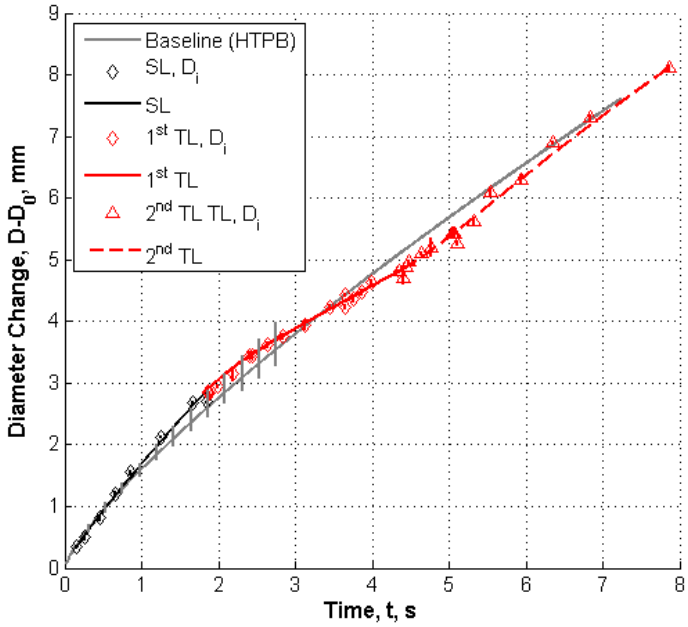

Figure A.8: Test No. 03HT, diameter change in time (see Eq. A.1 for SL and Eq. A.3 for TLs). Sampled diameters of 1^{st} TL smoothed with step 3, data of 2^{nd} TL smoothed with step 7.

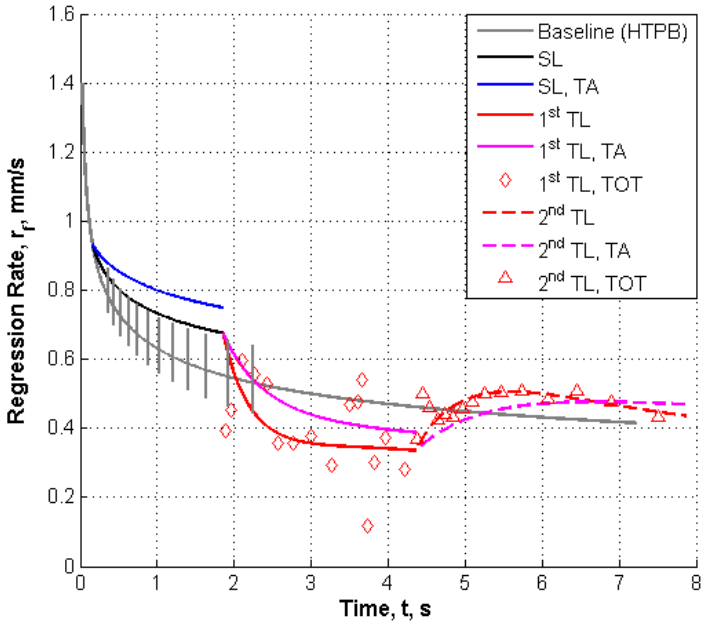

Figure A.9: Test No. 03HT, r_f vs. t (r_f defined as time–derivative of Eq. A.1 for SL and Eq. A.3 for TLs). Sampled diameters of 1^{st} TL smoothed with step 3, data of 2^{nd} TL smoothed with step 7.

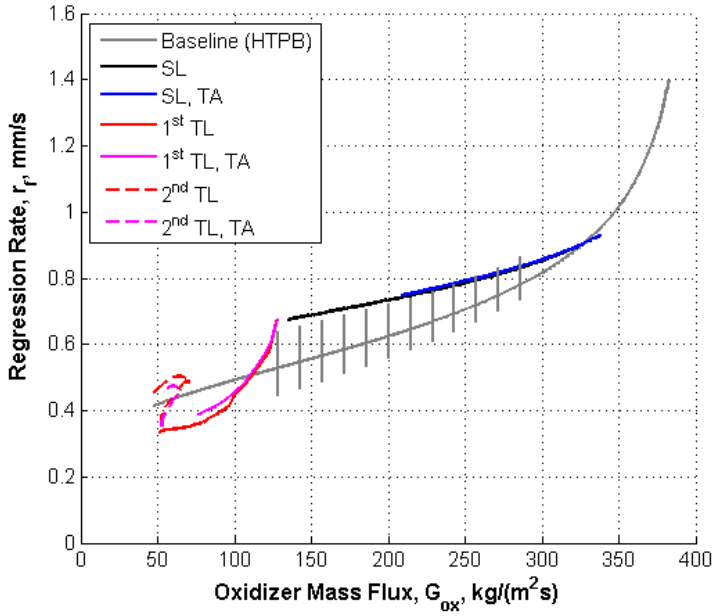

Figure A.10: Test No. 03HT, r_f vs. G_{ox} (r_f defined as time–derivative of Eq. A.1 for SL and Eq. A.3 for TLs). Sampled diameters of 1^{st} TL smoothed with step 3, data of 2^{nd} TL smoothed with step 3.

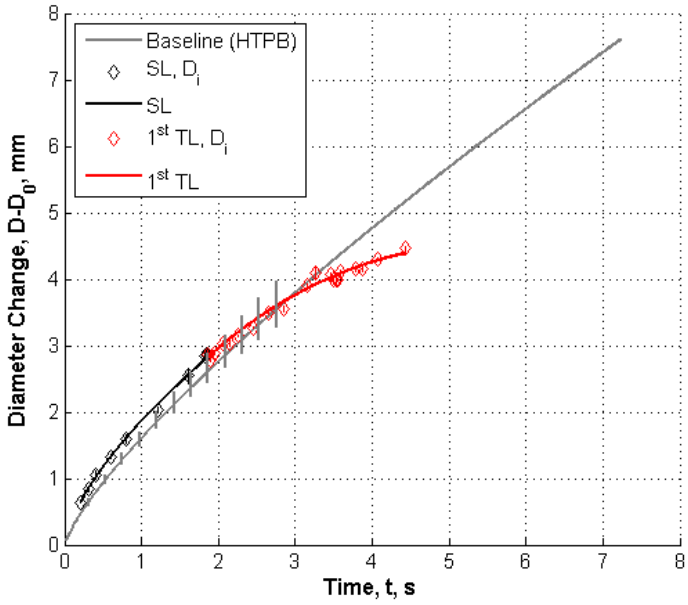

Figure A.11: Test No. 04HT, diameter change in time (see Eq. A.1 for SL and Eq. A.3 for 1^{st} TL). Sampled diameters of 1^{st} TL smoothed with step 5, combustion quality hindered possible data treatment for 2^{nd} TL.

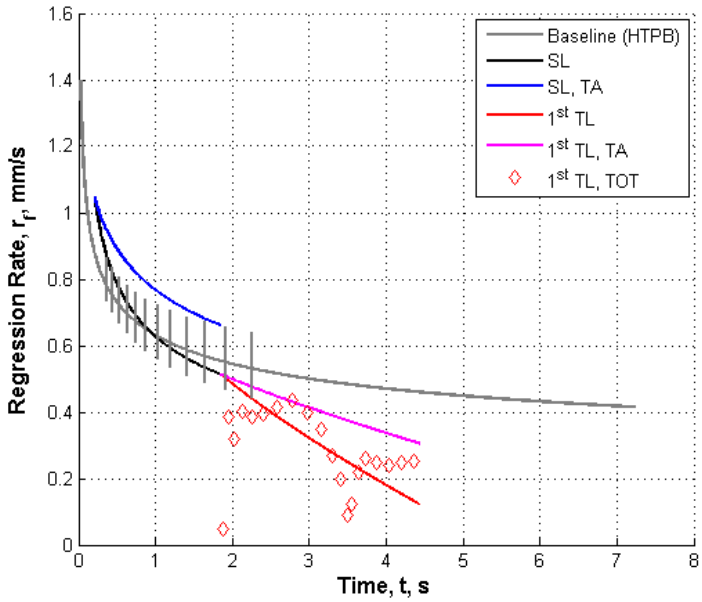

Figure A.12: Test No. 04HT, r_f vs. t (r_f defined as time–derivative of Eq. A.1 for SL and Eq. A.3 for 1^{st} TL). Sampled diameters of 1^{st} TL smoothed with step 5, combustion quality hindered possible data treatment for 2^{nd} TL.

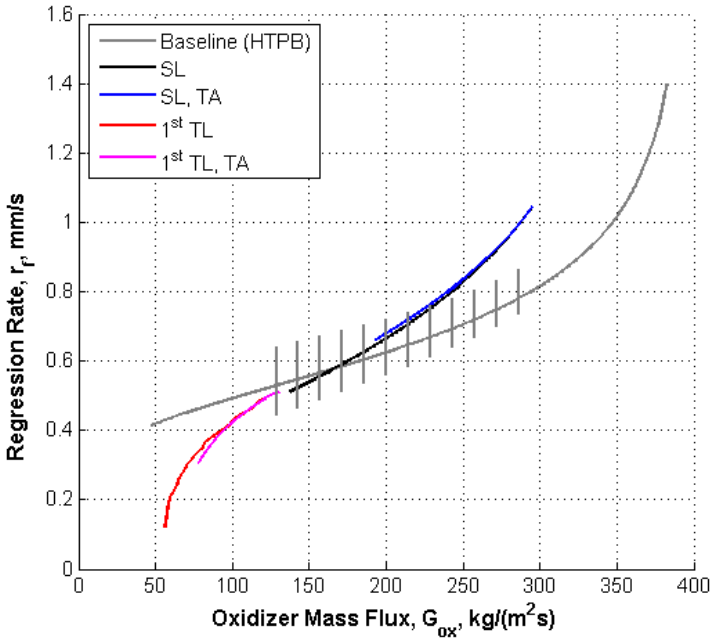

Figure A.13: Test No. 04HT, r_f vs. G_{ox} (r_f defined as time–derivative of Eq. A.1 for SL and Eq. A.3 for TLs). Sampled diameters of 1^{st} TL smoothed with step 3, combustion quality hindered possible data treatment for 2^{nd} TL.

BIBLIOGRAPHY

[1] Annovazzi, A. and L.T. DeLuca. 2009. Solid Rocket Motors. In: Energetic Problems in Aerospace Propulsion, 3rd Edition - Notes for Students. Edited by L.T. DeLuca, Premani, Pantigliate - Milano. Chapter 11, pp. 1–104.

[2] Boccaletto, L. and L.T. DeLuca. 2009. Liquid Rocket Engines. In: Energetic Problems in Aerospace Propulsion, 3rd Edition - Notes for Students. Edited by L.T. DeLuca, Premani, Pantigliate - Milano. Chapter 10, pp. 1–58.

[3] DeLuca, L. T. 2009. Hybrid Rocket Engines. In: Energetic Problems in Aerospace Propulsion, 3rd Edition - Notes for Students. Edited by L.T. DeLuca, Premani, Pantigliate - Milano. Chapter 12, pp. 1–92.

[4] Altman, D. and A. Holzman. 2007. Overview and History of Hybrid Rocket Propulsion. In: Fundamentals of Hybrid Rocket Combustion and Propulsion, Edited by M.J. Chiaverini, and K.K. Kuo, AIAA Progress in Astronautics and Aeronautics, Volume 218. Chapter 1, pp. 1–36.

[5] Boardman, T.A. 2001. Hybrid Propellant Rockets. In: Rocket Propulsion Elements, 7th Edition. Edited by G.P. Sutton and O. Biblarz. John Wiley and Sons, 2001. Chapter 15, pp. 579 – 607.

[6] Marxman, G.A. and M. Gilbert. 1963. Turbulent Boundary Layer Combustion in the Hybrid Rocket. In: 9th International Symposium on Combustion, Academic Press, Inc., New York. 371-383.

[7] Marxman, G.A. 1967. Boundary Layer Combustion in Propulsion. In: Proceedings of the 11th Symposium (International) on Combustion, The Combustion Institute. Pittsburgh, Pennsylvania. Pp. 269-289.

[8] Marxman, G.A. and C.E. Wooldridge. 1968. Research on the Combustion Mechanism of Hybrid Rockets. In: Advances in Tactical Rocket Propulsion, edited by Penner, S.S., AGARD Conference Proceedings No. 1, pp. 421-477.

[9] SPARTAN Project Homepage: http://www.spartanproject.eu.

[10] Scaled Composites Homepage: http://www.spacedev.com.

[11] Chiaverini, M.J. 2007. Review of Solid Fuel Regression Rate Behavior in Classical and Nonclassical Hybrid Rocket Motors. In: Fundamentals of Hybrid Rocket Combustion and Propulsion. Edited by M.J. Chiaverini, and K.K. Kuo, AIAA Progress in Astronautics and Aeronautics, Volume 218. Chapter 2, pp. 37–125.

[12] Risha, G.A., B.J. Evans, E. Boyer, and K.K. Kuo. 2007. Metals, Energetic Additives and Special Binders Used in Solid Fuels for Hybrid Rockets. In: Fundamentals of Hybrid Rocket Combustion and Propulsion. Edited by M.J. Chiaverini, and K.K. Kuo, AIAA Progress in Astronautics and Aeronautics, Volume 218. Chapter 10, pp. 413–456.

[13] Karabeyoglu, M.A., D. Altman, and B.J. Cantwell. 2002. Combustion of Liquefying Hybrid Propellants: Part 1, General Theory. In: Journal of Propulsion and Power, Vol. 18, No. 3.

[14] Karabeyoglu, M.A. and B.J. Cantwell. 2002. Combustion of Liquefying Hybrid Propellants: Part 2, Stability of Liquid Films. In: Journal of Propulsion and Power, Vol. 18, No. 3.

[15] ORPHEE Project Homepage: http://www.orphee–fp7–space.eu.

[16] Maisonneve, Y. and G. Lengellé. 2002. Hybrid Propulsion: Past, Present and Future Perspectives. In: Proceedings of the 8th International Workshop on Combustion and Propulsion, Naples.

[17] Monti, R., S. Sorge, and V. Recchi. 1973. Design and Preliminary Tests of an Hybrid Propellant Rocket. L'Aerotecnica, Missili e Spazio, No. 6 (in Italian).

[18] Monti, R. and Mazzola, M. 1978. Continuous Regression Rate Measurements in Hybrid Rockets. Experimental Diagnostics in Combustion of Solids, AIAA Progress in Aeronautics and Astronautics, Edited by T.L. Boggs and B.T. Zinn, Vol. 63. Pp. 111-128.

[19] Russo Sorge, A. 2002. The state of art of hybrid propulsion research in Italy. Proceedings of the 8th International Workshop on Combustion and Propulsion, Pozzuoli, pp. 09,1 – 09,7.

[20] Cauty, F., C. Carmicino, and A. Russo Sorge. 2005. The Pressure Sensitivity of the Ultrasonic Waves Velocity: a Contribution to a Better Determination of the Energetic Material Regression Rate. Presented at 6th ISICP, Santiago, Chile.

[21] Carmicino, C. and A. Russo Sorge. 2003. Investigation of the Fuel Regression Rate Dependence on Oxidizer Injection and Chamber Pressure in a Hybrid Rocket. AIAA Paper No. 2003-4591.

[22] Carmicino, C., G. Giulietti, T. Marchione, F. Lavorgna, and A.M. Russo Sorge. 2003. Regresson Rate Measurements in a Hybrid Rocket. In: Volume 8 of IWCP (International Workshop on Chemical Propulsion) – Rocket Propulsion: Present and Future. Edited by L.T. DeLuca, Grafiche CSS Bergamo, Italy. Chapter 13.

[23] Carmicino, C. and A. Russo Sorge. 2005. Role of Injection in Hybrid Rockets Regression Rate Behavior. Journal of Propulsion and Power, Vol. 21, No. 3.

[24] Carmicino, C., O. Orlandi, A. Russo Sorge, F. Dauch, A. De Amicis, and M. De Rosa. 2009. Basic Aspects of the Hybrid Engine Operation. AIAA Paper No. 2009-4937.

[25] Carmicino, C., A. Russo Sorge, O. Orlandi, H. Blanchard, P. Yvart, and P. Gautier. 2011. Advanced Solid Fuels for Hybrid Propulsion: the Research Activity in Europe. AIAA Paper No. 2011–5820.

[26] Casalino, L. and D. Pastrone. 2005. Optimal Design and Control of Hybrid Rockets for Access to Space. AIAA Paper 2005–3547.

[27] Casalino, L. and D. Pastrone. 2005. Oxidizer Control and Optimal Design of Hybrid Rockets for Small Satellites. Journal of Propulsion and Power, Vol. 21, No. 2, pp. 230–238.

[28] Pastrone, D., L. Casalino, M. Rosa Sentinella, and C. Carmicino. 2007. Acoustic Analysis of Hybrid Rocket Combustion Chambers. AIAA Paper 2007–5368.

[29] Lazzarin, M., M. Faenza, F. Barato, N. Bellomo, A.Bettella, D.Pavarin, and M. Grosse. 2011. CFD Simulation of a Hybrid Rocket Motor with Liquid Injection. AIAA Paper No. 2011–5537.

[30] Barato, F., N. Bellomo, M. Faenza, M. Lazzarin, A. Bettella, D. Pavarin. 2011. A Numerical Model to Analyze the Transient Behavior and Instabilities on Hybrid Rocket Motors. AIAA Paper 2011–5538.

[31] Bosisio, F., H. Raina, A. Colombo, G. Colombo, L. Galfetti, and L. T. DeLuca. 2006. Setting up an Hybrid Microcombustor. Proceedings of the 3rd AAAF On Board Energetic Equipment Conference, Avignon, France, 26—28 Jun.

[32] DeLuca, L.T., L. Galfetti, F. Bosisio, H. Raina, F. Maggi, G. Colombo. 2006. An Hybrid Micro–combustor for Regression Rate Measurements. Proceedings of the 57th IAC (International Astronautical Congress), Valencia, Spain, 2—6 October. IAC-06-C4.2.01.

[33] Galfetti, L., L.T. DeLuca, P. Grassi, C. Paravan, V. Luoni, A. Bandera, G. Colombo, L. DeCillia, R. Sempio, and H. Raina. 2008. Combustion Behavior Investigation of Solid Fuels Using a Micro-sized Hybrid Rocket Motor. In: Advancements in Energetic Materials and Chemical Propulsion, edited by Kenneth K. Kuo, and Keiichi Hori. Begell House. Pp. 199–213.

[34] Paravan, C., M. Viscardi, L.T. DeLuca, and L. Prada López. 2009. Anisotropy Effects in Hybrid Fuels Burning in a Micro-burner. Proceedings of XX AIDAA Congress, Milan, Italy, 29 Jun–03 Jul.

[35] Galfetti, L., L.T. DeLuca, C. Paravan, L. Merotto, and M. Boiocchi. 2009. Regression Rate and CCPs Measurement of Metallized Solid Fuels. Presented at the 8th ISICP (International Symposium on Chemical Propulsion). Cape Town, South Africa.

[36] Paravan, C., M. Viscardi, L.T. DeLuca, and A. Kazakov. 2009. Regression Rates and Anisotropy Effects in Hybrid Rockets Microburner. Presented at 3rd EUCASS (European Conference for Aerospace Sciences) Conference, Versailles, France 04–07 Jul 2009.

[37] DeLuca, L.T., C. Paravan, A. Reina, M. Marchesi, F. Maggi, A. Bandera, G. Colombo, B.M. Kosowski. 2010. Aggregation and Incipient Agglomeration in Metallized Solid Propellants and Solid Fuels for Rocket Propulsion. AIAA Paper 2010-6752.

[38] DeLuca, L.T., L. Galfetti, F. Maggi, G. Colombo, A. Reina, S. Dossi, D. Consonni, and M. Brambilla, 2011. Innovative Metallized Formulations for Solid or Hybrid Rocket Propulsion. Presented at International Autumn Seminar on Propellants, Explosives and Pyrotechnics (IASPEP) 2011, Nanchino, China, 20–23 Sep.

[39] DeLuca, L.T., L. Galfetti, F. Maggi, G. Colombo, C. Paravan, A. Reina, P. Tadini, A. Sossi, and E. Duranti. 2011. An Optical Time-Resolved Technique of Solid Fuels Burning for Hybrid Rocket Propulsion. AIAA Paper 2011-5753.

[40] Paravan, C., A. Sossi, A. Reina, G. Massini, M. Manzoni, E.Duranti, G. Rambaldi, A. Adami, E. Seletti, and L.T. De Luca. 2011. Time-Resolved Regression Rate of Innovative Hybrid Solid Fuel Formulations. Submitted for pubblication in Advances in Propulsion Physics, Vol. 3rd. Paper under review.

[41] Estey, P., D. Altman, and J. McFarlane. 1991. An Evaluation of Scaling Effects for Hybrid Rocket Motors. In: Proceedings of the 27th AIAA/ASME/SAE/ASEE Joint Propulsion Conference. AIAA Paper No. 91–2517. June 24-26, 1991.

[42] Strand, L.D., M.D. Jones, R.L. Ray, and N.S. Cohen. 1994. Characterization of Hybrid Rocket Internal Heat Flux and HTPB Fuel Pyrolysis. In: Proceeding of the 30th AIAA/ASME/SAE/ASEE Joint Propulsion Conference. AIAA Paper No. 1994–2876. June 27-29, 1994.

[43] Chiaverini, M.J., K.K. Kuo, A. Peretz, and G.C. Harting. 2001. Regression Rate and Heat-Transfer Correlations for Hybrid Rocket Combustion. In: Journal of Propulsion and Power, Vol. 18, No. 3, May-June 2001.

[44] Chiaverini, M.J., N. Seryn, D.K. Johnson, Y.-C. Lu, K.K. Kuo, and G.A. Risha. 2000. Regression Rate Behavior of Hybrid Rocket Solid Fuel. In: Journal of Propulsion and Power, Vol. 16, No. 1. Pp. 125–132.

[45] Cauty, F., N. Seryn, and D. Gramer. 2007. Solid–fuel Pyrolysis Phenomena and Regression Rate, Part 2: Measurement Techniques. In: Fundamentals of Hybrid Rocket Combustion and Propulsion. Edited by M.J. Chiaverini, and K.K. Kuo, AIAA Progress in Astronautics and Aeronautics, Volume 218. Chapter 4, pp. 167–205.

[46] Risha, G.A., G.C. Harting, K.K. Kuo, A. Peretz, D.E. Koch, H. Stephen Jones, and J.P. Arves. 1998. Pyrolysis and Combustion of Solid Fuels in Various Oxidizing Eenvironments. AIAA Paper No. 1998–3184–556.

[47] George, P., S. Krishnan, P.M. Varkey, M. Ravindran, and L. Ramachandran. 1998. Fuel Regression Rate Enhancement Studies in HTPB/GOX Hybrid Rocket Motors, In: Proceedings of the 34th AIAA/ASME/SAE/ASEE Joint Propulsion Conference and Exhibit. AIAA Paper A98-35064.

[48] Smoot, L. D. and C.F. Price. 1965. Regression Rates of Nonmetalized Hybrid Fuel Systems. In: AIAA Journal, Vol. 3, No. 8. Pp. 1408-1413.

[49] Smoot, L. D. and C.F. Price. 1965. Regression Rates of Metalized Hybrid Fuel Systems. In: AIAA Journal, Vol. 4, No. 5. Pp. 910–915.

[50] Smoot, L. D. and C.F. Price. 1966. Pressure Dependence of Hybrid Fuel Regression Rates. In: AIAA Journal, Vol. 5, No. 1.

[51] Gater, R.A. and M.R.L. L'Ecuyer. 1970. A Fundamental Investigation of the Phenomena that Chracterize Liquid Film Cooling. International Journal of Heat and Mass transfer, Vol.13, No.3. Pp. 1925–1939.

[52] Knuth, W.A., M.J. Chiaverini, J.A. Sauer, and D.J. Gramer. 2002. Solid–Fuel Regression Rate Behavior of Vortex Hybrid Rocket Engines. Journal of Propulsion and Power, Vol. 18, No. 3. Pp. 600–609.

[53] Haag, G., M. Sweeting, and G. Richardson. 2000. An Alternative Geometry Hybrid Rocket for Spacecraft Orbit Transfer Manoeuvers. IAF Paper 00–W.2.07.

[54] Lee, C., Y. Na, e G. Lee. 2005. The Enhancement of Regression Rate of Hybrid Rocket Fuel by Helical Grain Configuration and Swirl Flow. AIAA Paper No. 2005-3906.

[55] Shin, K.H., C. Lee, and S.Y. Chang. 2005. The Enhancement of Regression Rate of Hybrid Rocket Fuel by Various Methods. AIAA Paper No. 2005-0359.

[56] Frederick, R.A., J.J. Whitehead, L.R. Knox, and M.D. Moser. 2007. Regression Rates Study of Mixed Hybrid Propellants. In: Journal of Propulsion and Power, Vol.23, No.1.

[57] Lips, H.R. 1976. Metal Combustion in High Performance Hybrid Rocket Propulsion Systems. AIAA Paper 76-640.

[58] Strand, L.D., R.L. Ray, F.A. Anderson, and N.S. Cohen. 1992. Hybrid Rocket Fuel Combustion and Regression Rate Study. AIAA Paper 92-3302.

[59] Price, E.W. 1984. Combustion of Metalized Propellants. In: Fundamentals of Solid Propellants Combustion. Edited by K.K. Kuo, and M. Summerfield, AIAA Progress in Aeronautics and Astronautics, Vol. 90. AIAA. Chapter 9, pp. 479–513.

[60] DeLuca, L.T. 2009. Metal Combustion. In: Energetic Problems in Aerospace Propulsion, 3rd Edition - Notes for Students. Edited by L.T. DeLuca. Premani, Pantigliate–Milano. Chapter 6, pp. 1–37.

[61] Natan, B. and A. Gany. 1991. Ignition and Combustion of Boron in the Flowfiled of a Solid Fuel Ramjet. Journal of Propulsion, Vol. 7, No. 1, Jan–Feb 1991. Pp. 37–43.

[62] Karadimitris, A., C. Scott, and A. Gany. 1991. Regression and Combustion of Boron Containing Fuels for Solid Fuel Ramjets. Journal of Propulsion, Vol. 7, No. 3, May–Jun 1991. Pp. 341–347.

[63] Gany, A. 2006. Comprehensive Consideration of Boron Combustion in Airbreathing Propulsion. AIAA Paper No. 2006–4567.

[64] Ilyin A.P., A.A. Gromov, and G.V. Yablunovski. 2001. Reactivity of Aluminum Powders. Combustion Explosion and Shock Waves, Vol.37, No.4. Pp. 418–422.

[65] Storozhenko, P.A., S.L. Guseinov, and S.I. Malashin. 2009. Nanodispersed Powders: Synthesis Methods and Practical Applications. Nanotechnology in Russia, Vol. 04, Nos. 05-06. Pp. 262-274.

[66] Ivanov, Y.F., M.N. Osmonoliev, V.S. Sedoi, V.A. Arkhipov, S.S. Bondarchuk, A.B. Vorozhtsov, A.G. Korotkikh, and V.T. Kuznetsov. 2003. Productions of Ultra-Fine Powders and Their Use in High Energetic Compositions. In: Propellants, Explosives, Pyrotechnics, Vol.28, No. 6. Pp. 319-333.

[67] Gromov, A.A., A. Ilyin, V. An, F. Faubert, C. de Izarra, A. Espagnacq, and L. Brunet. 2002. Characterization of Aluminum Powders: I. Parameters of Reactivity of Aluminum Powders. In: Propellants, Explosives, Pyrotechnics, Volume 27, Issue 6. Pp. 361-364.

[68] Gromov, A.A., A. Ilyin, U. Forter-Barth, Teipel. 2006. Characterization of Aluminum Powders: II. Aluminum Nanopowders Passivated by Non-Inert Coatings. In : Propellants, Explosives, Pyrotechnics, Volume 31, Issue 5. Pp. 401-409.

[69] Levitas, V.I., B.W. Asay, S.F. Son, and M. L. Pantoya. 2007. Mechanochemical Mechanism for Fast Reaction of Metastable Intermolecular Composites Based on Dispersion of Liquid Metal. journal of Applied Physics, Volume 101. Pp. 4231-4235.

[70] Dikici, B., S. W. Dean, M. L. Pantoya, V. I. Levitas, and R. J. Jouet. 2009. Influence of Aluminum Passivation on the Reaction Mechanism: Flame Propagation Studies. Energy Fuels, Volume 23. Pp. 4231-4235.

[71] Risha, G.A., A. Ulas, E. Boyer, S. Kumar, and K.K. Kuo. 2001. Combustion of Solid Fuels Containing Nano-sized Energetic Powder in a Hybrid Rocket Motor. AIAA Paper 2001-3535.

[72] Risha, G.A., B. Evans, E. Boyer, R.B. Wehrman, and K.K. Kuo. 2003. Nano-sized Aluminum, and Boron-based Solid Fuel Characterization in a Hybrid Rocket Engine. AIAA Paper 2003-4593.

[73] Sarner, S.F. 1966. Propellant Chemistry. Reinhold Publishing Corporation.

[74] Osmon, R.V. 1966. An Experimental Investigation of a Lithium Aluminum Hydride–Hydrogen Peroxide Hybrid Rocket. In: Aerospace Chemical Engineering. Edited by D.J. Simkin. Chemical Engineering Progress Symposium Series, Vol. 62, No. 21, American Institute of Chemical Engineers. Pp. 92–102.

[75] Larson, B.D., E. Boyer, T. Wachs, K.K. Kuo, J.D. DeSain, T.J. Curtiss, and B.B. Brady. 2011. Characterization of the Performance of Paraffin / $LiAlH_4$ Solid Fuels in a Hybrid Rocket System. AIAA Paper 2011-5822.

[76] DeSain, J.D., T.J. Curtiss, K. Metzler, and B.Brady. 2011. Testing Hypergolic Ignition of Paraffin Wax/LiAlH4 Mixtures. AIAA Paper 2011-6636.

[77] Humble, R.W. 2000. Fuel Performance Enhancements for Hybrid Rockets. AIAA Paper 2000–3437.

[78] Calabro, M., L.T. DeLuca, L. Galfetti, and C. Perut. 2007. Advanced Hybrid Solid Fuels. IAC-07-C4.2.09, 58th International Astronautical Congress, Hyderabad, India.

[79] Maggi, F., G. Gariani, L. Galfetti, and L.T. DeLuca. 2012. Theoretical Analysis of Hydrides in Solid and Hybrid Rocket Propulsion. Journal of Hydrogen Energy, Vol. 37. Pp. 1760–1769.

[80] DeLuca, L.T., L. Galfetti, F. Severini, L. Rossettini, L. Meda, G. Marra, B. D'Andrea, V. Weiser, M. Calabro, A.B. Vorozhtsov, A.A. Glauznov, G.J. Pavlovets. 2007. Physical and Ballistic Characterization of AlH3-based Space Propellants. Aerospace Science and Technology, No. 11. Pp. 18-25.

[81] Bazyn, T., R. Eyer, H. Krier, N. Glumac. 2004. Dehydrogenation and Burning of Aluminum Hydride at Elevated Pressures. AIAA Paper 2004–789.

[82] Rossettini, L. 2008. Aluminum Hydride Analysis and Applications in Advanced Space Propulsion. PhD Dissertation. Politecnico di Milano, Energetics Department.

[83] Klager, K. 1984. Polyurethanes, the most versatile binder for Solid Rocket Propellants. AIAA Paper No. 84–1239.

[84] Haska, S.B., E. Bayramli, F. Pekel, and S. Ozkar. 1997. Mechanical Properties of HTPB–IPDI–based Elastomers. Journal of Applied Polymer Science. Pp. 2347–2354.

[85] Layton L.H. 1975. Chemical Structural Aging Studies on an HTPB Propellant. AD-A010 731, Thiokol Corporation, Brigham City, Utah.

[86] Akbas, A., S. Aksoy, and N. Hasirci. 1994. Effects of Thermal Ageing on the Properties and Lifetime Prediction of Hydroxyl–Terminated Polybutadiene. Polymer Journal, Vol. 35, No. 12. Pp. 2568–2572.

[87] Kinney G.F. 1957. Engineering Properties and Applications of Plastics. John Wiley & Sons. Chapter 18, pp. 233–238.

[88] Advanced Powder Technologies Website. 2011. www.nanosized–powders.com

[89] Sossi, A., E. Duranti, C. Paravan, L.T. DeLuca, A. B. Vorozhtsov, A.A. Gromov, M. I. Lerner, N. G. Rodkevich, B. M. Kosowsky, and T. I. Sigfusson. 2011. Experimental Study of Aluminum Nanopowders Produced by EEW and Coated by Hydrocarbon and Fluorohydrocarbon Coatings. Paper submitted for publication to Journal of Nanoparticle Research.

[90] Kwon, Y., A.A. Gromov, A. P. Ilyin, and G. H. Rim. 2003. Passivation Process for Superfine Aluminum Powders Obtained by Electrical Explosion of Wires. In : Applied Surface Science, Volume 211, Issues 1-4, pp. 57-67.

[91] 3M Material Safety Data Sheet FC–2175 Fluorel (TM) Brand Fluoroelastomer, 10/13/2010.

[92] Kwon, Y., A.A. Gromov, and J. I. Strokova. 2007. Passivation of the Surface of Aluminum Nanopowders by Protective Coatings of the Different Chemical Origin. In: Applied Surface Science, Volume 253, Issue 12, pp. 5558-5564.

[93] Chen, L., W. L. Song, J. Lv, L. Wang, and C. S. Xie. 2009. Effect of Heating Rates on TG-DTA Results of Aluminum Nanopowders Prepared by Laser Heating Evaporation. In: Journal of Thermal Analysis and Calorimetry, Volume 96, No. 1, pp. 141-145.

[94] Ilyn, A.P., G.V. Yablunovskii, and A.A. Gromov. 1996. Influence of Additives on Combustion of Ultradisperse Aluminum Powder and Chemical Binding of Air and Nitrogen. Combustion Explosion and Shock Waves, Vol. 32, No. 2. Pp. 211–213.

[95] Ivanov, V.G. and O.V. Gavrilyuk. 1999. Specific Features of the Oxidation and Self-Ignition of Electroexplosive Ultradisperse Metal Powders in Air. Combustion, Explosion and Shock Waves, No. 35. Pp. 648–655.

[96] Gromov, A.A., Y. Strokova, A. Kabardin, A. Vorozhtsov, and U. Teipel. 2009. Experimental Study of the Effect of Metal Nanopowders on the Decomposition of HMX, AP and AN. Propellant Explosives and Pyrotechnics, No. 34. Pp. 506–512.

[97] MACHI website. 2012. www.machichemicals.com

[98] Thome, V., P.B. Kempa, and M. Herrmann. 2003. Structure, Chemical and Physical behavior of Aluminum Hydride. In: Proceedings ICT 2003, Paper P-104.

[99] Ismail, I.M.K. and T. Hawkins. 2005. Kinetics of Thermal Decomposition of Aluminum Hydride: I-non-isothermal Decomposition Under Vacuum and in Inert Atmosphere. Thermochimica Acta, No. 439. Pp. 32-43.

[100] Lee, G.J., J.H. Shim, Y.W. Cho. 2007. Catalytic Effect of Ti_5Si_3 on Thermal Decomposition of Li_3AlH_6. Journal of Material Science, Vol. 42. Pp. 6302–6305.

[101] Reina, A., G. Colombo, L.T. DeLuca, F. Maggi, I. Lesniak, D.B. Lempert, and G.B. Manelis. 2009. Magnesium and Aluminum Ignition in CO2 Atmosphere. Presented at 20th AIDAA Congress, Milan, Italy.

[102] Andreasen A. 2006. Effect of Ti–doping on the Dehydrogenation Kinetics of Lithium Aluminum Hydride. Journal of Alloys and Compounds, No. 419, pp. 40–44.

[103] Nielsen, L.E. 1974. Particulate Filled Polymers. In: Mechanical Properties of Polymers and Composites, Volume 2, Marcel Dekker Inc., New York. Chapter 7, pp. 379-441.

[104] Bronkhorst HI–TECH website. 2011. www.bronkhorst.com

[105] Kulite website. 2011. www.kulite.com

[106] DeLuca, L.T., L. Galfetti, F. Maggi, G. Colombo, L. Merotto, M. Boiocchi, C. Paravan, A. Reina, P. Tadini, and L. Fanton. 2012. Characterization of HTPB-Based Solid Fuel Formulations: Performance, Mechanical Properties, and Pollution. Submitted for pubblication to Acta Astronautica.

[107] Waterfall, R.C., R. He, P. Wolanski, and Z. Gut. 1999. Monitoring Flame Position and Stability in Combustion Cans Using ECT. Presented at 1st World Congress on Industrial Process Tomography, Buxton, Greater Manchester, 14–17 Apr.

[108] Houser, T.J. and M.V. Peck. 1964. Research in Hybrid Combustion. In: Vol. 15 of AIAA Progress in Astronautics and Aeronautics, Heterogeneous Combustion, Edited by H.G. Wolfhard, I. Glassman, and L. Green Jr. Academic Press, New York, NY, USA. Pp. 559-581.

[109] DeZilwa, G. Ziliac, M. Reinat, and M.A. Karabeyoglu. 2004. Time–Resolved Fuel–Grain Port Diameter Measurement in Hybrid Rockets. Journal of Propulsion and Power, Vol. 20, No. 4. Pp. 684–689.

[110] Evans, B., G.A. Risha, N.A. Favorito, E. Boyer, R.B. Wehrman, N. Libis, and K.K. Kuo. 2003. Instantaneous Regression Rate Determination in a Cylindrical X-ray Transparent Hybrid Rocket Motor. AIAA Paper 03-4592.

[111] Evans, B., E. Boyer, K.K. Kuo, G. Risha, and M.J. Chiaverini. 2009. Hybrid Rocket Investigations at Penn State University's High Pressure Combustion Laboratory: Overview and Recent Results. AIAA Paper 2009-5349.

[112] DeLuca, L.T., L. Galfetti, G. Colombo, F. Maggi, A. Bandera, M. Boiocchi, G. Gariani, L. Merotto, C. Paravan, and A. Reina. 2011. Time–Resolved Burning of Solid Fuels for Hybrid Rocket Propulsion. In: Advances in Propulsion Physics, Vol. 2. Taurus Press, Moscow. Pp. 341–362.

[113] DeLuca, L.T. 2009. Thermal Propulsion. In: Energetic Problems in Aerospace Propulsion, 3rd Edition - Notes for Students. Edited by L.T. DeLuca, Premani, Pantigliate - Milano. Chapter 9, pp. 1–68.

[114] Ohlemiller, T.J., and M. Summerfield. 1968. A critical analysis of arc image ignition of solid propellants. AIAA Journal, Vol.6, No.5, pp. 878-886.

[115] Incropera, F.P., and D.P. DeWitt. 1990. Fundamentals of Heat and Mass Transfer, 3rd Edition. Wiley, New York, p. 515.

[116] Kuo, K.K., J.P. Gore, and M. Summerfield. 1980. Transient Burning in Solid Propellants. In: Fundamentals of Solid Propellant Combustion, Edited by K.K. Kuo, and M.J. Summerfield, AIAA Progress in Astronautics and Aeronautics, Volume 90. Chapter 11, pp. 599–659.

[117] Schlichting, H. and K. Gersten. 2003. Unsteady Turbulent Boundary Layers. In: Boundary Layer Theory. Springer Verlag, Berlin. Chapter 21, pp. 645–649.

[118] Gromov, A.A., V. Vereshchagin, A.P. Ilyn, and A. Ditts. 2005. Combustion of Al–Al_2O_3 Mixtures in Air. Juornal of European Ceramic Society, Vol. 25, pp. 1575–1579.

[119] Ilyin, A.P., N.V. Bychin, and A.A. Gromov. 2001. Products of Combustion of Aluminum Hydride in Air. Combustion, Explosion, and Shock Waves, Vol. 37, No. 4, pp. 490–491.

[120] Greatrix, D.R. 2009. Regression Rate Estimation for Standard–Flow Hybrid Rocket Engines. Aerospace Science and Technology, No. 13, pp. 358–363.

[121] Mickley, H.S., R.C. Ross, A.L. Squyers, W.F. Stewart. 1954. Heat Mass and Momentum Transfer for Flow Over a Flat Plate with Blowing or Suction. NASA TN3208.

[122] Moffat, R.J. and W.M. Kays. 1958. The Turbulent Boundary Layer Over a Porous Plate: Experimental Heat Transfer with Uniform Blowing and Suction. International Journal of Heat and Mass transfer, No. 11, pp. 1547–1566.

[123] Evans, B., N.A. Favorito, and K.K. Kuo. 2005. Study of Solid Fuel Burning Rate Enhacement Behavior in a X–ray Translucent Hybrid Rocket Motor. AIAA Paper 2005–3909.

[124] Krishnamurty, V.S. and W. Shivy. 1997. Effect of Wall Roughness on the Flow Through Converging–Diverging Nozzles. Journal of Propulsion and Power, Vol. 13, No. 6, pp. 753–762.

[125] Karabeyoglu, M.A., B.J. Cantwell, and G. Ziliac. 2007. Development of Scalable Space—Time Averaged Regression Rate Expressions for Hybrid Rockets. Journal of Propulsion and Power, Vol. 23, No. 4, pp. 737–747.

[126] Gany, A. 2007. Similarity and Scaling Effects in Hybrid Rocket Motors. In: Fundamentals of Hybrid Rocket Combustion and Propulsion. Edited by M.J. Chiaverini, and K.K. Kuo, AIAA Progress in Astronautics and Aeronautics, Volume 218. Chapter 11, pp. 489–511.

[127] Gordon S. and B.J. McBride. 1994. Computer Program for the Calculation of Complex Chemical Equilibrium Compositions and Applications. NASA Technical Report RP–1311.

[128] CEA website at NASA GRC: www.grc.nasa.gov/WWW./CEAWeb/.

[129] Kubota, N. 2002. Propellants and Explosives, Thermochemical Aspects of Combustion. Wiley–VCH Verlag GmbH, Chapter 4, p. 71.

[130] Arisawa, H. and T.B. Brill. 1996. Flash Pyrolysis of Hydroxil Terminated Polybutadiene (HTPB) I: Analysis and Implications of the Gaseous Products. Combustion and Flame, Vol. 106, pp. 131–143.

[131] Arisawa, H. and T.B. Brill. 1996. Flash Pyrolysis of Hydroxil Terminated Polybutadiene (HTPB) II: Implications of the Kinetics to Combustion of Organic Polymers. Combustion and Flame, Vol. 106, pp. 144–154.

[132] Chiaverini, M.J., G.C. Harting, Y.C. Lu, K.K. Kuo, A. Peretz, S. Jones, B. Weygle, and J.P. Arves. 1999. Pyrolysis Behavior of Hybrid Rocket Solid Fuels Under Rapid Heating Conditions. Journal of Propulsion and Power, Vol. 15, No. 6, pp. 888–895.

[133] Lengellé, G. 2007. Solid Fuel Pyrolysis Phenomena Part I: Mechanism. In: Fundamentals of Hybrid Rocket Combustion and Propulsion. Edited by M.J. Chiaverini, and K.K. Kuo, AIAA Progress in Astronautics and Aeronautics, Volume 218. Chapter 3, pp. 127—163.

[134] Green, A. 2010. Effects of Ignition Transient on the Ballistics of Metallized Solid Fuels for Hybrid Rocket Propulsion. MSc. Thesis, Politecnico di Milano, Aerospace Engineering Department (in Italian).

[135] Fanton, L., C. Paravan, and L.T. DeLuca. 2012. Effects of Radiative Heat Transfer in a Hybrid Micro-Burner. Submitted for pubblication to International Journal of Aerospace Engineering (Special Issue on Chemical Rocket Propulsion).

[136] Karabeyoglu, M.A. 2007. Combustion Instability and Transient Behavior in Hybrid Rocket Motors. In: Fundamentals of Hybrid Rocket Combustion and Propulsion, Edited by M.J. Chiaverini, and K.K. Kuo, AIAA Progress in Astronautics and Aeronautics, Volume 218. Chapter 9, pp. 351–411.

[137] MATLAB User's Guide. 2011. http://www.mathworks.it/help/techdoc/index.html.

[138] Karabeyoglu, M.A. and D. Altman. 1999. Dynamic Modeling of Hybrid Rocket Combustion. Journal of Propulsion and Power, Vol. 15, No. 4, pp. 562–571.

ACKNOWLEDGEMENT

This work was partially supported by:

- ORPHEE (Operational Research Project on Hybrid Engine in Europe), European FP7 Program. Theme 9: Space, Area: SPA-2007.2.2.02 – Space Transportation, WP320.
- CNES (Centre National d'Études Spatiales), Commande Nr. 4700024752 / DLA090 and Commande Nr. 4700028003/DLA094

Advanced Powder Technology LLC (Tomsk, Russia) and MACH I (King of Prussia, Pennsylvania, USA) are aknowledeged for the supplied materials and the precious collaboration.